STRUCTURAL AND ETHYLENE OLIGOMERIZATION STUDIES OF HOMOGENEOUS AND IMMOBILIZED N^O- DONOR IRON(II), NICKEL(II) AND COBALT(II) CATALYSTS

By

Makhosonke Ngcobo

Thesis

Submitted in fulfilment of the requirement for the degree of

Doctor of philosophy

in

Chemistry

in the

College of Agriculture, Engineering and Science

University of KwaZulu-Natal

Pietermaritzburg

Supervisor: Prof Stephen Ojwach

August 2021

DECLARATION

I, **Makhosonke Ngcobo**, declare that this thesis has been compiled solely by me and I also confirm that it has not been submitted, in whole or in part, for any other degree or professional qualification except as specified. The work presented here including experiments and results, is entirely my own, except where it is stated otherwise by means of a reference or acknowledgement. The figures, tables and schemes contained in the text have been composed by me except where specified otherwise in the text acknowledged and/or referenced.

Signature [redacted] Date: 19th August 2021

Supervisor:

As the supervisor of the candidate, I have approved the submission of this PhD thesis for submission.

Signature: [redacted] … Date: 14th September, 2021

DEDICATION

This thesis is dedicated to my daughter, Kwamkuhle.

ACKNOWLEDGEMENTS

- I am forever thankful to God, the Alfa and the Omega, for giving me enough strength and perseverance to finish my PhD degree. God have been the pillar of my strength, source of comfort and the light in my darkest despair. I am earnestly appreciative be given the opportunity of a lifetime to brighten my future and become a Doctor of Philosophy in Chemistry.
- I would like to pass my sincere gratitude to my supervisor, Prof Stephen Ojwach. Your profound dedication, guidance, patience and constructive advices throughout the course of my research work gave me hope and strength to carry on, especially in the times where I felt like given up. You have been an inspiration and motivation in my endless journey of knowledge. Thank you very much for helping me to achieve my PhD degree, without your supervision it is without doubt that this would not have been possible.
- I am grateful to the University of KwaZulu-Natal and the School of Chemistry and Physics, of which all this whole work would have not been possible without. I would like to acknowledge the major role played by my colleagues in the School of Chemistry and the Microscopy and Microanalysis Unit (MMU).
- The financial assistance from the National Research Foundation (NRF) is highly appreciated and acknowledged.

- To my warm, loving and caring family, the family I always went back to for emotional, spiritual and moral support, I would like to pass a very special thanks and acknowledgement for their support, patience, care and love.

PREFACE

The discovery of homogeneous catalysts both early and late transition metal-based complexes was a major breakthrough in ethylene oligomerization to date. Their extensive research developments and advances in academic and industrial sectors also agrees precisely with their significant role they are currently playing in the production of vital short and long chain α-olefins ($C_4 – C_{20}$) which are used in the manufacturing of plasticizers, adhesives, lubricants and surfactants. Despite the attractive properties displayed by homogeneous catalysts their difficulties in separation from the reaction mixture and reusability still constitutes a major problem in their applicability in ethylene oligomerization reactions. As a result, immobilization of these homogeneous systems on solid supports such as silica (SBA-15 and MCM-41), silica-alumina and polymers will be very advantageous in ethylene oligomerization reactions since it will lead to the development of catalytically active, selective, recyclable and reusable hybrid catalysts for ethylene oligomerization processes. Catalysis main areas such as catalyst activity, selectivity and stability are the rationale behind this research study. In addition, the quest to develop recyclable and reusable single-site catalyst underlines the rationale of this thesis. This thesis constitutes seven chapters as follows:

Chapter one covers the background introduction on ethylene oligomerization reactions; highlighting the industrial significance of ethylene monomer and the role played by both homogeneous and heterogeneous late transition metal complexes in converting ethylene monomer into more valuable products during ethylene oligomerization reactions. This chapter further introduces immobilization techniques and the types of solid supports that can be used to produce separable single-site catalysts. Applications of olefins and their role in human daily live activities are also highlighted. **Chapter two** reviews relevant literatures on the use of immobilized late transition metal complexes in the oligomerization of ethylene reactions.

Recent advances in the immobilization of late-transition metal complexes, particularly, nickel(II), cobalt(II), iron(II) and palladium(II) complexes in order to achieved hybrid catalysts are discussed.

Chapter three describes the syntheses of homogeneous (ethylimino-methyl)phenol (N^O) cobalt(II) and iron(II) complexes and their catalytic performance in ethylene oligomerization reactions. The study focused on the role of the ligand architecture, metal and co-catalyst in ethylene oligomerization reactions using $EtAlCl_2$ and MAO co-catalysts and chlorobenzene and toluene solvents respectively. Computational calculation using DFT provided insights on the catalytic activity trends and effect of complex/ligand structure on the ethylene oligomerization reactions. The findings of this chapter have been published in *J. Mol. Catal.*, *478*, **2019**, 110590.

Chapter four covers the syntheses of Fe(II), Co(II) and Ni(II) complexes based on 2,4-dibromo-6-((pyridin-2-ylimino)methyl) (N^O donor) and ((quinolin-8-ylimino)methyl)phenol ligands (N^N^O donor) and their applications as potential catalysts for ethylene oligomerization reactions. This was aimed at examining the effect of introducing the electron withdrawing groups in the vicinity of the metal centre. These complexes formed highly active species after activation with $EtAlCl_2$ co-catalyst in chlorobenzene solvent and selectively converted ethylene monomer into C_4 and C_6 oligomers. Optimization of the reaction conditions such as Al/M molar ratio, time, pressure and temperature and the use of DFT calculations to rationalize the catalytic activity trends is described.

Chapter five deals with the synthesis of new recyclable Fe_3O_4 magnetic nanoparticles immobilized N^O phenol((triethoxysilyl)propylimino) Fe(II), Ni(II) and Co(II) complexes as potential catalysts for ethylene oligomerization reactions. The complexes formed active

catalysts in combination with $EtAlCl_2$ co-catalyst using *n*-heptane, *n*-hexane, toluene and chlorobenzene solvents. The influence of metal identity, catalyst loading, and reaction conditions are discussed. A detailed examination of the recyclability of the Fe_3O_4 magnetic nanoparticles immobilized complexes in ethylene oligomerization is also described.

Chapter six focuses on the synthesis and characterization of another series of silica (SBA-15 and MCM-41) immobilized Fe(II), Ni(II) and Co(II) complexes of N^O phenol((triethoxysilyl)propylimino) ligands and their evaluation as recyclable catalysts in the oligomerization of ethylene reactions. The main of this chapter was to probe the influence of employing other types of solid supports on the catalytic activity and catalyst recyclability of these metal complexes. Finally, **Chapter seven** provides general concluding remarks on the salient outcomes and key findings of this study and also provides future prospects derived from the present results.

RESEARCH OUPUTS

1. **Ngcobo, M**., Nyamato G. S., Ojwach, S. O. Structural elucidation of N^O (ethylimino-methyl)phenol Fe(II) and Co(II) complexes and their applications in ethylene oligomerization catalysis. *Molecular Catalysis **2019**, 478, 110590.*

2. **Ngcobo, M**., Ojwach, S. O. Ethylene oligomerization reactions catalyzed by recyclable Fe(II), Ni(II) and Co(II) complexes immobilized on Fe_3O_4 magnetic nanoparticles. *Molecular Catalysis, **2021**, 111583*.

3. **Ngcobo, M**., Ojwach, S. O. Synthesis and structural elucidation of 2,4-dibromo-6-(((4-methylpyridin-2-yl)imino)methyl)phenol (N^O donor) and 2,4-dibromo-6-((quinolin-8-ylimino)methyl)phenol (N^N^O donor) Fe(II), Co(II) and Ni(II) complexes and their applications as catalysts in ethylene oligomerization reactions. Manuscript status: Under preparation and will be submitted on European Journal of Inorganic Chemistry.

4. **Ngcobo, M**., Ojwach, S. O. Probing the effect solid supports using SBA-15 and MCM-41 immobilized Fe(II), Ni(II) and Co(II) complexes for ethylene oligomerization reactions. Manuscript status: Under preparation and will be submitted on Catalysis Letters.

Conference presentations:

1. Makhosonke Ngcobo, Stephen O. Ojwach. *Ethylene oligomerization reactions catalyzed by immobilized Fe(II), Co(II) and Ni(II) complexes.* EuropaCat 2019. Aachen, Germany. **18th – 23rd August 2019**.

2. Makhosonke Ngcobo, Stephen O. Ojwach. *Preparation of immobilized N^O donor Ni(II), Co(II) and Fe(II) complexes for ethylene oligomerization reactions.* College of agriculture, engineering and science Post-graduate research and innovation symposium. UKZN. **17th October 2019**.

3. Makhosonke Ngcobo, Stephen O. Ojwach. *Structural and ethylene oligomerization studies of chelated N^O (imino/amino)phenol nickel(II) complexes.* 2018 SACI Post-graduate Colloquium. Durban University of Technology (DUT). **2nd February 2018**.

4. Makhosonke Ngcobo, Stephen O. Ojwach. *Preparation of immobilized N^O donor Ni(II), Co(II) and Fe(II) complexes for ethylene oligomerization reactions.* 43rd National Convention of the South African Chemical Institute. Pretoria **2nd – 7th December 2018**.

ABSTRACT

Reactions of 2-[(2-hydroxyethyl)imino]methyl]phenol (**L1**), 2-[1-[(2-hydroxyethyl)imino]ethyl]phenol (**L2**) and 2-[{[(2-diethylamino)ethyl]imino}methyl]phenol (**L3**) with $CoCl_2$ and $FeCl_2$ salts produced the metal complexes [Co(**L1**)$_2$] (**1**), [Fe(**L1**)$_2$] (**2**), [Co(**L2**)$_2$] (**3**), [Fe(**L2**)$_2$] (**4**), [Co_2(**L3**)$_2Cl_4$)] (**5**) and [Fe_2(**L3**)$_2Cl_4$] (**6**), respectively. Molecular structures of **2** confirmed the formation of a mononuclear complex containing two tridentate bound anionic ligand **L1**. On the other hand, the solid-state structure of **5** established the formation of a dinuclear complex bearing a bidentate zwitterionic ligand **L3**. Activation of the Fe(II) and Co(II) complexes with $EtAlCl_2$ or MAO co-catalysts, gave active catalysts in oligomerization of ethylene to give C_4 and C_6 oligomers. Generally, the Co(II) complexes exhibited higher catalytic activities than their Fe(II) analogues. While activation with MAO produced mainly C_4 oligomers (96 %), $EtAlCl_2$ gave predominantly C_6 oligomers. Density functional theory data provided insights on the catalytic activity trends and effect of complex/ligand structure on the ethylene oligomerization reactions.

The second type of Fe(II), Co(II) and Ni(II) complexes were synthesized from 2,4-dibromo-6-((pyridin-2-ylimino)methyl)phenol (**L4**), 2,4-dibromo-6-(((4-methylpyridin-2-yl)imino)methyl)phenol (**L5**) and 2,4-dibromo-6-((quinolin-8-ylimino)methyl)phenol (**L6**) ligands. The complexes [Fe(**L4**)$_2$] (**7**), [Co(**L4**)$_2$] (**8**), [Ni(**L4**)$_2$] (**9**), [Fe(**L5**)$_2$] (**10**), [Co(**L5**)$_2$] (**11**), [Ni(**L5**)$_2$] (**12**), [Fe(**L6**)$_2$] (**13**), [Co(**L6**)$_2$] (**14**) and [Ni(**L6**)$_2$] (**15**) were obtained from the reactions of ligands **L4-L6** with $FeCl_2$, $CoCl_2$ and $NiCl_2$ metal precursors. The solid state of **13a**, the derivative of complex **13**, and **15** confirmed the isoleptic *bis*-chelated nature and the distorted octahedral arrangement of the mononuclear complexes. The UV spectra of the complexes were characterized by the presence of three bands around 230 nm, 250-300 nm and

350-482 nm assigned to π-π^* and n-π^* electronic transitions of the chromophores present in the ligands. The complexes formed active species after activation with $EtAlCl_2$ co-catalyst and selectively converted ethylene monomer into C_4 and C_6 oligomers. The catalytic activities and product distribution of the catalyst relied significantly on the complex structure. The reactions conditions such as Al/M molar ratio, time, pressure and temperature were also optimized.

Fe_3O_4 magnetic nanoparticles prepared utilizing the conventional method were used to synthesized immobilized ligands, phenol((triethoxysilyl)propylimino)ethyl@Fe_3O_4, **L7H**@Fe_3O_4 (**L7**) and phenol((triethoxysilyl)propylimino)methyl)@Fe_3O_4, **L8**@Fe_3O_4 (**L8**) Reactions of Fe_3O_4 magnetic nanoparticles immobilized ligands, **L7H**@Fe_3O_4 (**L7**) and **L8**@Fe_3O_4 (**L8**) with appropriate metal salts afforded the respective immobilized complexes [Ni(**L7**)$_2Cl_2$], (**16**), [Co(**L7**)$_2Cl_2$], (**17**), [Fe(**L7**)$_2Cl_2$], (**18**), [Ni(**L8**)$_2Cl_2$], (**19**), [Co(**L8**)$_2Cl_2$], (**20**) and [Fe(**L8**)$_2Cl_2$], (**21**). The ligands and complexes were characterized using FT-IR spectroscopy, thermogravimetric analyses (TGA), transmission electron microscopy (TEM), scanning electron microscopy (SEM), powder X-ray diffraction (PXRD), energy dispersive X-ray (EDX), inductively coupled plasma optical emission spectroscopy (ICP-OES) and vibrational sample magnetometry (VSM). Activation of the complexes with $EtAlCl_2$ co-catalyst in *n*-heptane, *n*-hexane, toluene and chlorobenzene afforded active catalysts in ethylene oligomerization reactions to give C_4-C_{10} oligomers and alkylated products depending on the solvent medium. Both the identity of the ligand motif and metal atom influenced the catalytic performance of the complexes in the ethylene oligomerization reactions. The complexes were recycled *via* magnetic separation in five successive runs without significant loss of catalytic activity and selectivity. Minimal leaching may be responsible for minor losses in catalytic activities in the recycling experiments.

A new family of N^O phenol((triethoxysilyl)propylimino) ligands immobilized on SBA-15 and MCM-41 solid supports **L8H**@SBA-15 (**L9**), **L8H**@MCM-41 (**L10**) were utilized to produce Fe(II), Ni(II) and Co(II) complexes, [Ni(**L9**)$_2$Cl$_2$], (**22**), [Co(**L9**)$_2$Cl$_2$], (**23**), [Fe(**L9**)$_2$Cl$_2$], (**24**) and [Ni(**L10**)$_2$Cl$_2$], (**25**). Activation of the complexes with $EtAlCl_2$ co-catalyst formed active species for the oligomerization of ethylene reactions. All the complexes exhibited appreciable catalytic activities upon activation with $EtAlCl_2$ co-catalyst, producing significant amounts of C_4 and C_6 oligomers as well as traces of C_8 and C_{10} oligomers. The SBA-15 immobilized complex was more active in comparisons to the MCM-41 immobilized complex. The complexes were separable using centrifugation and decantation and were reusable for up to three cycles with a noticeable drop of catalytic activity from 53 400 $g_{oligomers}$ mol^{-1}(Ni) h^{-1} of complex **22** to 19 500 $g_{oligomers}$ mol^{-1}(Fe) h^{-1} of complex **24**.

TABLE OF CONTENTS

CHAPTER THREE

CHAPTER FIVE

CHAPTER SEVEN

LISTS OF FIGURES

LIST OF SCHEMES

LIST OF TABLES

ABBREVIATIONS

Bpy	Bipyridine
EADC	Ethylaluminum dichloride
EASC	Ethylaluminum sesquichloride
ESI	Electron spray ionisation
GC	Gas chromatography
GC-MS	Gas chromatography-mass spectrometry
HDPE	High density polyethylene
HOMO	Highest occupied molecular orbitals
IR	Infrared spectroscopy
ILs	Ionic liquids
L	Ligand
LAO	Linear alpha olefins
LDPE	Low density polyethylene
LUMO	Lowest unoccupied molecular orbitals
MS	Mass spectrometry
MAO	Methylaluminoxane
MNPs	Magnetic nanoparticles
NMR	Nuclear magnetic resonance
SHOP	Shell higher olefin process

CHAPTER ONE

General introduction on ethylene oligomerization reactions and immobilization of single-site catalysts

1.1. Background information

Petrochemical industries extensively produce various organic chemicals in huge volumes world-wide.[1] These chemicals includes olefins and unsaturated aliphatic hydrocarbons. Collectively, these are called primary petrochemicals and **Figure 1.1** shows the consumption of these chemicals world-wide during year 2018 with ethylene consumption being the highest followed by propylene.[2] Characterized by the presence of one or more double bonds, olefins such as ethylene, propylene and butadiene are chemically reactive which make them suitable feedstocks for enormous variety of consumer and industrial chemical production. These olefins are capable of undergoing a number transformations including hydroformylation, hydrogenation, hydroesterification, hydrocarbonylation, oxidation, copolymerization, isomerization, polymerization and most importantly oligomerization to produce linear α-olefins which are more advantageous than the branched olefins because of the high biodegradability of their end user products.[3-4]

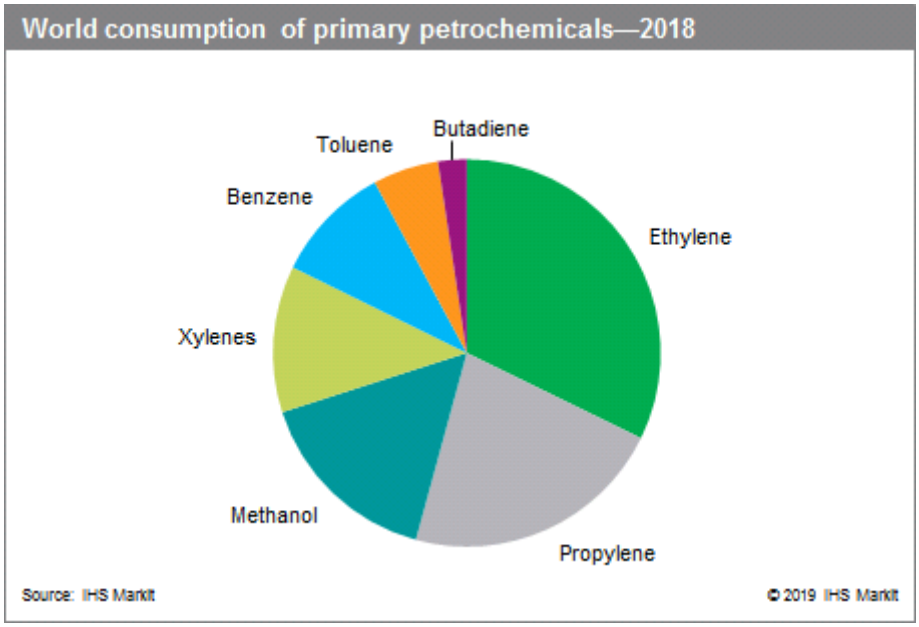

Figure 1.1: The global consumption of primary petrochemicals during the year 2018.[1]

Ethylene consumption has witnessed a great increase during the past few years in accordance with the daily evolving technology. This is because ethylene is the lightest olefin, paramount and is a readily accessible feedstock for the production of other linear α-olefins which are directly and indirectly applied in chemical industry. The world market has predicted an increase of 6.2 % on the use of ethylene from 2018 (USD 91.7) to 2026 (USD 146.8) with the Asian Pacific being on the highest note followed by Middle East Africa (MEA), Europe, North America and lastly Latin America being on a lowest note as shown in **Figure 1.2**. Ethylene oligomerization is the vital source of linear α-olefins which constitute the advantage of being biodegradable despite the non-selectivity problem observed in most industrial processes.[5] Nevertheless selectivity issue has created a problem since these processes produce massive amount of undesirable branched internal olefins which are difficult to separate and as a result industries are shying away from such process.

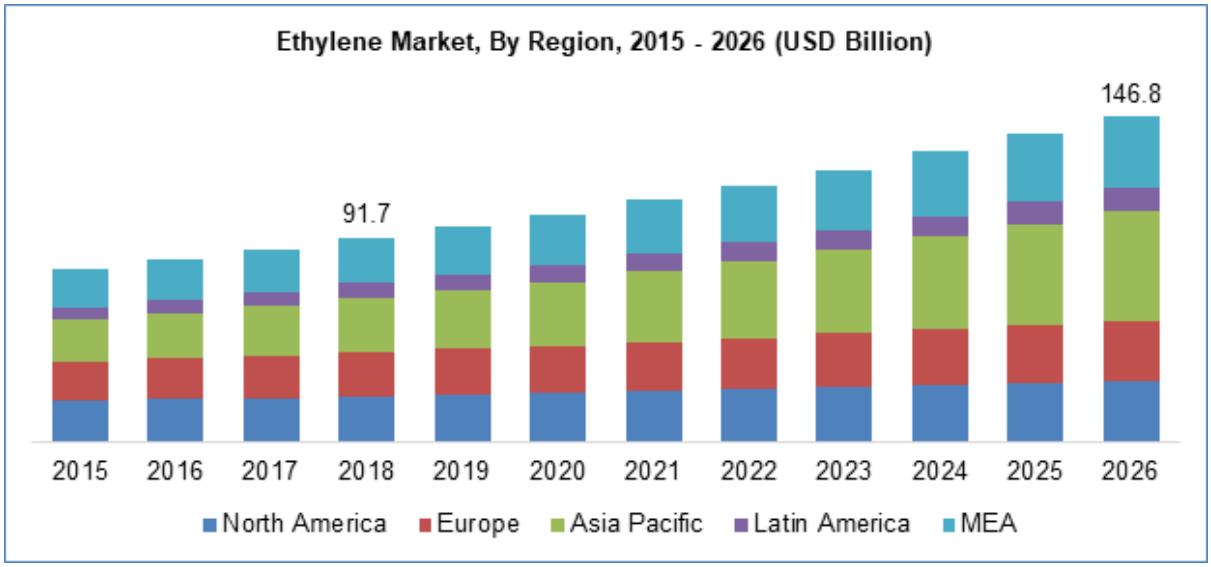

Figure 1.2: Predicted ethylene market by region between years 2015 – 2026.[6]

1.2. Structural properties of linear α-olefins (LAOs), and their applications

The structural properties of linear α-olefins determine their domestic and commercial applications. To give an example, the products of ethylene oligomerization reactions are used to manufacture high density polyethylene (C_2-C_8), surfactants (C_{12}-C_{20}), plasticisers (C_6-C_{10}), lubricants (C_6-C_8) and other fine and pharmaceutical products.[7-12] Linear alpha olefins are also served as co-monomers in the production of more flexible and resilient linear low density polyethylene (LLDPE) and small amounts of high density polyethylene (HDPE). General examples of end-user polyethylene products and their everyday lives applications are shown in **Figure 1.3**.[13] In 2004, it was predicted that a total of 35 million tons of LDPE and 25 million tons of HDPE were consumed nation-wide and this consumption was estimated to increase annually by >5 % until 2010.[14] Consequently, researchers have become particularly more interested in the production of large amounts of LAOs in order to meet the great demands of consumers.[15]

Figure 1.3: General distribution of polyethylene and applications of oligomers.[13]

1.3. Production of linear α-olefins

Production of α-olefins can be achieved by four well-known process *vis* the cracking paraffins, the dehydrogenation of paraffins, the dehydration of alcohols and the oligomerization of ethylene.[16] Ethylene oligomerization process which proceeds *via* chain growth remains the pillar of chemical transformation capable of converting low molecular weight olefins such as C_2-C_4 into more applicable and useful higher olefins (C_8-C_{30}) used in both domestic and industrial chemical production.[15] The vitality of ethylene oligomerization reactions is also observed in energy processing, production of bulk chemicals and fine chemicals, food processing sectors and packaging of goods.[15] There exist two different forms of catalysis, that is, heterogeneous catalysis and homogeneous catalysis, which can be applied in the ethylene oligomerization for the production of LAOs.

1.3.1. Homogeneous catalysts in olefin oligomerization and polymerization reactions

Homogeneous catalysts operate in single phased systems, whereby the catalyst, reactants and products all exists in liquid, solid or gaseous phase.[17] Over the past decade, homogeneous catalysts have been proven to efficiently catalyse ethylene oligomerization reactions with the nickel metal centre being the principal active site.[18] The nickel metal centre is usually stabilized by ligands of different moieties.[19-20] The examples of industrially commercialized processes that are capable of producing α-olefins *via* ethylene oligomerization includes, the Chevron Phillips process (Gulf); a one-step process capable of producing ethylene oligomers having Schultz-Flory distribution in the presence of triethylaluminum catalyst,[21] the Ethyl Corporation (INOES) process; a two-step process which uses the same catalyst and produces oligomers having Poisson distribution with comparatively narrow distribution, the well-known Shell-Higher Olefin Process (SHOP-**Figure 1.4**); a more sophisticated process that employs nickel complexes as catalysts for the tuneable production of ethylene oligomers possessing a Shultz-Flory distribution,[19] the Idemitsu Petrochemical process; recently developed process that employs a catalyst composed of a $ZrCl_4$ complex, a Lewis base and an alkylaluminum compound and capable of producing olefinic products that can be controlled by modifying the ligand architecture,[22] the CP Chemical Company (the Phillips) and lastly, the IFP process; a process which uses titanium Ziegler-type catalyst to dimerize acetylene to α-butene (**Scheme 1.1**).[19]

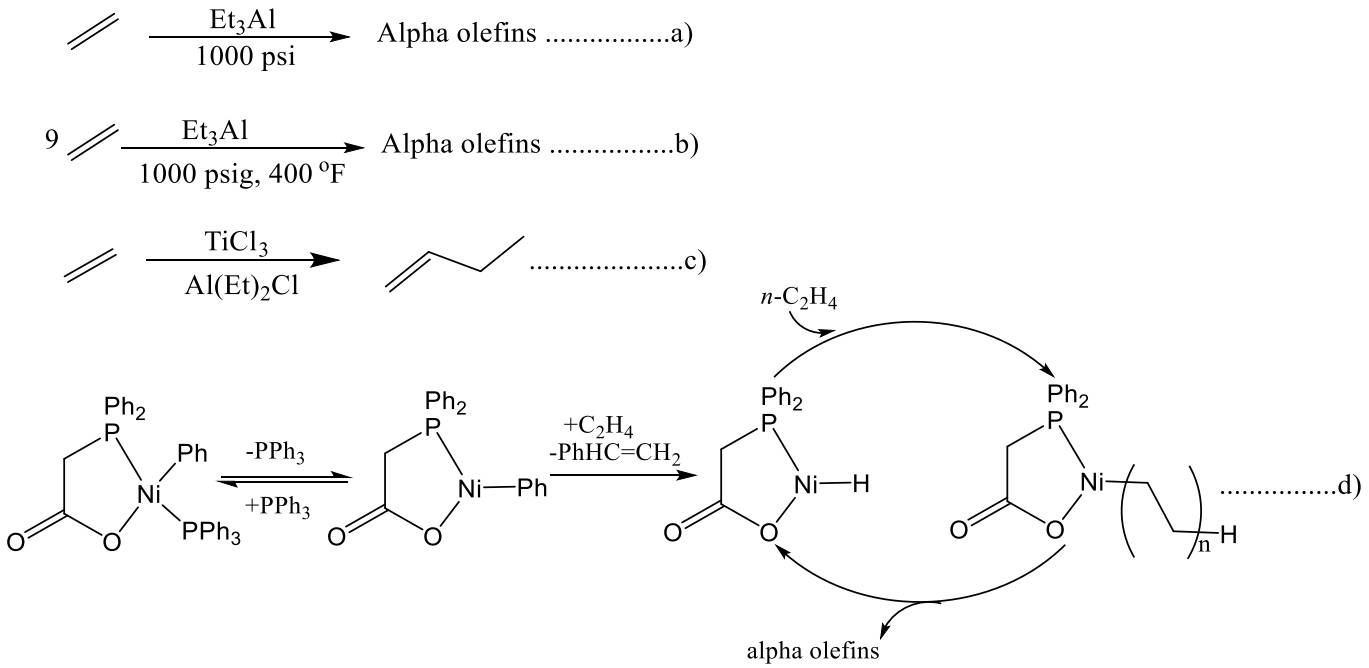

Scheme 1.1. Industrially commercialized processes capable of producing α-olefins *via* ethylene oligomerization, a) Chevron Phillips process (Gulf), b) INEOS process, c) Ziegler-Natta promoted catalysis, and the d) SHOP process.

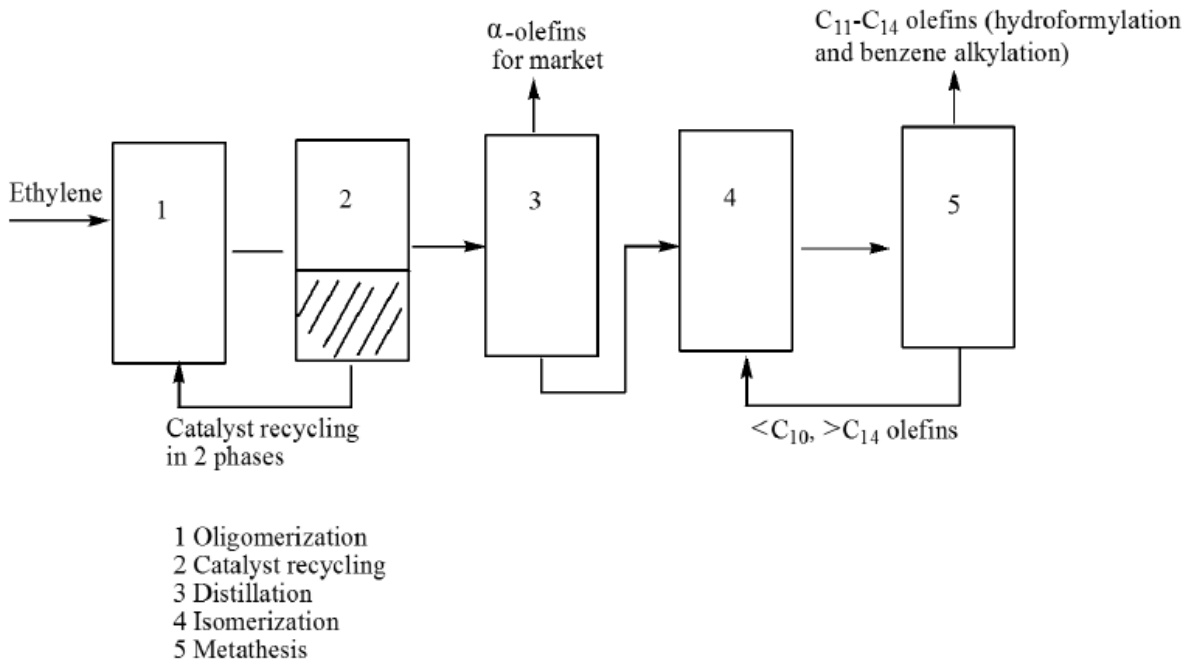

Figure 1.4: The flow chart for the production of α-olefins in a SHOP production plant.[23]

The first four previously mentioned processes produce a wide distribution of linear α-olefins while in contrast, the last two generate oligomers with the single α-olefin carbon number (1-hexene and 1-butene respectively), a selectivity phenomenon important for industrial applications. Another highly selective process is the Chevron Phillips trimerization process which is illustrated in **Scheme 1.2**. This process relies extensively on the formation of metallacycles intermediates as depicted in **Scheme 1.2**, and selectively produce 1-hexene oligomers.

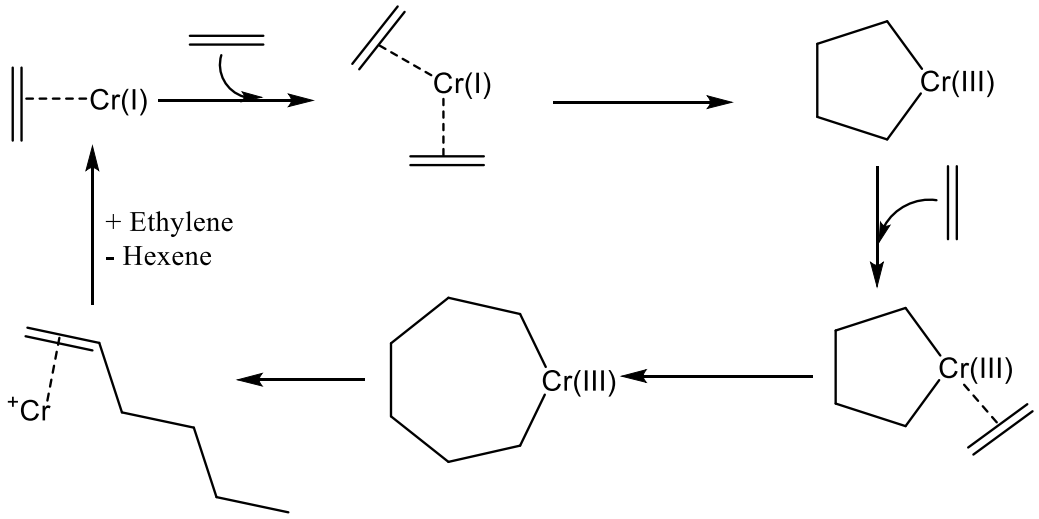

Scheme 1.2: The Chevron Phillips process for the production of ethylene trimers using chromium metallacycles.[24]

Despite enormous application of the homogeneous systems in the production of α-olefins, they still constitute some major drawbacks in their application. These catalytically inherent disadvantages include their toxicity, corrosive nature, high ligand costs, degradation of the utilised solvent, poor thermal stability, difficulty in catalyst handling and separation from the reaction mixture and also the creation of solid waste due to the production of un-wanted high molecular weight polyethylene by-product.[25-26] Difficulties in catalysts separation from products, their recovery and reuse have hindered their industrial commercialization. In addition, their high catalytic activities requires high pressure which calls for heavy engineering

works to eradicate reactor fouling and mass transport limitations.[27] These are the main and unresolved problems associated with using homogeneous catalysis to date.

1.3.2. Heterogeneous catalysts in olefin oligomerization and polymerization reactions

Heterogeneous catalysis is characterized by the presence of the catalyst in a different phase as the reactants and products. It usually constitutes of a catalytically active component carried on the surface of a solid support. Heterogeneous catalysts are widely used in the production of energy and fuels and commodity chemicals from olefin feedstocks.[28-29] Advantages associated with the use of heterogeneous catalysts over homogeneous ones includes ease in catalysts handling, separation, greater stability, recovery, regeneration and re-use.[30] The most commonly utilised method for the synthesis of heterogeneous catalysts is ion exchange, whereby the metal active site is loaded on the solid support such as silica, alumina and or silica alumina (**Figure 1.5**). Other preparation methods include sol-gel method, impregnation method and chemical deposition method.

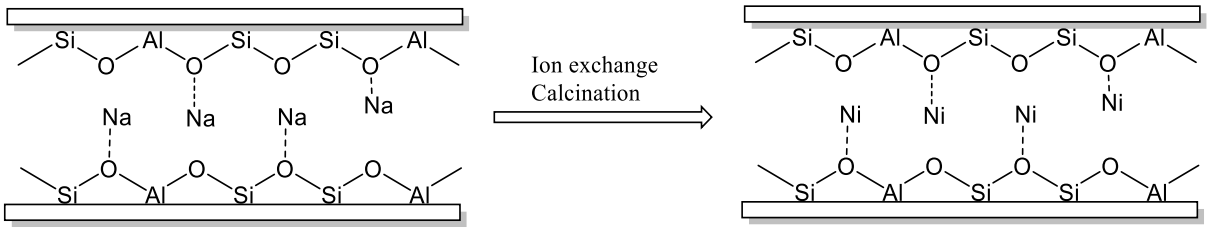

I

Figure 1.5. General protocol for preparing Ni metal based heterogeneous catalyst.

The significance of heterogeneous catalysis has also been witnessed in ethylene oligomerization producing oligomers with differing microstructures and polydispersity.[31] The MOGD process shown in **Figure 1.6** is a well-known process which was pioneered by Mobil

and make use of the heterogeneous acid catalysts based on Zeolite Socony Mobil-5 (ZSM-5) type medium pore zeolites still remains the far most promising industrial process for the fuel production from the oligomerization of light olefins.[32-33] This catalyst is capable of producing diesel fractions with high octane number at low temperature while using this catalyst at elevated temperature leads to the formation of the gasoline as major product.

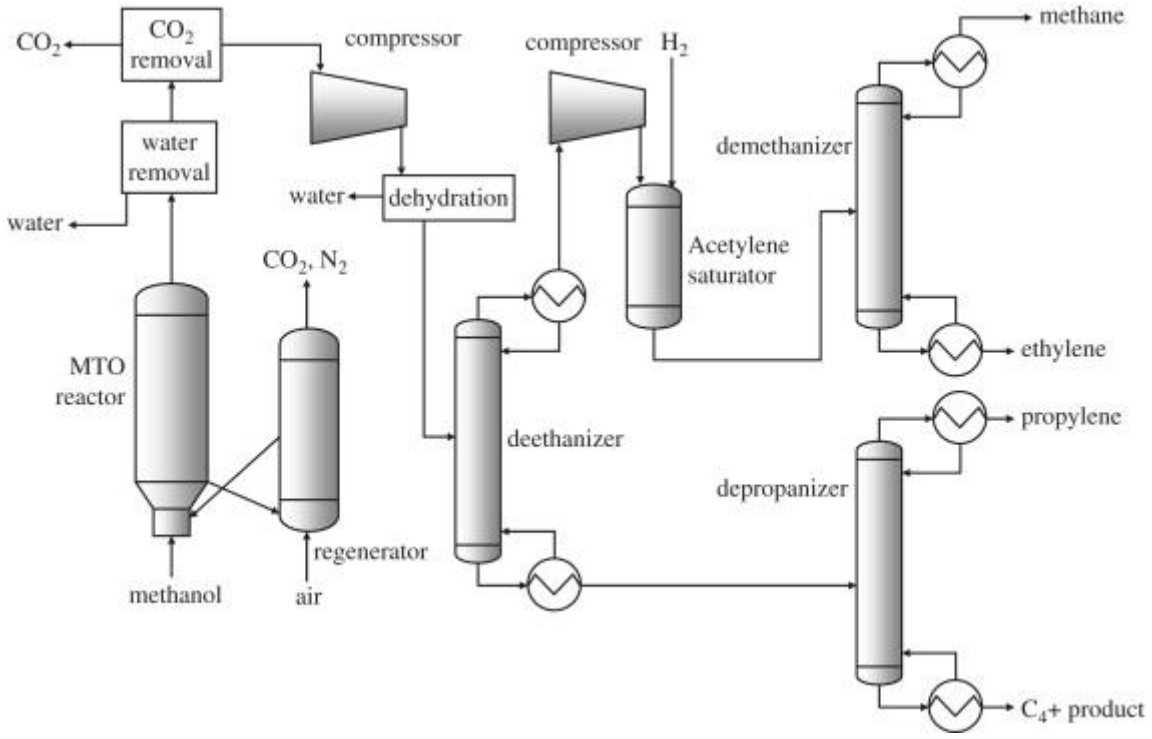

Figure 1.6: The Mobil's olefin to gasoline/distillate process which makes use of the medium pore zeolite ZSM-5 catalyst.

The Shell Polygasoline and Kero process (SPGK) reported in 1989,[34-36] is another oligomerization process that utilizes zeolites (ZSM-5) for the production of a high-octane gasoline, diesel or kerosene fractions with a high-octane number depending on the oligomerization conditions. Hydrocracking is a matured field and the main focus has been on modifying zeolite Y for the selective production of gasoline and olefin distillates.[37] Consequently, they have been major industrial developments in the petrochemical refineries

for the selective production of oligomers using fluid catalytic cracking (FCC). In **Figure 1.7** is shown a flow chart of modern refinery-process for the production of aromatics and olefins *via* FCC process.

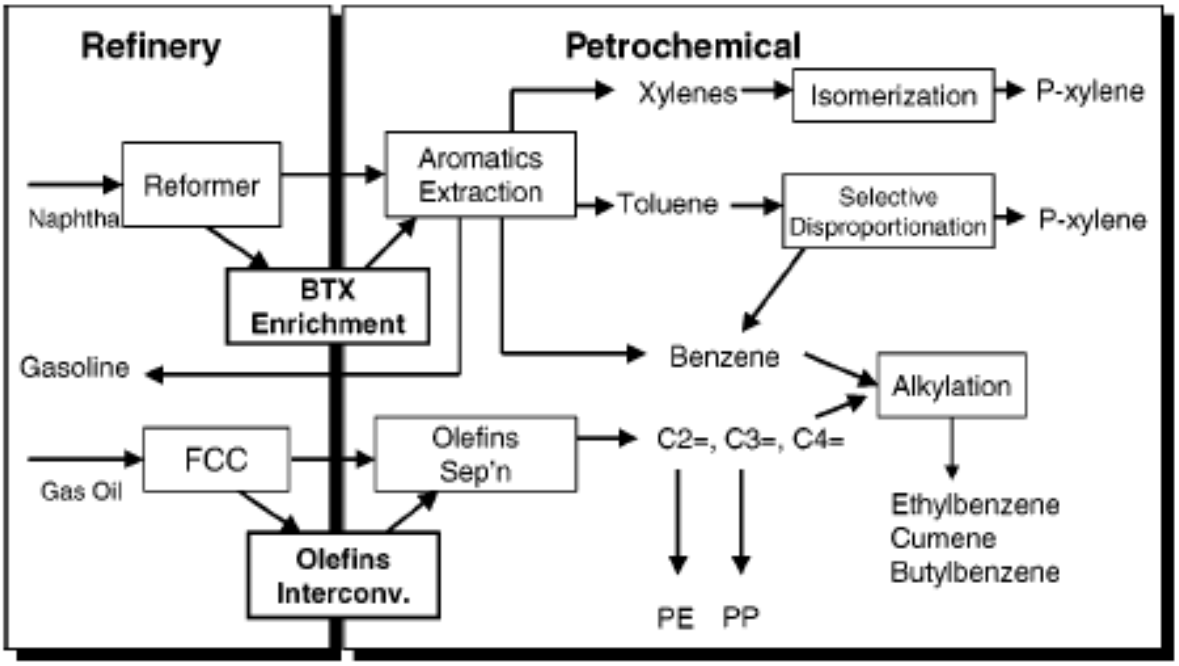

Figure 1.7: Flow-chart depicting modern refinery-process for the production of aromatic and olefinic products.

Nevertheless, heterogeneous catalysts constitute some major drawbacks which includes low atom efficiency due to limited number of active sites. In addition, poor selectivity of the heterogeneous catalysts poses another problem in their application. Furthermore, heterogeneous catalysts also display diffusion problems and mass transport limitations of the reactants and products into or from the pore system.[38]

1.4. Immobilization of homogeneous catalysts

Numerous strategies have been developed to "heterogenize" the homogeneous catalysts, in the pursuit of producing hybrid catalyst systems, which are both selective and recyclable. [28, 39-40] Tethering of the homogeneous catalysts through covalent bonding is the most commonly applied method which can be achieved using two strategies, that is, "grafting to" (convergent) and "grafting from" (sequential) approach as illustrated in **Figure 1.8**.[30] In the latter approach the ligand and the catalyst are constructed in a stepwise manner on the surface of the insoluble support. Whereas in the "grafting to" approach the catalyst is functionalized with a reactive group which can react with the silanol groups of the silica support to form a covalent bond.

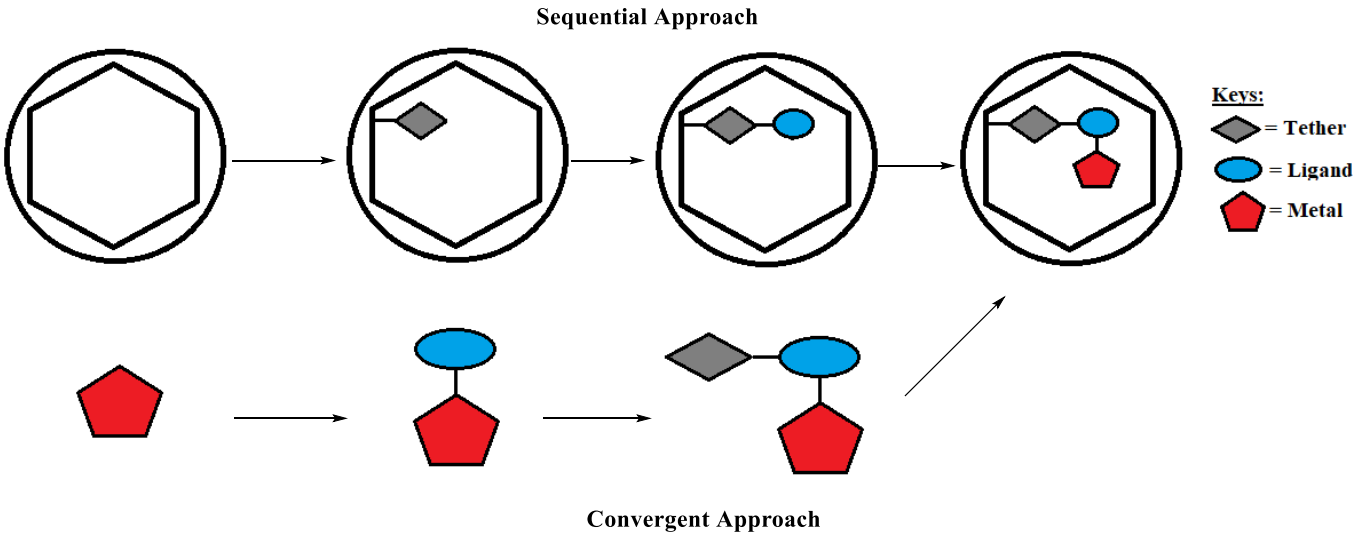

Figure 1.8: Immobilization of the homogeneous complex *via* the sequential and convergent approaches.

To date, various solid supports have been developed in order to convert single-site catalysts into immobilized counterparts. These supports are based on carbon, alumina, silica and their hybrids. Examples include clays, zeolites, silica, silica-alumina, polymers, magnetic nanoparticles, biphasic systems and molecular organic frameworks. In some instances, these solid supports are modified and functionalized for efficient immobilization of the homogeneous catalyst and to enhance catalytic properties of the immobilized catalysts.

1.4.1. Types of immobilization supports

1.4.1.1. Clays

Clays are a group of aluminosilicates including minerals such as montmorillonite, kaolin, hectorite, mica and can be used as inorganic supports carriers for single site catalysts.[41] For example, impregnating an aqueous suspension of clay particles with Brønsted acids such as $HNMe_2Ph^+$, drying and reacting with a metal complex mixture can affords an active catalyst for olefin oligomerization and polymerization reactions. Clays exhibit attractive features such as acidity, swelling ion-exchange properties, wide range of preparation methods, high versatility, milder reaction conditions, high yield and selectivity at low cost, ease of workup etc. **Figure 1.9**.[42]

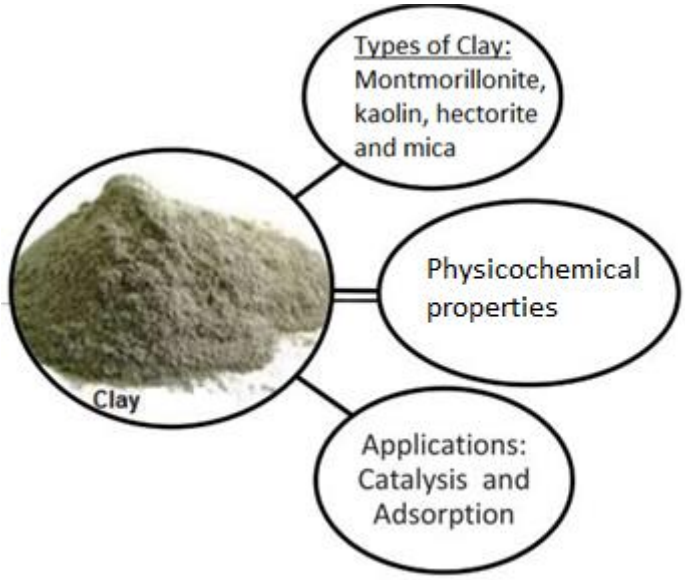

Figure 1.9: Types of clays, chemical properties and their applications.[43]

1.4.1.2. Zeolites

Zeolites are highly ordered crystalline aluminosilicates with well-defined pore geometries, and possessing minimum channel aperture in the range of 0.3 to 1.0 nm as shown in **Figure 1.10**.[44]

They are prepared by the dehydration of hydrated aluminosilicates. Zeolites are composed of AlO_4 and SiO_4 tetrahedral interconnected through shared oxygen atoms to form a 3-Dimensional network. This network made zeolites acidic in nature thus liberating or accepting protons. Due to their high stability both thermal and acidity, zeolites are also employed as catalysts in harsh conditions. Their sizes are determined by the silicon/aluminium ratio, size of the ring, type of cation present, and the nature of treatment involved such as calcination etc. Their high selective behaviour is associated with their defined pore structure that only allows certain molecules into the interior or specific product out.

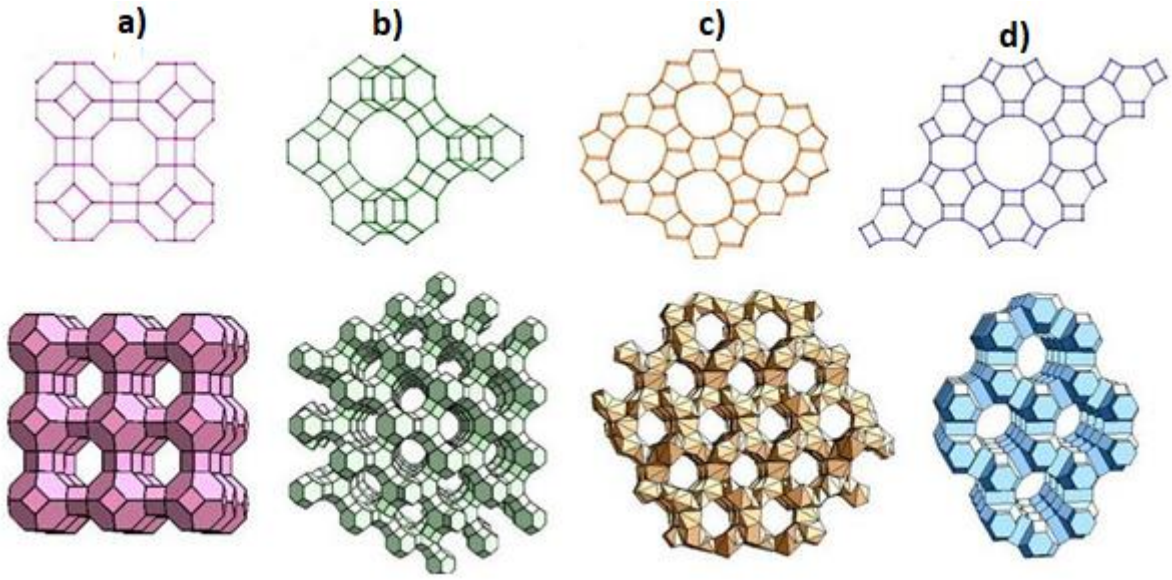

Figure 1.10: Porous zeolitic frameworks of a) zeolite A, b) zeolite Y, c) zeolite L an d) ZSM-5 used in heterogeneous catalysis.[45]

1.4.1.3. Silica-alumina

Silica-alumina are easily prepared using different silica and alumina ratios.[44] They are amorphous form of the dehydrated aluminosilicates. They are also porous in nature and lack a definitive geometry. Their acidity and thermal stability depend on silica/alumina rations.

Alumina content is responsible for the formation of the acid sites which in turn determines the product selectivity of the silica-alumina catalyst during ethylene oligomerization. Furthermore, high SiO_2/Al_2O_3 ratio provides high thermal stability.[46] Preparation of silica-alumina involves ion-exchange of the sodium with various other cations with ammonium or hydrogen ion included. Alumina silicate catalysts are prepared by aqueous ion exchange and ethylene oligomerization reactions involving these catalysts, particularly Ni(II) silica-alumina catalysts, are usually carried out in a slurry reactor.[47]

1.4.1.4. Mesoporous materials

Silica is an important building block of mesoporous materials, inexpensive, possesses high thermal stability, environmentally friendly, chemically inert and is available in large amounts on earth. Solid silica supports emerged during the early 1990s after the well-known zeolites. These supports consist of uniform pore sizes ranging from 2 nm to 50 nm, high surface area and large pore volume. They can be classified according to their pore diameters (d), as microporous ($d < 2$ nm), mesoporous ($2 \text{ nm} < d < 50$ nm) or macroporous ($d > 50$ nm), as given by the International Union of Pure and Applied Chemistry (IUPAC). These mesostructured materials possess different symmetric orientations. For example, MCM-41 and SBA-15 are hexagonally orientated, MCM-48 is in cubic form and lastly MCM-50 possesses a lamellar formation, **Figure 1.11**. SBA-15 is the most massively studied mesoporous material due to its attractive features including high surface area, frameworks thickness, flexible pore sizes and straightened cylindrical pores in comparisons to all other mesoporous silica materials.[48]

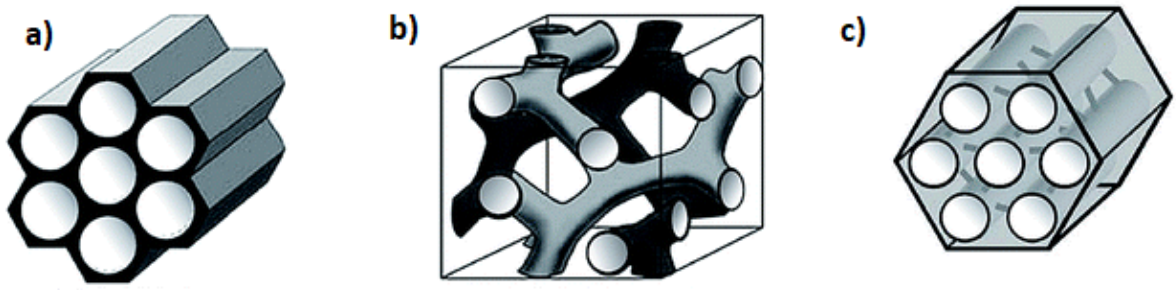

Figure 1.11: Examples of silica solid supports a) MCM-41, b) MCM-48 and c) SBA-15.

Their significance has been witnessed in catalysis since they provide efficient and excellent immobilization as they have well-functionalized silanol groups. These groups allow flexible functionalization and provide tuneable surface properties thereby allowing the control of the immobilized catalysts' position and density properties.[30] For brevity, incorporation of different metal centres in the SBA-15 matrix is the most exploited functionalization in the design and synthesis of recyclable and reusable catalysts in the field of catalysis. For example, in ethylene oligomerization, the SBA-15 silica support is functionalized by the organic ligand which is then loaded with the metal centre, **Figure 1.12**.[49-50]

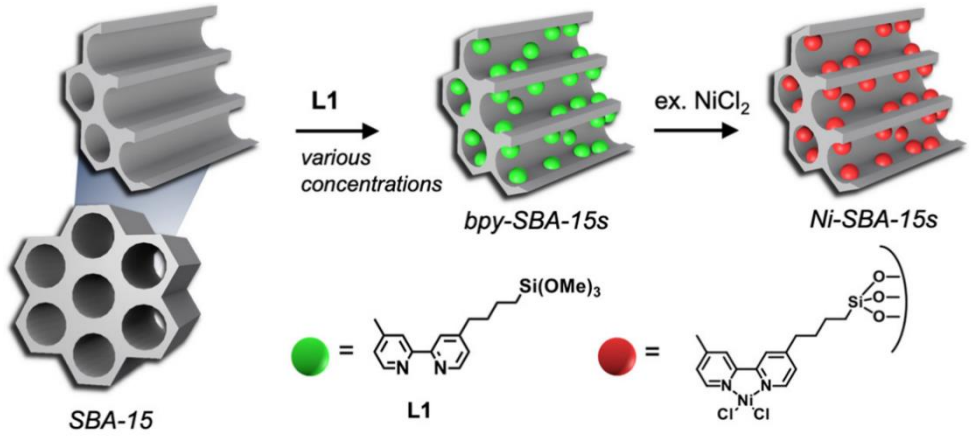

I

Figure 1.12: SBA-15 immobilized Ni(II) complex ligated by bipyridine (bpy) ligand employed in the oligomerization of ethylene.

1.4.1.5. Organic polymers as catalyst supports

Polymer supports belong the class of porous materials which are known for attractive properties such as large internal surface area than their non-porous counterparts.[51] Ethylene oligomerization process has benefited a lot in the usage of polystyrene- and polysiloxane-based organic polymer supported catalysts.[52] **Figure 1.13** gives examples of a diimine nickel catalysts supported on a crossed linked polystyrene and a zirconium based polysiloxane immobilized catalysts that have been synthesised for ethylene oligomerization. Cross-linking polystyrene, especially with poly(divinylbenzene) (PDVB) improves the homogeneity of the polymer supported catalysts.

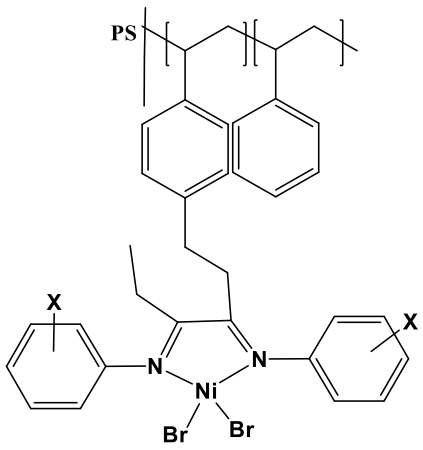

II

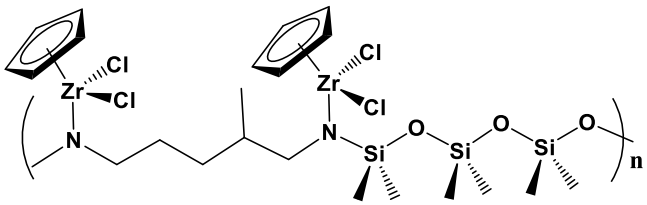

III

Figure 1.13: Diimine Ni(II) complex immobilized on a cross linked polystyrene and a zirconocene catalyst immobilized on polysiloxane copolymer support.

Other examples of porous materials that have been employed in the synthesis of immobilized catalysts for organic transformation includes metal organic frameworks (MOFs),[53] porous organic polymers (POPs)[51] and carbon organic frameworks (COFs)[54] as shown in by the flowchart in **Figure 1.14**. These porous materials are currently providing a solution in

immobilizing the homogeneous catalysts since the catalytically relevant ligands are directly bonded into the structure that possesses greater chemical stability because of the presence of strong covalent bonds including the carbon-carbon, carbon-oxygen and carbon-nitrogen bonds. Their high accessible surface areas also allow for the variety of chemical functionalities to be incorporated.

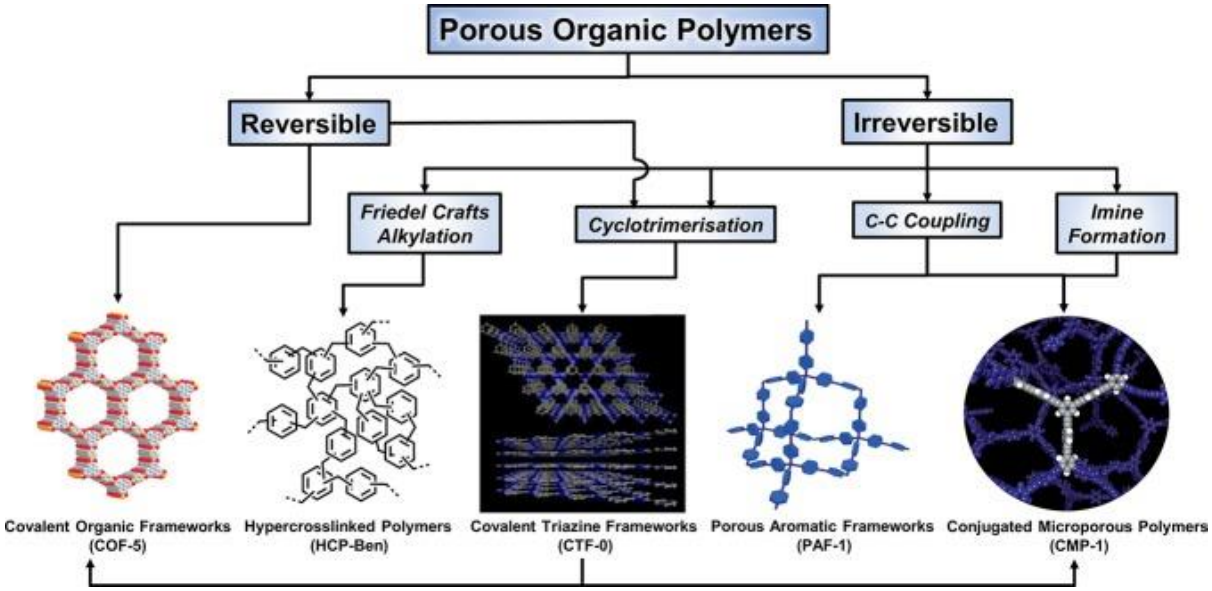

Figure 1.14: Different types of porous organic polymers frameworks and their coupling chemistries.[55]

1.4.1.6. Iron magnetic nanoparticles (Fe_3O_4 MNPs)

Iron magnetic silica nanoparticles have attracted significant attention in the immobilization of homogeneous catalysts.[56] This is because Fe_3O_4 magnetic nanoparticles display extraordinary physical and chemical properties such as chemical inertness, ease of separation from the reaction medium, low toxicity, high surface area, low cost and excellent thermal stability.[57] These vital properties have drawn a lot of attention in the use of nanoparticles as catalysts solid supports in bridging the gap between homogeneous and heterogeneous catalysis for the organic

synthesis such as ethylene oligomeration.[58-59] As a result, iron magnetic nanoparticles have recently received greater attention due to their widespread applications in various fields including catalysis,[60] data storage,[61] biomedicine,[62] environmental remediation,[63] magnetic fluids,[64] and electronic communication.[65] In catalysis, particularly, magnetic nanoparticles are currently adding value in catalysing C-C coupling, Suzuki-Miyura, Henry reaction, reduction, oxidation, asymmetric synthesis, vapor-phase reaction and elecrocatalysis reactions with palladium being the principal central metal atom,[66] as illustrated by the examples provided in **Figure 1.15**.

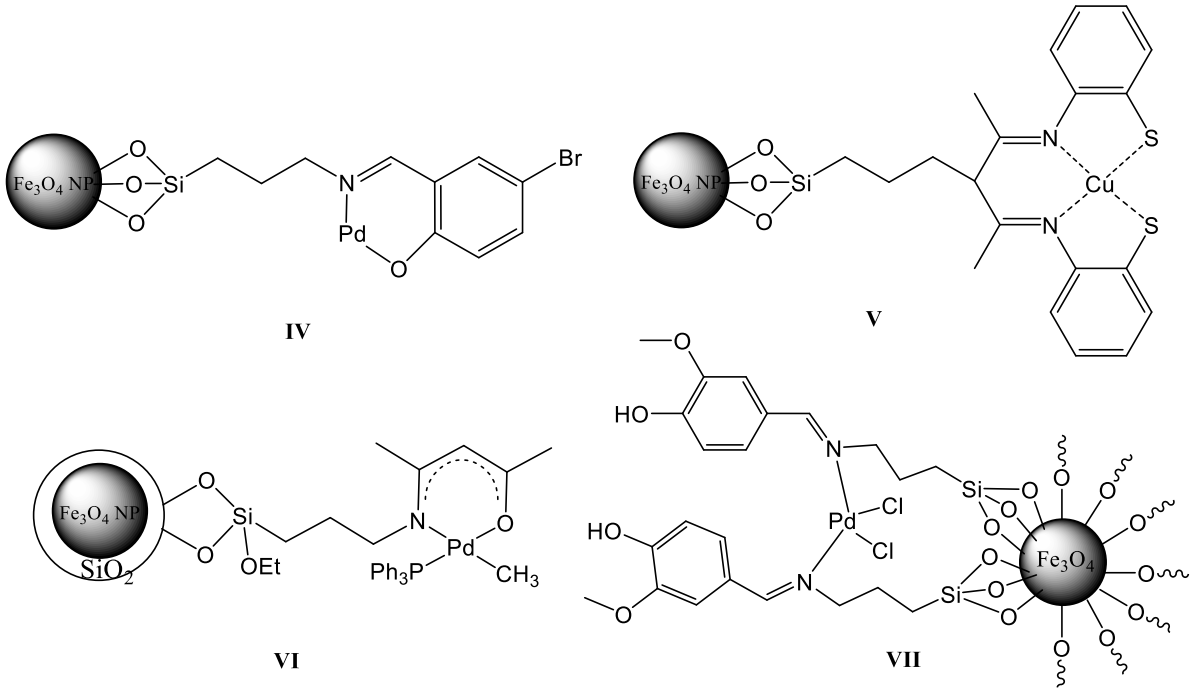

Figure 1.15: Examples of Fe_3O_4 magnetic nanoparticles-based catalysts that have been used in catalytic organic synthesis.[58-59, 67]

The most common, simple and efficient synthesis of Fe_3O_4 magnetic nanoparticles is based on the co-precipitation reaction between Fe(II) and Fe(III) in the presence of a strong base (**Figure 1.16**).[68] Other reported methods includes, hydrothermal reactions,[69] thermal decomposition,[70] micro-emulsion method,[71] sol-gel reactions,[72] aerosol or vapour phase method,[73] and electro-

thermal method[74] etc. are amongst other methods developed. Their distinctive feature lies in their ease of separation through the application of an external magnetic fields.[75] Structural and compositional properties that can affect the catalytic performance of the Fe_3O_4 magnetic nanoparticles include shape, size, structure, concentration, size distribution, surface charge, composition, surface area, surface functionality and porosity.[66]

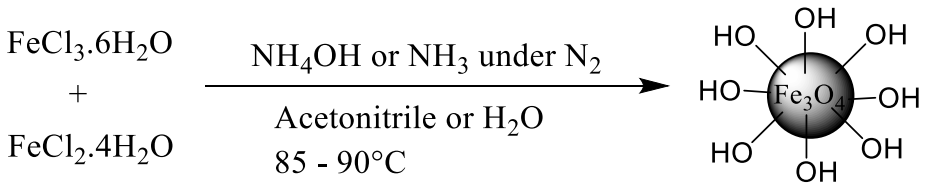

Figure 1.16: Synthesis of Fe_3O_4 magnetic nanoparticles using co-precipitation method.

Ethylene oligomerization processes have benefited a lot from the utilization of solid supports in the development of environmentally robust immobilized late transition metal catalysts aimed in solving the problems associated with both homogeneous and heterogeneous catalysis. The next chapter gives a literature survey report on the use of immobilized late transition metal catalysts in ethylene oligomerization reactions. Recent progress and advances on the development of selective and catalytically active immobilized catalysts for ethylene oligomerization are also presented.

1.5. References

1. Makharm, J. N., Tao, L., Davis, R., Voulis, N., Angenent, L. T., Ungerer, J., Yu, J., *Green Chem.* **2016**, *00*, 1-16.

2. Markit, I., *Chemical Economics Handbook* **2019**.

3. Lappin, G. R., Nemec, L, H., Sauer, J. D., Wagner, J. D., In *Higher Olefins, Kirk-Othmer Encyclopedia of Chemical Technology*, Wiley & Sons, Inc.: New York, N Y, USA, **2000**; Vol. *17*, pp 709-728.

4. Chen, E. Y.-X., Marks, T. J., *Chem. Rev.* **2000**, *100*, 1391-1434.

5. Flory, P. J., *J. Am. Chem. Soc.* **1935**, *62*, 1561.

6. Polaris, *Market Research Report* **2019-2020**.

7. Cotton, F. A., Wilkinson, G., Murillo, C. A., Bochmann, M., Advanced Inorganic Chemistry 6th Ed. John Wiley and Sons: New York, **1999**; p 835.

8. Elowe, P. R., Mc Cann, C., Pringle, P. G., Spitzmesser, S. K., Bercaw, J. E., *Organometallics.* **2006**, *25*, 5255-5260.

9. Liu, H., Zhang, L., Chen, L., Redshaw, C., Li, Y., Sun, W. -H., *Dalton Trans.* **2011**, *40*, 2614-2621.

10. Nelana, S. M., Darkwa, J., Guzei, A. L., Mapolie, S. F., *J. Organomet. Chem.* **2004**, *689*, 1835-1842.

11. Wang, S., Sun, W. -H., Redshaw, C., *J. Organomet. Chem.* **2014**, *751*, 714-717.

12. Zhang, M., Zhang, S., Hao, P., Jie, S., Sun, W. -H., Li, P., Lu, X., *Eur. J. Inorg. Chem.* **2007**, 3816-3826.

13. Siracusa, V., Blanco, I., *Polymers* **2020**, *12*, 1641-1658.

14. PlasticEurope Deutschland, W. S. a. M. R., **2004**.

15. Kissin, Y. V., *Kirk Othmer Encyclopedia of Chemical Technology.* Wiley & Sons: New York, **2005**; pp 253-260.

16. Speiser, F., Braunstein, P., Saussine, L., *Acc. Chem. Res.* **2005**, *38*, 783-793.

17. Stoltze, P.; Alborg University: Department of Chemistry and Applied Science.

18. Speiser, F., Braunstein, P., Saussine, L., *Organometallics* **2004**, *23*, 2625.

19. Skupinska, J., *Chem. Rev.* **1991**, *91*, 613-616.

20. Wang, Z., Liu, Q., Solan, G. A., Sun, W.-H., *Coord. Chem. Rev.* **2017**, *350*, 68-83.

21. Lapping, G. R., Sauser, J. D., Alphaolefins Applications Handbook. **1989**.

22. Shiraki, Y., Nakamoto, Y., Souma, Y., *j. Mol. Catal A: Chem.* **2002**, *187*, 283-294.

23. Keim, W., *Angew. Chem. Int. Ed.* **2013**, *52*, 12492-12496.

24. Zilbershtein, T. M., Kardash, V. A., Suvorova, V. V., Golovko, A. K., *Appl. Catal. A: Gen.* **2014**, *475*, 371-378.

25. Zhou, Z., Hao, X., Redshaw, C., Chen, L., Sun, W-H., *Catal. Sci. Technol.* **2012**, *2*, 1340-1345.

26. Yin, L., Liebscher, L., *J. Chem. Rev.* **2007**, *107*, 133-173.

27. Ojwach, S. O., PhD Thesis, *University of Johannesburg* **2008**.

28. Burwell, R. L., *Chem. Rev.* **1952**, *57*, 1034.

29. Keil, F. J., *Microporous Mesoporous Mater.* **1999**, *29*, 49-66.

30. Zhao, X. S., Bao, X. Y., Guo, W., Lee, F. Y., *Mater. Today* **2006**, *9*, 32-39.

31. Finiels, A., Fajula, F., Hulea, V., *Catal. Sci. Technol.* **2014**, *4*, 2412-2426.

32. Garwood, W. E., Caesar, P. D., Brennan, J. A., *U. S. Patent 4* **1972**, *150*, 062.

33. Garwood, W. E., Lee, W., *U. S. Patent 4* **1980**, *227*, 992.

34. van der Berg, J. P., Roebschlager, K. H. W., Maxwell, I. E., *Proceedings of the North American Catalysis Society Meeting* **1989**.

35. Degnan, J., *Top. Catal.* **2000**, *13*, 349.

36. Golombok, M., de Bruijin, J., *Ind. Eng. Chem. Res.* **2000**, *39*, 267.

37. Thomas, F., Degnan, Jr., *Top. Catal.* **2000**, *13*, 349-356.

38. Wulfers, M. J., Lobo, R. F., *Appl. Catal. A: Gen.* **2015**, *505*, 394-401.

39. Dos Santos, J. H. Z., Krug, c., da Rosa, M. B., Stedile, F. C., Dupont, J., Camargo Forte, M., *J. Mol. Catal A: Chem* **1999**, *139*, 199-207.

40. Huang, Y., Zhang, R., Liang, T., Hu, X., Solan, G, A., Sun, W.-H., *Organometallics* **2019**, *38*, 1143-1150.

41. Hlatky, G. G., *Chem. Rev.* **2000**, *100*, 1347-1376.

42. Kumar, B. S., Dhakshinamoorthy, A., Pitchumani, k., *Catal. Sci. Technol.* **2014**, *4*, 2378-2396.

43. Upadhyay, P. R., Srivastava, V., *Curr. Catal.* **2016**, *5*, 162-181.

44. Satterfield, C. N., *Heterogeneous Catalysis in Industrial Practice*, 2nd edition ed.; McGraw Hill: New York, **1991**.

45. Zheng, Y., Li, X., Dutta, P. K., *Sensors* **2012**, *12*, 5170-5194.

46. Haveling, J., Nicolaides, C. P., Scurrell, M. S., *Appl. Catal. A: Gen.* **1998**, *173*, 1-9.

47. Heydenrych, M. D., Nicolaides, C. P., Scurrell, M. S., *J. Catal.* **2001**, *197*, 49-57.

48. Chaudhary, V., Sharma, S., *J. Porous Mater.* **2016**, *DOI 10.1007/s10934-016-0311-z*.

49. Kim, M. J., Chang, S.H., Choi, J.S., Ahn, W.S., *Catal. Lett.* **2004**, *82*, 27-32.

50. Shin, D. Y., Yoon, J. H., Baik, H., Lee, S. J., *Appl. Catal. A: Gen.* **2020**, *590*, 117363.

51. Kim, M. J., Ahn, S., Yi, J., Hupp, J. T., Notestein, J. M., Farha, O. K., Lee, S. J., *Catal. Sci. Technol.* **2017**, *7*, 4351-4354.

52. Heurtefeu, B., Bouilhac, C., Cloutet, E., Taton, D., Deffieux, A., Cramail, H., *Progress in Polym. Sci.* **2011**, *36*, 89-126.

53. Metzer, E. D., Comito, R. J., Hendon, C. H., Dinca, M., *J. Am. Chem. Soc.* **2017**, *139*, 757-762.

54. Rozhko, E., Bavykina, A., Osadchii, D., Makkee, M., Gascon, J., *J. Catal.* **2017**, *345*, 270-280.

55. Lee, J. M., Cooper, A. I., *Chem. Rev.* **2020**, *120*, 2171-2214.

56. Naeimi, H., Lahouti, S., *Transit. Met. Chem.* **2018**, *https://doi.org/10.1007/s11243-018-0208-6*.

57. Karbach, F. F., *Silica-supported catalysts for ethylene oligomerization* **2004**, 15-21.

58. Keypour, H., Saremi, S. G., Noroozi, M., Veisi, H., *Appl. Organometal. Chem.* **2017**, *31*, 1-7.

59. Rezaei, S., Ghorbani-Choghamarani, A., Badri, R., *Appl. Organometal. Chem.* **2016**, *30*, 985-990.

60. Rossi, L. M., Costa, N.J.S., Silva, F. P., Wojcieszak, R., *Green Chem.* **2014**, *16*, 2906-2933.

61. Zhang, H. W., Liu, Y., Sun, S. H., *Front. Phys. Chin.* **2010**, *5*, 347-356.

62. Reddy, L. H., Arias, J. L., Nicolas, J., Couvreur, P., *Chem. Rev.* **2012**, *112*, 5818-5878.

63. Tang, S. C. N., Lo, I. M. C., *Water Res.* **2013**, *47*, 2613-2632.

64. Laurent, S., Dutz, S., Hafeli, U. O., Mahmoudi, M., *Adv. Colloid Interphase* **2011**, *166*, 8-23.

65. Li, X.-B., Gao, Y.-J., Wang, Y., Zhan, F., Zhang, X.-Y., Kong, Q.-Y., Zhao, N.-J., Guo, Q., Wu, H.-L., Li, Z.-J., et al., *J. Am. Chem. Soc.* **2017**, *139*, 4789-4796.

66. Gawande, M. B., Goswami, A., Asefa, T., Guo, H., Biradar, A. V., Peng, D.-L., Zboril, R., Varma, R. S., *Chem. Soc. Rev.* **2015**, *44*, 7540-7590.

67. Azarifar, D., Mahmoudi-GomYek, S., Ghaemi, M., *App. Organometal. Chem.* **2018**, *DOI: 10.1002/aoc.4541*, 1-13.

68. Petcharoen, K., Sirivat, A., *Mater. Sci. Eng. B-Adv.* **2012**, *177*, 421-427.

69. Li, H., Lu, Z., Cheng, G., Rong, K. F., Chen, F. X., Chen, R., *Rsc. Adv.* **2015**, *5*, 5059-5067.

70. Sharma, G., Jeevanandam, P., *RSC Adv.* **2013**, *3*, 189-200.

71. Okoli, C., Sanchez-Dominguez, M., Boutonnet, M., Jaras, S., Civera, C., Solans, C., Kuttuva, G. R., *Langmuir* **2012**, *28*, 8479-8485.

72. Ooi, F., DuChene, J. S., Qiu, J. J., Graham, J. O., Engelhard, M. H., Cao, G. X., Gai, Z., Wei, W. D., *Small* **2015**, *11*, 2649-2653.

73. Strobel, R., Pratsinis, S.E., *J. Mater. Chem.* **2007**, *17*, 4743-4756.

74. Karimzadeh, I., Aghazadeh,M., Doroudi, T., Ganjali, M. R., Kolivand, P. H., *Curr. Nanosci.* **2017**, *13*, 167-174.

75. Gawande, M. B., Branco, P. S., Varma, R. S., *Chem. Soc. Rev.* **2013**, *42*, 3371-3393.

Chapter Two

Literature review of immobilized late transition metal catalysts for ethylene oligomerization and polymerization reactions

2.1. Chapter introduction

Over the last decades, ethylene oligomerization and polymerization reactions have witnessed a tremendous development of new immobilized late transition metal catalysts.[1-3] This due to the lack of competitiveness of homogeneous catalysts against heterogeneous counterparts in comparisons of various drawbacks associated both homogeneous and heterogeneous catalysts. As a result, recent years have been devoted in the design and development of new strategies to immobilized ethylene oligomerization catalysts on various solid supports.[4-6] Functionalization of these solid supports to enhance catalysts catalytic activity and selectivity have been the main focus in current research and development.

This chapter provides a review of relevant literatures on immobilized late transition metal complexes as catalysts for ethylene oligomerization and polymerization reactions. This literature will be restricted on silica based, polymeric and magnetic nanoparticles solid supports. Late transition metal catalysts are suitable candidates for the oligomerization of ethylene due to their flexible nature. Since the emergence of this third generation of catalysts, ethylene oligomerization reactions have various solid supports have been developed and employed to immobilize nickel(II), iron(II), cobalt(II) and palladium(II) homogeneous complexes, therefore, the significant role played by these solid supports in controlling the catalytic performance of the catalysts in ethylene oligomerization is highlighted and discussed.

2.2. Silica immobilized transition metal catalysts

Over the past ten years, there has been a development of new attractive catalysts for ethylene oligomerization reactions including the well documented β-diimine nickel(II) complexes and the bis(imino)pyridine Fe(II) complexes discovered by Brookhart *et al.*,[7] and Gibson *et al*.[8] As a result, immobilization of these complexes on solid supports is believed to produce highly active and selective separable catalysts. This is due to improved diffusion of the reactants in the catalytic sites attributed to the increased pore sizes and reduced crystal sizes. Ever since the discovery of new tethering immobilization technique for the production of highly active and selective immobilized single-site catalysts apart from MAO supported catalysts, recent years have witnessed tremendous attention on the use of mesoporous silica materials as the solid supports in synthesis of separable catalysts for ethylene oligomerization reactions.

For example, Kaul *et al*,[9] independently synthesized *bis*(imino)pyridyl Fe(II) homogeneous and supported catalysts possessing variant spacer chain lengths as shown in **Figure 2.1**. The Karstedt catalyst was utilized in the synthesis of the immobilized complexes. Interesting, catalytic activity of the complexes increased with increasing alkenyl chain length at same temperature. For example, the complex **1** bearing the shortest alkenyl moiety, exhibited the lowest average catalytic activity of 6.61 x 10^3 kg of PE/((mol of Fe) h bar) whilst catalysts **2** and **3** bearing longer spacers displayed average catalytic activities of 9.31 x 10^3 kg of PE/((mol of Fe) h bar) and 9.71 x 10^3 kg of PE/((mol of Fe) h bar) respectively at 273 K. The catalytic activity of the immobilized complexes was lower by one order of magnitude compared to those of homogeneous analogues and also decreased with increasing temperature from 293 – 353 K. In addition, these immobilized complexes are known to produce polymers possessing bimodal

molecular weight distribution. The immobilized catalyst bearing **1** spacer group produced highest molecular weight polyethylene.

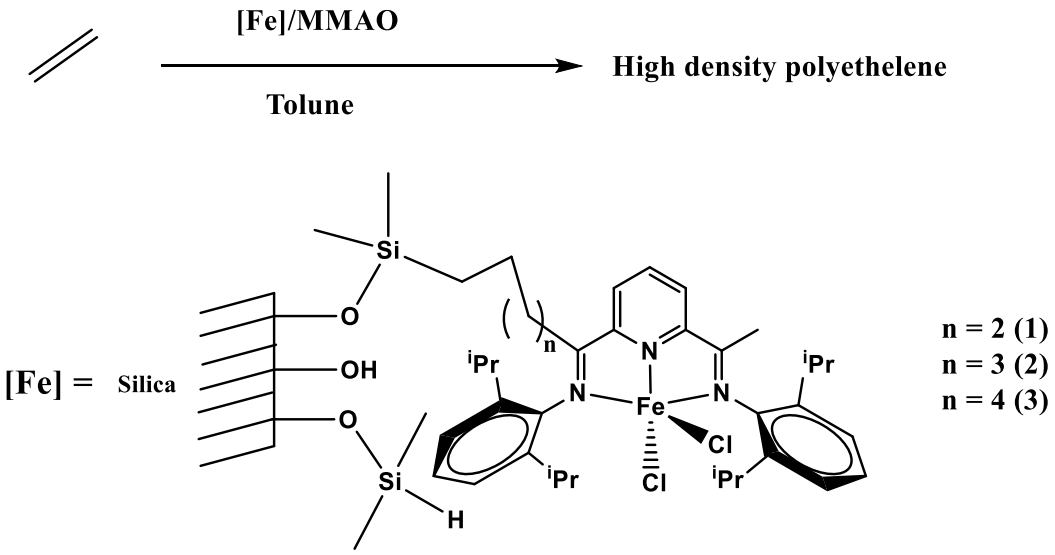

Figure 2.1: The *bis*(imino)pyridyl Fe(II) complexes immobilized on silica support for ethylene polymerization in the presence of MAO reported by Kaul *et al*.[9]

In another related work, Brookhart *et al*.[10] reported the preparation of aryl α-diimine nickel(II) supported catalysts immobilized through hydroxyl or amino functional groups which are reactive with trimethylaluminum pre-treated and activated silica support material as shown in **Scheme 2.1**. These supported catalysts formed active catalysts for slurry-phase polymerization of ethylene upon activation with $Et_3Al_2Cl_3$ or Et_3Al co-catalysts. Catalytic activities as high as 750 kg PE/g Ni were obtained when the immobilized Ni(II) aryl α-diimine pre-catalyst was activated with ethylaluminum sesquichloride (EASC) at an Al/Ni ratio of 700. The reported catalytic activity is 10-fold higher than the catalytic activity reported in literature for MAO-supported systems.[11-13] Furthermore, a more acidic co-catalyst like methylaluminum dichloride (MADC) have shown to give higher catalytic activity than EASC due to slow deactivation of the immobilized catalyst.[10] These results motivated the researchers to do more research work

on the development of new tethering strategies for immobilization of nitrogen donor late transition metal complexes for ethylene oligomerization.

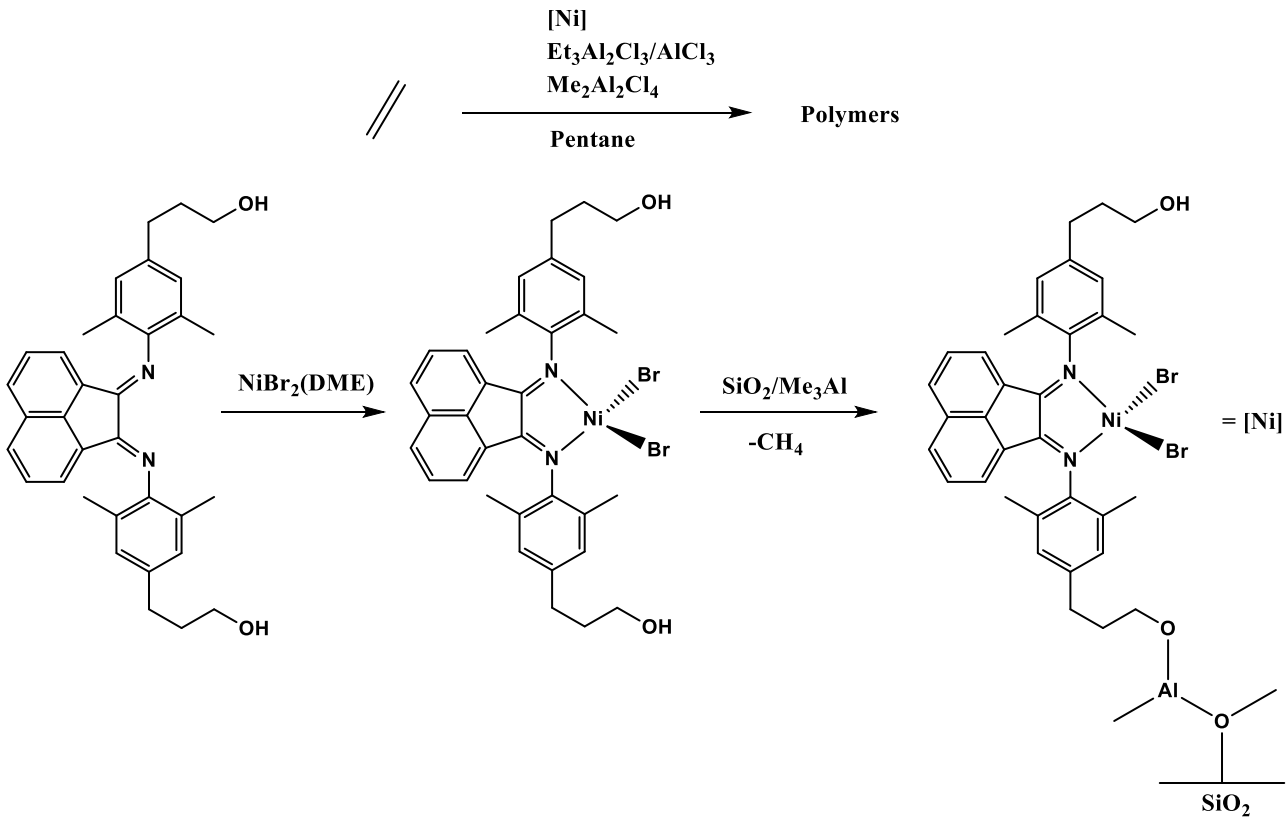

4

Scheme 2.1: Convergent approach for the synthesis of pre-treated silica immobilized nickel(II) aryl α-diimine catalysts for ethylene polymerization reported by Brookhart *et al*.[10]

In a follow up work, Schrekker *et al*.[14] reported new family of α-diimine Ni(II) immobilized complexes **5-9** bearing variable carbon chain lengths, silica-linkers and diimine bulky substituents as shown in **Figure 2.2**. In contrast to the previous Brookhart's system,[10] activation of these complexes with $Et_3Al_2Cl_3$ co-catalyst in pentane resulted to a formation of efficient catalysts for the polymerization of ethylene without any observed deactivation arising from the usage of excess amounts of the co-catalyst as reported previously. In general, the catalytic activity of the complexes ranged from 19 kg PE/g Ni to 450 kg PE/ g Ni depending on polymerization temperature, pressure, nickel concentration of the diimine Nil(II) complex on

silica support. Structural modifications, such as substitution of the *ortho*-methyl substituents in **6** by *i*-Pr bulky groups as in **7** resulted in a decline of the catalytic activities of the complexes.

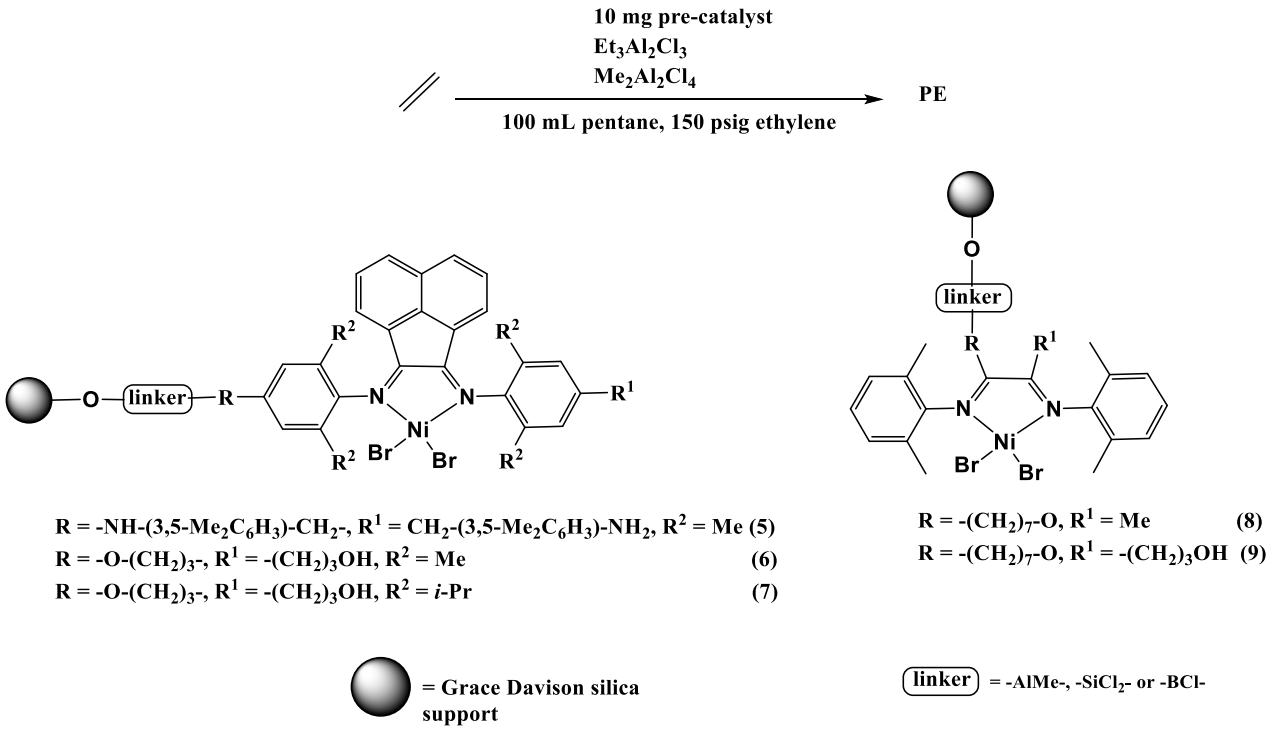

Figure 2.2: Linked silica immobilized α-diimine Ni(II) dibromide complexes employed for efficient slurry-phase conversion of ethylene to branched polyethylene.

Table 2.1: Ethylene slurry polymerization using catalysts **5-9** bearing different functional groups**.**

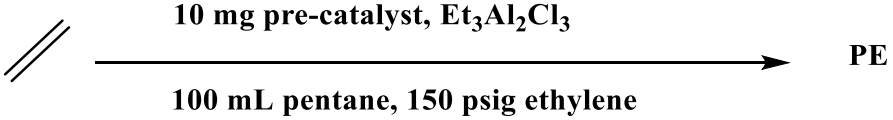

5: Grace Davison XPO-2402, calcined at 200 ^{o}C, -MeAl- as linker.
6: Grace Davison XPO-2402, calcined at 200 ^{o}C, -MeAl- as linker.
7: Grace Davison SP9-496, calcined at 500 ^{o}C, -MeAl- as linker.
8: Grace Davison SP9-496, calcined at 500 ^{o}C, -MeAl- as linker.
9: Grace Davison SP9-496, calcined at 500 ^{o}C, -MeAl- as linker.

Entry	Pre-catalyst	T (˚C)	Time (h)	Wt % Ni[a]	Al/Ni	kg PE/g 5-9	kg PE/g Ni	T_m[b] (˚C)	M_w[c] (g/mol)	PDI[c]	Branches /1000C[d]
1	**5**	60	2	1.0	280	3.3	330[e]	128	153k	3.6	n.d.
2	**6**	60	2	1.0	420	4.5	450[e]	126	131k	3.3	13
3	**7**	60	1	1.0	214	1.1	109	120	458k	4.5	54
4	**7**	60	1	2.0	214	1.7	84	118	369k	3.7	54
5	**8**	60	2	1.0	214	2.0[f]	197	n.d.	596k	15	38
6	**8**	80	2	1.0	214	0.7[f]	66	n.d.	262k	12	52
7	**9**	60	2	1.0	214	2.0[f]	208	n.d.	825k	18	31
8	**9**	80	2	1.0	214	0.9[f]	96	n.d.	415k	13	48

[a]Theoretical maximum Ni loadings. [b]Melting points determined by DSC. [c]Molecular weight and polydispersity determined by GPC/SEC. [d]Total branching determined by ^{1}H NMR. [e]Results reported based on the Ni loading previously determined by ICP-OES. [f]A small fraction of oligomers was detected (0.2-0.4 kg per gram of 8 and 9)

Different silica support linkers such as trimethylaluminium ($AlMe_3$), tetrachlorosilane ($SiCl_4$) and trichloroborane (BCl_3) have been proven to affect the catalytic performance of the immobilized α-diimine Ni(II) complexes. For example, treating Grace Davison SP9-496 silica with the $AlMe_3$, $SiCl_4$ and BCl_3 and attaching it to catalyst **6** resulted in catalytic activities of 355 kg PE/ g Ni, 268 kg PE/ g Ni and 277 kg PE/ g Ni respectively upon activation of each catalyst with EASC (Conditions: [Ni] = 1.0 wt % Ni; T = 60 ˚C; Al/Ni = 214; t = 2 h). The $AlMe_3$ silica linker was proven to give the best catalytic activities for the complexes. Interestingly, increasing the nickel loading from 1.0 to 3.0 wt % resulted in the enhanced productivities of the complexes.

Employment of the silica spacer groups between functionalities (-$(CH_2)_3$-) in the place of –OH and –CH_2(3,5-CH_3, CH_3-C_6H_2- in the case of NH_2) could results in improved catalytic activities. Notably, increasing the length of the carbon chain used for attachment is usually accompanied by an increase in the productivities of the immobilized catalysts. For example, catalyst **9** bearing longer chain length constituted high catalytic activity of 208 kg PE/g Ni than its analogue catalyst **8** (197 kg PE/g Ni) (**Table 2.1**, entries 7 *vs* 5). This phenomenon was also reported by Hermann *et al*.[9] using silica-attached *bis*(imino)pyridyl iron (II) catalysts (*vide-supra*, **Figure 2.1**). Substituents in the α-diimine ligand architecture played a marginal role in controlling the properties of the polyethylene product.

In a related study, Kim *et al*,[15] reported immobilization of Fe(II) and Co(II) catalysts **10** bearing *bis*(imino)pyridyl ligands on their pyridine ring using silicon ethoxide functional groups (**Figure 2.3**). Using MAO to activate the supported catalysts resulted in the formation of highly active catalytic systems for the polymerization of ethylene in toluene under atmospheric pressure between 10 and 50 °C. The Fe(II) supported catalyst illustrated polymerization

activity of 4.78 x 10^7 g(PE)/(mol(Fe) h bar) whilst Co(II) immobilized complex showed catalytic activity of 1.6 x 10^7 g(PE)/(mol(Fe) h bar) both at 50 °C. By all accounts, the supported catalysts were 100-times less active than their homogeneous counterparts. This can be reasoned to diffusion limitation of the acetylene monomer into the unevenly dispersed pores of the supported catalyst. In addition, reduction of the number of active sites and their deactivation upon immobilization also account for the decrease in the catalytic activity of the immobilized complexes. Poor metal to co-catalyst interaction also results in inactive catalytic sites as explained in the current study.

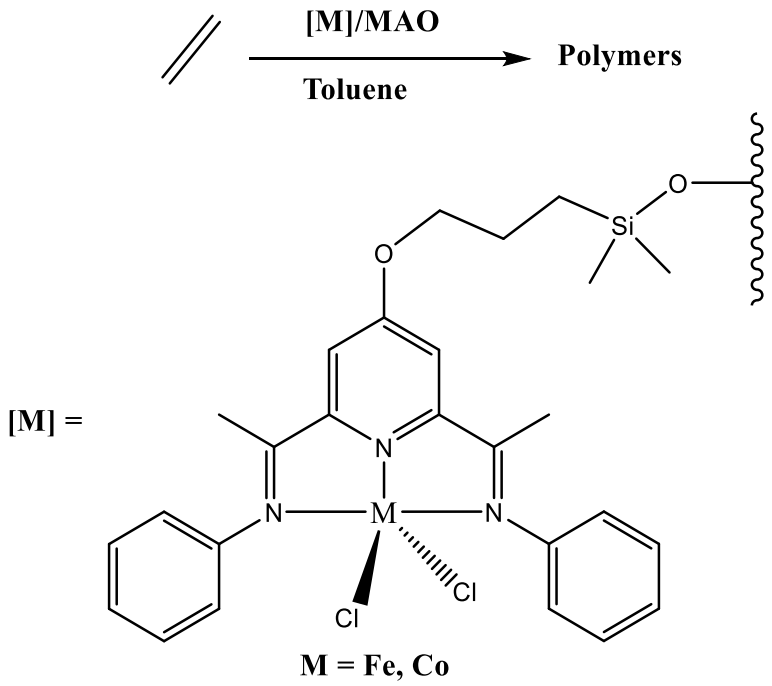

10

Figure 2.3: Immobilization of Fe(II) and Co(II) *bis*(imino)pyridyl complexes by tailing the pyridine functional group with silicon ethoxide.

Intrigue by the results obtained, Guo *et al*,[16] also reported the immobilization of *bis*(imino)pyridine Fe(II) complexes onto MAO-activated mesoporous MCM-41 and SBA-15. Activated with TEA (triethylaluminum) co-catalyst, the immobilized complexes demonstrated

appreciable catalytic activity on ethylene oligomerization towards the formation of mostly linear α-olefins at high reaction temperature. Nevertheless, the catalytic activity of the immobilized complexes extensively relied on the temperature and Al/Fe molar ratio. Unfortunately, all the immobilized catalysts regenerated and reused in this study were inactive due to the dissociation of the active species from the support. This usually caused by solvent treatment upon heating damaging the structure of the immobilized catalyst. Better selectivity towards the production of low α-olefins by MCM-41 complexes in comparison with SBA-15 is related to narrow pore sizes of MCM-41 as opposed larger pore sizes of SBA-15.

Studies have shown that when dealing with the immobilized pre-catalysts, the concentration of the active species in the heterogenized catalyst plays an important role in controlling the catalytic activity and selectivity of the supported pre-catalyst. In most instances, increasing the metal concentration is accompanied by a negative effect on the catalytic activity of the immobilized catalysts. For example, Brookhart and Preishuber-Pflugl,[10] using immobilized diimine Ni(II) catalysts for ethylene polymerization reported an activity loss of about 220 kg PE/g Ni of the catalyst's original catalytic activity of 750 kg PE/g Ni when the metal loading (weight %) was increased from 0.60 % to 2.0 %. The reason behind this trend is well explained by Mlinar *et al*.[17] that while effective dispersion of active sites at lower loading is possible, catalyst agglomeration at higher metal loadings may hinder ethylene monomer adsorption. Increasing metal contents does not only causes the catalytic activity of the immobilized catalysts to decrease but it also shifts the product distribution towards the formation of higher molecular weight side products.[18]

Using bipyridine Ni(II)Cl_2 catalysts **11** immobilized on SBA-15, Shin *et al*.[19] disclosed new highly active heterogeneous catalyst and a sophisticated way to avoid the production of

unwanted polymeric side products during ethylene oligomerization (**Figure 2.4**). Activated with diethylaluminium chloride (Et_2AlCl) in *n*-heptane solvent, these complexes formed highly active species for the oligomerization of ethylene into C_4, C_6, C_8 and C_{10} depending on the extent of Ni(II) metal loading density on SBA-15 and reaction time. Notably, lower catalysts loading showed much better catalytic activity of the immobilized catalysts. For example, catalyst loaded with 0.21 wt % of Ni displayed intrinsic activity (IA) towards butene of 3605 ± 28 $mol_{product}/mol_{Ni}h$ which was better than that of the catalyst loaded with 2.25 wt % of Ni metal (IA = 911 ± 28 $mol_{product}/mol_{Ni}h$). These results further illustrated that the formation of higher molecular weight polymeric side products which are the main cause of reactor fouling, could be inhibited by reducing the local concentration of the metal catalyst on the solid silica support as shown in **Figure 2.4**. Furthermore, prolonged reaction times resulted in the drop of the IA of the catalysts due to the blockage of the active catalysts' sites by the accumulated high molecular weight products leading to rapid deactivation of the catalysts.[19]

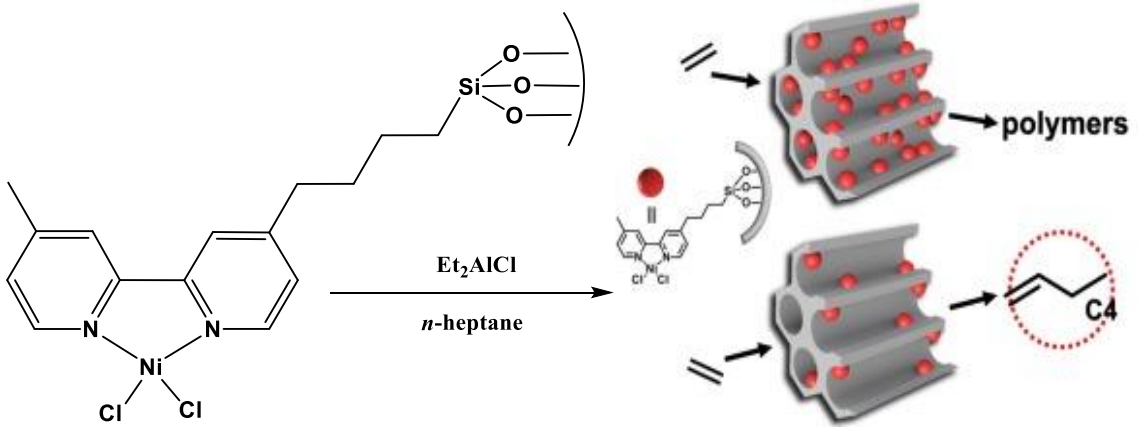

11

Figure 2.4: Mesoporous bipyridine (bpy)Ni(II)Cl_2 silica immobilized complex prepared by Shin *et al*.[19] for the oligomerization of ethylene to give mainly butenes or polymers depending on the metal concentration.

Immobilized catalysts structural morphological properties such shape, particle size, pore sizes and crystallinity play a significant role in controlling the catalytic abilities of the heterogenized catalysts. The pore size and topology of the solid support is another vital factor which dictates the catalytic activity, selectivity and the lifetime of the catalyst.[20] It is well established that while larger pore size is advantageous for the diffusion of high molecular weight oligomers, smaller pore size is usually accompanied by very high catalytic activity of the catalyst and the formation of more dimers and other low molecular weight oligomers.[19, 21] To give a supporting example on the effect of catalyst particle size on catalytic performance is provided Henry *et. al*.[22] who independently compared the catalytic performance of Ni-H-Beta(microcrystalline) and Ni-H-Beta(nanocrystalline). The Ni-H-Beta(microcrystalline) catalyst displayed lower conversion rate than Ni-H-Beta(nanocrystalline) catalyst due to their larger particle size which present longer diffusion path. Furthermore, the transportation of the reactants and products in the interphase of the active site and the catalyst surface is limited thereby leading to the building up of larger products inside the pores and finally deactivation of the catalyst.[23]

Antonov *et al*,[24] has recently reported the synthesis of both homogeneous and silica-alumina immobilized dichloride and dibromide nickel(II) complexes **12-14** supported on 2-iminopyiridine and 2-iminoquinoline novel ligands bearing electron withdrawing groups (**Figure 2.5**). These complexes were capable of dimerizing ethylene into 1-butene and *cis* and *trans*-2-butene at a rate of up to 19.2 x 10^6 g of oligomers mol(Ni)$^{-1}$ h^{-1} for homogeneous counterparts. On the other hand, the supported catalysts displayed lower catalytic activity of 10.7 oligomers mol(Ni)$^{-1}$ h^{-1}. The selectivity of the nickel(II) complexes supported on silica-alumina (SiO_2/Al_2O_3) was comparable to that of homogeneous complexes. The choice of Lewis acid activator governed the selectivity of the complexes. For example, this study have shown that in the presence of a more acidic Lewis acid activator like $Et_3Al_2Cl_3$ with either homo or

supported catalysts, products such as mono and dibutyltoluenes and butylethyltoluenes are formed during ethylene dimerization. Ligand architecture played a marginal role in controlling the catalytic activity of both homogeneous and silica-alumina immobilized complexes.

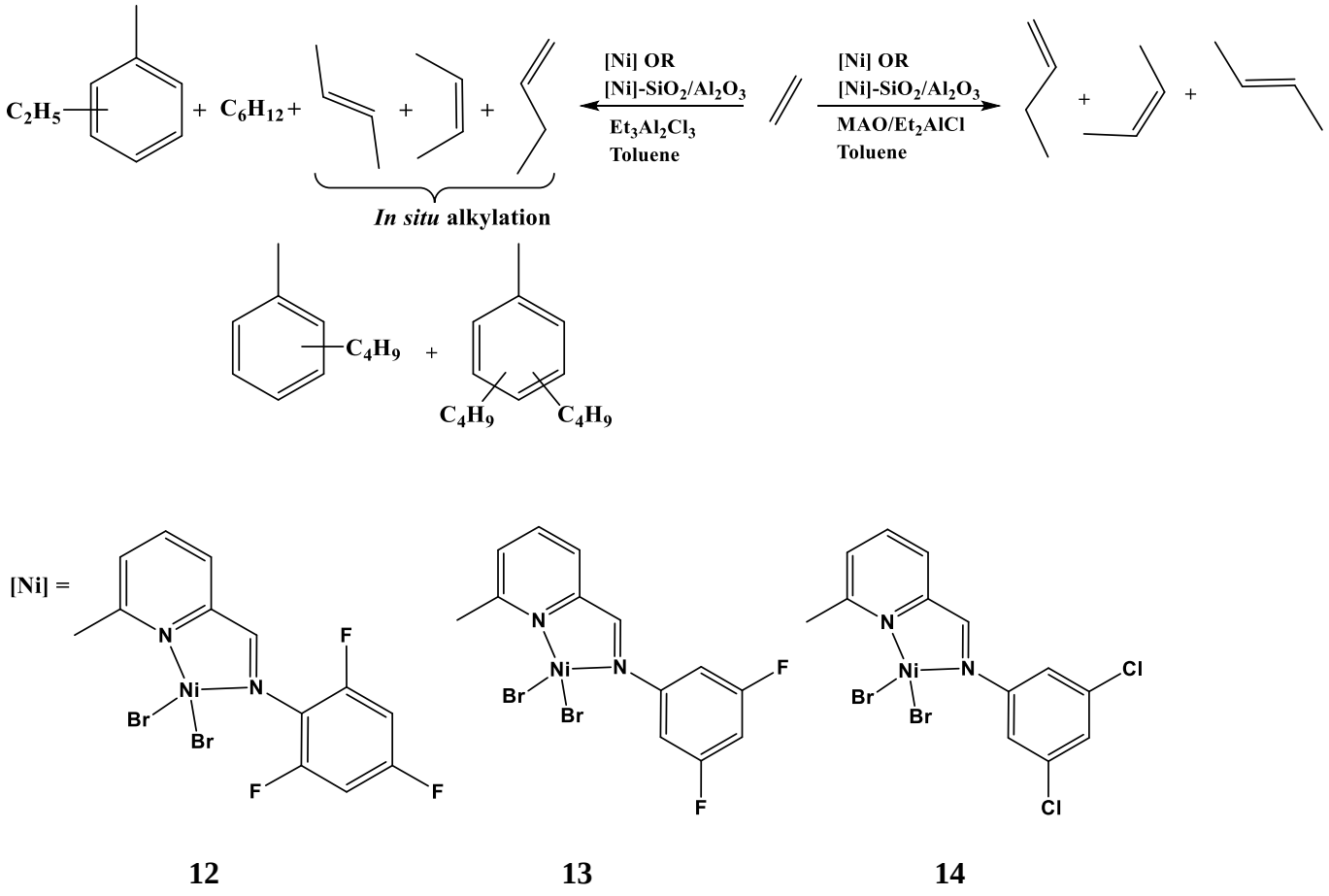

Figure 2.5: Dimerization of ethylene to butene isomers using homogeneous and silica-alumina immobilized Ni(II) complexes and formation of unwanted Friedel-Crafts alkylation products promoted by $Et_3Al_2Cl_3$ co-catalyst.

Rossetto and co-workers independently prepared both MCM-41 [25] and SBA-15 [26] supported Ni(II) complexes based on diimine ligands, that is, 2-(phenyl)amine-4-(phenyl)imine-2-pentene and 2-(2,6-dimethylphenyl)amine-4-(2,6-dimethylphenyl)imine-2-pentene as shown in **Figure 2.6**. Activated by EASC co-catalyst, the catalysts displayed good catalytic activity to a tune of 18.1 x 10^3 h^{-1} with high selectivity towards the formation of C_4 (98 %), C_6 and

alkylated toluene products. Notably, both the MCM-41 immobilized complexes were more catalytically active and more selective than their SBA-15 immobilized counterparts revealing the effect of the solid support on the catalysts catalytic performance of the silica immobilized catalysts. Essentially, the MCM-41 immobilized catalysts could be recycled up to three times while SBA-15 immobilized catalysts were recycled twice without marginal loss in the catalytic activity and C_4 oligomer selectivity.

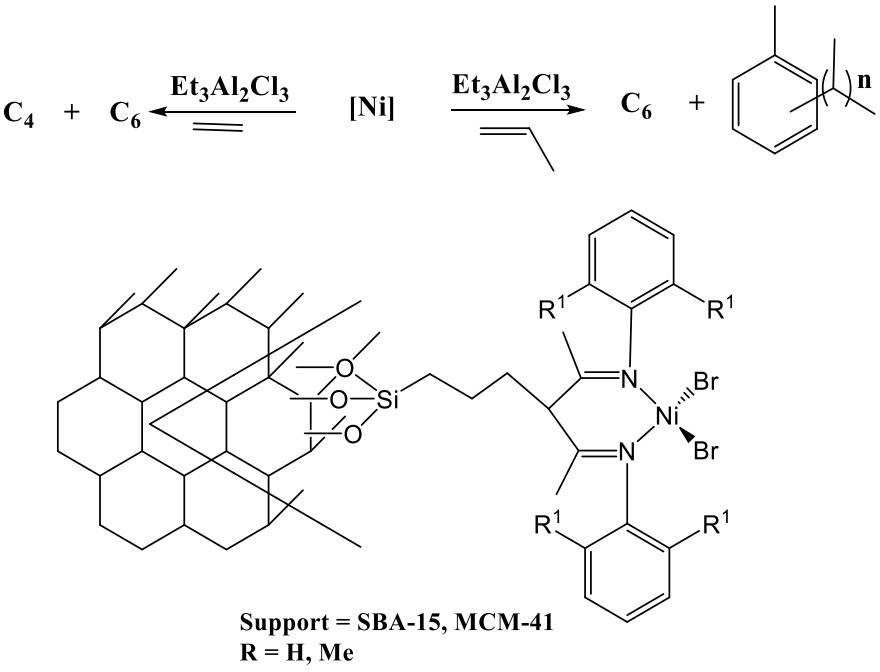

15

Figure 2.6: Diimine Ni(II) complexes anchored on MCM-41 and SBA-15, synthesized by Rossetto *et al.*[25-26] for the production of C_4 and C_6 oligomers during ethylene oligomerization and formation of C_6 and alkylated toluene products during propylene oligomerization.

In a subsequent study by Kumar *et al.*[27] synthesized both homogeneous and MCM-41 immobilized *N*-(2-pyridinylmethylene)-3-(triethoxysilyl-1-propamine) and *N*-(1-(pyridin-2-yl)ethylidene)-3-(triethoxysilyl)-1-propanamine Ni(II) complexes for ethylene oligomerization reactions **Figure 2.7**. Immobilized complexes showed lower catalytic activities of 239 kg mol^{-1} h^{-1} and 261 kg mol^{-1} h^{-1} compared to the catalytic activities of 374 kg mol^{-1} h^{-1} and 566 kg

mol^{-1} h^{-1} displayed by their homogeneous counterparts. Interestingly, the immobilized catalysts were only activated with $EtAlCl_2$ from the initial run and were active throughout the subsequent recycling experiments. The leak of oxygen to the reaction mixture was accountable for the observed gradual reduction in the catalytic activity upon recycling. Another intriguing results observed were in the complete alkylation of the preformed oligomers by the supported catalysts which could attributed to the high acidic aspect of the solid support. Reaction parameters such as temperature, pressure Al/M ratio and time had a marginal effect on the catalytic activity and selectivity of the complexes.

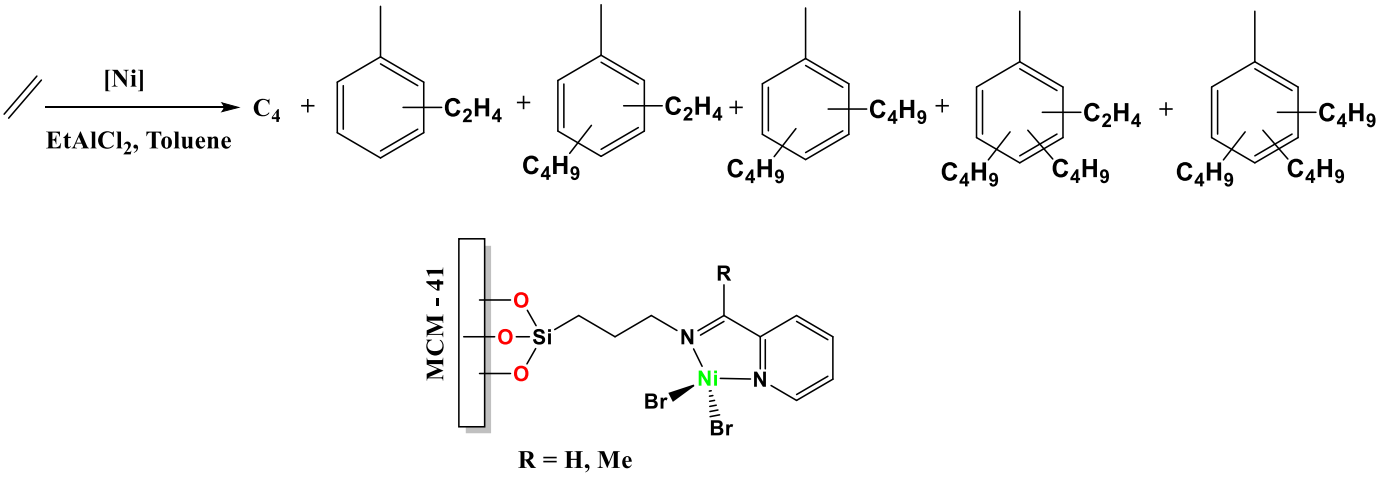

16

Figure 2.7: Ethylene dimerization and formation alkylated toluene products catalyzed by immobilized *N*-(2-pyridinylmethylene)-3-(triethoxysilyl-1-propamine) and *N*-(1-(pyridin-2-yl)ethylidene)-3-(triethoxysilyl)-1-propanamine Ni(II) complexes by Kumar and coworkers.[27]

It has become a common practice for the researchers to simultaneously compare both homogeneous complexes and their immobilized counterparts under one roof. Recently, Tuskaev *et al*.[28] disclosed some intriguing results using both homogeneous and silica anchored Ni(II) tripodal N^N^N ligated complexes (**Figure 2.8**). The homogeneous and immobilized complexes were both activated with Et_2AlCl and $Et_3Al_2Cl_3$ co-catalysts in toluene solvent.

Intriguingly, the catalytic activity and selectivity of 92-158 kg mol^{-1} h^{-1} atm^{-1} and 60-70 % respectively towards 1-butene for the immobilized complexes exceeded that of homogeneous counterparts of 12-129 kg mol^{-1} h^{-1} atm^{-1} and 25-54 % respectively. Profoundly, increasing the pore diameter of the supported catalysts has a negative effect on their catalytic performance. For example, varying pore diameters from 60 nm, 100 nm, 300 nm and 500 nm they recorded catalytic activities of 158 kg mol^{-1} h^{-1} atm^{-1}, 120 kg mol^{-1} h^{-1} atm^{-1}, 105 kg mol^{-1} h^{-1} atm^{-1} and 92 kg mol^{-1} h^{-1} atm^{-1} respectively, pointing to the decline of catalytic activity with increasing pore diameter of the Ni(II) tridentate immobilized catalysts.

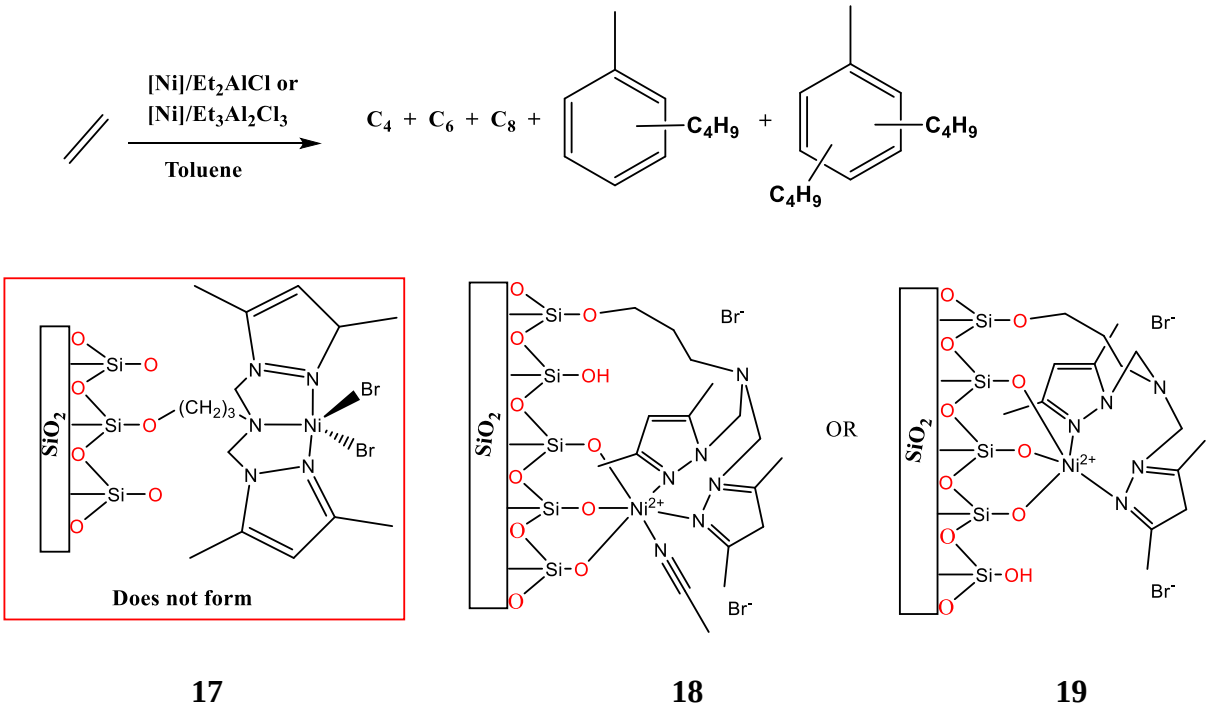

17 **18** **19**

Figure 2.8: Silica immobilized N^N^N tripodal Ni(II) complexes for the production of butenes as major products during ethylene oligomerization reactions reported by Tuskaev *et al.*[28]

Due to the lack of competitiveness of the homogeneous catalysts against heterogeneous catalysts, Favero *et al.*[29] by adopting a silica linker approach reported by Schrekker *et al.*[14] recently developed a sophisticated method for the synthesis of MCM-41 immobilized binary Ni(II) diimine catalysts. As illustrated in **Scheme 2.2**, the precursor is either attached alone as

a single precursor or together with a second precursor to form a sophisticated binary precursor. The binary system combines the characteristics of two polymers in one product. These immobilized systems form inactive species in combination with MAO. On the other hand catalytic activities as high as 3 876 kg PE mol Ni^{-1} h^{-1} were obtained for the binary precursor and single precursor reached catalytic activity of 3964 kg PE mol Ni^{-1} h^{-1} when activated with $Et_3Al_3Cl_3$ co-catalyst. The binary systems produced polymers of distinct characteristics of the homopolymer an evidence that both precursors are active. This work evidenced that methods of immobilization are still evolving and nurturing.

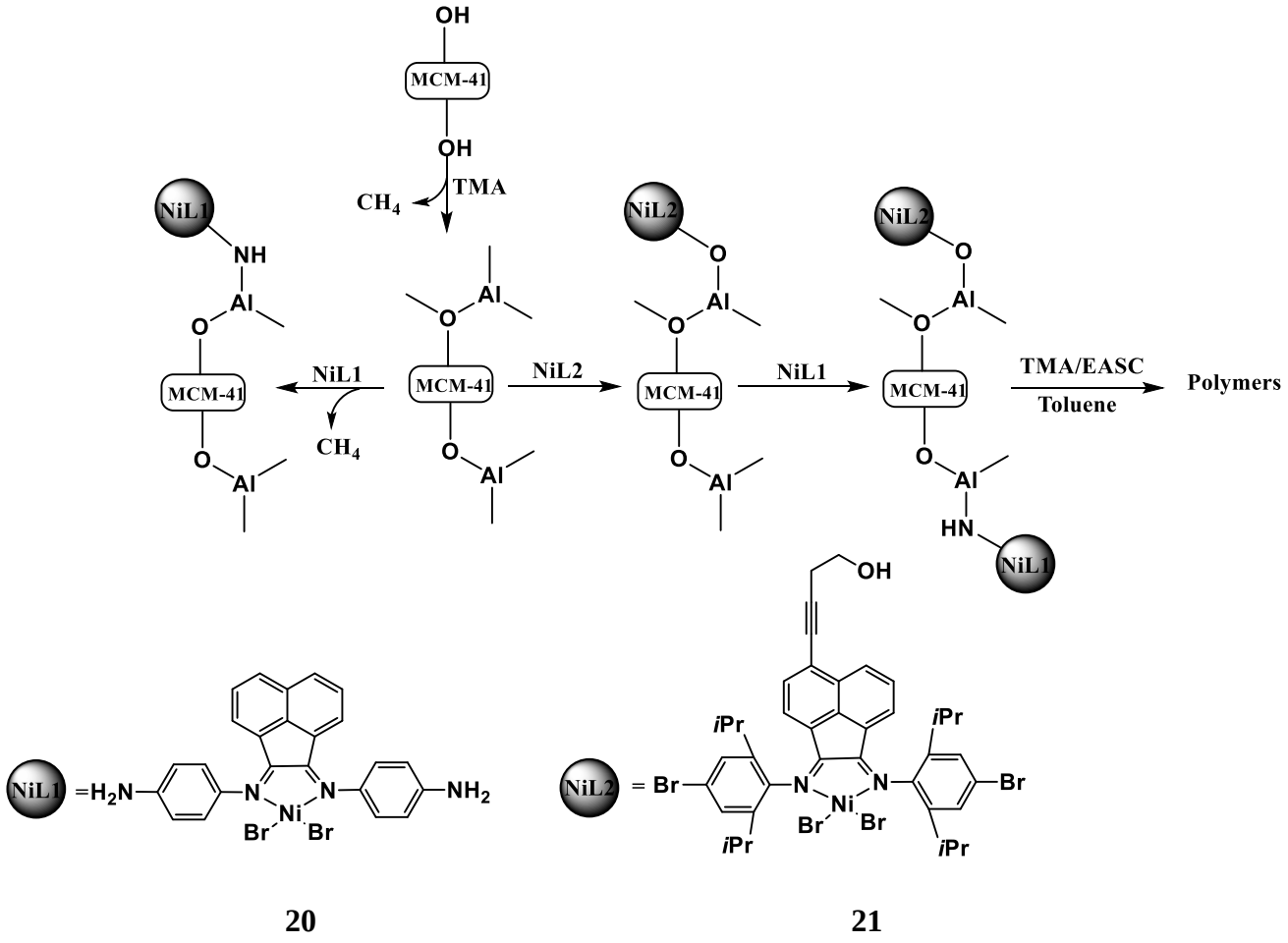

20 **21**

Scheme 2.2: Synthesis of MCM-41 immobilized single and binary precursors for ethylene polymerization to give polymer products.[29]

. The ion exchange samples, in particular the nickel ions, contains two distinctly different types of active sites, that is, nickel with oxidation state of 0, +1 or +2 and Brønsted acid sites. These sites are responsible for the variations in the catalytic activity and selectivity of the heterogenized catalysts under same conditions during ethylene oligomerization reactions.[30] The samples were confirmed to constitute grafted Ni^{2+} and Ni^{2+} counter ions, NiO particles and small amounts of Ni^{0}.[31] Progressively, Henry *et al*.[22] using FT-IR spectroscopy probed the nature of the active site by binding the CO to the accessible sites after interaction with ethylene. Notably, the species with oxidation state below +2 and Brønsted acid sites participated in the adsorption and reaction of ethylene under specified conditions excluding the participation of NiO and grafted Ni^{2+} in the process. The CO-FTIR results pointed to ion exchanged Ni^{2+} species to be the most likely active sites in heterogeneous catalysts as illustrated in **Scheme 2.3**.

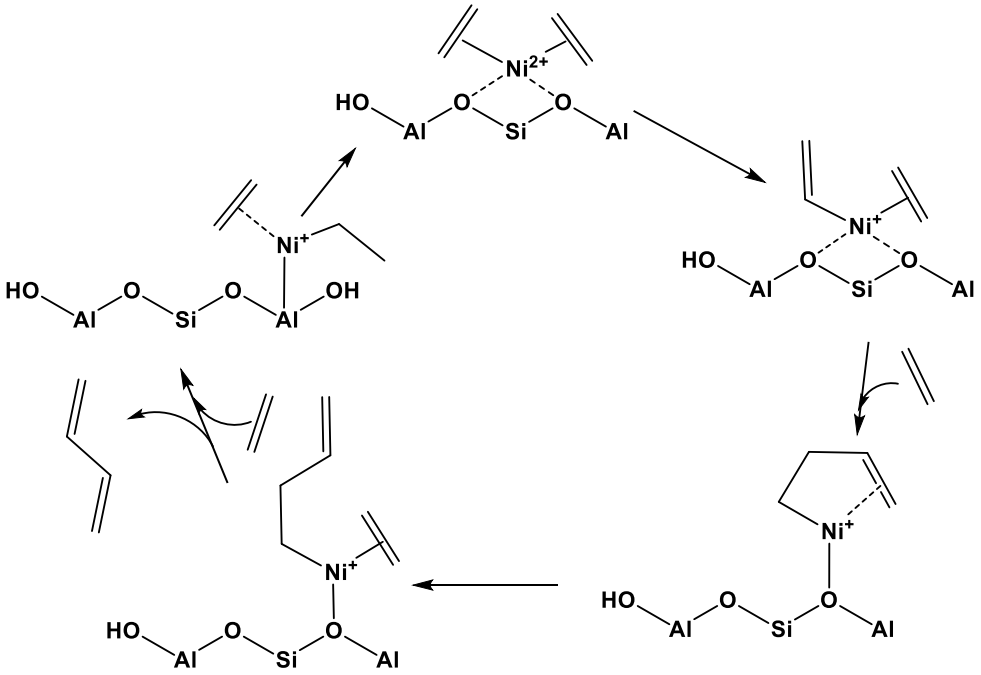

Scheme 2.3: Formation of the active sites from the reaction of ethylene with Ni^{2+} ions during ethylene oligomerization.[22]

2.3. Polymer immobilized transition metal catalysts

Immobilization of single-site catalysts on versatile, inexpensive and easily handled porous polymer supports forms another innovative field of study worthy of time investment and investigation. The most prominent advantage achieved in immobilizing early and late transition metal complexes on polymer materials is in the elimination of inorganic ash in the final oligomeric and polymeric products.[32] In addition, poor chemical stability of the heterogenized catalysts manifested in their low productivities and turn over numbers (TONs) can be overcome by the use of porous organic polymers which have the catalytically relevant ligand directly attached into a highly stable polymer structure. Heurtefeu *et al*.[33] highlighted the significance of polystyrene and polysiloxane in the immobilization of late and early transition metal catalysts for ethylene oligomerization reactions. Under the family of porous organic polymers we also have porous organic polymers (POPs),[34] carbon organic frameworks (COFs) [35] and metal organic frameworks (MOFs) [36] which have played a marginal role in the immobilization of single-site catalysts for ethylene oligomerization reactions.

For example, Kim *et al*.[34] recently reported a new *bis*-pyridine chelated Ni(II) complex immobilized on a porous organic polymer as illustrated in **Figure 2.9**. This Ni(II) catalyst was incorporated into a new porous organic polymer material prepared using a "click reaction" and complexed with $NiCl_2$ precursor. In the presence of Et_2AlCl co-catalyst in *n*-heptane solvent at 20 bar and 25 ˚C, the complex show good catalytic activity to a tune of 1198 $mol_{product}/mol_{Ni}$ h) with an intrinsic activity (IA) towards butene of 800 ±79 $mol_{product}/mol_{Ni}$ h and 54 % product selectivity. Under mild conditions, i.e. T = 0 ˚C and P = 5 bar in *n*-heptane solvent, they were able to recover and reuse the catalyst for four consecutive cycles with a decline of catalytic activity after each run due to polymer building up.

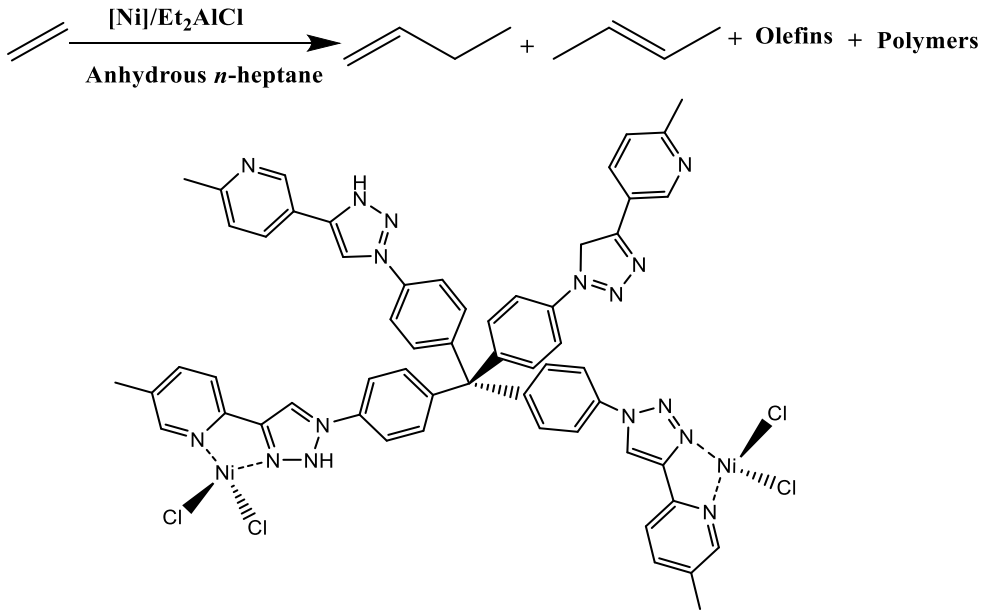

22

Figure 2.9: Typical examples of porous materials reported in literature by Kim *et al*.[34] for the production of mainly butene oligomers, olefins and polymers.

In another study by Rozhko *et al*,[35] two different families of porous aromatic frameworks (PAFs) *vis*, covalent triazine frameworks (CTFs) comprising of both micro- and mesoporous structures and lamellar structured imine-linked polymer network (IL-PON) were surveyed. **Figure 2.10** shows the structure of the mesoporous solid material prepared. On activation by triethylaluminum solution (Et_3Al) in *n*-heptane solvent at 15 bar, the catalysts showed high catalytic activities (TONs) for production of C_4, C_6, C_8 and C_{10} oligomers depending on catalysts textural properties. The imine-linked polymer network based catalyst **23** showed the greatest catalytic activity per metal atom of 370 ± 60 h^{-1}, followed by the mesoporous CTF solid catalyst **25** (301 ± 50 h^{-1}) and lastly the microporous CTF solid catalyst **24** (252 ± 6 h^{-1}) being the least active. The catalytic activity results revealed a direct link between the accessibility of the active sites and the catalytic performance of the catalysts. Porous polymer

materials with smaller pore sizes are prone to suffer from internal diffusion limitations thereby displaying low catalytic activity. Even though, the catalytic activity of the immobilized catalysts did not surpass that of homogenous catalyst (2240 ± 100 h^{-1}), but their full activity and selectivity could be recovered upon rinsing the catalysts with dichorobenzene solvent.

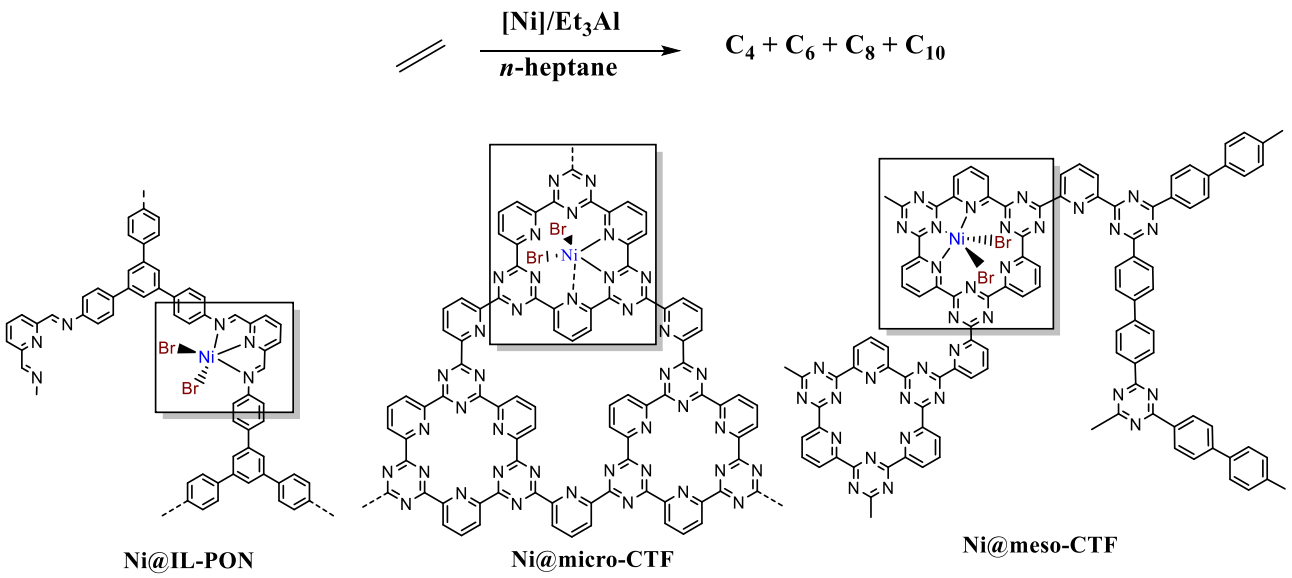

23 **24** **25**

Figure 2.10: Porous aromatic frameworks as polymeric supports for the immobilization of Ni(II) catalysts for the production of C_4-C_{10} oligomers from ethylene, reported by Rozhko *et al.*[35]

The quest for the development of robust catalysts for the oligomerization of ethylene has recently led to the development of sophisticated metal organic frameworks (MOFs). For example, Canivet and co-workers,[37] recently disclosed a one-pot synthesis of (Fe)MIL-101 MOFs immobilized Ni(II) complexes for the selective dimerization of ethylene to form 1-butene as illustrated in **Figure 2.11**. The metal content of the catalysts played a significant role in controlling the catalytic activity of the catalysts. Notably, the catalyst loaded with 2.8 µmol of Ni metal showed lower catalytic activity of 3166 h^{-1} whilst high catalytic activity of 3215 h^{-}

[1] was obtained for the catalyst with Ni metal content of 8.4 µmol. Conclusively, decreasing Ni metal content improves the catalytic activity per Ni active site. Interestingly, the catalysts could be recovered through filtration and can be reused after careful washings and drying for at least two catalytic cycles without marginal loss of activity and selectivity. Leaching tests revealed that no activity could be quantified when the filtrate is subjected under catalytic conditions in the presence of a co-catalyst.

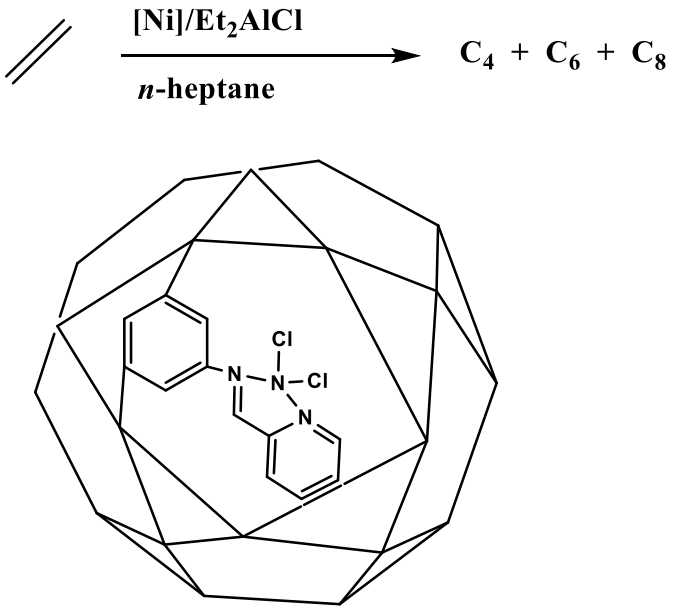

26

Figure 2.11: Fe-MIL-101 metal organic frameworks immobilized Ni(II) complex for ethylene oligomerization to give C_4 – C_8 oligomers reported by Canivet *et al.*[37]

Subsequently, Metzger *et al.*[38] reported a selective dimerization of ethylene to 1-butene using a Ni(II) catalyst **27** which is based on MFU-4l (MFU-4l = $Zn_5Cl_4(BTDD)_3$, H_2BTDD = *bis*(1H-1,2,3-triazolo[4,5-b],[4′,5′-i])dibenzo[1,4]dioxin)) MOFs secondary building subunits (**Figure 2.12**). Activation of the catalysts with MAO in toluene afforded catalytically active porous materials that consumed ethylene at a rate of 41 000 mole per mole of Ni per hour with up to 96.2 % 1-butene selectivity. In contrast, replacement of MAO co-catalyst with either Et_2AlCl

or Et_3Al led to a diminished catalytic activity of the Ni(II) immobilized complexes. For example, turn over frequencies of 21 000 h^{-1} and 4 700 h^{-1} were obtained when 10 % Ni catalyst was activated by same equivalences of MAO and Et_2AlCl co-catalysts respectively.

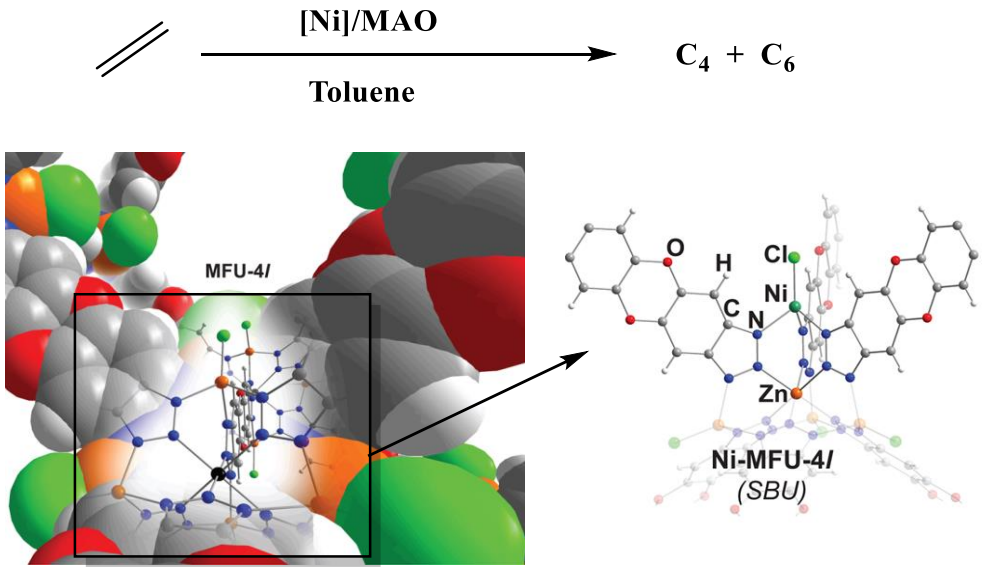

27

Figure 2.12: The 3-D representation and ball and stick model of the MFU-4l metal organic frameworks immobilized Ni(II) material used for selective production of 1-butene from ethylene.[38]

As shown by previous studies, increasing the total metal contents of the immobilized complexes results in a decline in the catalytic activity of the catalyst. Accordingly, Metzger *et al*.[38] reported Ni(II) catalyst immobilized on MFU-4l MOFs with molar Ni loadings of 10 % and 30 % of the total Ni contents to afford TOFs of 27 000 and 9 100 mole of ethylene consumed per mole Ni per hour respectively under optimal conditions. Intriguingly, the immobilized catalysts could be recycled and reused continuously for 8 cycles with only minor decrease in the catalytic activity. The selectivity of MOFs immobilized Ni(II) catalysts towards 1-butene, to date, surpass that of industrially applied homogeneous catalysts, that of ion exchange zeolites and mesoporous silica based complexes.[36]

2.4. Catalysts supported on iron magnetic nanoparticles

Recent years are experiencing an exponential growth of the application of magnetic nanoparticles in catalysis due to the development of bottom up or sequential approaches. Magnetic nanoparticles have received a wide spread in catalysing an enormous number of reactions including, hydrogenation reactions,[39] oxidation reactions,[40] carbon-carbon coupling reactions,[41] photocatalytic reaction,[42] hydroformylation reactions[43] and carbonylation reactions.[44] To date, Pd(II) metal still remains the most catalytically active metal centre in various kinds of organic transformations. Consequently, it is highly like to find literature studies on Pd/magnetic nanoparticles supported catalysts for the development of environmentally robust catalysts.[45] The ease of separation of magnetic nanoparticles through the application of an external magnetic field (**Figure 2.13**) have made them powerful tools for the fast, efficient, environmentally friendly and energy saving separation of catalysts from the reaction mediums.[46]

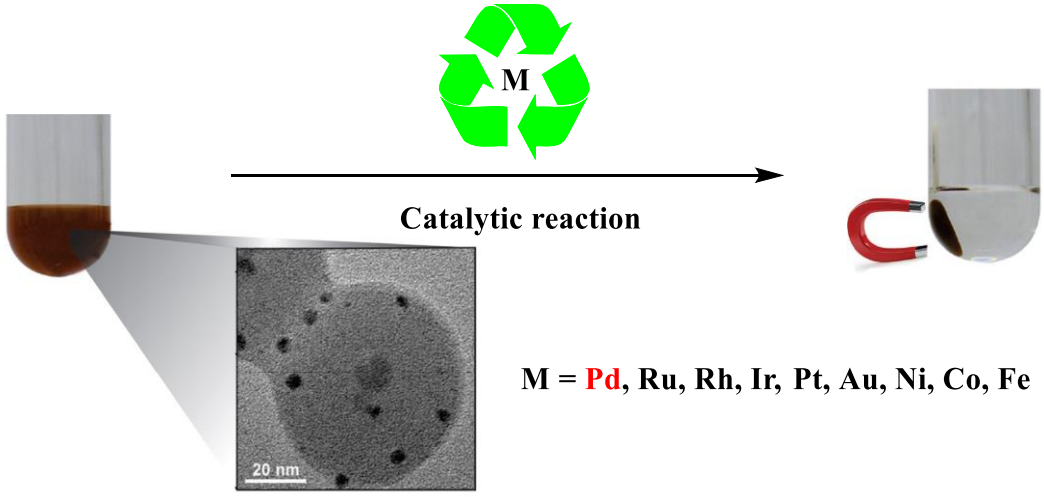

Figure 2.13: Recyclability of magnetic nanoparticles *via* an application of an external magnetic field in various reactions.

Despite the unlimited applications of Fe_3O_4 MNPs in various fields of catalytic transformation, it is strange that their use in ethylene oligomerization catalysis is yet to be fully appreciated. To date and to the best of our knowledge, there is no report on the use of magnetic nanoparticles either as solid supports of homogeneous catalysts for ethylene oligomerization reactions. This lacuna thus provides the opportunity to design and develop magnetically supported transition metal catalysts in ethylene oligomerization/polymerization reactions.

In conclusion, the design and development of immobilized late transition metal catalysts for ethylene oligomerization and polymerization revolves around these principal aspects; ligand architecture, choice of support and technique, particles size and metal loadings. These pillars greatly control the catalytic outcomes of the immobilized catalysts. As a result, careful modification of the ligands architecture and particle size, choice of immobilization support and usage of optimized or threshold amount of the metal concentration can lead to the full exploitation of the high catalytic activities and selectivities of these separable single-site catalysts.

2.5. Problem statement

Comparisons of homogenous catalysts with heterogeneous catalysts have reveals that both these catalysts suffer dismally from certain valuable aspects. Firstly, despite excellent catalytic activity and selectivity displayed by homogeneous catalysts, they still suffer a lot from poor catalyst separation, recovery and reuse. On the other hand, heterogeneous catalysts possess good stability and are separable and recoverable yet display low atom efficiency due to various active sites available. Therefore, the main challenge to date is coming up with new complexes for the oligomerization of ethylene reactions that will constitute advantageous properties of both homogeneous and heterogeneous catalyst. The design and synthesis of a catalyst which

will possess the catalytic activity and selectivity of a homogeneous system and also be separable as the heterogeneous catalysts will be a major breakthrough in the field of ethylene oligomerization reactions.

2.6. Rationale of study

The discovery of homogeneous catalysts both early and late transition metal based complexes was a major breakthrough in ethylene oligomerization to date. Their extensive research development in academic and industrial sectors agrees precisely with their significant role they are currently playing in the production of vital short and long chain α-olefins ($C_4 – C_{20}$) which are used in the manufacturing of plasticizers, adhesives, lubricants and surfactants. As a result, immobilization of these homogeneous systems on solid supports such as silica (SBA-15 and MCM-41), silica-alumina and polymers will be very advantageous in ethylene oligomerization reactions since it will lead to the development of catalytically active, selective, recyclable and reusable hybrid catalysts for ethylene oligomerization processes.

The literature review revealed that all the documented immobilized catalysts for ethylene oligomerization and polymerization reactions are based on homoleptic nitrogen donor ligands. As a result, there is still shortage of literature reviews reporting on the immobilization of mixed donor ligands for the synthesis of metal complexes used in ethylene oligomerization reactions. Based on the information that mixed donor ligands offer attractive electronic and steric properties, this project is directed in finding high catalytically active, selective and recyclable immobilized catalysts for ethylene oligomerization reactions.

Furthermore, based on the high catalytic activity, efficient recyclability and reusability of the late transition metal complexes immobilized on Fe_3O_4 magnetic nanoparticles in other C-C

forming catalytic reactions such as Heck reaction, Suzuki Miyaura coupling reaction and Sonogashira reaction,[47] this project also seek to find highly stable, catalytically active, selective, recyclable and reusable late transition metal based catalysts for ethylene oligomerization immobilized on Fe_3O_4 magnetic nanoparticles. Due to the limited number of publications on the Fe_3O_4 magnetic nanoparticles immobilized catalysts for ethylene oligomerization, this project will be of great importance in expanding the use of Fe_3O_4 magnetic nanoparticles as solid supports in immobilization of late transition metal catalysts for ethylene oligomerization reactions.

2.7. Aims of study

The main aim of the project is to synthesize and characterize homogeneous and immobilized Fe(II), Ni(II) and Co(II) complexes and investigate their applications in the oligomerization process of ethylene. The first part of the project is aims to fine-tune the steric and electronic properties of the catalysts to achieve optimum catalytic activity and selectivity. The second part of the thesis aims to immobilize the homogeneous catalysts on solid supports in order to produce hybrid catalysts that are not only selective, but also recyclable.

2.8. Objectives of the study

From the above broad aim, the specific objectives of this research project can be broken down as follows:

1. To synthesize and characterize Ni(II), Fe(II) and Co(II) complexes bearing N^O and N^N^O Schiff base ligands. This was aimed at studying the influence of ligand moieties on the catalytic activity and selectivity of the homogeneous complexes.

2. To synthesize new separable (ethylimino-methyl)phenol (N^O donor) Ni(II), Fe(II) and Co(II) single-site catalysts immobilized on Fe_3O_4 magnetic nanoparticles solid support in order to produce recyclable and reusable single-site catalysts.

3. To probe the influence of applying different solid supports on the catalytic activity and selectivity of the (ethylimino-methyl)phenol (N^O donor) Fe(II), Ni(II) and Co(II) immobilized complexes, both SBA-15 and MCM-41 silica supports are employed to immobilized the single site catalysts.

4. To study the behaviour of the complexes towards ethylene oligomerization reactions and to investigate and optimize the effect of reaction conditions such as pressure, time, solvent, co-catalyst and aluminium to metal ratio on the catalytic performance of the complexes.

5. To apply computational theories (DFT) in order to ascertain an in-depth understanding of the catalytic behaviour of the homogeneous catalysts towards ethylene oligomerization reactions.

The aim and the objectives are realized in Chapters 3-6 while Chapter 7 provides the overall summary of conclusions.

2.9. References

1. Bahuleyan, B. K., Park, D.-W., Ha, C.-S., Kim, I., *Catal. Sury, Asia.* **2006**, *10*, 65.

2. Hubner, S., de Vries, J. G., Farina, V. , *Adv. Synth. Catal.* **2015**, *358*, 3-25.

3. Zhang, H., Li, X., Zhang, Y., Lin, S., Li, G., Chen, L., Fang, Y., Xin, H., Li, X., *Energy Environ. Focus.* **2014**, *3*, 246-256.

4. Connor, C. T., Kojima, M.; Elsevier Science Publishers. B. V.: South Africa, **1990**, p 329-349.

5. Wight, A. P., Davis, M. E., *Chem . Rev.* **2002**, *102*, 3589-3614.

6. Wei, W., Jiang, Y., Wu, H., Lv, C.-S., Luo, M.-J., Ning, Y.-N., Mao, G.-L., *Chin. Sci. Bull.* **2013**, *58*, 1741-1750.

7. Svejda, S. A., Brookhart, M., *Organometallics* **1999**, *18*, 65-74.

8. Lappin, G. R., Nemec, L, H., Sauer, J. D., Wagner, J. D., In *Higher Olefins, Kirk-Othmer Encyclopedia of Chemical Technology*, Wiley & Sons, Inc.: New York, N Y, USA, **2000**; Vol. *17*, pp 709-728.

9. Kaul, F. A., Puchta, G. T., Schneider, H., Bielert, F., Mihalios, D., Herrmann, W. A., *Organometallics* **2002**, *21*, 74-82.

10. Preishuber-Pflugl, P., Brookhart, M., *Macromolecules* **2002**, *35*, 6074-6076.

11. Canich, J. A. M., Gindelberger, D. E., Matsunaga, P. T., Vaughan, G. A., Squire, K. R., *WO 9748736*.

12. Bennett, A., M., McLain, S. D., *WO 9856832*.

13. Killian, C. M., Lavoie, G. G., MacKenzie, P. B., Moody, L. S., *WO 9962968*.

14. Schrekker, H. S., Kotov, V., Preishuber-Pflugl, P., White, P., Brookhart, M., *Macromelecules* **2006**, *39*, 6341-6354.

15. Kim, I., Han, B. H., Ha, C.-S., Kim, J.-K., Suh, H., *Macromelecules* **2003**, *36*, 6689-6691.

16. Guo, C.-Y., Xu, H., Zhang, M., Zhang, X., Yan, F., Yuan, G., *Catal. Commun.* **2009**, *10*, 1467-1471.

17. Mlinar, A. N., Shylesh, S., Ho, C. O., Bell, A. T., *ACS. Catal.* **2014**, *4*, 337-343.

18. Hartmann, M., Poppl, A., Kevan, L., *J. Phys. Chem.* **1996**, *100*, 9906-9910.

19. Shin, D. Y., Yoon, J. H., Baik, H., Lee, S. J., *Appl. Catal. A: Gen.* **2020**, *590*, 117363.

20. Finiels, A., Fajula, F., Hulea, V., *Catal. Sci. Technol.* **2014**, *4*, 2412-2426.

21. Hulea, V., Fajula, F., Bousquet, J., *J. Catal.* **2004**, *225*, 213-222.

22. Henry, R., Komurcu, M., Ganjkhanlou, Y., Brogaard, R. Y., Lu, L., Jens, K.-J., Berlier, G., Olsbye, U., *Catal. Today* **2018**, *299*, 154-163.

23. Wulfers, M. J., Lobo, R. F., *Appl. Catal. A: Gen.* **2015**, *505*, 394-401.

24. Antonov, A. A., Semikolenova, N. V., Soshnikov, I. E., Talsi, E. P., Bryliakov, K. P., *Top. Catal.* **2019**, *https://doi.org/10.1007/s11244-019-01208-8*.

25. Rossetto, E., Nicola, B. P., de Souza, R. F., Bernardo-Gusmao, K., Pergher, S. B. C., *J. Catal.* **2015**, *323*, 45-54.

26. Rossetto, E., Nicola, B. P., de Souza, R. F., Bernardo-Gusmao, K., Pergher, S. B. C., *Appl. Catal. A: Gen.* **2015**, *502*, 221-229.

27. Kumar, K., Godeto, T., Darkwa, J., *J. Organomet. Chem* **2016**, *818*, 137-144.

28. Tuskaev, V. A., Zubkevich, S. V., Saracheno, D., Gagieva, S. Ch., Dorovatovskii, P. V., Kononova, E. G., Khrustalev, V. N., Zarubin, D. N., Bulychev, B. M., Kissin, Y. V., *J. Mol. Catal.* **2019**, *464*, 29-38.

29. Favero, C., Closs, M. B., Galland, G. B., Stieler, R., Rossetto, E., Bernardo-Gusmao, K., *J. Catal.* **2019**, *377*, 63-71.

30. Haveling, J., van der Beek, A., de Pender, M., *Appl. Catal.* **1998**, *42*, 325-336.

31. Martinez, A., Arribas, M. A., Concepcion, P., Moussa, S., *Appl. Catal. A: Gen.* **2013**, *467*, 509-518.

32. Kitagawa, T., Uozumi, T., Soga, K., Takata, T. , *Polymer* **1997**, *38*, 615-620.

33. Heurtefeu, B., Bouilhac, C., Cloutet, E., Taton, D., Deffieux, A., Cramail, H., *Progress in Polym. Sci.* **2011**, *36*, 89-126.

34. Kim, M. J., Ahn, S., Yi, J., Hupp, J. T., Notestein, J. M., Farha, O. K., Lee, S. J., *Catal. Sci. Technol.* **2017**, *7*, 4351-4354.

35. Rozhko, E., Bavykina, A., Osadchii, D., Makkee, M., Gascon, J., *J. Catal.* **2017**, *345*, 270-280.

36. Metzer, E. D., Comito, R. J., Hendon, C. H., Dinca, M., *J. Am. Chem. Soc.* **2017**, *139*, 757-762.

37. Canivet, J., Aguado, S., Schuurman, Y., Farrusseng, D., *J. Am. Chem. Soc.* **2013**, *135*, 4195-4198.

38. Metzger, E. D., Brozek, C. K., Comito, R. J., Dinca, M., *ACS. Cent. Sci.* **2016**, *2*, 148-153.

39. Pelisson, C. H., Vono, L. L. R., Hubert, C., Denicourt-Nowicki, A., Rossi, L. M., Roucoux, A., *Cata. Today* **2012**, *183*, 124-129.

40. Silva, F. P., Jacinto, M. J., Landers, R., Rossi, L. M., *Catal. Lett.* **2011**, *141*, 432-437.

41. Zhang, Q., Su, H., Luo, J., Wei, Y., *Catal. Sci. Technol.* **2013**, *3*, 235-243.

42. Subramanian, V., Wolf, E. E., Kamat, P. V., *J. Am. Chem. Soc.* **2012**, *126*, 4943-4950.

43. Abu-Reziq, R., Alper, H., Wang, D. S., Post, M. L., *J. Am. Chem. Soc.* **2006**, *128*, 5279-5282.

44. Prasad, A. S., Satyanarayana, B., *J. Mol. Catal A: Chem.* **2013**, *370*, 205-209.

45. Polshettiwar, V., Basset, J.-M., Astruc, D., *Chemsuschem.* **2012**, *5*, 6-8.

46. Rossi, L. M., Costa, N.J.S., Silva, F. P., Wojcieszak, R., *Nanotechnol. Rev.* **2013**, *2*, 597-614.

47. Jang, S., Hira, S. A., Annas, D., Song, S., Yusuf, M., Park, J. C., Park, S., Park, K. H., *Processes* **2019**, *7*, 422-453.

CHAPTER THREE

Structural elucidation of N^O (ethylimino-methyl)phenol Fe(II) and Co(II) complexes and their applications in ethylene oligomerization catalysis

3.1. Introduction

Complexes based on late transition metals have attracted appreciable interest in the development of novel olefin oligomerization catalysts.[1-3] This is largely due to the significance of the oligomerization products which are useful intermediates for the production of lubricants, surfactants and plasticizers.[4] According to literature data, the ligand framework has been manifested to play a principal role in controlling both the electronic and steric properties of metal complexes, which in turn greatly affects their catalytic performance.[5] As such, diverse ligand architectures of mixed donor atoms, such as bidentate N^N,[6-8] N^O,[9-11] N^P,[12] O^P[13] and tridentate N^N^N,[14-15] N^N^P,[16] N^O^P,[17-18] N^O^N[19-20] systems have been extensively studied in olefin oligomerization reactions.

Despite the major successes witnessed in the design of late transition metal complexes as catalysts for ethylene transformation reactions, balancing the three pillars of catalytic activity, selectivity and stability remains elusive.[21-23] The chelation of the metal complexes with hybrid ligands appear to be an attractive alternative in filling these lacunas, since it provides distinct dynamic properties such as hemi-lability.[24-25] A recent review by Suo *et al.*,[26] highlights another advantage of employing phenoxyimine, an N^O donor ligand, over α-imine (N^N donor ligands), which is their ability to tolerate polar functional groups. Wang *et al.*,[27] for example, have reported the dimerization and trimerization of ethylene using cobalt and nickel

complexes bearing symmetrical 2,6-*bis*(imino)phenoxy ligands. In this study the nickel complexes were superior to cobalt complexes in terms of catalytic activity.

In addition, the presence of pendant donor groups have been proven to improve catalytic activities of the complexes as observed by Small *et al*.[28] using iron complexes bearing α-diimine ligands. In a related study, Boudier and co-workers,[20] employed Ni(II) complexes of imino-imidazole chelating donor ligands. These ligands were either bearing SR, OR, NR_2 or PR_2 pendant donor groups. In this study, substitution of a thioether by an ether pedant group was shown to result in improved catalytic activities of the resultant catalysts. In our recent report using nickel(II) complexes anchored on amino/imino phenol bidentate N^O donor ligands, we were able to demonstrate the effect of a ligand structure on catalytic activity and stability in ethylene oligomerization reactions.[29] Herein, we report the syntheses of Fe(II) and Co(II) complexes of 2-[(ethylimino)methyl]phenol ligands as potential catalysts for ethylene oligomerization reactions to expand our knowledge on the effect of ligand moieties and metal centre on the coordination chemistry of these compounds and inherent influence on their catalytic behaviour. Detailed structural characterization and effect of complex structure on the ethylene oligomerization reactions have been performed and are herein discussed.

3.2. Experimental section

3.2.1. Experimental components and instrumentation

All synthetic manipulations were performed under a nitrogen atmosphere using standard Schlenk-line techniques. All solvents were purchased from Merck and were dried and distilled prior to use. Methanol and ethanol were dried over calcium oxide whilst dichloromethane was

dried under CaH_2. Toluene was dried over sodium/benzophenone reagent and stored in 4A molecular sieves prior to their use. The chemicals; salicylaldehyde (98%), 2'-hydroxyacetophenone (98%), ethanolamine (99%), *N,N*-(diethyl)ethylenediamine (99%), cobalt(II) chloride (97%), iron(II) chloride (97%), methylaluminoxane solution (7 % w/w in toluene) and ethylaluminum dichloride solution (1.0 M in hexanes) were obtained from Sigma Aldrich and used without any further purification.[29] All ^{1}H NMR and $^{13}C\{^{1}H\}$ NMR (100 MHz) spectra were collected on a 400 MHz Bruker Ultra shield NMR spectrometer using deuterated solvents, i.e. either $CDCl_3$ or DMSO-d_6. The infrared spectra were collected on an Agilent Technologies, Cary 630 FTIR and Perkin Elmer Spectrometer 100. Mass spectrometric data collection was performed using an LC Premier micro-mass Spectrometer model LCMS-2020. Determination of the compounds elemental compositions was done utilizing a Thermal Scientific Flash 2000. Magnetic moment measurements were done on an Evans balance (Sherwood MK-1). Varian CP-3800 gas chromatograph equipped with a flame ionization detector (FID) and a CP-Sil 5 CB (30 m x 0.2 mm x 0.25 µm) capillary column was used for GC analyses (GC conditions: starting temperature 40 ˚C for 5 min, the heating rate of 10 ˚C/min up to 250 ˚C) while GC-MS analyses were performed on a Shimadzu GCMS-QP2010SE respectively.

3.2.2. Syntheses of Schiff base ligands and their respective iron(II) and cobalt(II) dichloride complexes

*3.2.2.1. Synthesis of phenol,2-[1-[(2-hydroxyethyl)imino]ethyl] (**L1**)*

A 30 mL ethanolic solution of 2'-hydroxy acetophenone (1.50 g, 11.00 mmol) was added to ethanolamine (0.67 g, 11.00 mmol). Then catalytic amount of Para toluene sulfonic acid (5.00 mg) was added forming a light green solution which was allowed to reflux for 24 h at 60 °C.

After the reaction period, ethanol solvent was removed under reduced pressure to give **L1** as brown liquid oil. Yield: 2.58 g (80%). ^{1}H NMR (400 MHz, $CDCl_3$): δ_H/ppm: 2.40 (s, 3H, H_a); 3.75 (t, 2H, $^{3}J_{HH}$ = 8.0 Hz, H_b); 3.99 (t, 2H, $^{3}J_{HH}$ = 8.0 Hz, H_c); 6.75 (d, 1H, $^{3}J_{HH}$ = 8.0 Hz, H_d); 6.92 (d, 1H, $^{3}J_{HH}$ = 8.0 Hz H_e); 7.28 (dd, 1H, $^{3}J_{HH}$ = 8.0 Hz, H_f), 7.48 (d, 1H, $^{3}J_{HH}$ = 8.0 Hz, H_g). $^{13}C\{^{1}H\}$ NMR ($CDCl_3$): δ/ppm: 42.62 (C_a), 58.25 (C_b), 63.70 (C_c), 116.59 (C_d), 128.25 (C_e), 130.72 (C_f), 133.08 (C_g), 136.47 (C_h), 162.37 (C_i), 173.40 (C_j). FT-IR (cm^{-1}): $\nu_{(O-H)}$: 3164; $\nu_{(C=N)}$:1604. TOF MS ESI: *m/z* (%), 180.1028 [$M^+ + H^+$, 100%]. HRMS for $C_{10}H_{13}NO_2$, 180.1025, found, 180.1028 [$M^+ + H^+$].

*3.2.2.2. Synthesis of phenol,2-[(E)-[(2-hydroxyethyl)imino]methyl] (**L2**)*

Similarly, ligand **L2** was synthesized through a reflux reaction between salicyaldehyde (1.50 g, 0.01 mol) and ethanolamine (0.73 g, 0.01 mol) in ethanol (30 mL) in the presence of 5.00 mg of Para toluene sulfonic acid. Ligand **L2** was obtained as a brown oily product after solvent removal using rotary evaporator under reduced pressure. Yield: 1.87 g (84 %). ^{1}H NMR (400 MHz, $CDCl_3$): δ_H/ppm: 3.79 (t, 2H, $^{3}J_{HH}$ = 4.0 Hz, H_a); 3.96 (t, 2H, $^{3}J_{HH}$ = 4.0 Hz, H_b); 6.89 (t, 1H, $^{3}J_{HH}$ = 8.0 Hz, H_c); 6.98 (d, 1H, $^{3}J_{HH}$ = 8.0 Hz, H_d); 7.28 (d, 1H, $^{3}J_{HH}$ = 8.0 Hz, H_e); 7.36 (d, 1H, $^{3}J_{HH}$ = 8.0 Hz, H_f), 8.42 (s, 1H, H_g). ^{13}C $\{^{1}H\}$ NMR ($CDCl_3$): δ/ppm: 61.73 (C_b), 62.12 (C_a), 117.08 (C_c), 118.68 (C_d), 131.46 (C_f), 132.47 (C_e), 161.20 (C_i), 166.94 (C_j). FT-IR (cm^{-1}): $\nu_{(O-H)}$: 3353; $\nu_{(C=N)}$:1631. TOF MS ESI: m/z (%), 166.09 [$M^+ + H^+$, 100%]. HRMS for $C_9H_{11}NO_2$, 166.0868, found, 166.0866 [$M^+ + H^+$].

*3.2.2.3. Synthesis of phenol,2-[(E)-{[2-(diethylamino)ethyl]imino}methyl] (**L3**)*

Ligand **L3** was prepared following similar method described for ligand **L1** and **L2**. Reflux reaction of salicyladehyde (1.50 g, 0.01 mol) and N, N-diethylethane-1,2-diamine (1.43 g, 0.01 mol) in ethanol (30 mL) afforded a liquid brown oil. Yield: 2.60 g (87 %). ^{1}H NMR (400 MHz,

$CDCl_3$): δ_H/ppm: 1.11 (t, 6H, $^3J_{HH}$ = 8.0 Hz, H_a); 2.68 (q, 4H, $^3J_{HH}$ = 8.0 Hz, H_b); 2.83 (t, 2H, $^3J_{HH}$ = 8.0 Hz, H_c); 3.72 (d, 2H, $^3J_{HH}$ = 4.0 Hz, H_d); 6.88 (d, 1H, $^3J_{HH}$ = 8.0 Hz, H_e); 6.98 (d, 1H, $^3J_{HH}$ = 8.0 Hz, H_f), 7.33 (qd, 2H, $^3J_{HH}$ = 8.0 Hz, H_g), 8.38 (s, 1H, H_h). FT-IR (cm^{-1}): $\nu_{(H\text{-}O)}$: 3061; $\nu_{(C=N)}$:1631. TOF MS ESI: m/z (%), 219.15 [M^+ - H^+, 100%], 220.15 [M^+, 40%]. HRMS for $C_{13}H_{20}ON_2$, 219.1497, found, 219.1499 [M^+ - H^+].

*3.2.2.4. Synthesis of [Co(**L1**)$_2$] (**1**)*

Addition of a yellow solution of ligand **L1** (0.11 g, 0.60 mmol) in dichloromethane (5 mL) to a blue solution of $CoCl_2$ (0.08 g, 0.60 mmol) in dichloromethane (5 mL) resulted in a brown mixture which was stirred for 24 h. After the reaction period, the mixture was filtered, and the precipitate was washed several times with dichloromethane (3 x 10 mL) to afford complex **1** as an analytically pure brown solid. Yield: 0.12 g (60 %). FT-IR (cm^{-1}): $\nu_{(Et\text{-}OH)}$: 3186 (broad peak); $\nu_{(Ph\text{-}OH)}$: 2951 (weak peak); $\nu_{(C=N)}$: 1640. TOF MS ESI: *m/z* (%), 387.0446 [Co(**L1**)$_2$, 100%], 223.0283 [Co(**L1**), 70%]. μ_{obs} = 4.49 BM. Anal. Calcd for $C_{18}H_{22}N_2O_4Co{\cdot}CH_2Cl_2$: C 48.32, H 4.70, N 5.93. Found: C 49.09, H 4.99, N 6.26.

The rest of the complexes were prepared following the procedure described for **1**.

*3.2.2.5. Synthesis of [Fe(**L1**)$_2$] (**2**)*

$FeCl_2$ (0.26 g, 1.30 mmol) and **L1** (0.27 g, 1.30 mmol). Layering of the methanol solution of **2** with diethylether yielded orange block crystals which eased X-ray crystallographic analysis. Yield: 0.12 g (32 %). FT-IR (cm^{-1}): $\nu_{(H2O)}$: 3551(weak peak); $\nu_{(Et\text{-}OH)}$: 3244 (weak band); $\nu_{(Ph\text{-}OH)}$: 2942 (weak), $\nu_{(C=N)}$: 1627. TOF MS ESI: *m/z* (%), 384.0696 [Fe(**L1**)$_2$, 100%]. μ_{obs} = 4.96 BM. Anal. Calcd for $C_{18}H_{22}N_2O_4Fe{\cdot}\,CH_2Cl_2{\cdot}H_2O$: C 46.84, H 4.97, N 5.75 Found: C 47.12, H 4.81, N 5.39.

*3.2.2.6. Synthesis of [Co(**L2**)$_2$] (**3**)*

L2 (0.24 g, 1.20 mmol) and $CoCl_2$ (0.13 g, 1.20 mmol). Yield: 0.32 g (86%). FT-IR (cm^{-1}): $\nu_{(Et\text{-}OH)}$: 3435; $\nu_{(Ph\text{-}OH)}$: 2940; $\nu_{(C=N)}$: 1628. TOF MS ESI: *m/z* (%), 237.0003 [Co(**L2**), 100%], 416.0782 [Co(**L2**)$_2$, 70%]. μ_{obs} = 3.96 BM. Anal. Calcd for $C_{20}H_{26}NO_2Co$: C 57.83, H 5.82, N 6.74. Found: C 57.65, H 5.53, N 6.44.

*3.2.2.7. Synthesis of [Fe(**L2**)$_2$] (**4**)*

$FeCl_2$ (0.11 g, 0.56 mmol) and **L2** (0.10 g, 0.56 mmol). Dark brown product obtained. Yield: 0.17 g (89%). FT-IR (cm^{-1}): $\nu_{(Et\text{-}OH)}$: 3259 (broad); $\nu_{(Ph\text{-}OH)}$: 2941; $\nu_{(C=N)}$: 1626. TOF MS ESI: *m/z* (%), 412.1161 [Fe(**L2**)$_2$, 20%]. μ_{obs} = 4.92 BM. Anal. Calcd for $C_{20}H_{26}N_2O_4Fe$: C 58.27, H 5.87, N 6.80. Found: C 58.37, H 5.70, N 6.69.

*3.2.2.8. Synthesis of [Co$_2$(**L3**)$_2$Cl$_4$] (**5**)*

$CoCl_2$ (0.06 g, 0.45 mmol) and **L3** (0.10 g, 0.45 mmol). Green shiny crystals suitable single X-ray crystal determination of **5** were obtained after recrystallization from acetonitrile/diethyl-ether solution mixture. Yield: 0.12 g (72%). FT-IR (cm^{-1}): $\nu_{(Ph\text{-}OH)}$: 2978; $\nu_{(C=N)}$: 1631. TOF MS ESI: *m/z* (%), 348.0462 [Co(**L3**)Cl_2, 100%]. μ_{obs} = 3.86 BM. Anal. Calcd for $C_{26}H_{40}N_2O_2Co_2Cl_4$: C 44.59, H 5.76, N 8.00. Found: C 44.22, H 5.74, N 8.11.

*3.2.2.9. Synthesis of [Fe$_2$(**L3**)$_2$Cl$_4$] (**6**)*

$FeCl_2$ (0.14 g, 0.45 mmol) and **L3** (0.10 g, 0.45 mmol). Yield: 0.11 g (70%). FT-IR (cm^{-1}): $\nu_{(Ph\text{-}OH)}$: 2985; $\nu_{(C=N)}$: 1599. TOF MS ESI: *m/z* (%), 334.9539 [(Fe(**L3**)Cl)+Na^+, 100%]. μ_{obs} = 4.96 BM. Anal. Calcd for $C_{26}H_{40}N_4O_2Fe_2Cl_4$: C 45.00, H 5.81, N 8.07. Found: C 45.26, H 5.41, N 8.18.

3.2.3. X-ray crystallography data collection

The X-ray crystallographic measurements for compounds **2** and **5** were performed on a Bruker APEX-II CCD diffractometer fitted with a low temperature device operating at temperature of 100(2) K. Molecular structure solution and refinement parameters of **2** and **5** are summarized and laid out in **Table 3.1**. The crystallographic data acquisition for the complexes was accomplished using a radiation of Mo Kα type (λ = 0.71073 Å) and crystal-to-detector distance of 50 mm. The data collections were performed utilizing both Ω and Φ scans with exposures kept at 30 W X-ray power and 0.50˚ frame width using APEX2.[30] Data reduction was achieved with SAINT software[30] through the application of a combination of correction parameters *vis*, outlier rejection, standard Lorentz, scan-speed scaling, and also polarisation correction factors. The data was further refined by applying the SADABS semi-empirical multi-scan absorption correction. Using Olex2[31], the structure was solved with the SHELXS structure solution program, using the direct methods solution method. The model was refined with version 2016/6 ShelXL[32] using Least Squares Minimization. All non-hydrogen were located in the difference map and refined anisotropically using SHELXS-2016 software.[33] In contrast, all hydrogen atoms were located in a calculated position and refined in an isotropic manner which allowed them to be included as ideal contributors in the refinement process using least square method.

*3.2.4. Paramagnetic studies of **2** and **5** using EPR*

EPR measurements were carried out on a Bruker EMX-plus X-band spectrometer at 77 K and 298 K temperatures. The solid crystalline powders of **2** and **5** were grounded to fine powders and their spectra were recorded by using the following parameters: microwave frequency: 9.870185 GHz; gain: 2.00 X 10^3; modulation amplitude: 5.0 G; conversion time; 37 ms; resolution: 3150 points; sweep width: 6500 G; 5 scans. The samples were then dissolved in acetonitrile and the solution phases spectra were recorded in a quartz flat cell under similar acquisition parameters.

3.2.5. Typical ethylene oligomerization catalysis protocol

The ethylene oligomerization reactions carried out using a stainless-steel reactor fitted with a 100 mL glass chamber and a magnetic stirrer bar. A pre-weighed amount of the synthesized pre-catalyst (10.0 µmol) in chlorobenzene (10 mL) was transferred into a dry Schlenk tube *via* a cannula under nitrogen atmosphere. This was followed by addition of the respective co-catalyst ($EtAlCl_2$ or MAO) using a syringe. The resultant solution in the Schlenk tube was then transferred using a cannula into the pre-evacuated reactor, followed by addition of 20 mL of chlorobenzene or toluene solvent to give total volume of 30 mL. The reactor was then purged with ethylene gas and pressure and temperature set at 10 bar and 30 ˚C, respectively, and the reaction initiated by switching on the magnetic stirrer for 1 h. Upon completion of oligomerization process, the reactor was cooled to about -10 °C using liquid nitrogen and the unreacted ethylene vented. This was followed by quenching the mixture through addition of 5 mL of 10% HCl (5 mL). Aliquots of the reaction sample were placed in GC-vials and analyzed to determine both the catalytic activity and oligomer compositions. N-heptane was used as internal standard[34] while GC-MS data were used to establish the molecular mass of the oligomer products.

3.2.6. Density Functional Theory (DFT) studies

DFT calculations were performed in a gas phase to identify the energy-minimized structures based on B3LYP/LANL2DZ (Los Almos National Laboratory 2 double ζ) level theory.[6, 35] A split bases set, LANL2DZ for Fe(II) and Co(II), and 6-311G for all other atoms was used to optimize the geometries and energies of the complexes and ethylene. The Gaussian09 suite of programs was used for all the computations.[36]

3.3. Results and discussion

3.3.1. Syntheses and characterization of iron(II) and cobalt(II) complexes

The ligands, 2-[(E)-[(2-hydroxyethyl)imino]methyl]phenol (**L1**), 2-[1-[(2-hydroxyethyl)imino]ethyl]phenol (**L2**) and 2-[(E)-{[(2-diethylamino)ethyl]imino}methyl]-phenol (**L3**) were achieved through the reaction of equimolar amounts of 2'-hydroxy acetophenone or salicylaldehyde with either ethanolamine or N, N-diethylethane-1,2-diamine in ethanol solvent in the presence of *para*-toluene sulphonic acid catalyst (**Scheme 3.1**).[29, 37] The ligands were obtained in appreciably high yields (80 % – 87 %) and were characterized using ^{1}H and ^{13}C NMR spectroscopy, mass spectrometry and IR spectroscopy.

The ^{1}H NMR spectrum of **L1** in **Figure 3.1**, shows the successful formation of the imine ligand by the presence of all the expected protons in their respective chemical shifts. For instance, a singlet peak around 2.35 ppm which was due to the imine methyl while the triplet peaks around 3.60-3.80 ppm corresponds to the ethylene protons. The sharp singlet peak around 3.45 ppm was assigned to the hydroxyl proton in the methyl substituted ligand **L1,** whilst other trace peaks were assigned to the traces of the available ethanol solvent used for the synthesis. For example, the peak at chemical shift of 2.56 ppm was due to the ethanolic OH. Similarly, the ^{13}C {^{1}H} NMR spectrum of ligand **L1** (**Figure 3.2**) was found to be consistent with the ^{1}H NMR of the molecule. For example, the imine carbon appeared around 164.05 ppm (peak **h**) while the methyl carbon appeared around 14.61 ppm (peak **a**). In addition, the number of fragment peaks observed were in good agreement with the number of carbons present in the molecule.

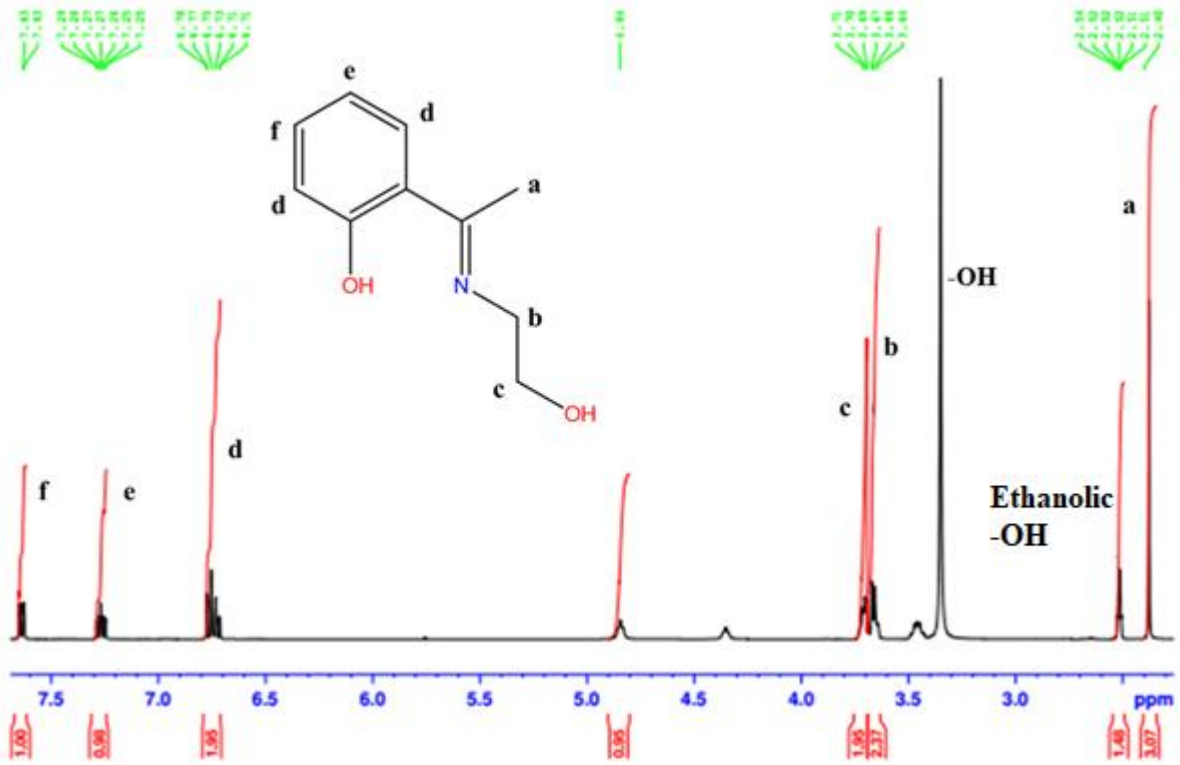

Figure 3.1: ^{1}H NMR spectrum of ligand **L1** showing the presence of imine methyl protons at ~ 2.35 ppm.

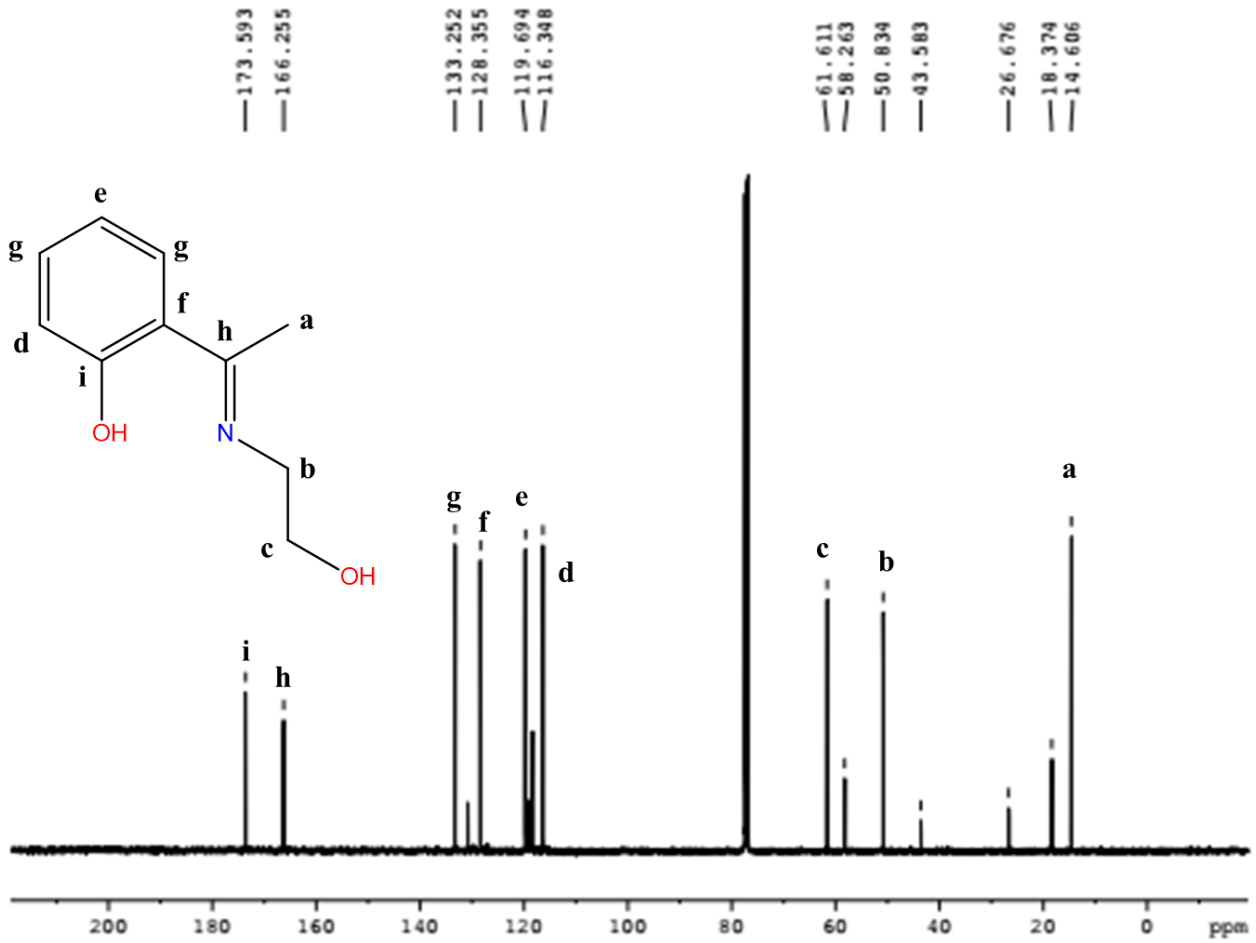

Figure 3.2: $^{13}C\{^{1}H\}$ NMR of spectrum of the imine ligand, **L1**.

The mass spectrometry also confirmed the formation of the imine ligands, **L1**-**L3**. For example, **Figure 3.3** is the mass spectrum of ligand **L1** showing the base peak at m/z = 180.1028 amu which corresponds to $[M]^+$ fragment of the imine ligand, **L1**.

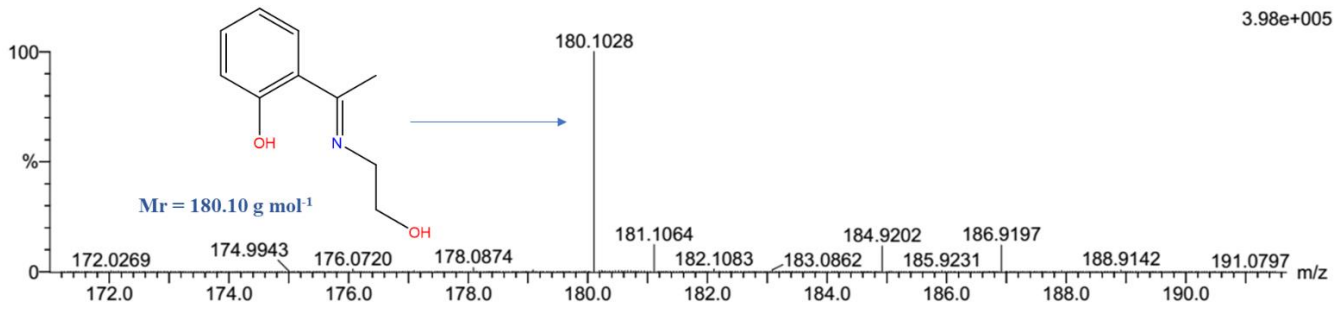

Figure 3.3: The mass spectrum of **L1** showing the base peak at m/z = 180.1028 amu corresponding to $[M]^+$ fragment of the ligand.

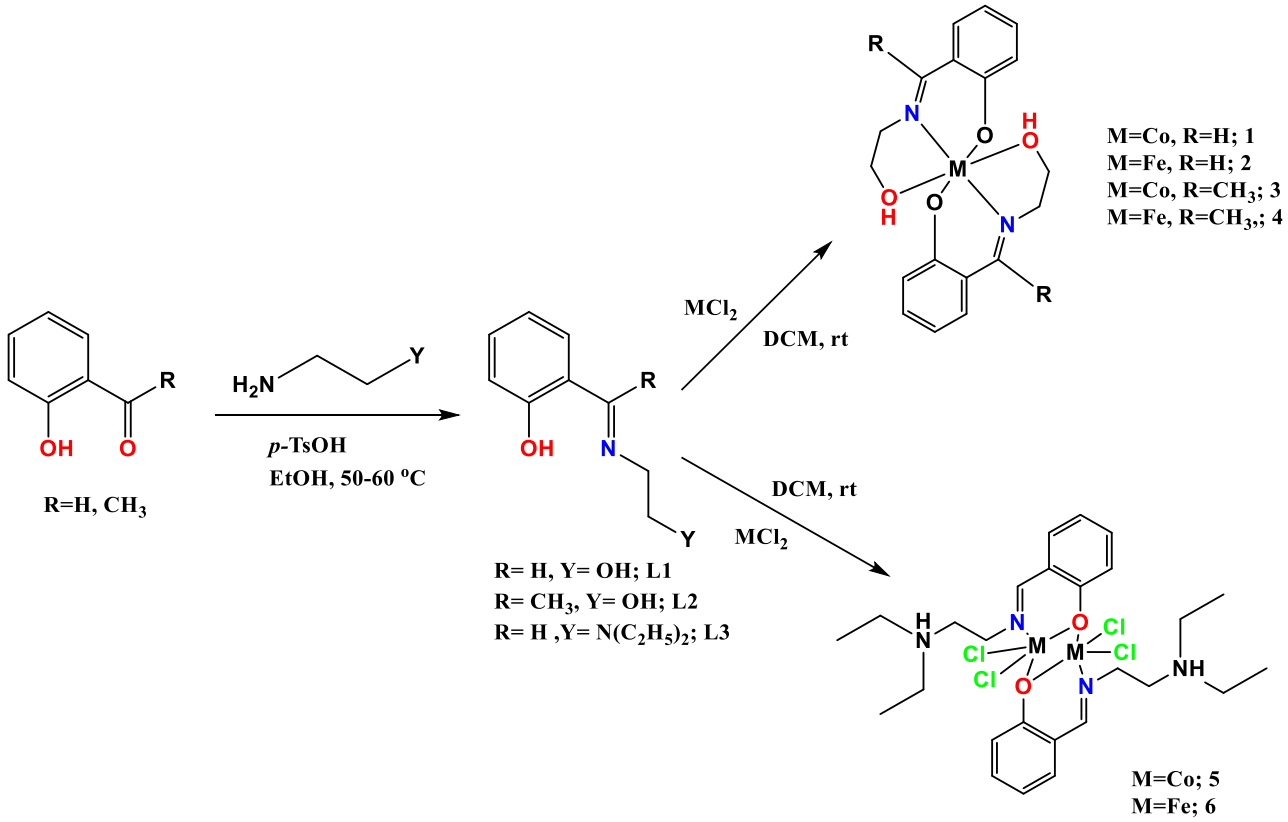

Scheme 3.1. Synthetic protocol of N^O donor (ethylimino)methyl)phenol ligands and their respective Fe(II) and Co(II) complexes.

The synthesis of the Fe(II) and Co(II) metal complexes was achieved by reacting ligands **L1**-**L3** with equimolar amounts of either $FeCl_2$ or $CoCl_2$ salts in dichloromethane (**Scheme 3.1**). The Co(II) complexes, **1**, **3** and **5** were isolated as brown, blue and green powders, respectively, whilst the Fe(II) complexes were obtained as brown solids, in low to high yields (10% – 89%). All the compounds were highly hygroscopic and had to be kept under moisture free conditions. The metal complexes were characterized with the aid of infrared spectroscopy, mass spectrometry, single crystal X-ray crystallography, magnetic moment measurements, epr and elemental analyses. The IR spectra showed shifts of the $\nu_{(C=N)}$ signals from ~1604 cm^{-1} in the free ligands to higher frequencies (1626-1640 cm^{-1}) in the respective Co(II) and Fe(II) complexes. Another useful information from the IR spectra was derived from the O-H vibration

frequencies. For instance, the broad bands around 3186-3435 cm^{-1} recorded in complexes **1-4** which were assigned to the pendant $\nu_{(O-H)}$ signal. These signals established the absence of deprotonation of the pendant group O-H groups, consistent with the proposed structures in **Scheme 3.1**.

Mass spectrometry was also useful in the structural elucidation of the complexes. For example, the mass spectrum of **5** in **Figure 3.4** showed a signal at m/z = 348.0462 amu, corresponding to the [Co(**L3**)Cl_2] fragment. Similar mass spectral data was observed for complex **6**. These mass spectral data indicate that the dinuclear complexes readily dissociate to form the respective mononuclear species.

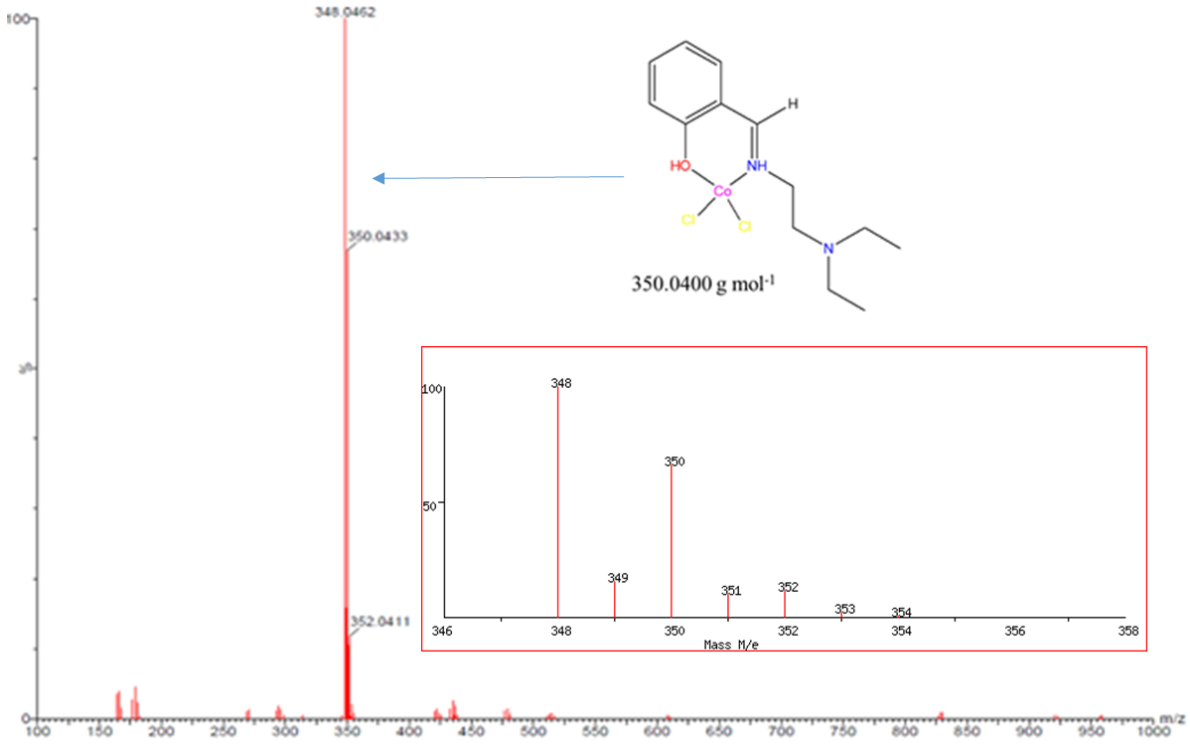

Figure 3.4: The mass spectrum of **5** revealing the presence of the monochelated, mononuclear Co(II) complex molecular ion peak at m/z of 348.0462 amu. Isotopic distribution of the complex is inserted.

On other hand, complex **1** recorded an m/z signal at 387.0446 amu corresponding to the $[Co(\mathbf{L2})_2]^+$ fragment (**Figure 3.5**), and supports the proposed structure in **Scheme 3.1**. In addition, complexes **2**, **3** and **4** exhibited similar fragmentation patterns as **1** which is also in consistent with the predicted structures in **Scheme 3.1**.

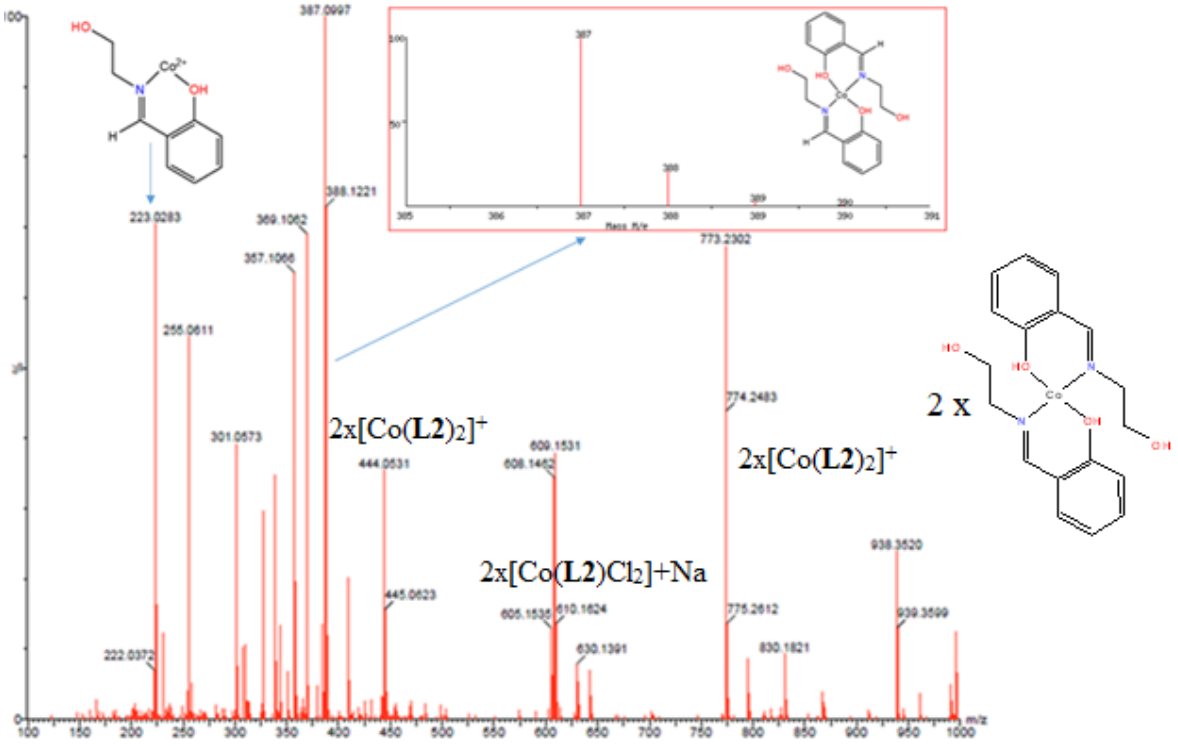

Figure 3.5: The mass spectrum of the Co(II) complex **1** showing the formation of a *bis*-chelated complex at m/z of 387.0997 amu. Isotopic distribution inserted.

The magnetic moments of the Co(II) complexes **1**, **3** and **5** were recorded as 4.49, 3.96, and 3.86 BM, respectively. While the magnetic moments of **3** and **5** were in good agreement with the spin only value of 3.88 BM, the magnetic moment recorded for **1** was found to be higher than the spin only value of 3.88 BM, but falls within the expected range of 4.30 - 5.20 BM for the high spin d^7 Co(II) complexes.[38] This variation could be attributed to the ligand field effect and spin-orbital contributions from the ligands.[39] Interestingly, the magnetic moments of the Fe(II) complexes **2**, **4** and **6** of 4.96 BM, 4.92 BM and 4.96 BM, respectively, were all in good

agreement with the spin only value of 4.90 BM for high spin d^6 Fe(II) complexes. Elemental analyses data of complexes **1**- **4** were consistent with two ligands units per metal atom, while the elemental analyses data recorded for complexes **5** and **6** tallied with one ligand unit per metal atom consistent with the empirical formula of the structures shown in **Scheme 3.1**.

*3.3.2. Molecular structures of complexes **2** and **5***

Single crystals suitable for X-ray analysis of complex **2** were obtained by slow diffusion of *n*-hexane solvent into a dichloromethane solution at room temperature while crystals of complex **5** were grown from acetonitrile solution by slow evaporation at room temperature. The molecular structure of complex **2** unambiguously established the coordination environment around the metal center as having two anionic **L1** units per Fe atom (**Scheme 3.1**). We assumed that complexes **1**, **3** and **4**, would adopt this coordination behavior, as they contain the same ligand (**L1**) or similar ligand (**L2**). **Table 3.1** is a summary of the crystallographic data and structure refinement parameters while **Figures 3.6** and **3.7** represent the molecular structures, packing diagrams, and selected bond lengths and angles for complexes **2** and **5**, respectively. In the solid state, complex **2** adopts a bis(chelated) mononuclear structure and the O^N^O tridentate coordination mode of the ligand is established. The formation of complex **2** is likely to occur through HCl salt elimination, during recrystallization, as has been reported for a number of Fe(II) and Ni(II) complexes.[29, 40-41]

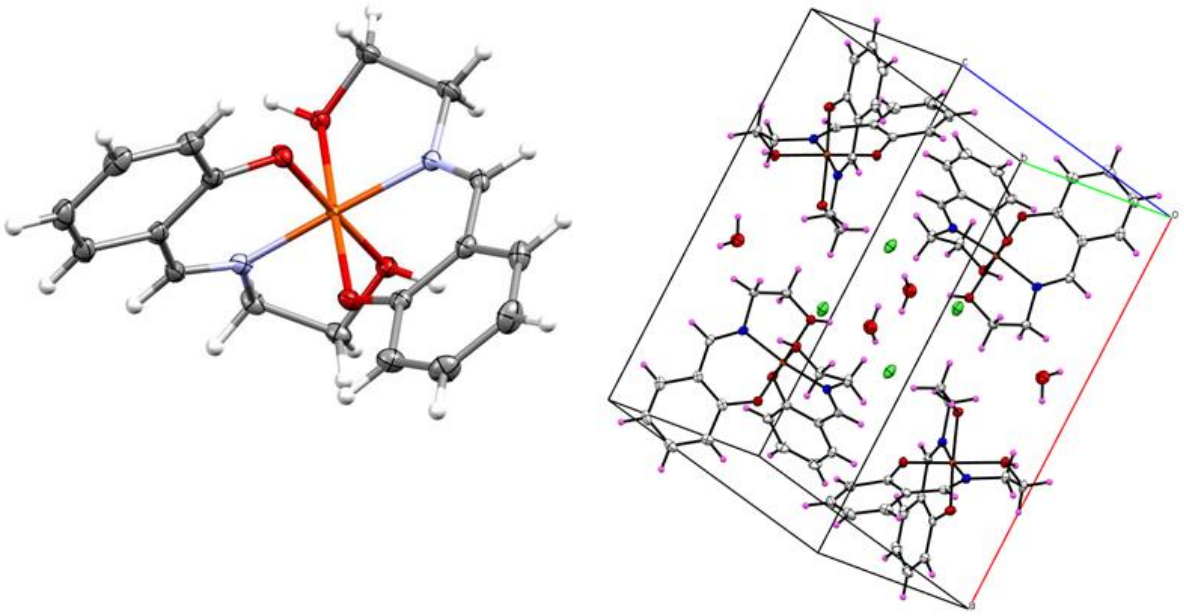

A **B**

Figure 3.6: Molecular structure of complex **2** shown with 50% probability ellipsoid (A). Packing diagram of the Fe(II) complex **2** (B). Selected bond lengths (Å) and angles (˚): Fe(1)-O(1), 1.8581(11); Fe(1)-O(2), 1.8564(11); Fe(1)-O(3), 1.9609(11); Fe(1)-O(4), 1.9556(11); Fe(1)-N(1), 1.8903(13); Fe(1)-N(2), 1.8956(13); O(1)-Fe(1)-O(4), 178.36(5); O(1)-Fe(1)-O(3), 91.92(5); O(2)-Fe(1)-O(1), 91.24(5); O(2)-Fe(1)-O(4), 90.13(5); O(4)-Fe(1)-O(3), 86.72(5); O(2)-Fe(1)-O(3), 176.78(5); N(1)-Fe(1)-N(2), 173.69(5).

The average bond lengths for Fe(1)-$O(3)_{alkoxy}$ and Fe(1)-$O(4)_{alkoxy}$ of 1.9609(11) Å and 1.9556(11) Å, respectively, are longer than the average bond lengths for Fe(1)-$O(1)_{phenolic}$ and Fe(1)-$O(2)_{phenolic}$ of 1.8381(11) Å and 1.8564(11) Å respectively. Similar results have been reported in literature for comparable complexes.[42,43-44] The mean bond distance for Fe-$O_{phenolic}$ and Fe-O_{alkoxy} of 1.857 Å and 1.958 Å of complex **2** were found to be shorter than the minimum values of 1.877±0.044 Å and 2.012±0.055 Å reported in 9 and 11 similar structures respectively.[44] Similarly, the average bond distance for Fe-N_{imine} of 1.893 Å is shorter than the

minimum value of 2.060±0.028 Å reported for 15 similar structures.[44] Expectedly, the bond distances for Fe(1)-N_{imine}(1) of 1.8903(13) and Fe(1)-N_{imine}(2) of 1.8956(13) are statistically similar, consistent with the symmetrical nature of the complex. The bond angles for $O(1)_{phenolic}$-Fe(1)-$O(3)_{alkoxy}$, O_{alkoxy}(4)-Fe(1)-O_{alkoxy}(3) of 91.92(5)° and 86.72(5)° of **2** deviate from the expected 90˚ for a perfect octahedral geometry.[43] Similarly, the axial bond angle for N_{imine}(1)-Fe(1)-N_{imine}(2) of 173.69(5)° deviate from linearity by 7° consistent with a distorted octahedral geometry.

The X-ray structure of the cobalt complex **5** shows a dinuclear structure in which each cobalt atom is coordinated to two bridging phenolate oxygen atoms, one imine nitrogen and two terminal chloride ligands complete the coordination spheres to give five-coordinated metal centres. The presence of the two chloride ligands is consistent with the zwitterionic **L3** ligand resulting in a neutral complex. The formation of a zwitterion in **L3** is aided by the presence of negative and positive charges on the Ph-O^- and CH_2-CH_2-$N^+H(Et)_2$ groups, respectively.[45-46] The structure of complexes **6** is also believed to adopt this coordination environment as it contains the same ligand (**L3**).

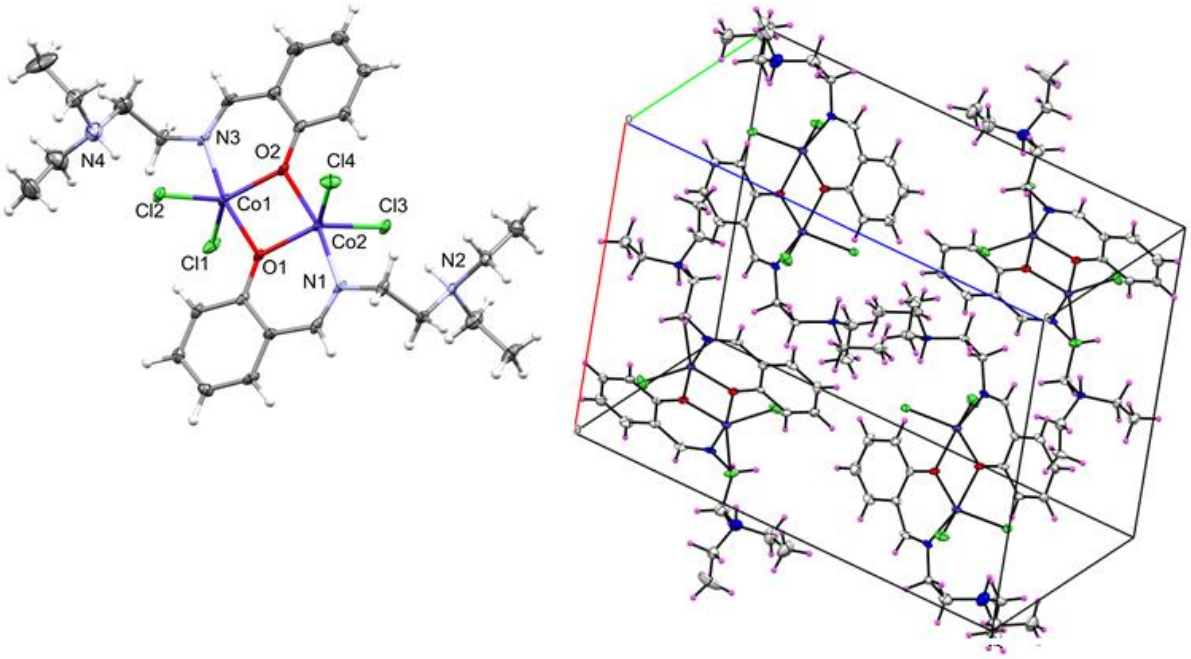

A **B**

Figure 3.7: ORTEP plot of Co(II) complex **5** (A). Ellipsoids are drawn at 50 % probability. Packing diagram of the Co(II) complex (B). Selected bond lengths (Å) and angles (˚): Co(1)-Cl(1), 2.327(2); Co(1)-Cl(2), 2.3409(18); Co(1)-N(3), 2.105(5); Co(1)-O(1), 2.188(4); Co(1)-O(2), 1.979(5); N(3)-Co(1)-O(2), 91.30(2); O(1)-Co(1)-Cl(1), 95.01(14); O(2)-Co(1)-O(1), 76.89(18); N(3)-Co(1)-Cl(2), 92.88(16); Cl(1)-Co(1)-Cl(2), 114.73(7); Co(1)-O(2)-Co(2), 102.90(19); Co(1)-O(1)-Co(2), 102.75(19).

Table 3.1: Crystallographic data and structure refinement for the **2** and **5** complexes.

Parameter	**2**	**5**
Empirical Formula	$C_{18}H_{22}ClFeN_2O_5$	$C_{26}H_{40}Cl_4Co_2N_4O_2$
$Density_{calc.}$/ g cm^{-3}	1.519	1.550
μ/mm^{-1}	0.960	1.493
Formula Weight	437.67 g/mol	700.28 g/mol
Appearance	clear orange	Green
Shape	Block	Irregular
Size/mm^3	0.41×0.20×0.12	0.33x0.18x0.11
T/K	100(2)	100(2)
Crystal System	Monoclinic	Monoclinic
Space Group	$P2_1/c$	$P2_1/c$
a/Å	16.3156(6)	15.1648(14)
b/Å	10.0596(4)	9.5521(9)
c/Å	11.6899(5)	20.7530(2)
α/°	90	90
β/°	94.158(2)	93.2600(5)
γ/°	90	90
V/Å^3	1913.59(13)	3001.3(5)
Z	4	4
Z'	1	1
Wavelength/Å	0.71073	0.71073
Radiation type	MoK_α	MoK_α
Θ_{min}/°	2.380	1.345
Θ_{max}/°	27.449	26.499
Measured Refl.	16486	41169
Independent Refl.	4331	6032
Reflections Used	3950	4516
R_{int}	0.0234	0.0680
Parameters	258	323
Restraints	13	0
Largest Peak	0.321	5.530
Deepest Hole	-0.401	-1.069
GooF	1.030	1.047
wR_2 (all data)	0.0644	0.2701
wR_2	0.0630	0.2422
R_1 (all data)	0.0292	0.1214
R_1	0.0261	0.0961

The average Co-Cl bond lengths of complex **5** of 2.3368 Å is higher than the mean Co-Cl bond length of 2.290±0.022 Å reported in 11 structures with similar coordination patterns,[47] but is comparable with the maximum bond distance of 2.337±0.022 Å reported for a related complex.[47] Interestingly, an intra-comparison of the Co-$O_{phenolic}$ bond lengths revealed that

Co(1)-O(1) and Co(2)-O(2) average bond length of 2.181 Å is greater than the mean bond length for Co(1)-O(2) and Co(2)-O(1) of 1.974 Å. Furthermore, the two Co-N_{imine} bond lengths were statistically similar (Mean = 2.104 Å), but higher than the mean value of 2.043±0.029 Å reported in 8 similar structures.[47] The bond angles for O(2)-Co(1)-O(1) and O(2)-Co(1)-N(3) of 76.89(18)˚ and 91.30(2)˚, respectively, deviate slightly from the expected 90˚ angle for trigonal bipyramidal geometry. Similarly, the bond angles for O(2)-Co(1)-Cl(1), O(2)-Co(1)-Cl(2) and Cl(1)-Co(1)-Cl(2) of 128.12(16)˚, 116.93(16)˚ and 114.73(7)˚, respectively, differ slightly from the expected 120˚ and thus displayed a slightly distorted trigonal bipyramidal coordination geometry.[48]

*3.3.3. Electron Spin Resonance (ESR) spectra of complexes **2** and **5**.*

The solid and solution (acetonitrile) phase ESR spectra of complexes **2** and **5** were recorded at 298 K and 77 K, respectively. The results can be summarized as follows; **2** in solid: g=2.0673, $g_{\perp}$=2.2825, $g_{\parallel}$=2.0686; in solution: g=2.0630, $g_{\perp}$=2.2571, $g_{\parallel}$=1.9958. **5** in solution: g=2.0261, $g_{\perp}$=2.0841, $g_{\parallel}$=1.9789; in solid: g=2.0680, $g_{\perp}$=2.2654, $g_{\parallel}$=2.0139. Both the solid and solution state EPR spectra of the complexes in **Figure 3.8** showed an axial g-tensor with a dx^2-y^2 ground state doublet. The EPR spectrum of the bis(chelated) dinuclear **2** complex showed a g-value of **2** (2.065), which is close to the 'free' electron g-value (g_e) of 2.002,[49] consistent with some degree of covalency from the metal to ligand interactions.[50] The ESR spectrum of complex **5** revealed a diagnostic sharp one-line spectrum in acetonitrile solution whilst a background noise was observed in the solid state spectrum. The ESR spectrum of complex **5** shows an axial symmetry about the Co(II) atom.[51] The EPR spectrum is typical of low spin d^7 (S=1/2) and five-coordinate Co(II) environment, with the unpaired electron residing on the dx^2 orbital. The

solution state spectra of the complexes show highly resolved signals when compared to the solid state spectra, possibly due to the M-M interactions in the solid state.[52]

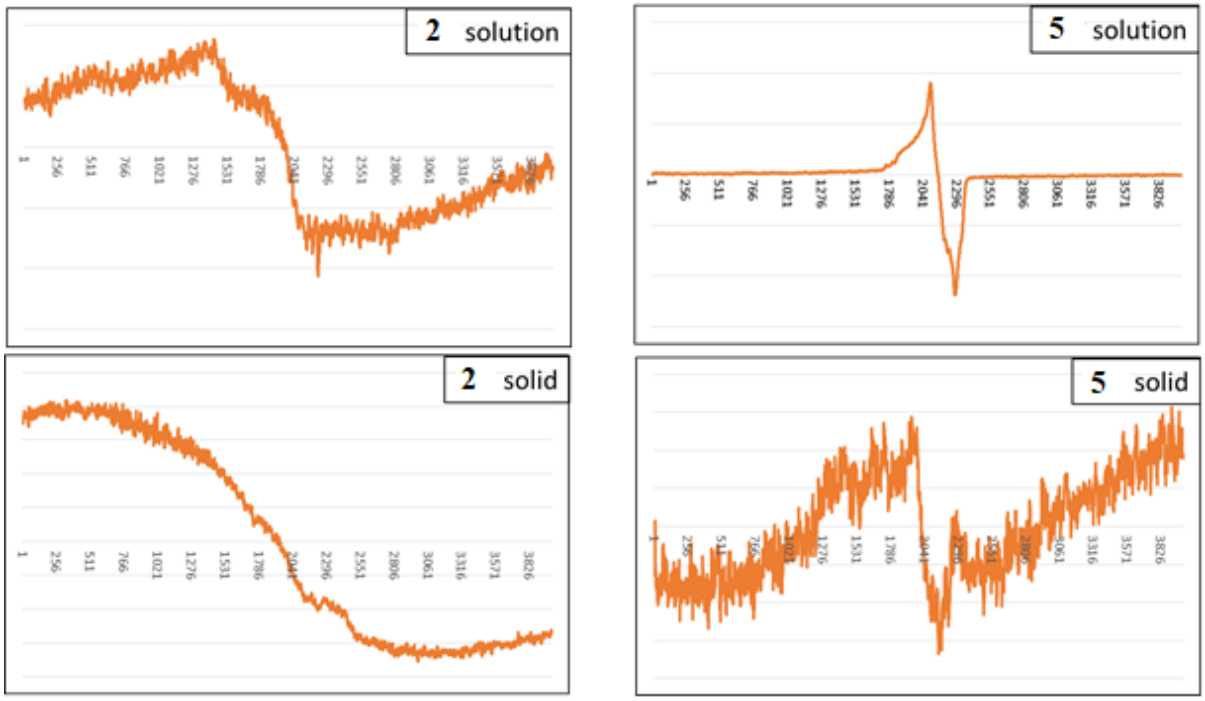

Figure 3.8: The x-band EPR spectra of complexes **2** and **5** in solid and acetonitrile solution at 298 K and 77 K, respectively.

3.3.4. Ethylene oligomerization reactions catalyzed by Fe(II) and Co(II) complexes

Preliminary investigations of the Fe(II) and Co(II) complexes as ethylene oligomerization catalysts were probed using ethylaluminium dichloride ($EtAlCl_2$) and methylaluminoxane (MAO) as co-catalysts in chlorobenzene and toluene solvents, respectively (**Table 3.2.**). Moderate to high catalytic activities, ranging from 5 160 $kg_{oligomers}$ mol^{-1}(M) h^{-1} to 17 600 $kg_{oligomers}$ mol^{-1}(M) h^{-1}, were obtained which depended on the complex and co-catalyst employed. GC and GC-MS analyses were used to establish the identity and distributions of the products. In all cases, butenes and hexenes were the major products (**Figures 3.9 - 3.10** and **Figure 3.11** respectively).

Table 3.2: Summary of ethylene oligomerization data catalyzed by Co(II) and Fe(II) complexes.

Entry	Catalyst	Co-catalyst	Yield[b] (kg)	Activity ($kg_{oligomers}$ $mol^{-1}(M)\ h^{-1})$[c]	Product Distribution (%)[d]	
					C_4 (α-C_4)	C_6 (α-C_6)
1	**1**	$EtAlCl_2$	0.0867	8670	38 (84)	62 (24)
		MAO	0.132	13200	95 (90)	5 (51)
2	**2**	$EtAlCl_2$	0.0643	6430	23 (92)	77 (23)
		MAO	0.118	11800	96 (98)	4 (47)
3	**3**	$EtAlCl_2$	0.0673	6730	44 (92)	56 (28)
		MAO	0.116	11600	94 (95)	6 (37)
4	**4**	$EtAlCl_2$	0.0516	5160	22 (89)	78 (26)
		MAO	0.0645	6450	94 (93)	6 (37)
5	**5**	$EtAlCl_2$	0.0912	9120	40 (90)	60 (24)
		MAO	0.176	17600	82 (84)	18 (41)
6	**6**	$EtAlCl_2$	0.0722	7220	29 (79)	71 (24)
		MAO	0.138	13800	90 (91)	10 (29)

[a]Reaction conditions: complex, 10 µmol; solvent, chlorobenzene/toluene, 30 mL; temperature, 30 ^oC; time, 1 h; pressure, 10 bar; $EtAlCl_2$: Al/M=200; MAO: Al/M=1000. [b]Determined using GC and *n*-heptane served as an internal standard. [c]TON, kg oligomers produced per mol catalyst per hour. [d]Determined by GC and GC-MS.

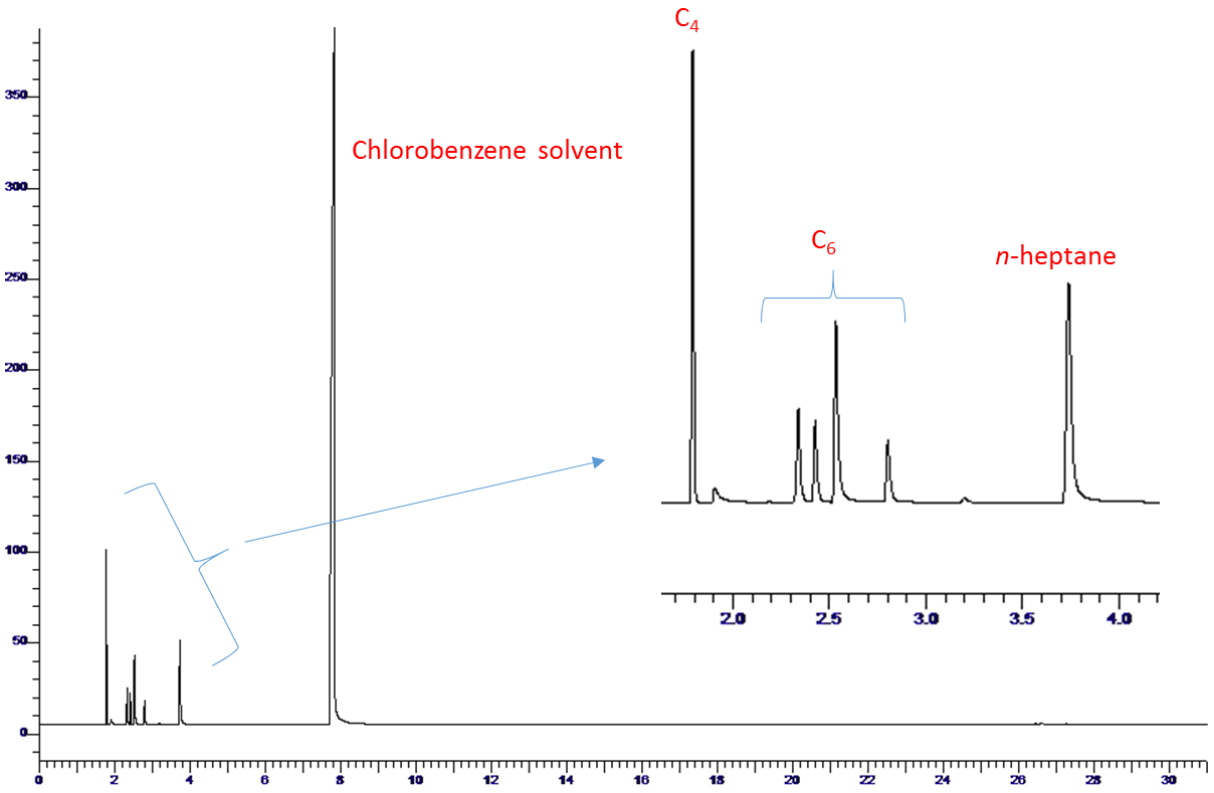

Figure 3.9: The GC-FID trace showing the oligomeric products obtained when the reaction was catalyzed by the **3**.

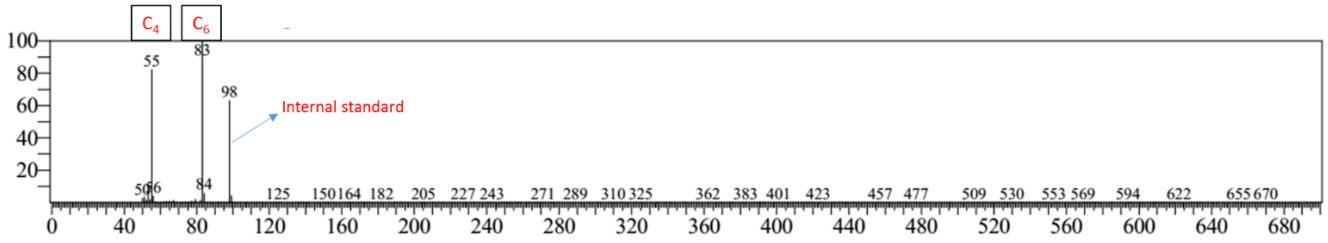

Figure 3.10: The GC-MS plot showing the products obtained when **2** was activated with $EtAlCl_2$ and used in catalysing ethylene oligomerization reaction.

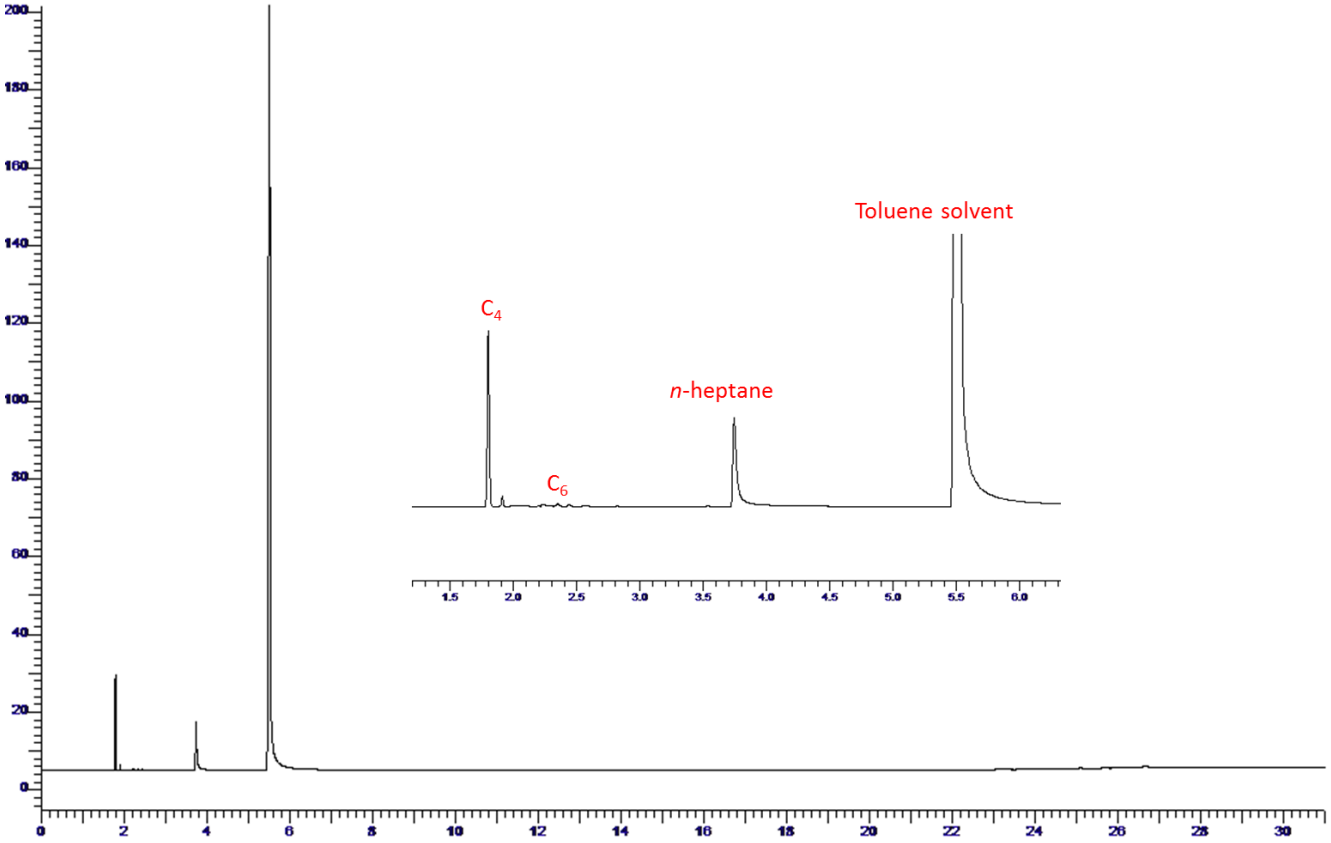

Figure 3.11: The GC-FID trace showing the products obtained when the reaction was catalyzed by the **6** after being activated with MAO.

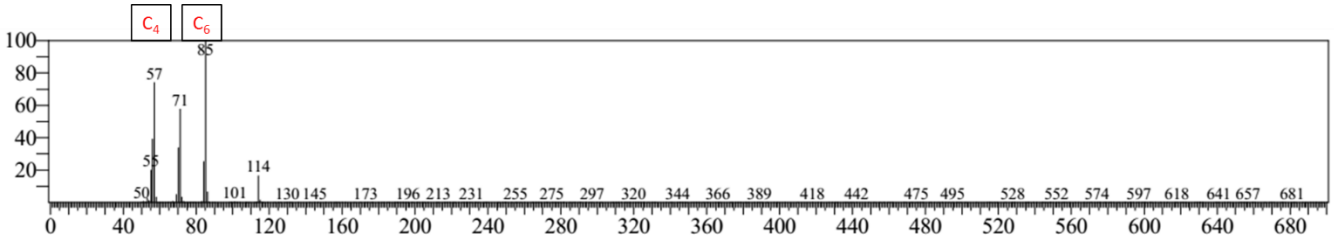

Figure 3.12: GC-MS plot obtained for **6** ethylene oligomerization reaction using MAO activator.

3.3.4.1 Effect of type of co-catalyst on catalytic activity and product distribution

In order to investigate the influence of the co-activator, pre-catalysts **1**-**5** and **2**-**6** were activated with $EtAlCl_2$ and MAO co-catalysts in chlorobenzene and toluene solvents, respectively (**Table 3.2** and **Figure 3.13**). In general, activation by MAO resulted in more active catalytic systems in comparison to the $EtAlCl_2$ co-catalyst (**Table 3.2**). For example, the catalytic activity of **2** increased from 6 430 $kg_{oligomers}$ mol^{-1}(M) h^{-1} to 11 800 $kg_{oligomers}$ mol^{-1}(M) h^{-1} on activation with $EtAlCl_2$ and MAO, respectively (**Table 3.2**, entry 2). This observation is consistent with a previous study in which activation of 2-(benzimidazol-2-yl)-1,10-phenanthrolyl Fe(II) complexes with Et_2AlCl and MAO afforded catalytic activities of 7.27 x 10^5 g.mol^{-1} Fe.h^{-1} and 11.4 x 10^5 g.mol^{-1} Fe. h^{-1}, respectively.[53] In terms of selectivity, the usage of MAO co-catalyst favored the formation of mainly C_4 oligomers, while $EtAlCl_2$ switched the oligomer distribution towards C_6 fractions (**Figure 3.13**). As an illustration, using complex **4**, 94% and 22% of C_4 were afforded using MAO and $EtAlCl_2$ co-catalysts, respectively (**Table 3.2**, entry 4).

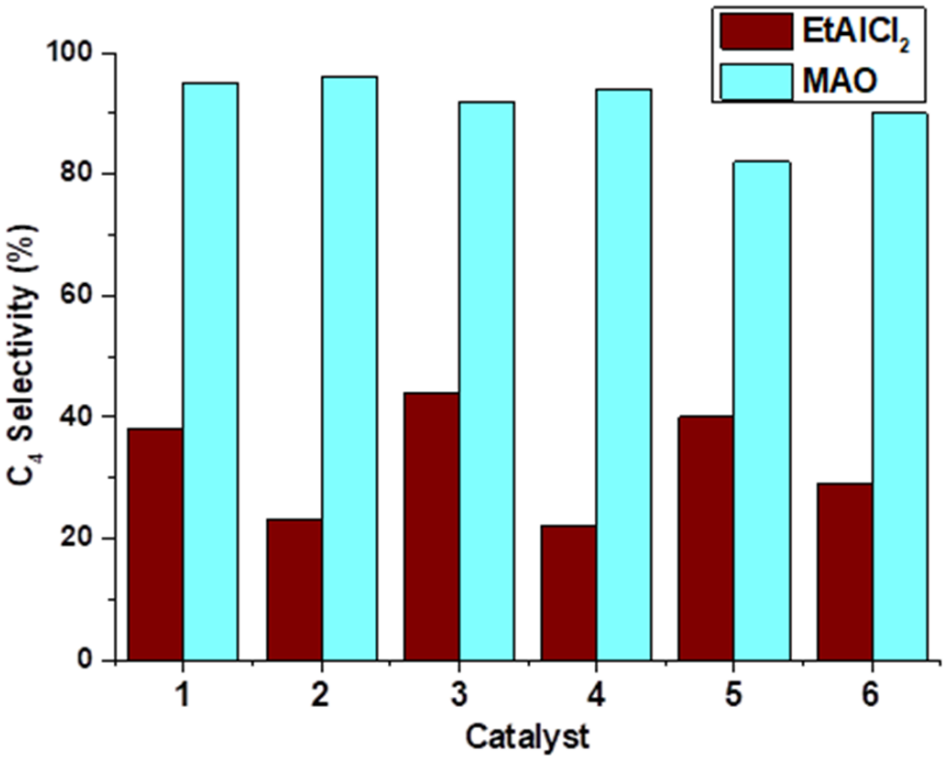

Figure 3.13: Influence of MAO and $EtAlCl_2$ co-catalysts on the selectivity of the Fe(II) and Co(II) complexes during ethylene oligomerization reactions.

3.3.4.2. Influence of the complex structure on ethylene oligomerization reactions

Having examined the influence of the co-catalysts on the catalytic abilities of the late transition metal complexes, we turned our attention to the role of complex structure in these ethylene oligomerization reactions. In general, the Co(II) complexes were superior to their Fe(II) counterparts in terms of catalytic activities. For instance, using $EtAlCl_2$, complexes **3** and **4** displayed catalytic activities of 6 730 $kg_{oligomers}$ mol^{-1}(M) h^{-1} and 5 160 $kg_{oligomers}$ mol^{-1}(M) h^{-1}, respectively (**Table 3.2**, entries 3 and 4). Similar results were reported using MAO as the co-catalysts and for the other complexes (**Table 3.2**). We also observed that the nature of ligands (**L1**-**L3**) coordinated to the metal atoms controlled the catalytic activities of the synthesized complexes, which may be linked to the overall coordination environment. For example, complexes **1** and **2**, supported on the unsubstituted ligand **L1**, exhibited higher catalytic

activities than complexes **3** and **4** bearing the anionic methyl substituted ligand **L2** (**Table 3.2.**, entries 1-4). The better performance of **1** and **2** may be ascribed to the complexes being more electropositive in comparison to their counterparts, complexes **3** and **4** respectively, chelated by the methyl substituted ligand **L2**.[54-55]

The pendant group could have also regulated the catalytic performance of the complexes. For instance, with $EtAlCl_2$ co-catalyst, lower catalytic activities of 8 670 $kg_{oligomers}$ mol^{-1}(M) h^{-1} and 6 430 $kg_{oligomers}$ mol^{-1}(M) h^{-1} were recorded for complexes **1** and **2**, respectively, bearing the hydroxyl pendant group (**L1**) in comparison to complexes **5** and **6** (9 120 $kg_{oligomers}$ mol^{-1}(M) h^{-1} and 7 220 $kg_{oligomers}$ mol^{-1}(M) h^{-1}), supported on **L3** with a diethylamine pendant group. This is likely to be due to stronger coordination of the O to Co(II)/Fe(II) metal centre, thus hindering ethylene coordination, while for **L3** in complexes **5** and **6**, the $N(C_2H_5)_2$ groups are non-coordinating. It is expected that in a hemilabile ligand design the labile donor atom be weakly coordinating to allow substrate coordination. Shi *et al*.[56], made a similar observation in ethylene oligomerization studies using palladium complexes of hemilabile PˆNˆO ligands. In this design, complexes bearing O-H groups were inactive due to the non-lability of the phenolate group.

The selectivity towards C_4 and C_6 oligomers was also affected by the central metal atom and ligand structure. For example, with $EtAlCl_2$ co-catalyst, the Co(II) complex **3** gave 44% of C_4 oligomers whilst 22% selectivity towards C_4 oligomers was obtained for its analogous Fe(II) complex **4** (**Table 3.2**, entries 3 and 4), consistent with rapid chain transfer for the highly active Co(II) complex.[57] Similarly, complexes **3** and **1**, bearing methyl substituted **L2** and unsubstituted **L1** ligands displayed 44% and 38% of C_4 oligomers, respectively. With respect

to isomerization reactions, higher amounts α-C_4 fractions (84-98 %) were obtained for all the complexes, compared to lower fractions for α-C_6 of 24–51 %. This is not unique, since greater number of C_6 isomers are possible compared to the C_4 oligomers.

3.3.4.3. Effect of reaction parameters on ethylene oligomerization reactions

The effect of catalytic reaction parameters such co-catalyst to complex ratio, reaction period and substrate pressure on the catalytic performance of Co(II) and Fe(II) complexes was probed using **5**/$EtAlCl_2$ system in chlorobenzene solvent and verified using the iron **2** complex (**Table 3.3**). We observed that increasing the Al/Co ratio from 150 to 200 resulted in an increase in catalytic activities of complex **5** from 6 750 $kg_{oligomers}$ mol^{-1}(M) h^{-1} to 9 120 $kg_{oligomers}$ mol^{-1}(M) h^{-1}, respectively (**Table 3.3**, entries 1 and 2). However, further increase of Al/Co ratio to 300 was marked by decreased catalytic activity to 6 380 $kg_{oligomers}$ mol^{-1}(M) h^{-1} (**Table 3.3**, entries 3 and 4) giving an optimum Al/Co ratio of 200. In a parallel investigation using **5**/MAO, an optimum Al/Co ratio of 1000 was achieved corresponding to TOF of 17 600 $kg_{oligomers}$ mol^{-1}(M) h^{-1} (**Table 3.3**, entry 7). The variation of Al/M ratio also affected the selectivity and oligomer distribution. For example, increasing Al/Co ratio from 150 to 200 resulted in a significant increase in the composition of C_4 oligomers from 25% to 40% (**Table 3.3**, entries 1 and 2). This may be attributed to increased number of active sites, favoring chain transfer to the Al co-catalyst to form shorter chain oligomers.[58]

Table 3.3: Variation of aluminum to catalyst ratio using **5**/$EtAlCl_2$ and **5**/MAO catalytic systems[a].

Entry	Catalyst	Co-catalyst	Al/Ni	Yield[b] (kg)	Activity ($kg_{oligomers}$ mol^{-1}(M) h^{-1})[c]	Oligomer Distribution (%)[d]	
						C_4 (α-C_4)	C_6 (α-C_6)
1	**5**	$EtAlCl_2$	150	0.0675	6750	25 (79)	75 (24)
2	**5**	$EtAlCl_2$	200	0.0912	9120	40 (90)	60 (24)
3	**5**	$EtAlCl_2$	250	0.0784	7840	52 (94)	48 (23)
4	**5**	$EtAlCl_2$	300	0.0638	6380	58 (94)	42 (26)
5	**5**	MAO	200	0.0150	150	89 (92)	11 (35)
6	**5**	MAO	500	0.0275	2750	94 (98)	6 (39)
7	**5**	MAO	1000	0.176	17600	82 (84)	18 (41)
8	**5**	MAO	1500	0.145	14500	99 (96)	1 (45)
9	**1**	MAO	1000	0.132	13200	95 (90)	5 (51)
10	**2**	MAO	1000	0.118	11800	96 (98)	4 (47)

[a]Reaction conditions: Complex, 10 µmol; solvent, chlorobenzene or toluene, 30 mL; Time, 1 h; Pressure, 10 bar; Reaction temperature, 30°C. [b]Determined GC and *n*-heptane as an internal standard; [c]TON, kg oligomers produced per mol catalyst per hour. [d]Determined by GC.

The stability of the catalysts was also examined using complex **5** by variation of the reaction periods from 0.5 h to 2 h (**Table 3.4**, entries 1-5). Increasing reaction period from 0.5 h to 1 h was followed by an increase in TON from 6 460 to 9 120 $kg_{oligomers}$ mol^{-1}(M) h^{-1}, respectively (**Table 3.4**, entries 1-3). However, a further increase in reaction time to 2 h had a negative effect on the catalytic activity of **5**, giving a TOF of 3 475 $kg_{oligomers}$ mol^{-1}(M) h^{-1} (**Table 3.4**, entry 5). The increase in the catalytic activities of **5** between 0.5 h and 1 h is in accordance with the initiation period, whilst the decline in the catalytic activities of **3** between 1 h to 2 h may be attributed to catalyst degradation **(Figure 3.14)**.[59] In general, prolonged reaction times favored the formation of more C_6 oligomers than the C_4 fractions (**Table 3.4**, entries 3 and 4, respectively). This trend could be explained by re-combination of the preformed C_4 oligomers and ethylene monomer to give the C_6 fraction.[60]

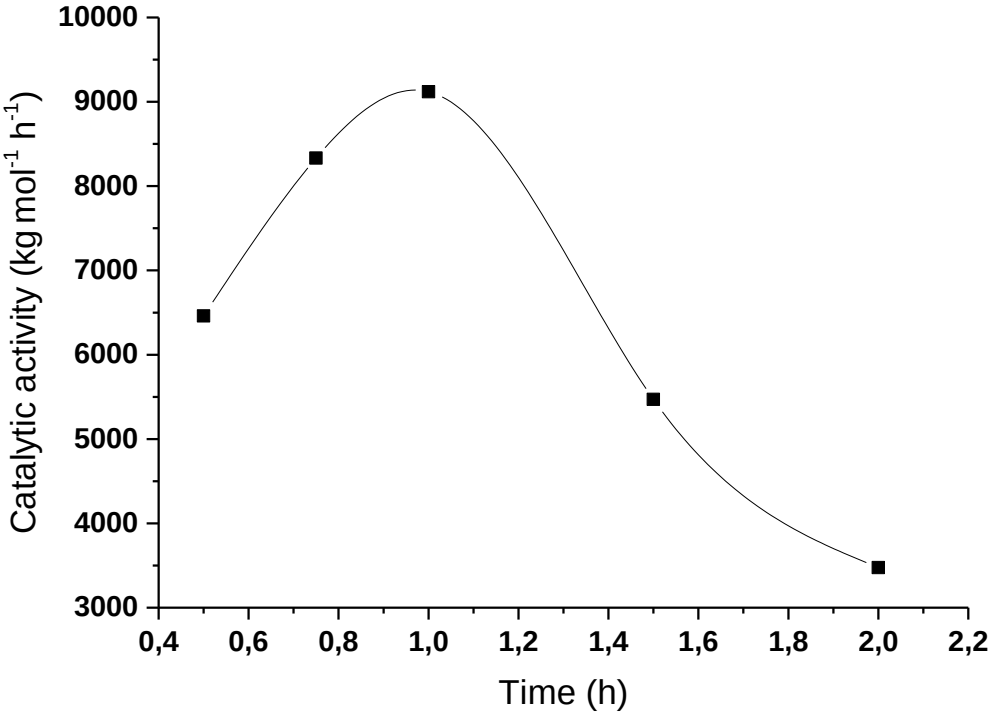

Figure 3.14: The effect of time in the catalytic behavior of **3**, showing a decline in the catalytic activity of **3** after 1 h.

Table 3.4: The influence of time and ethylene pressure on the catalytic activity and selectivity of the **5** and **2** complexes[a]

Entry	Period (h)	Ethylene pressure (bar)	Yield[b] (kg)	Activity ($kg_{oligomers}$ $mol^{-1}(M)$ h^{-1})[c]	Oligomer Distribution (%)[d]	
					C_4 (α-C_4)	C_6 (α-C_6)
1	0.5	10	0.0323	6460	72 (98)	28 (23)
2	0.75	10	0.0625	8333	67 (96)	33 (23)
3	1	10	0.0912	9120	40 (90)	60 (24)
4	1.5	10	0.0820	5470	23 (92)	77 (35)
5	2	10	0.0695	3475	20 (89)	80 (26)
6	1	20	0.100	10000	58 (98)	42 (23)
7	1	30	0.120	12000	72 (98)	28 (23)
8	1	40	0.105	10500	46 (60)	54 (26)
9	1	50	0.0580	5800	22 (89)	78 (22)
10[e]	1	30	0.0832	8320	29 (90)	71 (21)
11[f]	1	10	0.176	17600	82 (84)	18 (41)
12[f]	1	30	0.264	26400	94 (97)	6 (30)

[a]Reaction conditions: Complex **5**, 10 µmol; solvent, chlorobenzene or toluene, 30 mL; Co-catalyst, $EtAlCl_2$: Al/M=200; MAO: Al/M=1000; Temperature, 30°C. [b]Determined by GC and *n*-heptane as the internal standard. [c]TON, kg oligomers produced per mol catalyst per hour. [d]Determined by GC. [e]**2**/$EtAlCl_2$ system. [f]**5**/MAO.

To study the influence of ethylene concentration on the ethylene oligomerization reactions, ethylene pressure was varied from 10 bar to 50 bar using complex **5** (**Table 3.4**, entries 3, 6-9). Unsurprisingly, enhanced catalytic activities from 9 120 $kg_{oligomers}$ mol^{-1}(M) h^{-1} to 12 000 $kg_{oligomers}$ mol^{-1}(M) h^{-1} were obtained as the ethylene substrate pressure was adjusted from 10 bar to 30 bar, respectively (**Table 3.4**, entries 3 and 6-7). A similar trend was recorded for the **5**/MAO system with catalytic activities of 17 600 $kg_{oligomers}$ mol^{-1}(M) h^{-1} to 26 400 $kg_{oligomers}$ mol^{-1}(M) h^{-1} at 10 bar and 30 bar, respectively (**Table 3.4**, entries 11 and 12). It is important to note that a drastic decline in the catalytic activities from 10 500 $kg_{oligomers}$ mol^{-1}(M) h^{-1} to 5 800 $kg_{oligomers}$ mol^{-1}(M) h^{-1} of **3**/$EtAlCl_2$ was observed with a further increase in ethylene pressure from 40 bar and 50 bar, respectively (**Figure 3.15**). This negative change in catalytic activity at higher ethylene pressures has been associated with mass transport and diffusion limitations at higher ethylene concentrations.[61-63,64] The product distribution was affected by a change in ethylene pressure. For example, increasing ethylene pressure from 10 bar and 30 bar resulted in a concomitant increase in the C_4 fraction from 40% to 72%, respectively (**Table 3.4**, entries 3, 6-7). This could be ascribed to rapid chain transfer with increase in catalytic activities. The lower composition of C_4 oligomers of 22% recorded at 50 bar, further supported this argument (**Table 3.4**, entry 9) as decreased catalytic activities was observed.

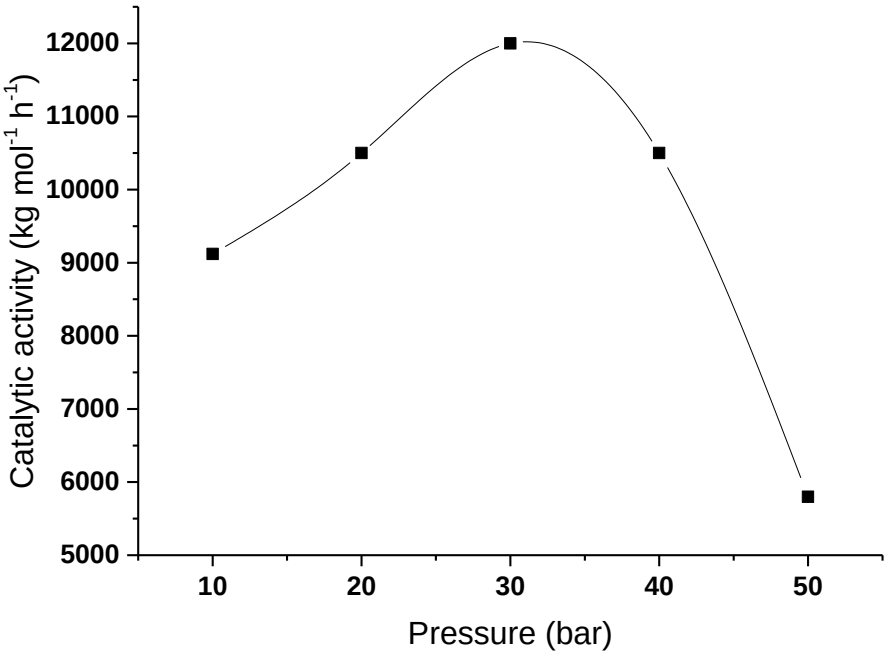

Figure 3.15: The plot of activity in $kg_{oligomers}$ mol^{-1}(M) h^{-1} units against pressure, showing an increase in the catalytic activity of **5**/$EtAlCl_2$ system with increasing pressure and a sharp decline in activity at 50 bar.

3.3.5. Density functional theoretical calculations of reactivity parameters

In order to gain an in-depth understanding of the catalytic behaviour and structural differences of the Fe(II) and Co(II) complexes density functional theory (DFT) calculations were performed on the ground-state electronic structures of the Fe(II) complexes **2**-**6** and to analyse the effect of the metal centre; **5** was included for comparison with **6** (**Table 3.5**). The computations were performed using a split basis set LANL2DZ for Fe(II) and Co(II), and 6311G(dp) for the remaining atoms. The HOMO–LUMO energy gaps [65] were investigated to study their influence on the catalytic activities of the respective complexes (**Table 3.5**). The energy gap (Δε), which was taken as the energy difference between pre-catalyst's LUMO

(E_{LUMO}) and ethylene's HOMO (E_{HOMO}), are given in **Table 3.5**. The HOMO and LUMO energy values for ethylene monomer are –7.7161 and –0.2661 eV, respectively.

Table 3.5: Theoretical and experimental data for complexes **2-6** and **5**

Quantity	2	4	6	5
NBO charge	0.498	0.522	0.562	0.723
$\boldsymbol{E_{HOMO}}$**/eV**	-4.3775	-4.1652	-4.7987	-5.7775
$\boldsymbol{E_{LUMO}}$**/eV**	-1.3540	-1.3127	-1.5423	-1.9157
[a]**Energy gap** $\boldsymbol{\Delta E}$**/eV=**$\boldsymbol{E_{LUMO}-E_{HOMO}}$	6.362	6.4033	6.1737	5.8003
Electrophilicity index/ω	0.3779	0.3565	0.4071	0.4827
[b]**Activity/kg$_{oligomers}$ mol^{-1}(M) h^{-1}**	6430	5160	7220	9120

[a]E_{LOMO} and E_{HOMO} are the LUMO and HOMO orbital energy values of the metal complexes and ethylene molecule, respectively. [b]Reaction conditions: [Complex], 10 μmol; solvent, chlorobenzene (30 mL), temperature, 30 ˚C; time, 1 h; pressure, 10 bar; $EtAlCl_2$, Al/M = 200.

The energy differences between the pre-catalysts' LUMO and ethylene's HOMO were lower than the energy differences between pre-catalysts' HOMO and ethylene's LUMO, which is consistent with ethylene oligomerization reaction being a nucleophilic attack of the metal centre by the ethylene monomer.[65] It is expected that a smaller HOMO-LUMO gap is expected to promote coordination of ethylene substrate to the metal centre.[66] From **Table 3.5** and **Figure 3.16**, it is evident that the HOMO-LUMO gap could have influenced the catalytic activities of the complexes, given that the catalytic activities increased with decrease in energy gaps (Δε).

Indeed complex **5**, with the lowest HOMO-LUMO energy gap, recorded the highest catalytic activity of 9120 kg mol^{-1} h^{-1}, consistent with recent reports.[67]

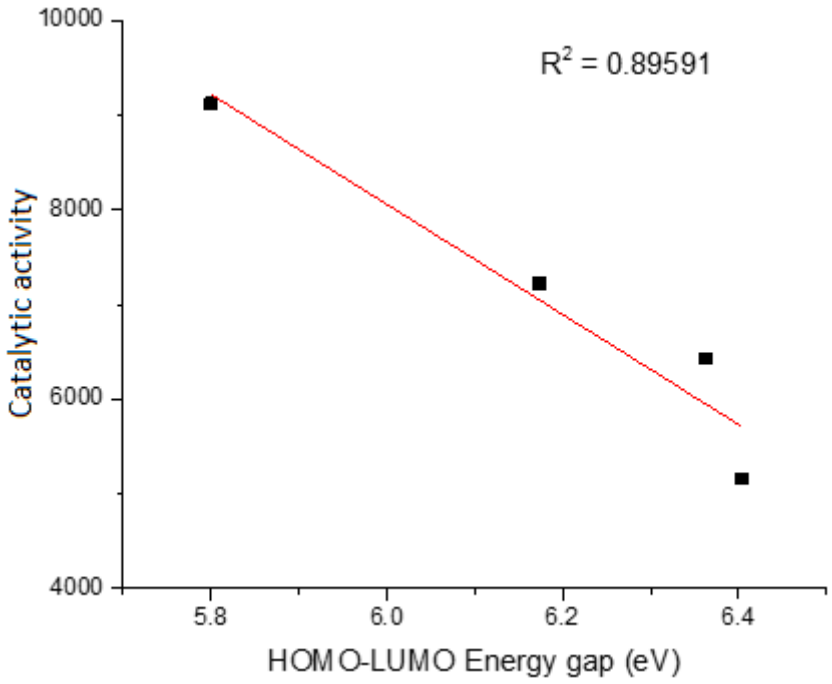

Figure 3.16: Plot of catalytic activity ($kg_{oligomers}$ mol^{-1}(M) h^{-1}**)** against HOMO-LUMO energy gap illustrating the influence of HOMO-LUMO energy gap on catalytic activity.

The NBO charge, which denotes the individual atomic charge, of **5** was higher than that of **6**, consistent with the observed catalytic activities. However, the NBO charges of the Fe(II) complexes **2-6** contradicts the expected behaviour.[37] Thus, it is conceivable to conclude that the catalytic activities were not significantly influenced by the charge on the metal atom. Meanwhile a linear relationship was obtained between the catalytic activities and the electrophilicity indices, which designates the resulting charge of the entire complex (**Figure 3.17**). For example, complex **5** (0.4827), which was the most electrophilic, also displayed the highest catalytic activity. From a ligand design perspective, it is evident that the introduction of the electron-donating methyl group in **4** (ligand **L2**) could have contributed to the increased

overall negative charge on the ligand moiety through electron delocalisation, and consequently led to a lower overall charge of the complex. Considering that electrophilicity index is superior to NBO charge in predicting the reactivity of metal complexes,[68] it is therefore reasonable to understand the why complex **4**, carrying a higher NBO charge (0.522) on the Fe atom was catalytically less active than complex **2**, with a lower NBO charge (0.498) on the metal atom.

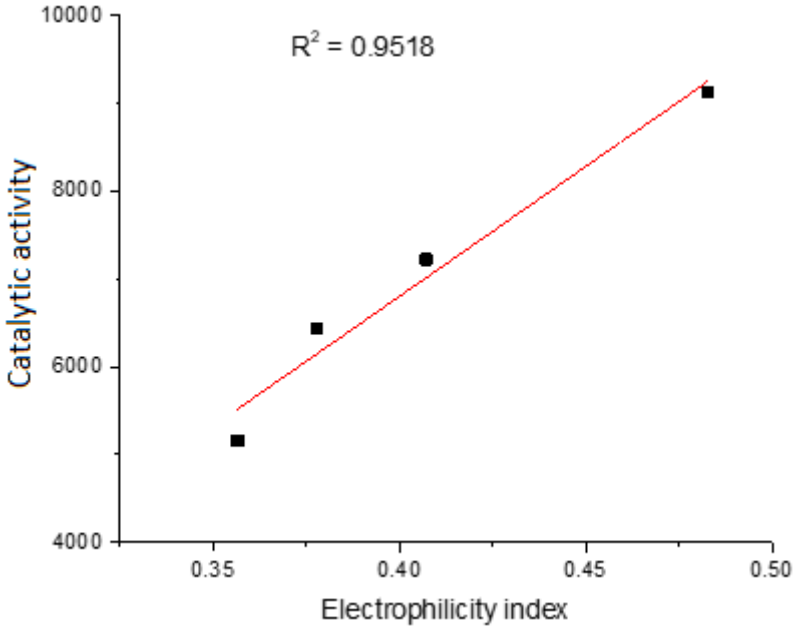

Figure 3.17: Plot of catalytic activity in $kg_{oligomers}\ mol^{-1}(M)\ h^{-1}$ against electrophilicity index (ω) depicting clear dependence of catalytic activity on the electrophilicity index of the complexes.

3.4. Conclusions

In this study, the diverse coordination modes of the Co(II) and Fe(II) complexes have been established and found to be dependent on the identities of N^O ligands. Both mononuclear and dinuclear complexes with ligands adopting either bidentate or tridentate coordination modes are formed. The structural characterization of the Co(II) and Fe(II) complexes was achieved using a combination of IR spectroscopy, mass spectrometry, electron-paramagnetic resonance and single crystal X-ray crystallography. Activation of the Co(II) and Fe(II) complexes with $EtAlCl_2$ or MAO gave active catalysts in ethylene oligomerization reactions to afford dimers and trimers of ethylene. The catalytic activity and selectivity of the late transition metal catalysts were marginally influenced by the complex structure, type of co-catalyst used and reaction conditions. Co(II) complexes generally displayed higher catalytic activities than their corresponding Fe(II) complexes, while activation with MAO was superior to $EtAlCl_2$ co-catalyst. In addition, higher proportions of C_4 oligomers were formed using MAO, while activation with $EtAlCl_2$ favoured the formation of C_6 oligomers. Computational calculations using DFT also showed a direct relationship between the catalytic activities of the complexes **2**-**6** and **5,** and the nature of ligand structure. The electrophilicity index of the complexes largely controlled the catalytic activities of the complexes.

3.5. References

1. McMorn, P., Hutchings, G. J, *Chem. Soc. Rev.* **2004**, *33*, 108.

2. Severn, J. R., Chadwick, J. C., Duchateau, R., Friederichs, N., *Chem. Rev.* **2005**, *105*, 4073-4147.

3. Sydora, O. L., *Organometallics* **2019**, *38*, 99-1010.

4. Zhang, J., Liu, S., Li, A., Ye, H., Li, Z., *New. J. Chem.* **2016**, *40*, 7027-7030.

5. Sun, W.-H., Zhang, S., Zuo, W., *C. R. Chimie* **2008**, *11*, 307-316.

6. Azoulay, J. D., Schneider, Y., Galland, G. B., Bazan, G. C., *Chem. Commun.* **2009**, 6177-6179.

7. Trofymchuk, O. S., Gutsulyak, D. V., Quintero, C., Parvez, M., Daniliuc, C. G., Piers, W. E., Rojas, R. S., *Organometallics* **2013**, *32*, 7323-7333.

8. Zhang, D., Nadres, E. T., Brookhart, M., Daugulis, O., *Organometallics* **2013**, *32*, 5136-5143.

9. Ainooson, M. K., Ojwach, S. O., Guzei, I. A., Spencer, L. C., Darkwa, J., *J. Organomet. Chem.* **2011**, *696*, 1528-1535.

10. Hu, T., Tang, L. -M., Li, X.-F., Li, Y.-S., Hu, N.-H, *Organometallics* **2005**, *24*, 2628-2631.

11. Kermagoret, A., Braunstein, P., *Dalton Trans.* **2008**, *4*, 1564-1573.

12. Speiser, F., Braunstein, P., Saussine, L., *Organometallics* **2004**, *23*, 2633-2641.

13. Piel, C., Kaminsky, W., Kulickle, Ing. W. -M., *Dissertation: Hamburg, Chem.* **2005**.

14. Sun, W.-H., Zhang, S., Jie, S., Zhang, W., Li, Y., Ma, H., Chen, J., Wedeking, K., Frohlich, R. , *J. Organomet. Chem.* **2006**, *691*, 4196.

15. Zhang, M., Zhang, S., Hao, P., Jie, S., Sun, W. -H., Li, P., Lu, X., *Eur. J. Inorg. Chem.* **2007**, 3816-3826.

16. Hou, J., Sun, W.-H., Zhang, S., Ma, H., Deng, Y., Lu, X., *Organometallics* **2005**, *25*, 236.

17. Braunstein, P., Chauvin, Y., Mercier, S., Saussine, L., *C. R. Chimie* **2005**, *8*, 31.

18. Speiser, F., Braunstein, P., Saussine, L., *Dalton Trans.* **2004**, *45*, 1539.

19. Ajellal, N., Kuhn, M. C. A., Boff, A. D. G., Hoener, M., Thomas, C. M., Carpentier, J.-F., Casagrande Jr., O. L., *Organometallics* **2006**, *25*, 1213-1219.

20. Boudier, A., Breuil, P. R., Magna, L., Olivier-Bourbigou, H., Braunstein, P., *J. Organomet. Chem.* **2012**, *718*, 31-37.

21. Ai, P., Chen, L., Guo, Y., Jie, S., Li, B-G., *J. Organomet. Chem* **2012**, *705*, 51-58.

22. Bahuleyan, B. K., Ahn, I. Y., Appukuttan, V., Lee, S. H., Ha, C. -S., Kim, I., *Macromol Res.* **2010**, *18*, 701-704.

23. Zabel, D., Schebert, A., Wolmershauser, G., Jones Jr, R. L., Thiel, W. R., *Eur. J. Inorg. Chem.* **2008**, 3648-3654.

24. Adams, G. M., Weller, A. S., *Coord. Chem. Rev.* **2018**, *355*, 150-172.

25. Jeffrey, C. J., Rauchfuss, T. B., Tucker, P. A., *Inorg. Chem.* **1980**, *19*, 3306-3316.

26. Suo, H., Solan, G. A., Ma, Y., Sun, W.-H., *Coord. Chem. Rev.* **2018**, *372*, 101-116.

27. Wang, L., Sun, W. -H., Han, L., Li, Z., Hu, Y., He, C., Yan, C., *J. Organomet. Chem.* **2002**, *650*, 59-64.

28. Small, B. L., Rios, R., Fernandez, E. R., Carney, M. J., *Organometallics* **2007**, *26*, 1744-1749.

29. Ngcobo, M., Ojwach, S. O., *J. Organomet. Chem.* **2017**, *846*, 33-39.

30. Bruker, *A.*, *SAINT and SADABS*, Bruker AXS Incl., Madison, Wisconsin, USA. , **2012**.

31. Dolomanov, O. V., Bourhis, L. J., Gildea, R. J., Howard, J. A. K., Puschmann, H., *J. Appl. Cryst.* **2009**, *42*, 339-341.

32. Sheldrick, G. M., *Acta Cryst.* **2015**, *C12*, 3-8.

33. Sheldrick, G. M., *Acta Crystallogr., Sect. A: Found. Crystallogr.* **2007**, *64*, 112-122.

34. Rome, K., Mclntyre, A., *Chromatography Today.* **2012**, *52*, 52-55.

35. Frisch, M. J. T., Trucks, G. W., Schlegel, H. B., Scuseria, G. E., Robb, M. A., Cheeseman, J. R., Scalmani, G., Barone, V., Mennucci, B., Petersson, G. A., Nakatsuji, H., Caricato, M., Li, X., Hratchian, H. P., Izmaylov, A. F., Bloino, J., Zheng, G., Sonnenberg, J. L., Hada, M., Ehara, M., Toyota, K., Fukuda, R., Hasegawa, J., Ishida, M., Nakajima, T., Honda, Y., Kitao, O., Nakai, H., Vreven, T., Montgomery, J. A., Peralta, Jr., J. E., Ogliaro, F., Bearpark, M., Heyd, J. J., Brothers, E., Kudin, K. N., Staroverov, V. N., Kobayashi, R., Normand, J., Raghavachari, K., Rendell, A., Burant, J. C., Iyengar, S. S., Tomasi, J., Cossi, M., Rega, N., Millam, J. M., Klene, M., Knox, J. E., Cross, J. B., Bakken, V., Adamo, C., Jaramillo, J., Gomperts, R., Stratmann, R. E., Yazyev, O., Austin, A. J., Cammi, R., Pomelli, C., Ochterski, J. W., Martin, R. L., Morokuma, K., Zakrzewski, V. G., Voth, G. A., Salvador, P., Dannenberg, J. J., Dapprich, S., Daniels, A. D., Farkas, O., Foresman, J. B., Ortiz, J. V., Cioslowski, J., Fox, D. J., *GAUSSIAN 09 (Revision A.1), Gaussian, Inc., Wallingford, CT,* ***2009.***

36. Frisch, M., Trucks, G., Schlegel, H., Scuseria, G., Robb, M., Cheeseman, J., Scalmani, G., Barone, V., Mennucci, B., Petersson, G., *Gaussian Inc. Wallingford* **2010**.

37. Nyamato, G. S., Ojwach, S. O., Akerman, M. P., *Dalton Trans.* **2016**, *45*, 3407-3416.

38. Cotton, F. A., Wilkinson, G., Murillo, C. A., Bochmann, M., Advanced Inorganic Chemistry 6th Ed. John Wiley and Sons: New York, **1999**; p 835.

39. Housecroft, C. E., Sharpe, A. G., Inorganic Chemistry 3rd Ed. Pearson: London, **2008**; pp 672-674.

40. Boltina, S., Yankey, M., Guzei, I. A., Spencer, L. C., Ojwach, S. O., Darkwa, J., *S. Afr. J. Chem.* **2012**, *65*, 75-83.

41. Tshabalala, T. A., Ojwach, S. O., Akerman, M. A., *J. Mol. Catal. A: Chem.* **2015**, *406*, 178-184.

42. Celen, S., Gungor, E., Kara, H., Kara, A., Azaz, d., *J. Coord. Chem.* **2013**, *66*.

43. Allan, F. H., *Acta Cryst.* **2002**, *B58*, 380-388.

44. Bruno, I. J., Cole, J. C., Edgington, P. R., Kessler, M., Macrae, C. F., McCabe, P., Pearson, J., Taylor, R., *Acta Cryst. Sec. B: Strcuct. Sci.* **2002**, *58*, 389-397.

45. Fliedel, C., Rosa, V., Vileto, B., Parizel, N., Choua, S., Gourlaoouen, C., Rosa, P., Turek, P., Braunstein, P., *Inorg. Chem.* **2015**, *55*, 4183-4198.

46. Kuzu, I., Krummenacher, I., Hewitt, I. J., Lan, Y., Mereacre, V., Powell, A. K., Hofer, P., Harmer, J., Breher, F., *J. Chem. Eur.* **2009**, *15*, 4350-4365.

47. Bruno, I. J., Cole, J. C., Edgington, P. R., Kessler, M., Macrae, C. F., McCabe, P., Pearson, J., Taylor, R., Cooper, I. R., Harris, S. E., Orpen, A. G., *J. Chem. Inf. Comput. Sci.* **2004**, *44*, 2133-2144.

48. Banerjee, I., Jana, A., Singh, S., Marek, J., de Barco, E., Ali, M., *Polyhedron* **2013**, *66*, 162-166.

49. Jackson, S. D., Hargreaves, J. S. J., *Metal Oxide Catalysis.*; MILEY-VCH Verlag GmbH & Co.: Weinheim, **2009**.

50. Walker, F. A., *J. Am. Chem. Soc.* **1970**, *92*, 4235-4243.

51. Sugiura, Y., *J. Am. Chem. Soc.* **1980**, *102*, 5216-5221.

52. Khare, G. P., Lee-Ruff, E., Lever, a. B. P., *Can. J. Chem.*, **1976**, *54*, 3424-3431.

53. Zhang, M.; Hao, P.; Zuo, W.; Jie, S.; Sun, W.-H., *J. Organomet. Chem.* **2008**, *693*, 483-491.

54. Gao, R., Xiao, L., Hao, X., Sun, W.-H., Wang, F., *Dalton Trans.* **2008**, *28*, 5645-5651.

55. Sun, W.-H., Tang, X., Gao, T., Wu, B., Zhang, W., Ma, H., *Organometallics* **2004**, *23*, 5037-5047.

56. Shi, P.-Y. L., Y.-H.; Peng, S.-M.; Liu, S.-T. , *Organometallics* **2002**, *21*, 3203-3207.

57. Sun, W.-H.; Tang, X.; Gao, T.; Wu, B.; Zhang, W.; Ma, H., *Organometallics* **2004**, *23*, 5037-5047.

58. Nyamato, G. S., Ojwach, S. O., Akerman, M. P., *J. Mol. Catal. A: Chem.* **2014**, *394*, 274-282.

59. Zhang, C., Sun, W.-H., Redshaw, C., *Dalton Trans.* **2013**, *42*, 8988-8997.

60. Zhang, X. F., Duan, B. G., Sun, W.-H., Hsu, S. L., Yang, X. Z., *Sci. China Ser. B-Chem.* **2009**, *52*, 48-55.

61. Li, C., Wang, F., Lin, Z., Zhang, N., Wang, J. , *J. Appl. Organomet. Chem.* **2017**, *e3756*, 1-8.

62. Moeti, L. P., Darkwa, J., *S. Afr. J. Chem.* **2016**, *69*, 236-243.

63. Svejda, S. A., Brookhart, M., *Organometallics* **1999**, *18*, 65-74.

64. Helldorfer, M., Alt, H. G., *J. Appl. Polym. Sci.* **2003**, *89*, 1356-1361.

65. Yang, W., Yi, J., Sun, W.-H., , *Macromol. Chem. Phys.* **2015**, *216*, 1125-1133.

66. Chattaraj, P. K., Maiti, B., *J. Am. Chem. Soc.* **2003**, *125*, 2705-2710.

67. Huo, P., Liu, W., He, X., Wang, H., Chen, Y., *Organometallics* **2013**, *32*, 2291-2299.

68. Wekesa, I. M. J., D., *Dalton Trans.* **2014**, *43*, 2549-2558.

CHAPTER FOUR

Synthesis and structural elucidation of dibromo-multidentate N^N and N^N^O Fe(II), Co(II) and Ni(II) complexes and their applications as catalysts in ethylene oligomerization reactions

4.1. Introduction

Olefins are major industrial raw materials extensively used in the production of detergents, lubricants, plasticizers, oil field chemicals, and comonomers used for branched polyolefins.[1-4] In the matrix of olefin production, we have late transition metal catalysts which have shown better catalytic activity and selectivity and also outstanding tolerance of heteroatom functionalities as compared to their early transition metal counterparts.[5] As a result, the past decades have witnessed a significant progress in the usage of late transition metal complexes as ethylene oligomerization catalysts.[6-7] For example, Ni(II) complexes are currently applied industrially in the Shell Higher Olefin Process (SHOP), which primarily uses ethylene as a feedstock to produce higher olefins.[8] The pioneering work of Brookhart *et al*,[9] and Gibson *et al*,[10] on the application of α-diiminonickel(II) complexes in olefin oligomerization and polymerization reactions stimulated the development of new modified Ni(II) complexes.[11] As a result, numerous reports have shown that Ni(II) complexes are promising olefin oligomerization catalysts due to their high catalytic activities and selectivity, especially in the oligomerization of ethylene.[12-16]

Other late transition metal catalysts, most notable, Fe(II) and Co(II) systems ligated on Schiff base imines, those initially discovered individually by the groups of Brookhart and Gibson are known for their appreciable catalytic activity and good selectivity towards the formation of

linear and branched polyethylenes.[7] Subsequent research works have focused more on modifying these catalysts' models and devising their alternative models in the pursuit of achieving well-balanced catalytic systems with respect to activity, selectivity and stability.[17-19] However, of the small-scaled models of Fe(II) and Co(II) complexes reported in literature,[7, 20-21] few of them are displaying good catalytic activities toward ethylene oligomerization and polymerization when compared with catalytic activities displayed by Ni(II) complexes. Collectively, these catalysts possess differing bi- or tridentate Schiff base ligands that display interesting coordination chemistries and consequently, have attracted much attention for polymerization and oligomerization of ethylene.[22-23] For example, the use of bidentate salicylaldehyde ligands and their derivatives as chelating agents with late transition metal complexes has had a good impact in the development of catalytically active and selective ethylene oligomerization catalysts.[9-10] Nevertheless, studies on Schiff base ligands of 3,5-dibromo salicylaldehyde and their late transition metal complexes are rather scarce.

The Fe(II) and Co(II) complexes bearing ligands of 2-[(ethylimino)methyl]phenol moieties have been previously reported.[24-25] Inspired by their outstanding catalytic performances herein is the report on the continued pursuit of investigating more on the catalytic effect of the mixed donor ligands. Consequently, the objective of this study was to synthesize iron, cobalt and nickel complexes of Schiff base ligands containing 3,5-dibromosalicylideneimine moiety and investigate the potential of complexes as catalysts for olefin oligomerization reactions. Density functional theory studies have been performed to further acquire an insight on the effect of the complex structure on the catalytic behaviour of these complexes in ethylene oligomerization reactions.

4.2. Experimental section

4.2.1. Materials and instrumentation

All solvents were of analytical grade and were dried and distilled prior to use. The reagents 3,5-dibromosalicylaldehyde (98%), 2-aminopyridine (99%), 2-amino-4-methylpyridine (99%) and 8-aminoquinoline (98%) were purchased from Sigma-Aldrich; anhydrous $CoCl_2$ (98%), $FeCl_2.4H_2O$ (98%), [$NiBr_2$(DME)] (DME = ethylene glycol dimethyl ether) (97%), modified methylaluminoxane (MMAO-12, 7 % w/w in toluene) and ethylaluminum dichloride (1.0 M in hexanes) were purchased from Merck and used as received without further purification. All ^1H NMR and $^{13}C\{^1H\}$ NMR (100 MHz) spectra were collected on a 400 MHz Bruker Ultra shield NMR spectrometer using deuterated solvents, i.e., either $CDCl_3$ or DMSO-d_6. The infrared spectra were collected on an Agilent Technologies, Cary 630 FTIR and Perkin Elmer Spectrometer 100. Mass spectrometric data collection was performed using an LC Premier micro-mass Spectrometer model LCMS-2020. Determination of the compounds elemental compositions was done on a Thermal Scientific Flash 2000. Magnetic moment measurements were determined using Evans balance (Sherwood MK-1). UV-Visible spectra of the complexes were recorded on a Varian Cary 100 Bio UV-Visible spectrophotometer with an attached Varian Peltier temperature-controller within ± 0.1 ˚C using acetonitrile solutions in 1.0 cm path length quartz cuvettes. Varian CP-3800 gas chromatograph equipped with a flame ionization detector (FID) and a CP-Sil 5 CB (30 m x 0.2 mm x 0.25 µm) capillary column was used for GC analyses (GC conditions: starting temperature 40 ˚C for 5 min, the heating rate of 10 ˚C/min up to 250 ˚C) while GC-MS analyses were performed on a Shimadzu GCMS-QP2010SE.

4.2.2. Synthesis of Schiff base ligands.

*4.2.2.1. 2,4-dibromo-6-((pyridin-2-ylimino)methyl)phenol (**L4**)*

To the ethanolic (10 mL) solution of 2-aminopyridine (0.19 g, 2 mmol), 3,5-dibromosalicylaldehyde (0.56 g, 2 mmol) in ethanol (10 mL) was added drop wise and stirred at room temperature for 24 h. The orange powder formed was filtered washed with ethanol and dried to obtain pale orange powder. Yield: 0.61 g (81%). ^{1}H NMR (400 MHz, $CDCl_3$, δ ppm): 9.42 (s, 1H, imine HC=N-), 8.55 (d, 1H, $^{3}J_{HH}$ = 9.2 Hz, Py-CH=N), 7.84 (t, 1H, $^{3}J_{HH}$ = 7.2 Hz, Py-H), 7.80 (s, 1H, Ph-H), 7.60 (s, 1H, Ph-H), 7.34 (t, 1H, $^{3}J_{HH}$ = 7.2 Hz, Py-H), 7.31 (d, 1H, $^{3}J_{HH}$ = 9.2 Hz, Py-H); ^{13}C NMR ($CDCl_3$): δ/ppm: 110.22, 113.57, 120.60, 123.45, 124.46, 134.51, 138.79, 138.88, 149.19, 153.84, 159.76, 162.28; IR ν_{max}/ cm^{-1}: 3058 (ν_{OH}), 1606 ($\nu_{C=N}$). ESI-MS: *m/z* (%) 354.87 (100%) $[M-H]^+$.

*4.2.2.2. 2,4-dibromo-6-(((4-methylpyridin-2-yl)imino)methyl)phenol (**L5**)*

Ligand **L5** was synthesized following the same procedure adopted for **L4** using 2-amino-4-methylpyridine (0.21 g, 2 mmol) and 3,5-dibromosalicylaldehyde (0.56 g, 2 mmol) to give orange powder. Yield: 0.65 g (82%). ^{1}H NMR (400 MHz, CDCl3, δ ppm): 9.39 (s, 1H, imine HC=N-), 8.39 (d, 1H, $^{3}J_{HH}$ = 9.2 Hz, Py-CH=N), 7.80 (s, 1H, Ph-H), 7.59 (s, 1H, Ph-H), 7.18 (s, 1H, Py-H), 7.12 (d, 1H, $^{3}J_{HH}$ = 9.2 Hz, Py-H), 2.45(s, 3H, Py-CH_3); ^{13}C {^{1}H} NMR ($CDCl_3$): δ/ppm: 20.99, 110.87, 112.57, 120.38, 121.29, 124.46, 134.43, 138.79, 148.81, 150.32, 155.84, 158.76, 162.08; IR ν_{max}/ cm^{-1}: 3069 (ν_{OH}), 1623 ($\nu_{C=N}$); HRESI-MS: m/z 368.90 (100%) $[M-H]^+$.

*4.2.2.3. 2,4-dibromo-6-((quinolin-8-ylimino)methyl)phenol (**L6**)*

Ligand **L6** was synthesized following the same procedure adopted for **L4** and **L5**, using 8-aminoquinoline (0.29 g, 2 mmol) and 3,5-dibromosalicylaldehyde (0.56 g, 2 mmol) to give reddish orange powder. The ligand on recrystallization in dichloromethane obtained X-ray quality reddish orange single crystals. Yield: 0.76 g (89%). ^{1}H NMR (400 MHz, CDCl3, δ ppm): 9.03 (d, 1H, $^{3}J_{HH}$ = 9.2 Hz , quin HC=N-), 8.99 (s, 1H, imine HC=N-), 8.24 (d, 1H, $^{3}J_{HH}$ = 9.2 Hz, quin-H), 7.82 (d, 1H, $^{3}J_{HH}$ = 9.2 Hz, quin-H), 7.80 (s, 1H, Ph-H), 7.63 (s, 1H, Ph-H), 7.60 (d, 1H, $^{3}J_{HH}$ = 9.2 Hz, quin-H), 7.53(t, 2H, $^{3}J_{HH}$ = 7.2 Hz, quin-H); ^{13}C {^{1}H} NMR ($CDCl_3$): δ/ppm: 109.20, 113.59, 119.37, 120.49, 120.05, 126.49, 127.18, 129.25, 133.59,136.09,138.62, 141.88, 142.37, 150.76, 160.09, 161.76; IR ν_{max}/ cm^{-1}: 3068 (ν_{OH}), 1609 ($\nu_{C=N}$); HRESI-MS: m/z 404.91 (100%) $[M-H]^+$.

4.2.3. Synthesis of Fe(II), Co(II) and Ni(II) complexes

*4.2.3.1. Synthesis of [Fe(**L4**)$_2$] (**7**)*

To a solution of anhydrous $FeCl_2$ (0.06 g, 0.5 mmol) in methanol (10 mL), ligand **L4** (0.34 g, 1.00 mmol) dissolved in methanol (10 mL) was added drop wise and stirred overnight at room temperature. The black precipitate formed was filtered, washed with ethanol, methanol, and ether and dried to obtain a dark brown powder. Yield: 0.30 g (71%). TOF ESI-MS: m/z (%) 760 [M, 10%]$^+$. IR ν_{max}/ cm^{-1}: 3063 (ν_{OH}), 1613 ($\nu_{C=N}$); μ_{obs} = 5.60 BM. Anal. Calcd. for $C_{24}H_{14}Br_4FeN_4O_2 \cdot 2CH_3OH$: C 37.63, H 2.67, N 6.75. Found (%): C 37.85, H 2.76, N 7.19.

The complexes **10**-**13**, **8**-**14** and **9**-**15** were synthesized following the procedure described for complex **7**.

*4.2.3.2. Synthesis of [Co(**L4**)$_2$] (**8**)*

Anhydrous $CoCl_2$ (0.06 g, 0.5 mmol), Ligand **L4** (0.36 g, 1.00 mmol). Yield: 0.28 g (65 %); TOF ESI-MS: m/z (%) 769.78 [M, 10%]$^+$; IR ν_{max}/ cm^{-1}: 3063 (ν_{OH}), 1623 ($\nu_{C=N}$); μ_{obs} = 3.26 BM. Anal. Calcd. for $C_{24}H_{14}Br_4CoN_4O_2{\cdot}2CH_3OH$: C 37.49, H 2.66, N 6.73. Found (%): C 37.32, H 2.56, N 6.58.

*4.2.3.3. Synthesis of [Ni(**L4**)$_2$] (**9**)*

To a solution of [$NiBr_2$(DME)] (0.16 g, 0.50 mmol) in methanol (10 mL), ligand **L4** (0.36 g, 1.00 mmol) dissolved in methanol (10 mL) was added dropwise and stirred at room temperature for 12 h. The green precipitate formed was filtered, washed with ethanol, methanol, and ether and dried to obtain a green solid. Yield: 0.44 g (84%). TOF ESI-MS: m/z (%) 763 [Ni(**L4**)$_2$, 15%]$^+$; IR ν_{max}/ cm^{-1}: 3288 (ν_{OH}), 1634 ($\nu_{C=N}$); μ_{obs} = 2.82 BM. Anal. Calcd. for $C_{24}H_{14}Br_4NiN_4O_2{\cdot}2CH_3OH$: C 37.50, H 2.66, N 6.73. Found (%): C 37.49, H 2.84, N 6.64.

*4.2.3.4. Synthesis of [Fe(**L5**)$_2$] (**10**)*

Anhydrous $FeCl_2$ (0.07 g, 0.50 mmol), Ligand **L5** (0.37 g, 1.00 mmol). Yield: 0.32 g (72 %); TOF ESI-MS: m/z (%) 793.77 [Fe(**L5**)$_2$, 14 %]$^+$; IR ν_{max}/ cm^{-1}: 3063 (ν_{OH}), 1609 ($\nu_{C=N}$); μ_{obs} = 5.15 BM. Anal. Calcd. for $C_{26}H_{18}Br_4FeN_4O_2{\cdot}2CH_3OH$: C 39.20, H 3.05, N 6.53. Found (%): C 39.22, H 3.36, N 7.09.

*4.2.3.5. Synthesis of [Co(**L5**)$_2$] (**11**)*

Anhydrous $CoCl_2$ (0.06 g, 0.5 mmol), Ligand **L5** (0.37 g, 1.00 mmol). Yield: 0.29 g (68 %); ESI-MS: m/z (%) 819.74 [Co(**L5**)$_2$+Na, 22 %]$^+$; IR ν_{max}/ cm^{-1}: 1613 ($\nu_{C=N}$); μ_{obs} = 3.99 BM.

Anal. Calcd. for $C_{26}H_{18}Br_4CoN_4O_2 \cdot 2CH_3OH$: C 39.06, H 3.04, N 6.51. Found (%): C 38.98, H 2.60, N 7.00.

*4.2.3.6. Synthesis of [Ni(**L5**)$_2$] (**12**)*

[$NiBr_2$(DME)] (0.16 g, 0.50 mmol), Ligand **L5** (0.37 g, 1.00 mmol); Yield: 0.39 g (78 %); TOF ESI-MS: m/z (%) 818.87 [M+Na, 42 %]$^+$; IR ν_{max}/ cm^{-1}: 3063 (ν_{OH}), 1623 ($\nu_{C=N}$); μ_{obs} = 3.05 BM. Anal. Calcd. for $C_{26}H_{18}Br_4NiN_4O_2 \cdot 2CH_3OH$: C 39.07, H 3.04, N 6.51. Found (%): C 38.92, H 2.96, N 6.92.

*4.2.3.7. Synthesis of [Fe(**L6**)$_2$] (**13**)*

Anhydrous $FeCl_2$ (0.07 g, 0.50 mmol), Ligand **L6** (0.40 g, 1.00 mmol). Yield: 0.35 g (73 %); TOF ESI-MS: m/z 890 [Fe(**L6**)$_2$ + (2H+Na), 10 %]$^+$; IR ν_{max}/ cm^{-1}: 1614 ($\nu_{C=N}$); μ_{obs} = 5.43 BM. Anal. Calcd. for $C_{32}H_{18}Br_4FeN_4O_2$: C 44.38, H 2.10, N 6.47. Found (%): C 44.52, H 2.13, N 6.59.

*4.2.3.8. Synthesis of [Co(**L6**)$_2$] (**14**)*

Anhydrous $CoCl_2$ (0.06 g, 0.5 mmol), Ligand **L6** (0.40 g, 1.00 mmol). Yield: 0.33 g (72 %); TOF ESI-MS: m/z 868.87 [Co(**L6**)$_2$, 100 %]$^+$; IR ν_{max}/ cm^{-1}: 1619 ($\nu_{C=N}$); μ_{obs} = 3.59 BM. Anal. Calcd. for $C_{16}H_{10}Br_2Cl_2CoN_2O$: C 35.86, H 1.88, N 5.23. Found (%): C 35.82, H 1.66, N 5.29.

*4.2.3.9. Synthesis of [Ni(**L6**)$_2$] (**15**)*

$NiBr_2$(DME)] (0.16 g, 0.50 mmol), Ligand **L6** (0.40 g, 1.00 mmol). Recrystallization of the complex in methanol solvent by a slow evaporation afforded rod-shaped green coloured single crystals suitable for X-ray analyses. Yield: 0.42 g (75 %); TOF ESI-MS: m/z (%) 890.79 $[M+Na, 2\%]^+$; IR ν_{max}/ cm^{-1}: 1635 ($\nu_{C=N}$), 572 (ν_{Ni-O}); μ_{obs} = 2.78 BM. Anal. Calcd. for $C_{32}H_{18}Br_4NiN_4O_2$: C 44.24, H 2.09, N 6.45. Found (%): C 43.82, H 2. 66, N 6.29.

4.2.4. X-ray crystallography data collection

Single orange block-shaped crystals of **13a** (derivative of complex **13**) and green rod-shaped crystals of **15** were recrystallized from methanol solvent by slow evaporation. A suitable crystal of each complex was selected and mounted on a MITIGEN holder in paratone oil on a Bruker APEX-II CCD diffractometer. The crystal was kept at T = 100(2) K during data collection. Using **Olex2**,[26] the structure was solved with the **ShelXS-2013**,[27] structure solution program, using the direct solution method. The model was refined with version 2016/6 of **ShelXL**,[28] using Least Squares minimisation.

4.2.5. Ethylene oligomerization experiments

The ethylene oligomerization reactions were carried out utilizing a stainless-steel reactor fitted with a 100 mL glass chamber and a magnetic stirrer bar. A pre-weighed amount of the synthesized pre-catalyst (10.0 μmol) in chlorobenzene (10 mL) was transferred into a dry Schlenk tube *via* a cannula under nitrogen atmosphere. This was followed by addition of the respective co-catalyst ($EtAlCl_2$ or MMAO) using a syringe. The resultant solution in the Schlenk tube was then transferred using a cannula into the pre-evacuated reactor, followed by addition of 20 mL of chlorobenzene or toluene solvent to give total volume of 30 mL. The

reactor was then purged with ethylene gas and pressure and temperature set at 10 bar and 30 ˚C, respectively, and the reaction initiated by switching on the magnetic stirrer for 1 h. Upon completion of oligomerization process, the reactor was cooled to about -10 °C using liquid nitrogen and the unreacted ethylene vented. This was followed by quenching the mixture through addition of 10% HCl (2 mL). Aliquots of the reaction sample were placed in GC-vials and analyzed to determine both the catalytic activity and oligomer compositions. Heptane was used as internal standard[29] while GC-MS data were used to establish the molecular mass of the oligomer products.

4.2.6. Density Functional Theoretical (DFT) calculations

Theoretical calculations were performed using density functional theory (DFT) method executed by Gaussian 09W suite of programmes.[30] The structures were optimised using the hybrid Becke, 3-parameter, Lee-Yang-Parr (B3LYP) at the standard Los Alamos National Laboratory 2 double ζ (LANL2DZ) basis set.[31] The calculations for the optimized complexes were done at a singlet spin ground state. Gauss View 5.0 programme was used to visualise the optimised minimum energy structures of the complexes under investigation.[32] Electronic chemical potential (μ), chemical hardness (η), chemical softness (σ) and global electrophilicity indices (ω) for the complexes were calculated as per literature methods.[33] Natural bonding orbitals (NBO) analysis was used to determine localised atomic charges in the complexes .[34]

4.3. Results and discussion

4.3.1. Synthesis and characterization of ligands and their metal complexes

The Schiff's base ligands (**L4**–**L6**) were synthesized by condensation reactions of stoichiometric amounts of 3,5-dibromo salicylaldehyde with 2-aminopyridine, 4-methyl-2-

aminopyridine and 8-aminoquinoline, respectively in ethanol as depicted in **Scheme 4.1**. The ligands were obtainable in appreciable yields (81 - 89 %) and with high purity. The Schiff's base ligands were successfully characterized using a combination of ^{1}H and $^{13}C\{^{1}H\}$ NMR spectroscopies, IR spectroscopy and mass spectrometry. The reactions of ligands **L4**–**L6** with the respective salts, $FeCl_2$, $CoCl_2$ or $[NiBr_2(DME)]$ at room temperature resulted in the formation of the respective Fe(II), Co(II) and Ni(II) complexes in good yields of 65 % – 84 % as shown in **Scheme 4.2**. The complexes were found to be paramagnetic in nature and hence could not be characterized by NMR spectroscopy, consequently the complexes were characterized by IR spectroscopy, TOF ESI mass spectrometry, magnetic moment measurements, CHN elemental analyses and X-ray crystallography.

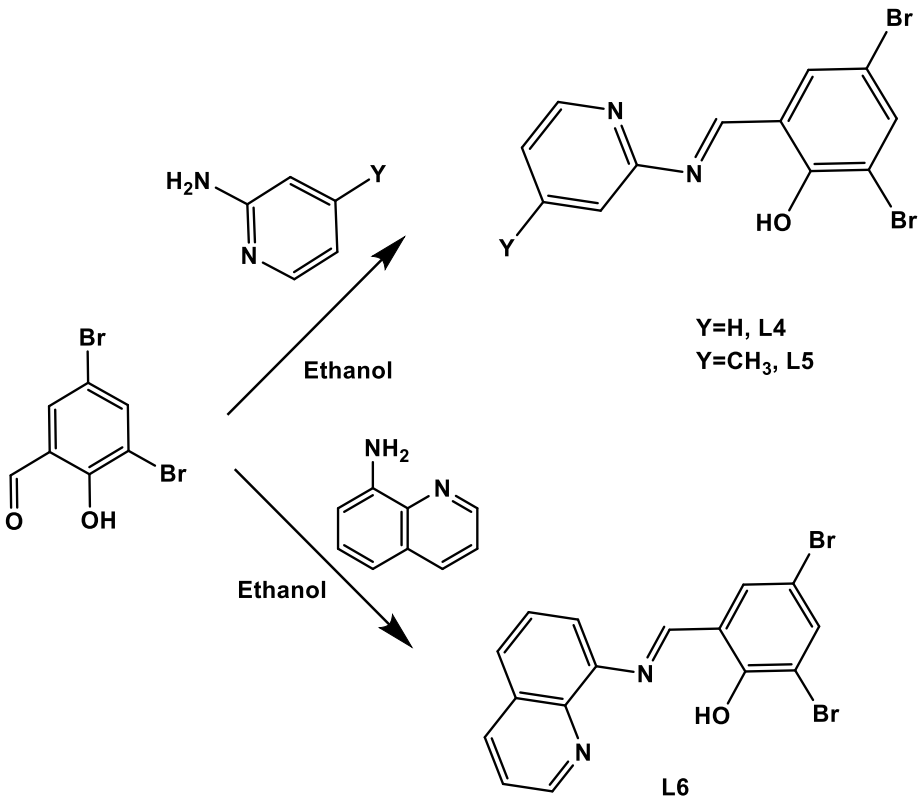

Scheme 4.1: Syntheses of dibromo substituted Schiff's base ligands

Characterization of the ligands **L4**–**L6** by ^{1}H NMR confirmed their formation. Evidently, the ^{1}H NMR of ligand **L4** in **Figure 4.1** shows a singlet signature peak for the proton on imine group (H-C=N) of ligand near 9.03-9.42 ppm which confirmed the success of the condensations reactions. The Schiff's base ligands **L4**–**L6** were also characterized using ^{13}C{^{1}H} NMR spectroscopy in order to determine the identities of carbons in the molecules. Exemplary, **Figures 4.2** shows the ^{13}C{^{1}H} NMR spectrum of ligand **L5**. The ^{13}C NMR spectra of ligands showed diagnostic signals of the imine carbon and aromatic/aliphatic carbon atoms. The formation of imine bond (C=N) was confirmed from the up-field NMR signals at 162.28 ppm (**L4**), 162.08 ppm (**L5**) and 161.76 ppm (**L6**) than that of corresponding aldehyde group (C=O) near 190-200 ppm.

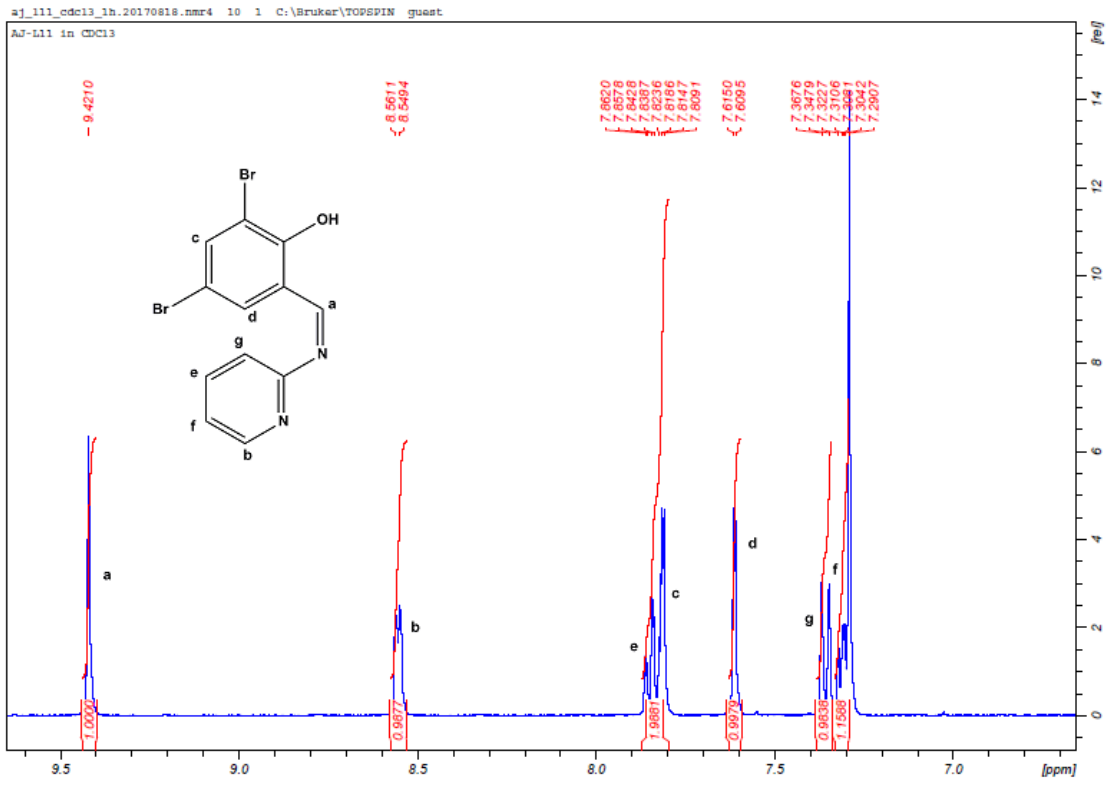

Figure 4.1: ^{1}H NMR spectrum of ligand **L4** in $CDCl_3$ showing the aldimine proton signal (**a**) at chemical shift of 9.4 ppm confirming the formation of the pyridine Schiff base ligand.

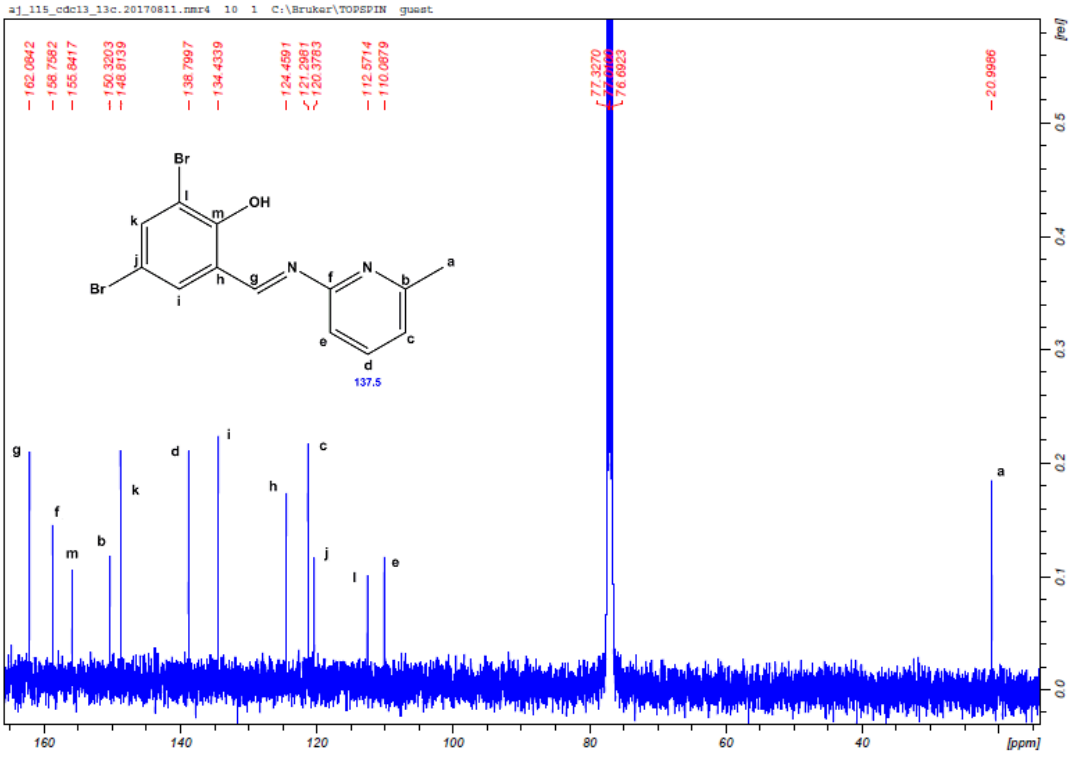

Figure 4.2: The $^{13}C\{^{1}H\}$ NMR spectrum of ligand **L5** in $CDCl_3$ solvent, showing the presence of the imine carbon (C=N) peak around 162.08 ppm.

The mass spectrometric technique was also used in the determination of the exact molecular mass of the synthesized ligands **L4**, **L5** and **L6**. The mass spectra of the ligands revealed the presence of the molecular ion peaks of the ligands having 100 % abundance in accordance to **Scheme 4.1**. To give an example, the mass spectrum of ligand **L4** in **Figure 4.3** showed the base peak at m/z = 354.8785 amu (100 %) corresponding to the ligand molecular ion peak as predicted in **Scheme 4.1**. The same was observed for the ligands **L5** (m/z = 369. 8875 amu, 100 %) and **L6** (m/z = 404.8969 amu, 100 %).

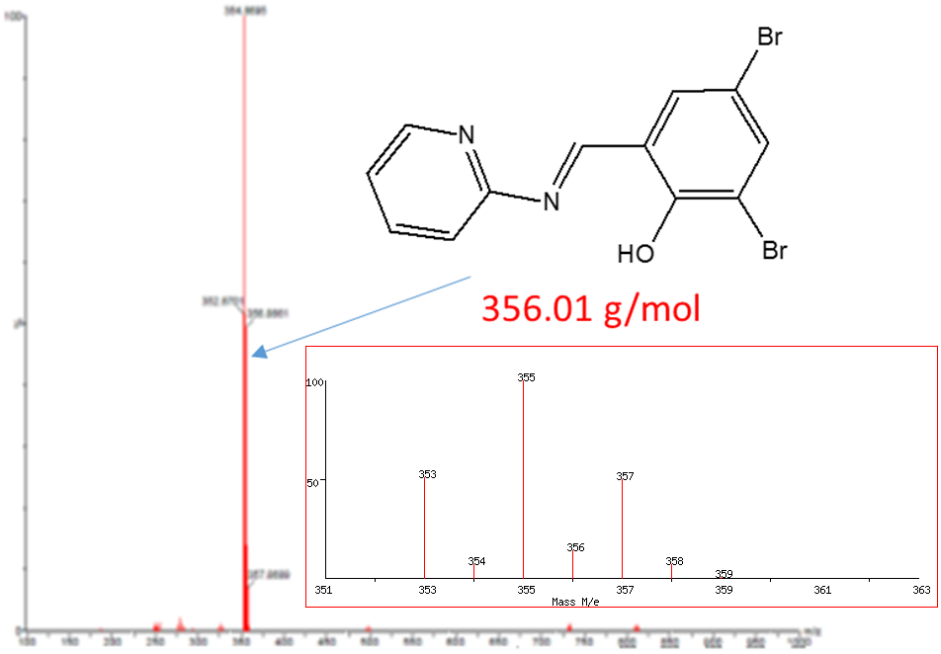

Figure 4.3: Mass spectrum of ligand **L4** showing the base peak at m/z = 354.8785 amu (100 %) corresponding to the ligand molecular ion of $[M-2H]^+$ and its predicted isotopic distribution inserted.

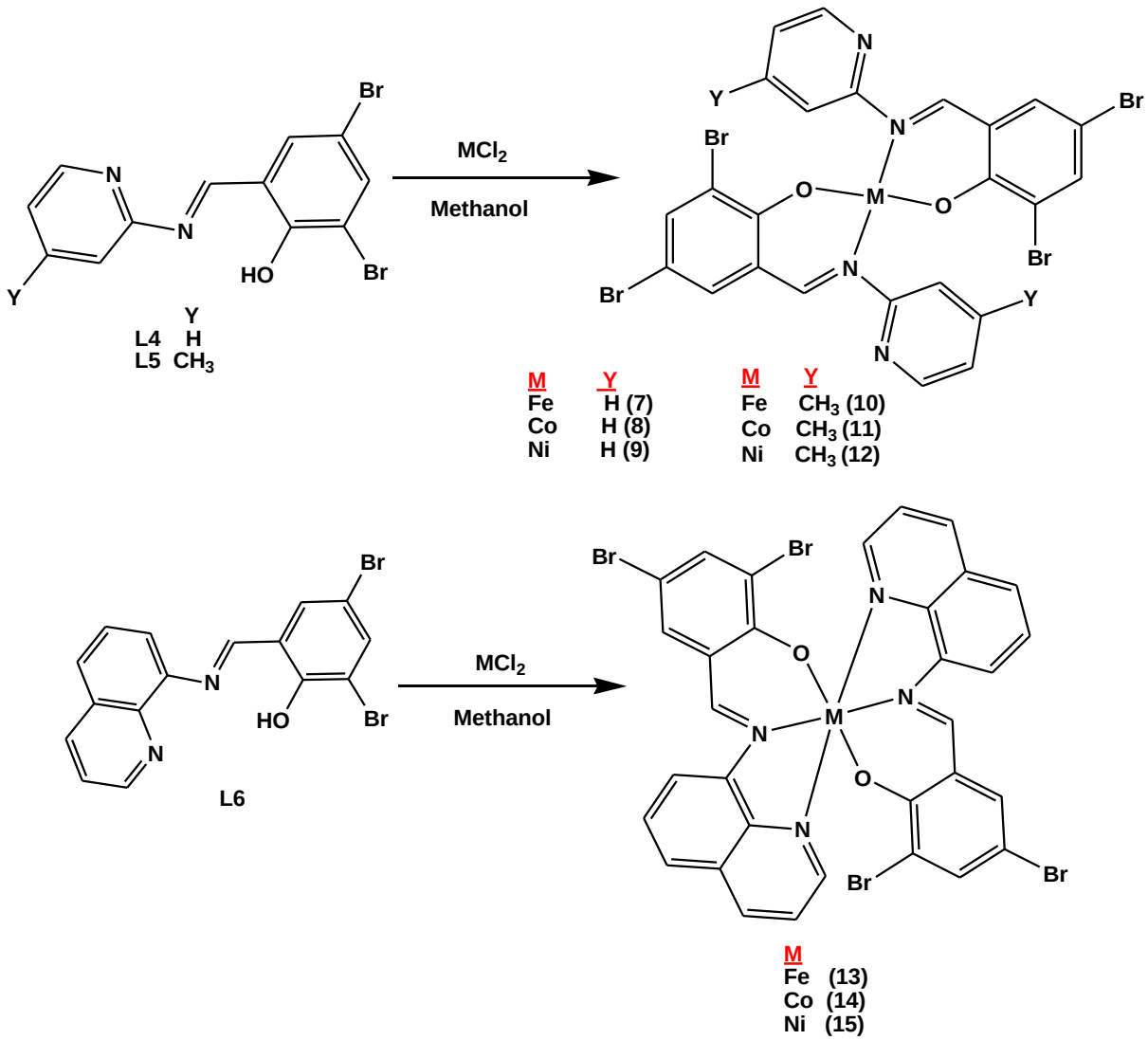

Scheme 4.2: Syntheses of dibromo(pyridine)iminophenol and (dibromoquinoline)iminophenol Fe(II), Co(II) and Ni(II) complexes.

All the complexes were characterized by IR spectroscopy and shown in **Figure 4.4** is the IR spectra of ligands **L4** and **L6** and their corresponding Fe(II), Co(II) and Ni(II) complexes. All the iron, cobalt and nickel complexes, showed sharp absorption bands characteristic of C=N stretching frequency near 1609-1617 cm^{-1}. Notably, the latter diagnostic absorption band was recorded at a lower frequency for the corresponding ligands which confirmed a successful complexation of the ligands. In addition, all complexes showed the absorption bands near 545-

760 cm^{-1} due to Metal-O stretching vibration. The deprotonation upon coordination of the ligands causes a shift in the OH stretching vibration of ligand and thus the ligands were anionic in consistent with the absence of halides in the metal coordination sphere.

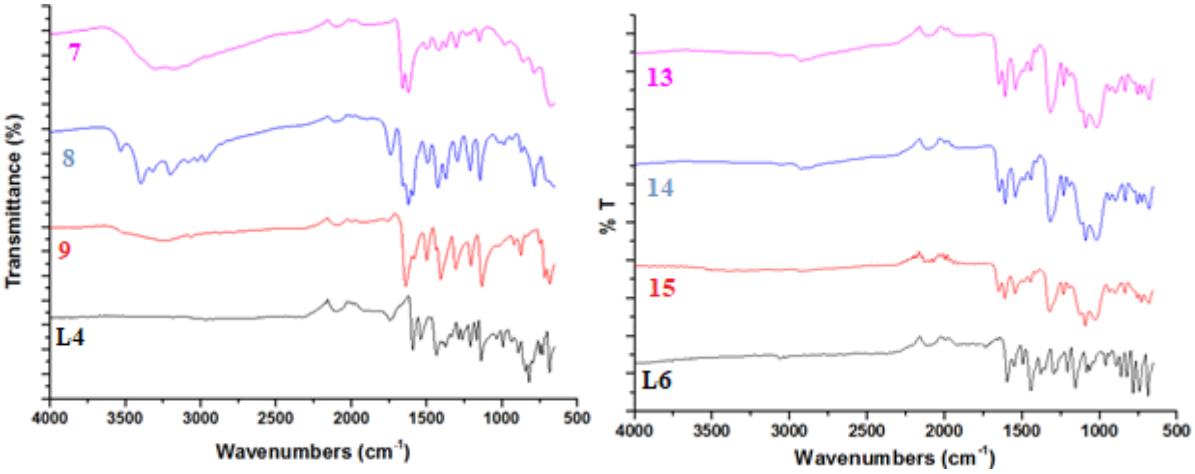

Figure 4.4: FTIR spectra of Schiff's base ligands **L4** and **L6** and their respective Fe(II), Ni(II) and Co(II) complexes showing a shift of the imine peak (C=N) from lower (1609-1617 cm^{-1}) to higher frequencies of 1620-1659 cm^{-1} upon the formation of the complexes.

Furthermore, mass spectrometry was also utilized in the confirmation of the molecular mass of the corresponding Fe(II), Co(II) and Ni(II) complexes of ligands **L4**–**L6**. The mass spectra of the complexes revealed the presence of *bis*-chelated complexes with the absence chloride ligands in the complex as depicted in **Scheme 4.2**. For instance, ESI mass spectrum of complex **14** in **Figure 4.5** showed molecular ion peak at m/z = 868.8691 amu (100 %) corresponding to the *bis*-chelated Co(II) species as depicted in **Scheme 4.2**. Nevertheless, it is noteworthy to mention that other complexes also showed peaks corresponding to the fragmentation with Na^+ ions. For example, ESI-mass spectrum of complex **11**, showed molecular ion peak at m/z of 818.7432 amu (25 %), corresponding to $[M + Na]^+$ fragment. Similarly, these fragmentation patterns were also observed in the mass spectra of complexes **12** and **15**.

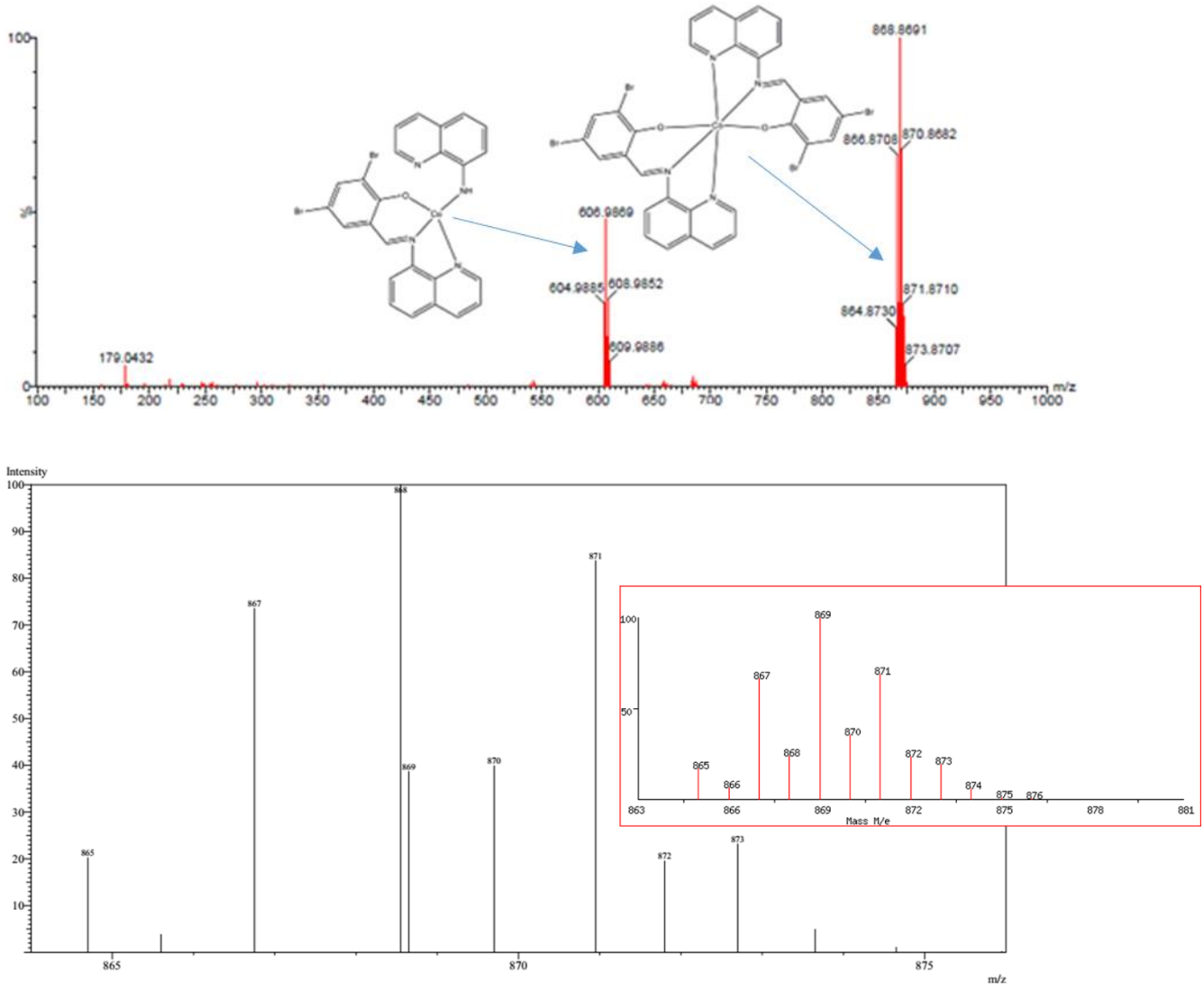

Figure 4.5: The mass spectrum of complex **14** showing the molecular ion peak at m/z = 868.8691 amu with 100 % abundance corresponding to the *bis*-chelated Co(II) species of complex **14** and the combination of experimental and the predicted isotopic distribution of the complex.

The paramagnetic nature of the complexes rendered the use of NMR spectroscopy unhelpful in their structural characterization. Consequently, their magnetic behaviour was examined using magnetic moment measurements. The magnetic susceptibility values of the d^6 Fe(II) complexes **7** – **13** was recorded as 5.60 BM, 5.15 BM and 5.43 BM respectively, which was

notably higher than the spin only value of 4.90 BM for the Fe(II) complexes at 300 K. Nevertheless, the recorded values fall within the expected range of high spin Fe(II) complexes of 5.10 – 5.70 BM at 300 K.[35] We also recorded values of 3.26 BM, 3.99 BM and 3.59 BM for the d^7 Co(II) complexes **8** – **14** respectively, which are comparable to the spin-only value of 3.87 BM for the high spin Co(II) complexes at 300 K. Similarly, the magnetic moment measurements of 2.82 BM, 3.05 BM and 2.78 BM recorded for d^8 Ni(II) complexes **9** – **15** respectively were consistent with spin only magnetic moments value of 2.83 BM and the expected range of 2.90 BM – 4.20 BM at 300 K for high-spin Ni(II) complexes.[36] The elemental analysis data of the complexes was found to be consistent with two ligand motifs per metal atom as illustrated in **Scheme 4.2**. In addition, the experimental CHN data of the dibromo(pyridine)iminophenol complexes **7**, **10**, **8**, **11**, **9** and **12** was found to balance after the addition of 2 molecules of methanol solvent which was can be considered as solvent of crystallization.

4.3.2. Crystal structures of complexes 13a and 15

The single block-shaped orange and rod-shaped green crystals of complexes **13a** (derivative of complex **13**) and **15** respectively, were obtained by slow evaporation recrystallization method in methanol solvent. **Table 4.1** is a summary of the crystallographic data and structure refinement parameters while **Figures 4.6** and **4.7** represent the molecular structures, packing diagrams, and selected bond lengths and angles for complexes **13a** and **15**, respectively. The molecular structures of complexes **13a** and **15** unambiguously confirmed the presence of isoleptic, *bis*-chelated mononuclear complexes in which the two isoelectronic ligands lie perpendicularly to each other around the metal centre. The oxidation state of Ni in compound **15** was found to be +2 while the molecular structure of **13a** constituted of a Cl^- counter ion

implying that Fe(II) in **13a** was further oxidized to give Fe(III), upon recrystallization. Oxidation of Fe(II) to Fe(III), possibly by the presence of moisture or oxygen is not uncommon and has been reported in literature.[37-39] Nevertheless, we believe the unoxidized structure of complex **13** is as shown in **Scheme 4.2**. This is evidently supported by the mass spectrometry and elemental analysis of the complex and a similar Fe(II) structure have also been reported in Literature. Multiple attempts to use different solvents to grow crystals of **13** suitable for X-ray analysis under inert conditions were not successful.

The crystal structures of the complexes **13a** and **15** exhibited two five and two six-membered chelate rings occupying a meridional position of the octahedral structure.[40] Furthermore, the four coordinating atoms that make up the basal plane were two phenoxo–O atoms and two quinoline-N atoms from the two Schiff bases, while the axial sites were occupied by two imine-N atoms. Based on the observed behaviour of the quinoline ligand **L6**, it is evident that the cobalt complex **14** also adopt the same coordination chemistry as proposed in **Scheme 4.2**. Unfortunately, multiple attempts to grow single crystals suitable for X-ray analyses for complexes, **7**, **9**, **8**, **10**, **12** and **11** ligated by either **L4** or **L5**, failed. Nevertheless, based on the mass spectrometric and CHN elemental results the structures of the complexes should be those proposed in **Scheme 4.2**.

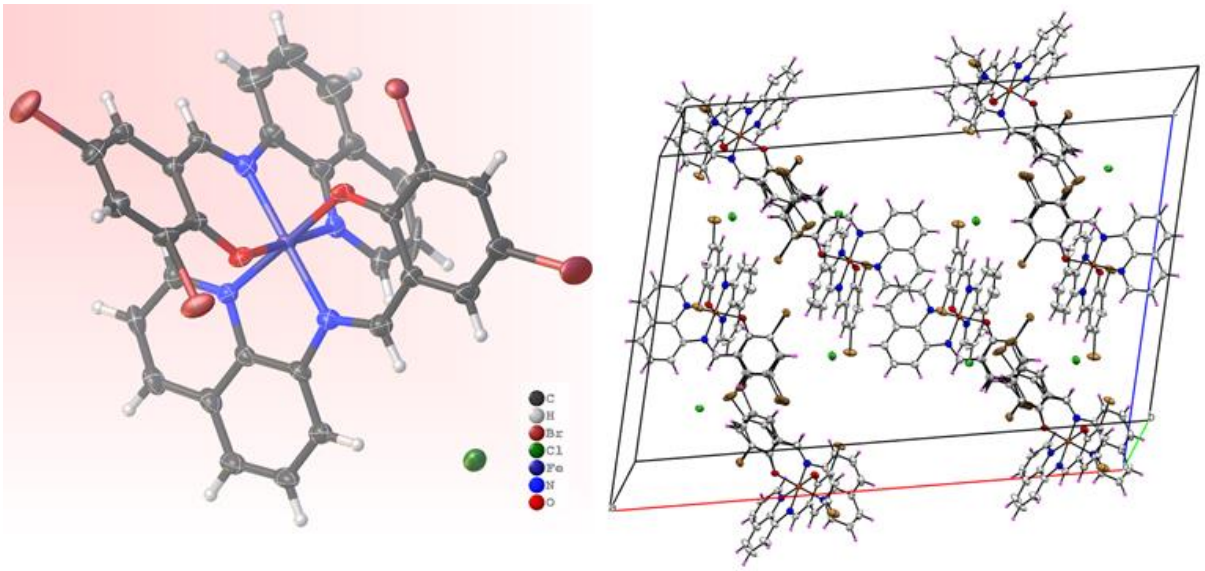

A **B**

Figure 4.6: The ORTEP plot of complex **13a** (A). Ellipsoids are illustrated at 50 % probability. Packing diagram of **13a** the derivative of the Fe(II) complex **13** (B). Selected bond lengths (Å) and angles (˚): Fe(1)-N(5), 1.897(5); Fe(1)-N(4), 1.931(5); Fe(1)-N(3), 1.955(5); Fe(1)-N(1), 1.912(5); Fe(1)-O(2), 1.885(4); Fe(1)-O(3), 1.881(4); O(3)-Fe(1)-N(4), 178.2(2); O(2)-Fe(1)-N(3), 178.6(2); O(2)-Fe(1)-O(3), 88.97(18); O(2)-Fe(1)-N(5), 88.27(18); O(3)-Fe(1)-N(5), 95.64(18); N(3)-Fe(1)-N(5), 91.9(2); N(1)-Fe(1)-N(5), 175.3(2); N(4)-Fe(1)-N(5), 84.6(2).

The average bond distance of Ni–$N_{quinoline}$ (2.0795 Å) in the Ni(II) complex **15** was observed to be longer than the mean Ni–N_{imine} bond distance of 2.0785 Å. Insiti *et al*,[41] reported an Ni-$N_{quinoline}$ bond length of 2.097 Å in their *bis*(4-bromo-2-(((quinolin-8-)imino)methyl)phenolato)-Ni(II) complex, which was found to be 0.0175 Å longer than our mean Ni-$N_{quinoline}$ bond length of 2.0795 Å. In addition, the mean Ni-$N_{quinoline}$ (2.0795 Å) and Ni-N_{imine} (2.0785 Å) bond distances obtained were longer than the mean bond lengths of 2.104 ± 0.027 Å and 2.055 ± 0.060 Å respectively, reported in 47 and 51 similar structures.[42] Statistical relevance of our structure was further confirmed by comparing the obtained average Ni-$O_{phenolic}$ bond length of 2.0635 Å with the mean shorter bond length of 2.024 ± 0.026 Å

calculated from 64 similar structures.[42] It is also noteworthy to mention that the reported Ni-$N_{quinoline}$ (2.0795 Å), Ni-N_{imine} (2.0785 Å) and the Ni-$O_{phenolic}$ (2.0635 Å) mean bond lengths all lie within the reported minimum and maximum bond distances of 2.044 Å – 2.182 Å, 1.977 Å – 2.239 Å and 1.956 Å – 2.092 Å respectively, reported in 47, 51 and 64 similar structures respectively.[43]

On the other hand, the Fe(II) complex, **13a** average Fe–N_{imine} bond distance was calculated to be 1.926 Å which was slightly longer than the observed averaged Fe–$N_{quinoline}$ bond length of 1.9216 Å. In addition, the obtained average Fe-$N_{quinoline}$, Fe-N_{imine} and Fe-$O_{phenolic}$ bond lengths of 1.9216 Å, 1.926 Å and 1.883 Å were all shorter than the mean Fe-$N_{quinoline}$, Fe-N_{imine} and Fe-$O_{phenolic}$ bond lengths of 2.036 ± 0.085 Å, 2.066 ± 0.087 Å and 1.905 ± 0.037 Å respectively, reported in 396, 323 and 453 similar structures respectively.[43] It is noteworthy mentioning that we reported the shortest mean Fe-N_{imine} bond distance since 1.933 Å was reported as the minimum Fe-N_{imine} bond length calculated from 323 similar structures.[43] The average M-$O_{phenolic}$ (M=Fe, Ni, Co) bond distance was shorter than both M-$N_{quinoline}$ and M-N_{imine} mean bond lengths in both **15** and **13a** complexes.

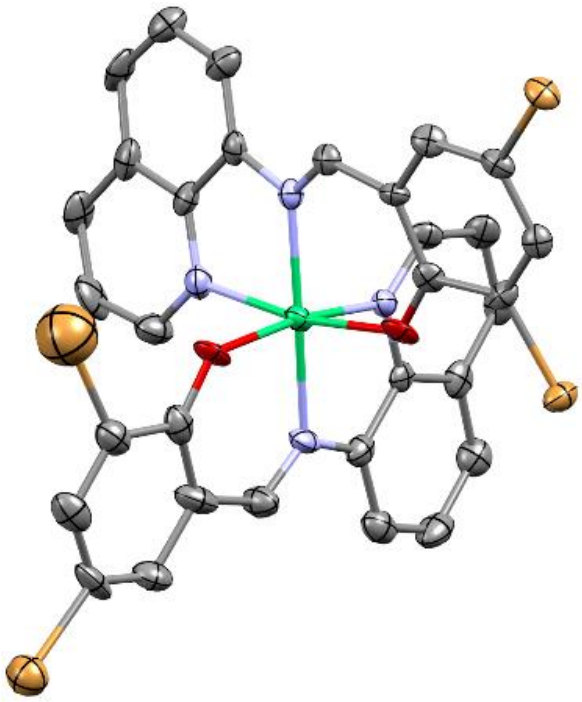

Figure 4.7: ORTEP view of complex **15** with atoms shown as 30% thermal ellipsoids, hydrogen atoms are removed for more clarity. Selected bond lengths (Å) and angles (˚): Ni(1)-O(2), 2.039(7); Ni(1)-N2(2), 2.069(8); Ni(1)-N(1), 2.088(8); Ni(1)-N(3), 2.112(8); Ni(1)-N(4), 2.047(8); Ni(1)-O(1), 2.088(7); O(1)-Ni(1)-N(1), 171.2(3); O(2)-Ni(1)-N(3), 169.7(3); N(4)-Ni(1)-N(2), 174.0(3); N(2)-Ni(1)-O(1), 91.0(3); N(2)-Ni(1)-N(1), 80.2(3); N(4)-Ni(1)-O(1), 92.9(3); N(4)-Ni(1)-N(1), 95.8(3).

The bond angles for O(3)-Fe(1)-N(4), O(2)-Fe(1)-N(3), and N(1)-Fe(1)-N(5) which are 175.3(2)˚, 178.6(2)˚ and 178.2(2)˚ respectively, in complex **13a** and the bond angles for O(1)-Ni(1)-N(1), O(2)-Ni(1)-N(3), and N(4)-Ni(1)-N(2) of 171.2(3)˚, 169.7(3)˚ and 174.0(3)˚ respectively in complex **15** deviate from the expected 180˚ linear geometry by 2-11˚ revealing a distorted octahedral geometry. The bite angle for a perfect octahedral complex is 90°, in the present structures, the five-N^N membered chelate bite angles and N^O the six-membered bite angles differ from an ideal octahedral coordination geometry by ~2° implying a slightly distorted octahedral structures of the complexes. For example, the average N^N five-membered

bite angle in complexes **13a** and **15** was calculated to be 88.25° and 88.0° respectively, while the mean N^O six-membered bite angle was found to be 91.55° in both cases. Therefore, it was evident that the solid state structures of the complexes possess slightly distorted octahedral geometries. In addition, the packing of **15** was observed to be stabilized by edge-to-edge π···π stacking, Br···H, C–H···π and nonconventional C–H···O hydrogen bonding interactions as shown in **Figure 4.8**. In contrast to the **15** complex crystal structure, no hydrogen bonding interactions and structure stabilizations could be quantified for the Fe(III) complex **13a**.

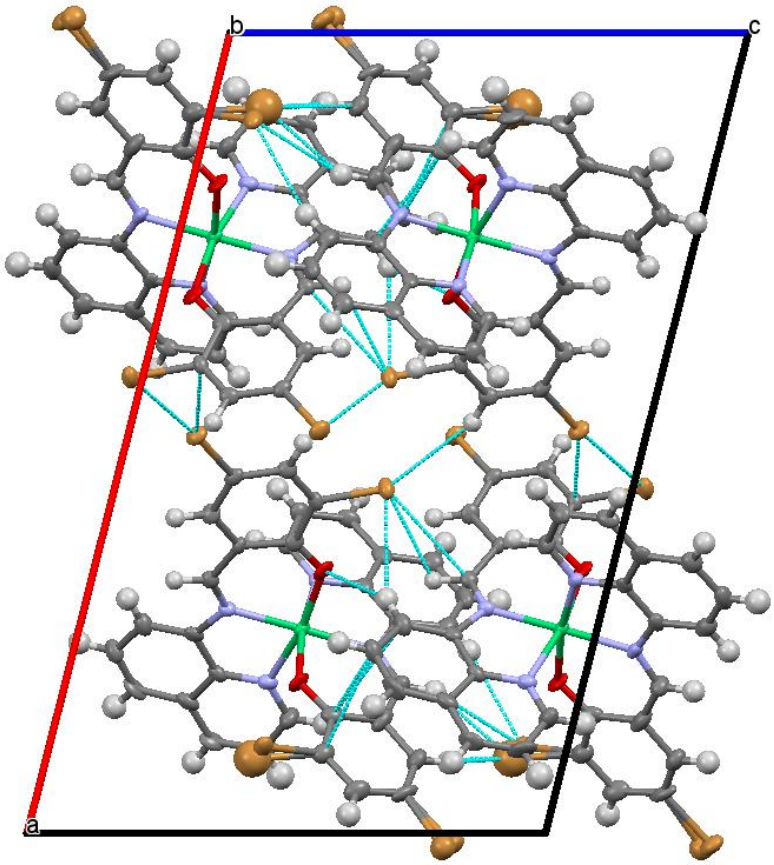

Figure 4.8: Packing diagram of Ni(II) complex **15** showing the stabilization of the complex by edge-to-edge π···π stacking, Br···H, C–H···π and nonconventional C–H···O hydrogen bonding interactions.

Table 4.1: X-ray crystallographic data and structure refinement for the **13a** and **15** complexes.

Compound	**13a**	**15**
Formula	$C_{32}H_{18}Br_4ClFeN_4O_2$	$C_{32}H_{18}Br_4N_4NiO_2$
$D_{calc.}$/ g cm^{-3}	1.630	1.981
μ/mm^{-1}	4.867	6.193
Formula Weight	901.44	868.85
Colour	orange	green
Shape	block	rod
Size/mm^3	0.23×0.15×0.11	0.31×0.22×0.14
T/K	100(2)	100(2)
Crystal System	monoclinic	monoclinic
Space Group	$C2/c$	$P2_1/c$
a/Å	33.700(4)	21.712(4)
b/Å	9.2687(11)	10.1595(17)
c/Å	24.484(3)	13.621(2)
α/°	90	90
β/°	106.157(2)	104.217(8)
γ/°	90	90
V/Å^3	7345.6(16)	2912.5(8)
Z	8	4
Z'	1	1
Wavelength/Å	0.71073	0.71073
Radiation type	MoK_a	MoK_a
Θ_{min}/°	1.258	1.935
Θ_{max}/°	27.495	25.998
Measured Refl.	60212	30407
Independent Refl.	8417	5655
Reflections Used	6346	4594
R_{int}	0.0556	0.0631
Parameters	461	401
Restraints	200	25
Largest Peak	3.076	4.520
Deepest Hole	-1.224	-1.323
GooF	1.069	1.140
wR_2 (all data)	0.1498	0.1792
wR_2	0.1412	0.1728
R_1 (all data)	0.0788	0.0955
R_1	0.0572	0.0787

Having determined the solid state of the complexes **13a** and **15**, UV-vis atomic spectroscopy was further utilized in order to ascertain the coordination geometry of the complexes. The UV spectra of the complexes were characterized by the presence of three bands around 230 nm,

250-300 nm and 350-482 nm assigned to π-π^* and n-π^* electronic transitions of the chromophores present in the ligands. The band around 400 nm was not observed for the Fe(II) complexes **7** and **10**. The band around 400 nm was a clear indication of the complexes formation (**Figure 4.9**). Upon complexation with the imine ligands, there is an appearance of the intense band between 440-500 nm regions of the spectrum. This band has been assigned to d-p* electron transfer.[44]

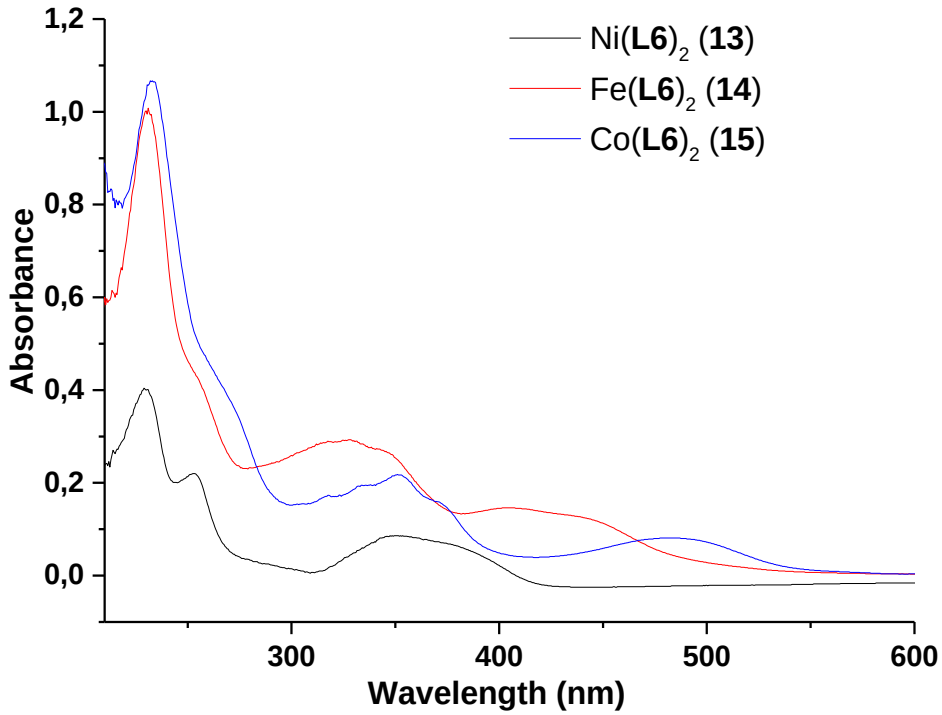

Figure 4.9: Comparisons of the UV-Vis spectra of the Fe(II), Ni(II) and Co(II) complexes of ligand **L6** in order to confirm the coordination of the Ni(II), Fe(II) and Co(II) complexes, **13-15** respectively.

4.3.3. Ethylene oligomerization reactions catalyzed by the Fe(II), Co(II) and Ni(II) complexes 10 - 15

Having gained the insight on the coordination chemistry of our complexes, we then shifted our focus to the examination of the complexes as catalyst precursors in ethylene oligomerization reactions. The complexes were investigated using MMAO-12 and $EtAlCl_2$ as activators in toluene and chlorobenzene respectively. Activation with MMAO-12 in toluene solvent resulted in inactive species for ethylene oligomerization reactions (**Table 4.2**, entry 10).[45-46] On the other hand, activation of the complexes with $EtAlCl_2$ co-catalyst in toluene medium selectively produced large amounts of alkylated products (**Table 4.2**, entries 11-13).[47] Thus the complexes were activated with $EtAlCl_2$ co-catalyst in chlorobenzene medium to avoid the formation of Friedel-Crafts alkylated products. In chlorobenzene solvent, the complexes displayed high catalytic activities to the tune of 1 608 $kg_{oligomers}$ $mol^{-1}(M)$ h^{-1}, producing mainly ethylene dimers and trimers as was confirmed by both GC and GC-MS (**Figures 4.10**). The obtained catalytic information of the complexes is summarized in **Table 4.2**.

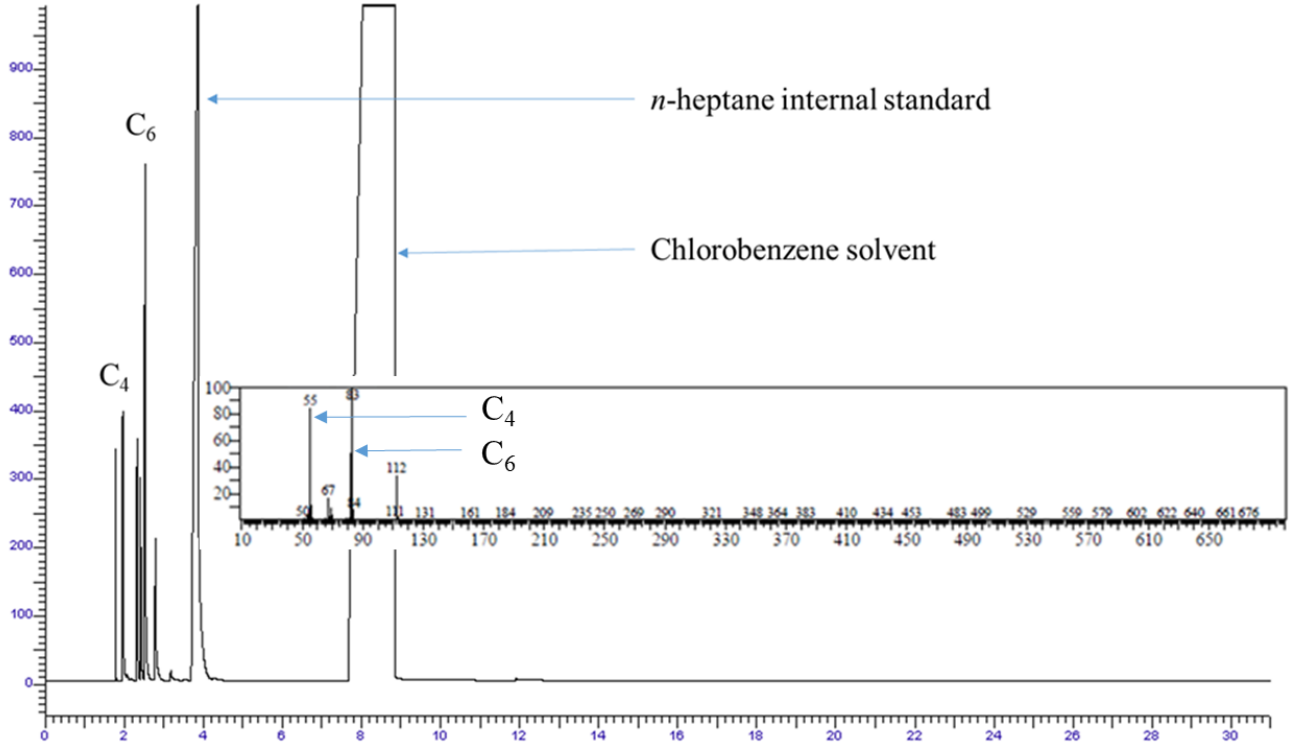

Figure 4.10: The GC-FID and GC-MS (inserted) chromatograms showing the product distribution and molar masses of the quantifiable oligomers when the Fe(II) complex **7** is activated by $EtAlCl_2$ co-catalyst and used to catalyze the oligomerization of ethylene monomer in chlorobenzene solvent (**Table 4.2**, entry 1).

Table 4.2: Ethylene oligomerization data catalyzed by Ni(II), Co(II) and Fe(II) complexes.[a]

Entry	Catalyst	Yield[b] (g)	Activity[c]	Product Distribution (%)[d]	
				C_4 (α-C_4)	C_6 (α-C_6)
1	**7**	9.18	918	39 (92)	61 (14)
2	**8**	10.36	1036	48 (95)	52 (18)
3	**9**	16.08	1608	60 (95)	40 (17)
4	**10**	8.65	865	41 (90)	59 (7)
5	**11**	9.14	915	53 (98)	47 (26)
6	**12**	12.82	1282	54 (96)	46 (10)
7	**13**	6.84	684	65 (93)	35 (19)
8	**14**	8.82	882	62 (93)	38 (15)
9	**15**	9.95	995	61 (88)	39 (15)
10[e]	**9**	0	0	nd	nd
11[f]	**9**	12.86	1286	32 (>99)	<1
12[f]	**12**	10.48	1048	37 (76)	<1
13[f]	**15**	7.21	721	5 (96)	<1

[a]Reaction conditions: complex, 10 μmol; solvent, chlorobenzene/toluene, 30 mL; temperature, 30 ˚C; time, 1 h; pressure, 10 bar; $EtAlCl_2$: Al/M=250; [b]Determined using GC and *n*-heptane served as an internal standard. [c]Catalytic activity in $kg_{oligomers}$ mol^{-1}(M) h^{-1}. [d]Determined by GC and GC-MS (%). [e]Using MMAO-12 co-catalyst. nd denotes not detected. [f]In toluene solvent, balance of products were alkylated toluene products.

4.3.3.1. The effect of complex structure on the catalytic performance in ethylene oligomerization reaction

The catalysts structural properties encompassing of metal identity, ligand architecture and its substituents inclusively, are known to be the principal factors associated with the observed catalytic behaviours of the catalysts. Evidently, the identity of the metal centre played a

significant role in controlling the catalytic activity of the complexes of which the Ni(II) complexes were superior than their Fe(II) and Co(II) analogues. For example, the highest catalytic activity of 1 608 $kg_{oligomers}$ mol^{-1}(M) h^{-1} was obtained for the Ni(II) complex **9**, while its analogous Fe(II) and Co(II) complexes, **7** and **8** respectively, afforded catalytic activities of 918 $kg_{oligomers}$ mol^{-1}(M) h^{-1} and 1 036 $kg_{oligomers}$ mol^{-1}(M) h^{-1} respectively. The superiority of Ni(II) metal over Co(II) and Fe(II) metal centre is well documented in literature and is associated with the high electro-positivity usually displayed by Ni(II) metal centre compared to Fe(II) and Co(II) metals.[22, 48] We have also recently reported the uncommon tendency of Co(II) metal centre in forming more catalytically active complexes than the Fe(II) metal centre in ethylene oligomerization.[49]

The ligand steric and electronic properties also played a crucial role in controlling the catalytic activity of the complexes. For example, comparisons of the aldimine dibromopyridine imine complexes (**7**, **8** and **9**) with their ketimine counterparts (**10**, **11** and **12**), revealed that introduction of the methyl substituent in the pyridine ring reduced the catalytic activities of the complexes. For example, **7** displayed activity of 918 $kg_{oligomers}$ mol^{-1}(M) h^{-1} whilst its analogous complex **10** showed lower catalytic activities of 865 $kg_{oligomers}$ mol^{-1}(M) h^{-1} (**Table 4.2**, entries 1*vs* 4 respectively). This trend may be attributed to the electronic factors of the complexes, where the unsubstituted complex **7** results in a more electropositive metal centre than the methyl substituted counterpart **10**.[50] The same results were evident with other complexes.

Furthermore, the catalytic activities of the complexes was compromised when the pyridine ring in complexes **7**, **8** and **9** was substituted by the quinoline group in complexes **13**, **14** and **15** respectively. For example, complex **13** displayed a lower catalytic activity of 684 $kg_{oligomers}$ mol^{-1}(M) h^{-1} compared to the catalytic activity of complex **7** of 918 $kg_{oligomers}$ mol^{-1}(M) h^{-1}, its

counterpart. This may be linked to the differing degree of π-back-bonding abilities of the pyridine ligand (**L4**) in comparison to the quinoline ligand (**L6**). The pyridine ring in the architecture of complex **7** and complexes **8** and **9** inclusive, is known to increase the dissociation of the labile donor group during substrate coordination due to its electron withdrawing effect from the metal centre *via* π-back-bonding.[51] Consequently, the π-back-bonding increases the net positive charge of the metal centre thereby promoting nucleophilic attack of the monomer and stabilizes the resulting intermediate transition state. In contradiction, the lower catalytic activity observed for the quinoline based complexes is due to the poor π-accepting ability of the quinoline ligand **L6**.[52]

The product distribution of the Fe(II), Ni(II) and Co(II) complexes was also driven by the structural variations of the complexes. Generally, Ni(II) complexes favoured more formation of C_4 than the their Co(II) and Fe(II) counterparts. For example, the proportion of C_4 oligomer produced by the **9** was 60 %, on the other hand, for its Co(II) and Fe(II) analogues i.e. complexes **8** and **7** respectively we obtained 48 % and 39 % respectively (**Table 4.2**, entries 1-3). In addition, the selectivity of complexes was also influenced by the ligand moieties. The more sterically hindered quinoline based complexes **13**, **14** and **15**, favoured the formation of the C_4 short chain oligomers than their pyridine counterparts **7**, **8** and **9** (**Table 4.2**, entries 1-3 *vs* 7-9). The complexes displayed no definitive extent of isomerism of the preformed C_4 oligomers. On the other hand, greater isomerism of the C_6 oligomer was observed.

Scheme 4.3 should be used in explaining the observed isomerism of the C_4 and C_6 oligomers formed from ethylene oligomerization reactions catalyzed by dibromosalicylideneimine-complexes. For example, complex **15** displayed a greater isomerism of the C_4 oligomer (88 % α-C_4) while complex **10** favoured more isomerism of C_6 oligomer since 7 % of α-C_6 was

obtained (**Table 4.2**, entries 9 and 4 respectively). This is because oligomerization involving higher number of carbon atoms in α-olefins like in the case of C_4 and C_6 a different enchainment becomes competitive.[53] Notably, the majority of the monomer insertions in our case occurred in a manner that favoured the formation of internal C_4 or C_6 oligomers from complex **5** which arose from chain walking mechanism of complex **5** to give intermediate **6**. Terminal oligomers produced from the chain termination of intermediate **4** *via* β-hydride elimination in **Scheme 4.3** were supressed. **Scheme 4.3** further illustrates that complex **3** can also undergo the successive monomer insertion during propagation or chain growth to form complex **7** giving rise to terminal and internal C_6, C_8, C_{10} and C_{n+} oligomers.[54] Nevertheless, the absence of C_{8+} oligomers implies that after the formation of C_6 oligomer, chain isomerism and termination was more favoured than chain propagation to form long chain C_{8+} oligomers.

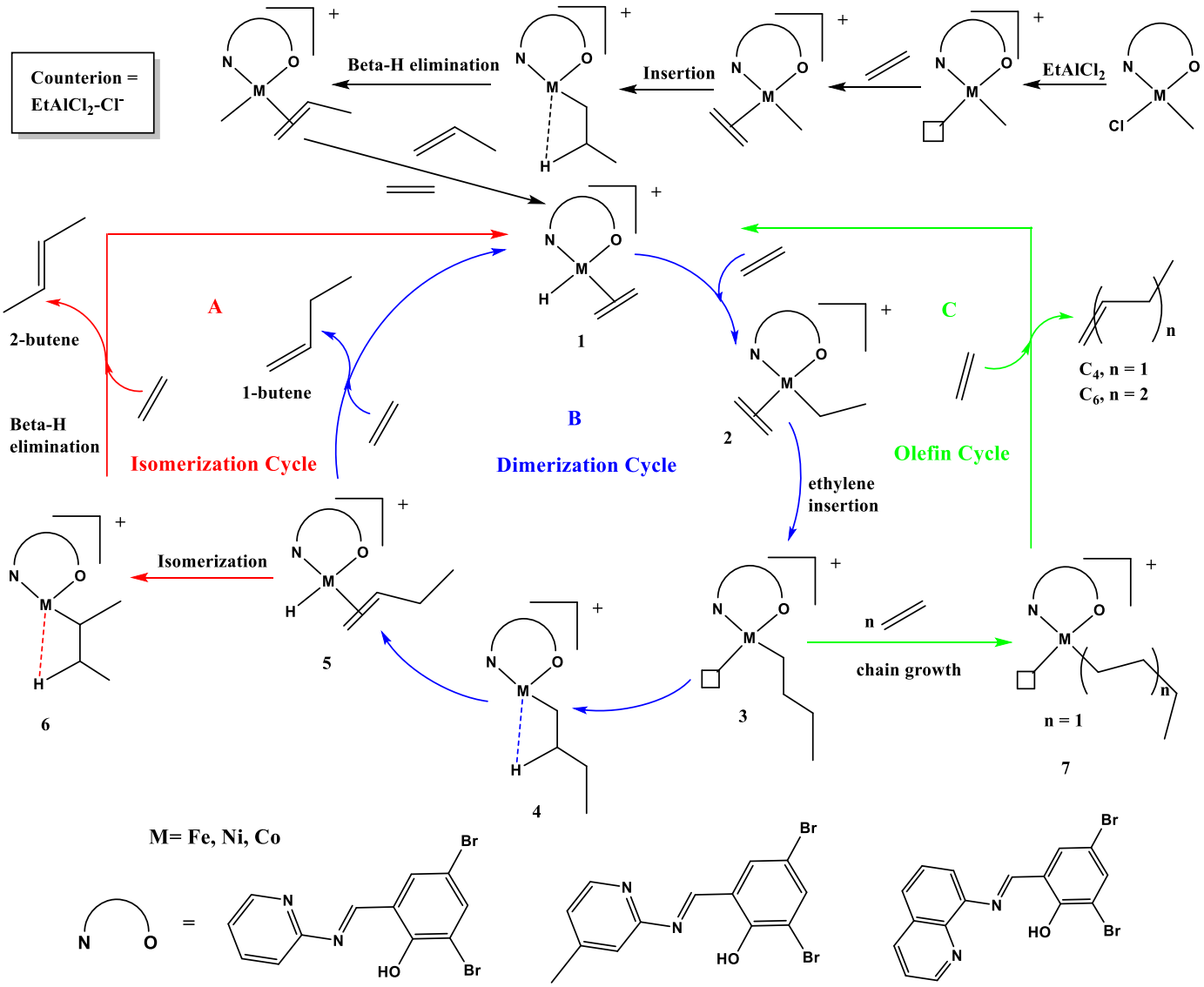

Scheme 4.3: The proposed mechanism for the formation of 1-butene, *cis* and *trans* isomers of 2-butene and the favoured production of internal hexene oligomers by the Fe(II), Co(II) and Ni(II) complexes.

4.3.3.2. Optimization of catalytic parameters using 9/EtAlCl₂ system

To achieve the optimal conditions for the oligomerization of ethylene reaction, we used the most active **9**/$EtAlCl_2$ system at varied Al/Ni ratio, time, pressure and temperature conditions. The catalytic performance of the complexes was greatly affected by the variation of the reaction conditions as summarized in **Table 4.3**. Firstly, the Al/Ni molar ratio was varied from 100 -

300 (**Table 4.3**, entries 1-5) at 30 ˚C for 1 h. An optimum Al/Ni ratio of 250 corresponding to catalytic activity of 1 608 $kg_{oligomers}$ mol^{-1}(M) h^{-1} was realized (**Table 4.3**, entry 4). The lower catalytic activities of 418 $kg_{oligomers}$ mol^{-1}(M) h^{-1} observed at Al/Ni molar ratio of 300 (**Table 4.3**, entry 5), could be assigned to accumulation alkylaluminium impurities, resulting in possible catalyst deactivation.[48] In general, higher Al/Ni molar ratios favoured the formation of more C_4 oligomers than C_6 oligomers. For example, increasing the Al/Ni molar ratio from 100 to 250, was accompanied by an increase in the selectivity of C_4 oligomer from 40 % to 60 % (**Table 4.3**, entries 1 and 4 respectively). This could be explained by favoured chain transfer due to an increased number of active sites.[49]

Table 4.3: Optimization of the reaction conditions in ethylene oligomerization reactions using **9**/$EtAlCl_2$ system.

Entry	Al/M	Time (h)	Pressure	Yield (g)[b]	Activity[c]	Product Distribution (%)[d]	
						C_4 (α-C_4)	C_6 (α-C_6)
1	**100**	1	10	2.23	223	40 (98)	60 (19)
2	**150**	1	10	4.59	459	46 (95)	54 (18)
3	**200**	1	10	8.66	866	54 (92)	46 (15)
4	**250**	1	10	16.08	1608	60 (95)	40 (17)
5	**300**	1	10	4.18	418	35 (97)	65 (13)
6	**250**	0.5	10	6.09	1218	75 (98)	25 (31)
7	**250**	2	10	18.50	925	52 (88)	48 (13)
8	**250**	1	5	15.50	1550	55 (92)	45 (17)
9	**250**	1	20	10.25	1025	46 (92)	54 (20)
10[e]	**250**	1	10	9.96	996	49 (79)	51 (11)
11[f]	**250**	1	10	6.60	660	52 (64)	48 (9)

[a]Reaction conditions: complex, 10 µmol; solvent, chlorobenzene, 30 mL; temperature, 30 ˚C; time, 1 h; pressure, 10 bar; Co-catalyst, $EtAlCl_2$; [b]Determined using GC and n-heptane served as an internal standard. [c]Catalytic activity in $kg_{oligomers}$ mol^{-1}(M) h^{-1}) [d]Determined by GC and GC-MS (%). [e]T=50 ˚C, [f]T=70 ˚C.

The catalyst stability also being the central aspect in the catalyst design was probed by varying reaction time from 0.5 h to 2 h (**Table 4.3**, entries 4, 6 and 7). It was observable that increasing the reaction time from 0.5 h to 1 h could result in an increase in the catalytic activity of the catalyst **9** from 1 218 $kg_{oligomers}$ mol^{-1}(M) h^{-1} to 1 608 $kg_{oligomers}$ mol^{-1}(M) h^{-1} respectively (**Table 4.3**, entries 6 *vs* 2). However, a further increase to 2 h resulted lower catalytic activity to 925 $kg_{oligomers}$ mol^{-1}(M) h^{-1}, indicating possible catalyst decomposition with time (**Table 4.3**, entry 7).[55] Thus reaction time of 1 h was recorded as the optimal time. The variation of reaction time also affected the selectivity of the catalyst **9**. For example, increasing reaction time form 0.5 h to 2 h, resulted in a decline of the C_4 oligomer distribution from 75% to 52% respectively (**Table 4.3**, entries 6 and 7). This phenomenon could be apportioned to pre-formed C_4 oligomers re-insertion and recombination with the ethylene monomer to give more of C_6 oligomers.[56] Furthermore, prolonged reaction periods occasioned enhanced isomerism as evident from the higher compositions of the internal olefin fractions (**Table 4.3**, entries 6 and 7).

The thermal stability of the complexes was also examined by varying the reaction temperatures from 30 ˚C to 70 ˚C (**Table 4.3**, entries 4, 10-11). A closer examination at the temperature variation results revealed that higher temperature had negative effect on the catalytic activity of the complexes. For example, a dramatic loss of catalytic activity from 1 608 $kg_{oligomers}$ mol^{-1}(M) h^{-1} to 996 $kg_{oligomers}$ mol^{-1}(M) h^{-1} was obtained when the temperature was increased from

30 ˚C to 50 ˚C (**Table 4.3**, entries 4 and 10 respectively). Similar observations have been made by Yu *et al.*,[57] using highly active *N*-(5,6,7-trihydroquinolin-8-ylidene)arylamino Ni(II) catalysts. This behaviour could be ascribed to fast thermal deactivation of the active species, pointing to lower thermal stability of the catalysts.[58] It is also noteworthy to mention that increasing the reaction temperature from 30 ˚C to 50 ˚C, resulted in a drastic drop in the composition of C_4 oligomer fractions from 60 % to 49 % respectively. **Figure 4.11** shows the product distribution obtained at 50 ˚C for complex **9**. Furthermore, it was also observable that temperature favours isomerism of the preformed oligomers due to facilitated re-insertion of the chain with opposite regiochemistry as shown in **Scheme 4.3**.[59]

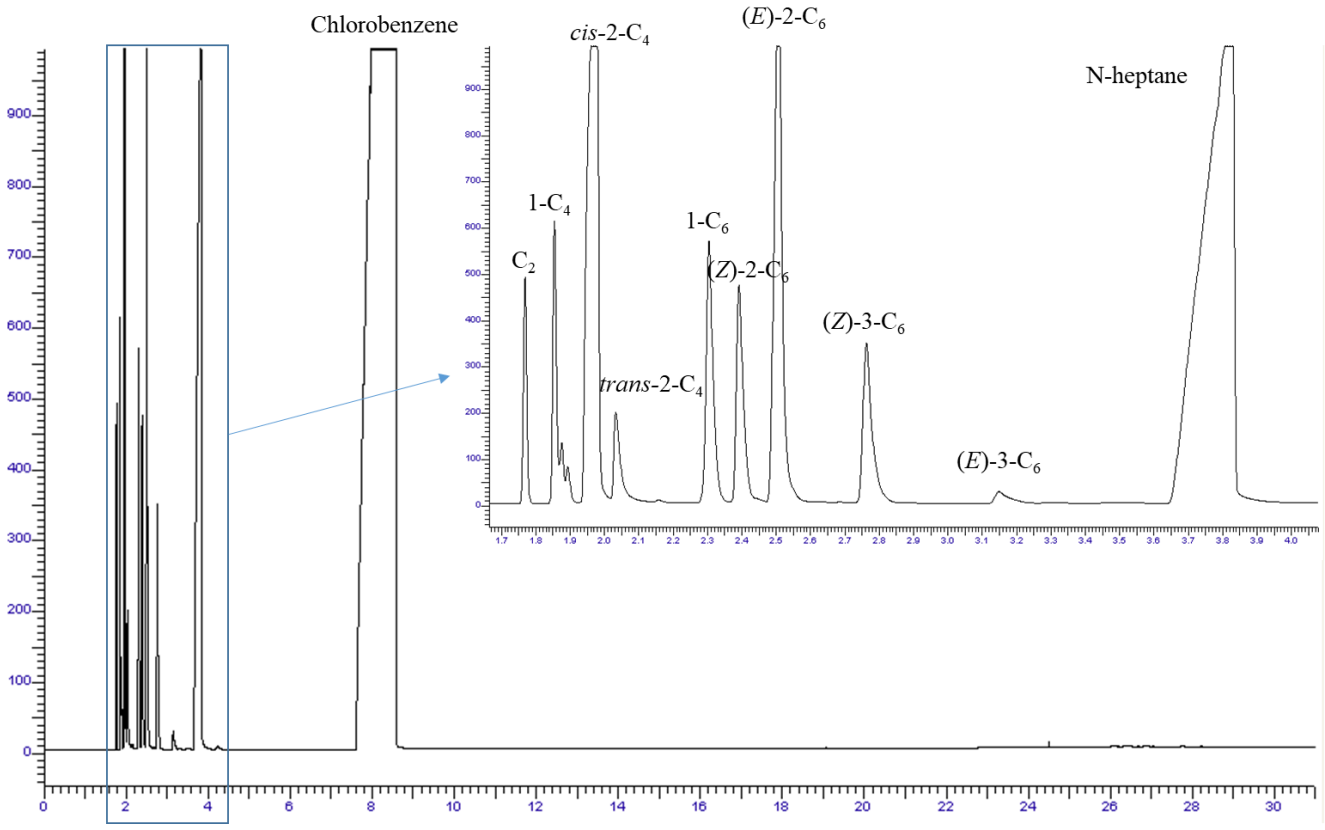

Figure 4.11: The GC-FID tarce of **9**/$EtAlCl_2$ system showing the product distribution obtained when the reaction temperature was increased from 30 to 50 ˚C. (**Table 4.3**, entry 10; T= 50 ˚C).

The effect of ethylene concentration on the catalytic performance of the catalyst **9** was probed by varying ethylene pressure from 5 bar to 20 bar (**Table 4.3**, entries 4, 8 and 9). As expected, increasing ethylene pressure from 5 bar to 10 bar was accompanied by an increase in the catalytic activities from 1 550 $kg_{oligomers}$ mol^{-1}(M) h^{-1} to 1 608 $kg_{oligomers}$ mol^{-1}(M) h^{-1} (**Table 4.3**, entries 4 and 8). In contrast, further elevation of ethylene pressure to 20 bar (**Table 4.3**, entry 9) was marked by a drastic decline in the catalytic activity of **9**/$EtAlCl_2$ system to 1 025 $kg_{oligomers}$ mol^{-1}(M) h^{-1}. This could be explained by mass transport limitations that impedes the diffusion of the ethylene monomer to the catalytically active metal centres.[60-62] The product distribution was also marginally affected by variation in ethylene pressure. A slight increase in the selectivity of the C_4 fraction from 55 % to 60 % was recorded at ethylene pressure of 5 bar and 10 bar respectively (**Table 4.3**, entries 8 and 4 respectively). This could be explained by rapid chain transfer at elevated ethylene pressure, consistent with higher catalytic activities witnessed at 10 bar.[24]

4.3.4. Density functional theory (DFT) studies for the reaction parameter of the complexes 9-15 and 7-13.

In attempts to gain more insight and understanding of the effects of the complex structure on the catalytic performance of these complexes in ethylene oligomerization reactions, Density Functional Theory (DFT) computational studies were performed. The ground state electronic structures of the Ni(II) complexes **9**-**15** and the Fe(II) complexes (**7**-**13**) were employed and to probe the effect of the metal centre (**Table 4.4**). The computational calculations were performed using the split basis set LAN2DZ (Las Alamos International 2 Double ζ) for Ni(II) and Fe(II) complexes, and 6311 G(dp) for the remaining atoms.[30, 63-64] The energy gaps were analysed to study their influence on the catalytic activities of the respective complexes (**Table 4.4**). The energy gaps (Δε), of the pre-catalysts were calculated as the energy difference

between pre-catalyst's LUMO (E_{LUMO}) and HOMO (E_{HOMO}) and are summarized in **Table 4.4**. The optimized geometry structures of the complexes (**Table 4.5**) also depict that the HOMO electron density is mainly located on the Ni(II) and Fe(II) metal centres, imine bond and dibromopyridine moiety. Notably, the LUMO electron densities of the complexes, **9** and **12** are predominately localized around the metal centre and other neighbouring atoms. On the other hand, the LUMO electron density of the quinoline based complex, **15** and Fe(II) complexes **7-13** is mainly localized around the ligand moieties and not on the metal centre showing the effect of the ligand moiety on the charge distribution of the complexes.

Table 4.4: Theoretical and experimental data for complexes to probe ligand effect on catalytic activity.

Parameter	**9**	**12**	**15**	**7**	**10**	**13**
NBO charge	0.881	0.778	0.777	0.767	0.767	0.336
$\boldsymbol{E_{HOMO}}$**/eV**	-6.1482	-5.4562	-5.5166	-5.2002	-5.7930	-4.8916
$\boldsymbol{E_{LUMO}}$**/eV**	-3.412	-3.2510	-2.2613	-2.6263	-2.5448	-2.6580
[a]**Energy gap** $\boldsymbol{\Delta E}$**/eV=**$\boldsymbol{E_{LUMO}-E_{HOMO}}$	2.7362	2.2052	3.2553	2.5739	3.2482	2.2336
Electrophilicity index/ω	0.6840	0.5513	0.8138	0.6434	0.8120	0.5584
[b]**Activity/kg mol^{-1} h^{-1}**	1 608	1282	995	918	865	684

[a]E_{LUMO} and E_{HOMO} are the LUMO and HOMO orbital energy values of the metal complexes and ethylene molecule, respectively. [b]Reaction conditions: complex, 10 µmol; solvent, chlorobenzene (30 mL), temperature, 30 ˚C; time, 1 h; pressure, 10 bar; $EtAlCl_2$, Al/M = 250.

From **Table 4.4**, it is clear that the NBO charges, which denotes the individual atomic charge, was the principal driving force on the observed catalytic activities of the complexes. For example, catalyst **9** of NBO charge of 0.881 showed higher catalytic activity of 1 608 $kg_{oligomers}$ $mol^{-1}(M)$ h^{-1}, than the analogous catalyst **15** with a charge of 0.777, displaying catalytic activity of 995 $kg_{oligomers}$ $mol^{-1}(M)$ h^{-1}. Thus in general, the higher the net positive charge on the central atom, the higher the catalytic activity of the complex due to the facilitated rate of ethylene monomer coordination to the central metal atom during initiation step. Notably, the **9** catalysts (NBO = 0.881) showed higher catalytic activities than its corresponding Fe counterparts **7** (NBO = 0.767) revealing the effect of the metal centre on overall complex electron distribution. In addition, the pyridine ring in the framework of complex **9**, being a better π-acceptor than the quinoline ring in complex **15**, resulted in more electropositive Ni(II) metal centre than complex **15** (**Figure 4.12**).[51-52] Interestingly, Fe(II) complexes **7** and **10** having the same NBO charge had catalytic activities of 918 $kg_{oligomers}$ $mol^{-1}(M)$ h^{-1} and 865 $kg_{oligomers}$ $mol^{-1}(M)$ h^{-1} respectively.

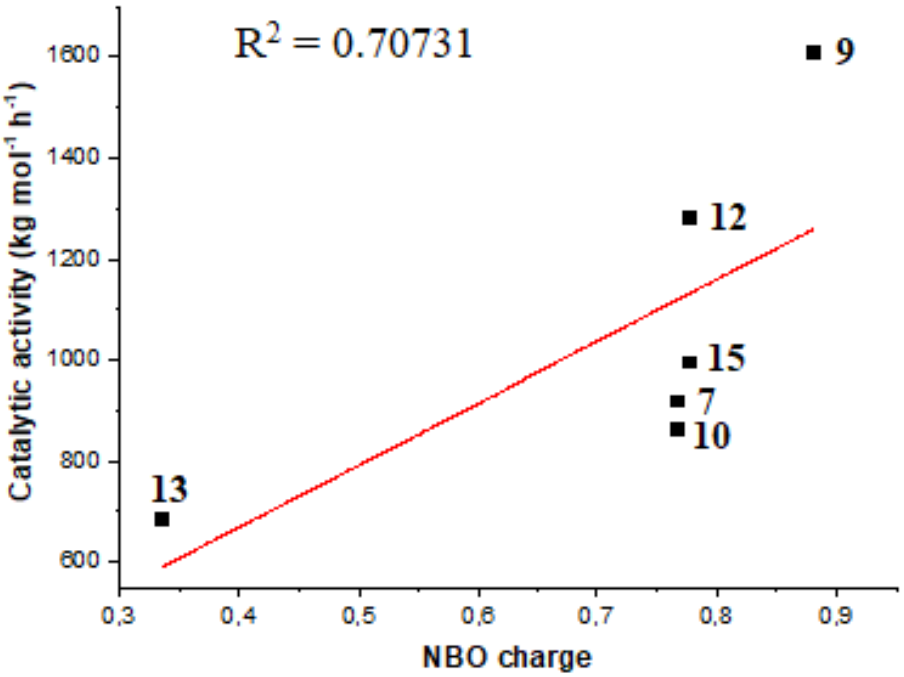

Figure 4.12: The plot of catalytic activity in $kg_{oligomers}$ mol^{-1}(M) h^{-1} versus the NBO charge illustrating the dependence of the catalytic activity of the complexes on the NBO charge of the central metal atoms.

Table 4.5: The optimized DFT HOMO, LUMO frontier molecular orbitals of the dibromopyridine and quinoline complexes.

Complex	HOMO map	LUMO map
9	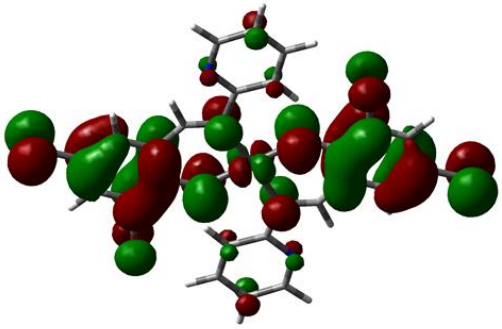	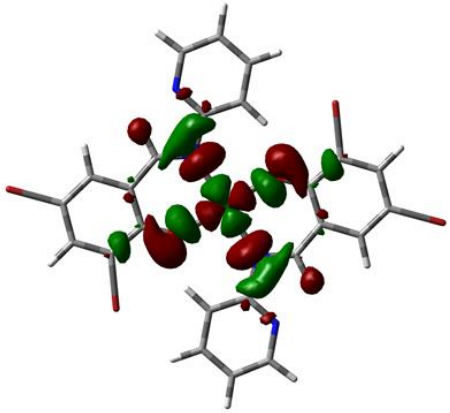
12	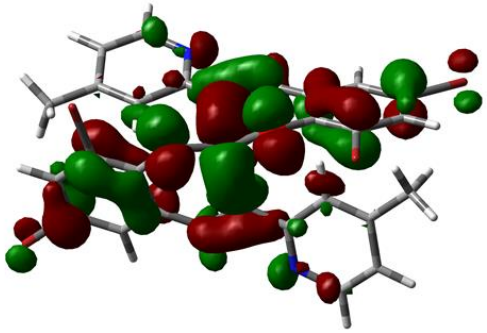	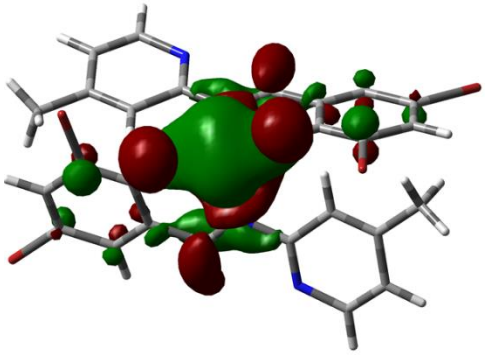
15	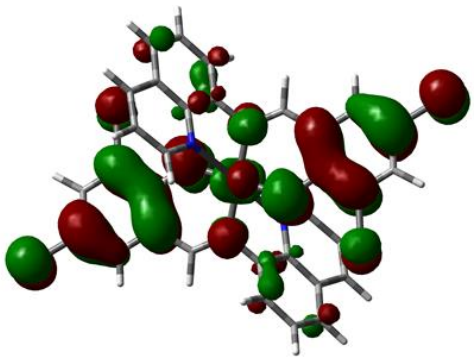	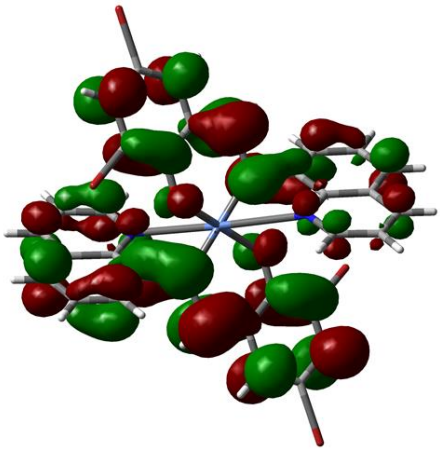

7

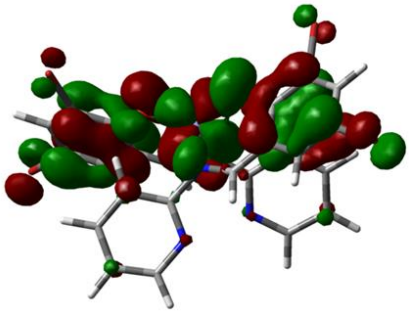

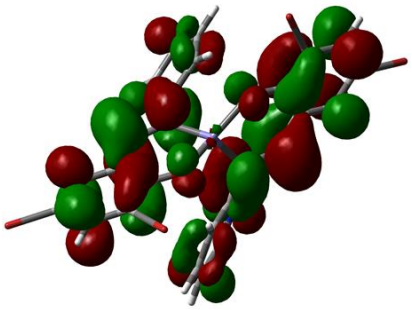

10

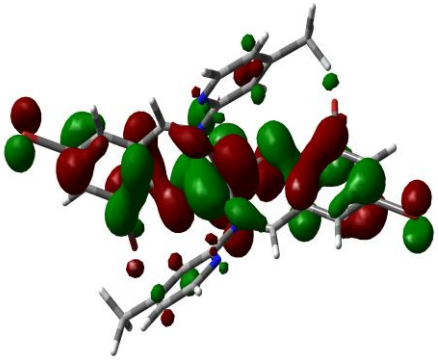

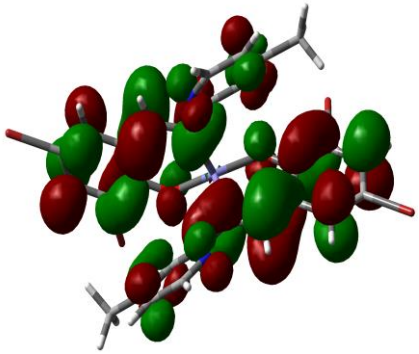

13

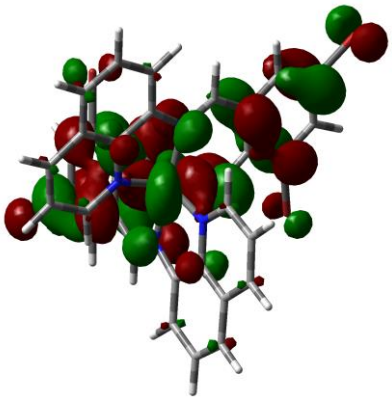

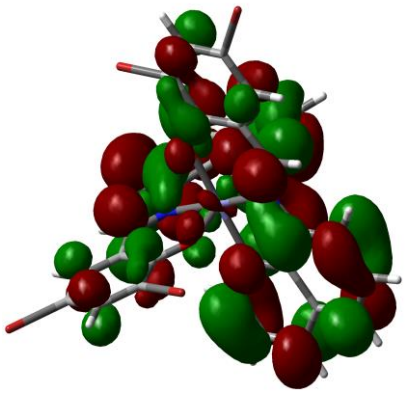

4.4. Conclusions

The Fe(II), Co(II) and Ni(II) complexes based on 2,4-dibromo-6-(((4-methylpyridin-2-yl)imino)methyl)phenol (N^O donor) and 2,4-dibromo-6-((quinolin-8-ylimino)methyl)phenol (N^N^O donor) ligands were successfully synthesized and characterized using IR spectroscopy, mass spectrometry, magnetic moment measurements, elemental analysis and X-ray crystallography. The solid state of complex **13a**, the derivative of **13** and **15** confirmed the isoleptic *bis*-chelated nature and the distorted octahedral arrangement of the mononuclear complexes. Activated with $EtAlCl_2$ co-catalyst led to the formation of moderate catalytically active catalysts to give mainly C_4 and C_6 oligomers. The catalytic activities and product distribution of the catalyst were significantly influenced by the complex structure. The reactions conditions such as Al/M molar ratio, time, pressure and temperature were also found to be the driving forces of the observed catalytic activity and selectivity of the complexes. From theoretical calculations, the NBO charge played a principal role in controlling the catalytic activities of the complexes.

4.5. References

1. Damavandi, S., Samadieh, N., Ahmadjo, S., Etemadinia, Z., Zohuri, G. H., *J. Eur. Polym.* **2015**, *64*, 118-125.

2. Ehlert, A. P. R., Carvalho, E. M., Thiele, D., Favero, C., Vicente, I., Bernardo-Gusmao, K., Stieler, R., de Souza, R. F., de Souza, M. O., *Catalysis Today* **2017**, *296*, 272-276.

3. Ghisolfi, A., Fliedel, C., Rosa, V., Manakhov, K. Y., Braunstein, P., *Organometallics* **2014**, *33*, 2523-2534.

4. Sun, W.-H., Jie, S., Zhang, W., Song, Y., Ma, H., Chen, J., *Organometallics* **2006**, *25*, 666-677.

5. Hang, W., Weidong, Y., Tao, J., Binbin, L., Wenqing, X., Jianjiang, M., Youliang, H., *J. Chin. Sci. Bull.* **2002**, *47*, 616.

6. Bryliakov, K. P., Antonov, A. A. , *J. Organomet. Chem.* **2018**, *867*, 55-61.

7. Xiao, L., Gao, R., Zhang, M., Li, Y., Cao, X.,Sun, W.-H., *Organometallics* **2009**, *28*, 2225-2233.

8. Kumar, K., Godeto, T., Darkwa, J., *J. Organomet. Chem* **2016**, *818*, 137-144.

9. Wang, S., Zhang, W., Du, S., Asuha, S., Flisak, Z., Sun, W.-H., *J. Organomet. Chem.* **2015**, *798*, 408-413.

10. Sun, Z., Huang, F., Qu, M., Yue, E., Oleynik, I. V., Oleynik, I. I., Zeng, Y., Liang, T., Li, K, Zhang, W., Sun, W.-H., *Rsc. Adv.* **2015**, *5*, 77913-77921.

11. Ojwach, S. O., Guzei, I. A., Benade, L. L., Mapolie, S. F., Darkwa, J., *Organometallics* **2009**, *28*, 2127-2133.

12. Adams, G. M., Weller, A. S., *Coord. Chem. Rev.* **2018**, *355*, 150-172.

13. Benito, J. M., de Jesus, E., de La Mata, F. J., Flores, J. C., Gomez, R., Gomez-Sal, P., *Organometallics* **2006**, *25*, 3876-3887.

14. Bianchini, C., Giambastiani, G., Rios, I. G., Mantovani, G., Meli, A., Segarra, M. A., *Coord. Chem. Rev.* **2006**, *250*, 1391-1418.

15. Zada, M., Guo, L., Zhang, R., Zhang, W., Ma, Y., Solan, G. A., Sun, Y., Sun, W.-H., *Appl. Organometal. Chem.* **2019**, *2019;e4749*, https://doi.org/10.1002/aoc.4749.

16. Gao, R., Sun, W-H., Redshaw, C., *Catal. Sci. Technol.* **2013**, *3*, 1172-1179.

17. Boulens, P., Pellier, E., Jeanneau, E., Reek, J. N. H., Olivier-Bourbigou, H., Breuil, P.-A. R., *Organometallics* **2015**, *34*, 1139-1142.

18. de Souza, M. O., Rodrigues, L. R., Gauvin, R. M., de Souza, F. R., Pastore, H. O., Gengembre, L., Ruiz, J. A. C., Gallo, J. M. R., Milanes, T. S., Milani, M. A., *Catal. Commun.* **2010**, *11*, 597-600.

19. Tavman, A., Boz, I., Seher Birteksoz, A., *Spectrochim. Acta. Part A* **2010**, *77*, 199-206.

20. Britovsek, G. J. P., Keim, W., Mecking, S., Sainz, D., Wagner, T., *J. Am. Chem. Soc.* **1993**, *23*, 1632-1634.

21. Britovsek, G. J. P., Mastrolanni, S., Solan, G. A., Bough, S. P. D., Redshaw, C., Gibson, V. C., White, A. J. P., Williams, D. J., Elsegood, M. R. J, *J. Chem. Eur.* **2000**, *6*, 2221-2231.

22. Ainooson, M. K., Ojwach, S. O., Guzei, I. A., Spencer, L. C., Darkwa, J., *J. Organomet. Chem.* **2011**, *696*, 1528-1535.

23. Trofymchuk, O. S., Gutsulyak, D. V., Quintero, C., Parvez, M., Daniliuc, C. G., Piers, W. E., Rojas, R. S., *Organometallics* **2013**, *32*, 7323-7333.

24. Ngcobo, M., Ojwach, S. O., *J. Organomet. Chem.* **2017**, *846*, 33-39.

25. Ngcobo, M.; Ojwach, S., *Inorg. Chim. Acta.* **2017**, *467*, 1-5.

26. Dolomanov, O. V., Bourhis, L. J., Gildea, R. J., Howard, J. A. K., Puschmann, H., *J. Appl. Cryst.* **2009**, *42*, 339-341.

27. Sheldrick, G. M., *Acta. Cryst.* **2008**, *A64*, 339-341.

28. Sheldrick, G. M., *Acta Cryst.* **2015**, *C12*, 3-8.

29. Rome, K., Mclntyre, A., *Chromatography Today.* **2012**, *52*, 52-55.

30. Frisch, M. J. T., Trucks, G. W., Schlegel, H. B., Scuseria, G. E., Robb, M. A., Cheeseman, J. R., Scalmani, G., Barone, V., Mennucci, B., Petersson, G. A., Nakatsuji, H., Caricato, M., Li, X., Hratchian, H. P., Izmaylov, A. F., Bloino, J., Zheng, G., Sonnenberg, J. L., Hada, M., Ehara, M., Toyota, K., Fukuda, R., Hasegawa, J., Ishida, M., Nakajima, T., Honda, Y., Kitao, O., Nakai, H., Vreven, T., Montgomery, J. A., Peralta, Jr., J. E., Ogliaro, F., Bearpark, M., Heyd, J. J., Brothers, E., Kudin, K. N., Staroverov, V. N., Kobayashi, R., Normand, J., Raghavachari, K., Rendell, A., Burant, J. C., Iyengar, S. S., Tomasi, J., Cossi, M., Rega, N., Millam, J. M., Klene, M., Knox, J. E., Cross, J. B., Bakken, V., Adamo, C., Jaramillo, J., Gomperts, R., Stratmann, R. E., Yazyev, O., Austin, A. J., Cammi, R., Pomelli, C., Ochterski, J. W., Martin, R. L., Morokuma, K., Zakrzewski, V. G., Voth, G. A., Salvador, P., Dannenberg, J. J., Dapprich, S., Daniels, A. D., Farkas, O., Foresman, J. B., Ortiz, J. V., Cioslowski, J., Fox, D. J., *GAUSSIAN 09 (Revision A.1), Gaussian, Inc., Wallingford, CT,* ***2009.***

31. Li, J., Xu, L.-C., Chen, J.-C., Zheng, K.-C., Ji, L.-N., *J. Phys. Chem. C.* **2006**, *110*, 8174-8180.

32. Cossi, M., Scalmani, G., Rega, N., Barone, V., *J. Chem. Phys.* **2002**, *117*, 43-54.

33. Parr, R. G., Szentpály, L. V., Liu, S., *J. Am. Chem. Soc.* **1999**, *121*, 1922-1924.

34. Frisc, M.; Trucks, G.; Schlegel, H.; Scuseria, G.; Robb, M.; Cheeseman, J.; Scalmani, G.; Barone, V.; Mennucci, B.; Petersson, G., Gaussian 09 (Revision C. 01). *Gaussian Inc, Wallingford* **2010**.

35. Nyamato, G. S., Alam, M. G., Ojwach, S. O., Akerman, M. P., *J. Organomet. Chem.* **2015**, *783*, 64-72.

36. Cotton, F. A., Wilkinson, G., Murillo, C. A., Bochmann, M., Advanced Inorganic Chemistry 6th Ed. John Wiley and Sons: New York, **1999**; p 835.

37. Chaggar, R. K., Fawcett, J., Solan, G. A., *Acta Cryst.* **2003**, ***E59***, 462-463.

38. Guo, L., Jing, X., Xiong, S., Liu, W., Liu, Y., Liu, Z., Chen, C., *Polymers* **2016**, *8*, 389-401.

39. Nienkemper, K., Kotov, V. V., Kehr, G., Erker, G., Fröhlich., R., *Eur. J. Inorg. Chem.* **2006**, *DOI: 10.1002/ejic.200500645*, 366-379.

40. Ghorai, P., Chakraborty, A., Panja, A., Mondal, T. K., Saha, A., *Rsc. Adv.* **2016**, *6*, 36020-36030.

41. Insiti, P., Jitthiang, P., Harding, P., Chainok, K., Chotima, R., Sirirak, J., Blackwood, S., Alkas, A., Telfer, S. G., Harding, D. J., *Polyhedron* **2016**, *114*, 242.

42. Bruno, I. J., Cole, J. C., Edgington, P. R., Kessler, M., Macrae, C. F., McCabe, P., Pearson, J., Taylor, R., *Acta Cryst. Sec. B: Strcuct. Sci.* **2002**, *58*, 389-397.

43. Bruno, I. J., Cole, J. C., Edgington, P. R., Kessler, M., Macrae, C. F., McCabe, P., Pearson, J., Taylor, R., Cooper, I. R., Harris, S. E., Orpen, A. G., *J. Chem. Inf. Comput. Sci.* **2004**, *44*, 2133-2144.

44. Amirnasr, M., Schenk, K. J., Gorji, A., Vafazadeh, R. , *Polyhedron* **2001**, *20*, 695-702.

45. Karam, A. R., Catari, E. L., Lopez-Linares, F., Agrifoglio, F., Agrifoglio, G., Albano, C. L., Diaz-Barrios, A., Lehmann, T. E., Pekerar, S. V., Albornoz, L. A., Atencio, R., Gonzalez, T., Ortega, H. B., Joskowics, P., *Appl. Catal. A: Gen* **2005**, *280*, 165-173.

46. Nelana, S. M., Kumar, K., Guzei, A. L., Mahamo, T., Darkwa, J.,, *J. Organomet. Chem.* **2017**, *323*, 45-54.

47. Wang, J., Hou, S., Wang, L., Hou, H., Zhang, N., Shi, W. , *J. Macromol. Sci. A.* **2019**, *https://doi.org/10.1080/10601325.2019.1670068*.

48. Nyamato, G. S., Ojwach, S. O., Akerman, M. P., *J. Mol. Catal. A: Chem.* **2014**, *394*, 274-282.

49. Ngcobo, M., Nyamato, G. S., Ojwach, S. O., *Mol. Catal.* **2019**, *478*, 110590.

50. Yu, J., Hu, X., Zeng, Y., Zhang, L., Ni, C., Hao, X., Sun, W-H., *New. J. Chem.* **2011**, *35*, 178-183.

51. Kinunda, G. A., *Tanz. J. Sci.* **2018**, *44*, 45-63.

52. Ongoma, P. O., Jaganyi, D., *Dalton Trans.* **2012**, *44*, 10724-10730.

53. Yakhvarov, D. G., Tazeev, D. I., Sinyashin, O. G., Giambastian, G., Bianchini, C., Segarra, A. M., Lonnecke, P., Hey-Hawkins, E., *Polyhedron* **2006**, *25*, 1607-1612.

54. Pierro, I., Zanchin, G., Parisini, E., Marti-Rujas, J., Canetti, M., Ricci, G., Bertini, F., Leone, G., *Macromelecules* **2018**, *51*, 801-814.

55. Gansukh, B., Zhang, Q., Flisak, Z., Liang, T., Ma, Y., Sun, W.-H., *Appl. Organometal. Chem.* **2020**, *e5471*, https://doi.org/10.1002/aoc.5471.

56. Nyamato, G. S., Ojwach, S. O., Akerman, M. P., *Organometallics* **2015**, *34*, 5647-5657.

57. Yu, J., Zeng, Y., Huang, W. Hao, X., Sun, W.-H., *Dalton Trans.* **2011**, *40*, 8436-8443.

58. Jones, D. J., Gibson, V. C., Green, S. M., Maddox, P. J., White, A. J. P., Williams, D. J. J., *Am. Chem. Soc.* **2005**, *127*, 11037-11046.

59. Zhang, Q., Zhang, R., Ma, Y., Solan, G. A., Liang, T., Sun, W.-H., *Appl. Catal. A: Gen.* **2019**, *573*, 73-86.

60. Helldorfer, M., Alt, H. G., *J. Appl. Polym. Sci.* **2003**, *89*, 1356-1361.

61. Li, C., Wang, F., Lin, Z., Zhang, N., Wang, J. , *J. Appl. Organomet. Chem.* **2017**, *e3756*, 1-8.

62. Longo, P., Oliva, L., Grassi, A., Pellecchia, C., *Makromol. Chem.* **1989**, *190*, 2357-2361.

63. Beck, A. D., *Chem. Phys.* **1993**, *98*, 5648.

64. Lee, C. T., Yang, W. T., Parr, R. . *Phys. Rev. B: Condens. Matter.* **1998**, *37*, 785-789.

65. Nyamato, G. S., Ojwach, S. O., Akerman, M. P., *Dalton Trans.* **2016**, *45*, 3407-3416.

CHAPTER FIVE

Ethylene oligomerization reactions catalyzed by recyclable Fe(II), Ni(II) and Co(II) complexes immobilized on Fe_3O_4 magnetic nanoparticles

5.1. Introduction

Transition metal homogeneous catalysts play a significant role in the production of commercially valuable oligomeric and polymeric products from ethylene oligomerization reactions.[1-2] Over the past decades, appreciable interest has been dedicated to the design of effective homogeneous catalysts for ethylene oligomerization, with emphasis on manipulation of the ligand motif.[3-5] Despite this success of homogeneous catalysts, they have a major drawback with respect to catalyst separation and recycling.[6] Heterogeneous catalysts, on the other hand, enjoy the benefits of better catalyst recycling, but they too so far from lack of catalyst selectivity.[7-8] As a result, numerous attempts have been made to "heterogenize" the homogeneous catalysts, in order to produce hybrid catalyst systems, which are both selective and recyclable.[9-11]

Examples of compounds that have been used to immobilize the homogeneous catalysts include mesoporous silica,[12] metal organic frameworks (MOFs),[13] porous organic polymers (POPs),[14] and ion exchange zeolites.[15] Depending on the type of the support material, hybrid catalysts systems have been realised with different outcomes with respect to stability, reusability, catalytic activity and selectivity. Magnetic nanoparticles (MNPs) have also attracted significant attention in the development of supported catalyst systems for various applications due to their ease of separation, high surface area and excellent thermal stability.[16-17] Keypour *et al.*[18] and Rezaei with co-workers[19] have independently reported the use of Fe_3O_4 anchored catalysts in the Heck coupling reactions.

Despite the unlimited applications of Fe_3O_4 MNPs in various areas, their use in ethylene oligomerization catalysis is still yet to be fully appreciated. Motivated by their attractive properties and as a slowly emerging field, herein we report the immobilization of Phenol((triethoxysilyl)propylimino)ethyl and Phenol((triethoxysilyl)propylimino)methyl N^O donor ligands on Fe_3O_4 magnetic nanoparticles, their late transition metal complexes and their characterization. Their applications as catalysts in the oligomerization reactions of ethylene is also provided in detail. The effects of complex properties and reaction conditions on the catalytic performance of the complexes are described. In line with the main objective of this work, the findings of the recyclability of the immobilized catalysts were also investigated and discussed.

5.2. Experimental section

5.2.1. General experimental details and instrumentation

All synthetic manipulations were performed using standard Schlenk-line techniques under nitrogen atmosphere. The solvents were obtained from Merck and dried or distilled using appropriate methods. Prior to use, ethanol was dried over calcium oxide whilst toluene solvent was treated under sodium/benzophenone reagent and shakenly stored is 4A molecular sieves. Similarly, acetonitrile was dried under calcium hydride and stored in 4A molecular sieves. The chemicals; $FeCl_3$ (98%), $FeCl_2$ (98%), $CoCl_2$ (98%) and $NiCl_2$ (98%) salicylaldehyde (98%), 2'-hydroxyacetophenone (98%), (3-aminopropyl)triethoxysilane (≥98%), modified methylaluminoxane solution (MMAO-12, 7 % w/w in toluene) and ethylaluminum dichloride solution (1.0 M in hexanes), were obtained from Sigma Aldrich and used as received. ^1H NMR and ^{13}C NMR (100 MHz) spectra were recorded on a 400 MHz Bruker Ultra shield NMR spectrometer in $CDCl_3$ and DMSO-d_6 solvents. The infrared spectra were recorded on a Perkin-

Elmer, Spectrometer 100. LC Premier micro-mass Spectrometer model LCMS-2020, was used for mass spectral analyses. Thermogravimetric data was collected on a Perkin-Elmer TGA 4000 instrument equipped with Pyris software at 50-900˚C with 20 ˚C/min. The ZEISS EVO L 15 scanning electron microscope (conventional SEM, low vacuum, ESEM and EDX) operating at 20 kV accelerating voltage was used to carry out microscopic analyses while energy dispersive X-ray (EDX) analyses were carried out using an Oxford make EDX detector. JEOL 1400 transmission electron microscope (brightfield, darkfield, diffraction, EDX) operating at an accelerating voltage of 200 kV was used to perform transmission electron microscopic data analyses. Inductively coupled plasma optical emission spectroscopy (ICP-OES) was performed using Varian 720-ES equipped with ICP Expert II software. Varian CP-3800 gas chromatograph equipped with a flame ionization detector (FID) and a CP-Sil 5 CB (30 m x 0.2 mm x 0.25 µm) capillary column was used for GC analyses (GC conditions: starting temperature 40 ˚C for 5 min, the heating rate of 10 ˚C/min up to 250 ˚C) while GC-MS analyses were performed on a Shimadzu GCMS-QP2010SE.

5.2.2. Preparation of Fe_3O_4 MNPs immobilized ligands and complexes

5.2.2.1. Preparation of Schiff base ligands

5.2.2.1.1. Phenol((triethoxysilyl)propylimino)ethyl ***(L7H)***

A typical synthetic procedure for ligand is as follows: Equimolar amounts of (3-aminopropyl)triethoxysilane (APTES; 2.21 g, 10.0 mmol) and 2'hydroxyacetophenone (1.36 g, 10.0 mmol) were dissolved in ethanol (30 mL) and the resultant yellow solution was refluxed for 24 h.[20] After the reaction period was over, the solvent ethanol was removed by rotary evaporation under reduced pressure. Yield 2.89 g, 85 %. ^{1}H NMR (400 MHz, $CDCl_3$): $\delta_{H/ppm}$:0.79(t, 2H, CH_2, J_{HH}=8Hz), 1.26(t, 9H, CH_3CH_2O, J_{HH}=8Hz), 1.92(p/m, 2H, CH_2, J_{HH}=8Hz), 2.38(s, 3H, $NCCH_3$), 3.60(t, 2H, N-CH_2, J_{HH}=8Hz), 3.85(q, 6H, CH_3CH_2O, J_{HH}=8Hz), 5.33(s,

1H, OH), 6.76(t, 1H, aromatic, J_{HH}=8Hz), 6.94(d, 1H, aromatic, J_{HH}=8Hz), 7.22(t, 1H, aromatic), 7.56(d, 1H, aromatic, J_{HH}=8Hz). $^{13}C\{^{1}H\}$ NMR ($CDCl_3$): $\delta_{/ppm}$: 8.19, 14.17, 18.31, 23.59, 51.44, 58.45, 116.48, 127.94, 130.71, 132.58, 136.46, 162.45, 165.30. FT-IR (cm^{-1}): $\nu_{(O-H)}$: 3240, 2974, 2927, 2885; $\nu_{(C=N)}$:1615; $\nu_{(Si-O)}$: 1072. TOF MS ESI: m/z (%): 362.0655 ($[M+Na]^+$, 100 %). Anal. Calcd. for $C_{17}H_{29}NO_4Si$: C 60.14, H 8.61, N 4.13. Found (%): C 60.96, H 8.15, N 4.96.

*5.2.2.1.2. Phenol((triethoxysilyl)propylimino)methyl) (**L8H**)*

The Schiff base organosilane pre-ligand **L8H** was synthesized following the same procedure described for pre-ligand **L7**. APTES (2.21g, 10 mmol) and salicylaldehyde (1.23 g, 10 mmol). Yield 3.30 g, 96 %. ^{1}H NMR (400 MHz, $CDCl_3$): $\delta_{H/ppm}$:0.71(t, 2H, CH_2, J_{HH}=8Hz), 1.26(t, 9H, CH_3CH_2O, J_{HH}=8Hz), 1.86(t, 2H, CH_2, J_{HH}=8Hz), 3.64(t, 2H, N-CH_2, J_{HH}=8Hz) 3.87(q, 6H, CH_3CH_2O, J_{HH}=8Hz), 6.89(t, 1H, aromatic, J_{HH}=8Hz), 6.98(d, 1H, aromatic, J_{HH}=8Hz), 7.26(d, 2H, aromatic, J_{HH}=8Hz), 8.34(s, 1H, N-CH). FT-IR (cm^{-1}): $\nu_{(O-H)}$: 3555, 2974, 2927, 2885, $\nu_{(C=N)}$: 1632, $\nu_{(Si-O)}$: 1072. $^{13}C\{^{1}H\}$ NMR ($CDCl_3$): $\delta_{/ppm}$: 8.53, 18.32, 24.39, 58.31, 62.02, 117.04, 118.90, 131.11, 132.05, 161.44, 164.78. TOF MS ESI: m/z (%): 348.1398 ($[M+Na]^+$, 100 %). Anal. Calcd. for $C_{16}H_{27}NO_4Si$: C 59.04, H 8.36, N 4.30. Found (%): C 58.98, H 8.23, N 4.19.

5.2.2.2. Preparation of iron magnetic nanoparticles, Fe_3O_4 (MNPs)

Fe_3O_4 magnetic nanoparticles were synthesized by employing the conventional method.[18] $FeCl_3$ (4.748 g, 0.029 mol) and $FeCl_2$ (1.840 g, 0.0145 mol) were first dissolved in deionized water (100 mL) at 85 ˚C under nitrogen atmosphere and with vigorous mechanical stirring forming a black solution. An aqueous solution of ammonia (12 mL, 25 %) was added quickly forming a deep red solution with bubbles, continuing with stirring more of aqueous ammonia

was added forming a black precipitate of magnetic nanoparticles. The solution was stirred for further 30 min. The reaction mixture was finally cooled to room temperature and using a magnet, the precipitates were collected and washed several times with deionized water (3 x 20 mL), ethanol (2 x 20 mL) and copious amounts of acetone and then dried under vacuum prior to their characterization.

5.2.2.3. Immobilization of Schiff base ligands on Fe_3O_4 magnetic nanoparticles

The immobilization of silanol Schiff base ligands **L7H** and **L8H** on Fe_3O_4 MNP surface was achieved through a usage of the grafting method. A carefully dried sample of Fe_3O_4 MNPs powder (approximately 1.00 g) was suspended in 50 mL dried toluene in a 100 mL round-bottomed flask previously flashed with nitrogen. The silanol ligands **L7H** (2.80 g) and **L8H** (3.23 g) were then added to the reaction suspension with stirring forming a dark solution which was refluxed for 24 h under nitrogen atmosphere. After reaction time was over, the reaction mixture was cooled to room temperature, filtered and brown filtrates of **L7H@Fe_3O_4** (**L7**) and **L8H@Fe_3O_4** (**L8**) were washed with ethanol (3 x 15 mL) and then dried under vacuum for 18 h.

*5.2.2.3.1. Synthesis of **L7H@Fe_3O_4 (L7)***

Fe_3O_4 MNPs (1.02 g) and **L7H** (2.80 g). Yield 1.066 g. FT-IR (cm^{-1}): $\nu_{(O-H)}$: 3345, 2889, 2022, $\nu_{(C=N)}$: 1606, 1496, $\nu_{(Si-O-Fe)}$: 1112, $\nu_{(Fe-O)}$: 772.

*5.2.2.3.2. Synthesis of **L8H@Fe_3O_4 (L8)***

Fe_3O_4 MNPs (1.01 g) and **L8H** (3.23 g). Yield 1.083 g. FT-IR (cm^{-1}): $\nu_{(O-H)}$: 3779, 2926, 2186, $\nu_{(C=N)}$: 1614, $\nu_{(Si-O-Fe)}$: 1121, 1027, $\nu_{(Fe-O)}$: 757.

5.2.2.4. Synthesis of the immobilized complexes

*5.2.2.4.1. Synthesis of [Ni(**L7**)$_2$Cl$_2$**@Fe$_3$O$_4$**] (**16**)*

In a 10:1 ratio, supported complex **16** was prepared by dispersing **L7** (0.31 g) in acetonitrile (15 mL) utilizing ultrasonic bath for 30 min. This was followed by the addition of an acetonitrile solution (15 mL) of $NiCl_2$ precursor (0.03 g). The complex was then separated by magnetic decantation and washed repeatedly with acetonitrile, water and acetone for the removal of the unattached substrates. Yield: 0.29 g (94 %). FT-IR (cm^{-1}): $\nu_{(C=N)}$: 1605; $\nu_{(Si-O)}$: 1220, $\nu_{(Fe-O)}$: 1027. Ms = 62.06 emu g^{-1}.

The complexes **17**, **18**, **19**, **20**, and **21** were prepared following the same synthetic procedure described for **16**.

*5.2.2.4.2. Synthesis of [Co(**L7**)$_2$Cl$_2$**@Fe$_3$O$_4$**] (**17**)*

L7 (0.31 g) and $CoCl_2$ (0.03 g). Yield: 0.27 g (87 %). FT-IR (cm^{-1}): $\nu_{(C=N)}$: 1601; $\nu_{(Si-O)}$: 1117, $\nu_{(Fe-O)}$: 1032. Ms = 54.46 emu g^{-1}.

*5.2.2.4.3. Synthesis of [Fe(**L7**)$_2$Cl$_2$**@Fe$_3$O$_4$**] (**18**)*

L7 (0.30 g) and $FeCl_2$ (0.03 g). Yield: 0.26 g (85 %). FT-IR (cm^{-1}): $\nu_{(C=N)}$: 1605; $\nu_{(Si-O)}$: 1114, $\nu_{(Fe-O)}$: 1028. Ms = 52.11 emu g^{-1}.

*5.2.2.4.4. Synthesis of [Ni(**L8**)$_2$Cl$_2$**@Fe$_3$O$_4$**] (**19**)*

L8 (0.31 g) and $NiCl_2$ (0.03 g). Yield: 0.26 g (86 %). FT-IR (cm^{-1}): $\nu_{(C=N)}$: 1613; $\nu_{(Si-O)}$: 1123, $\nu_{(Fe-O)}$: 1032. Ms = 67.96 emu g^{-1}.

*5.2.2.4.5. Synthesis of [Co(**L8**)$_2$Cl$_2$**@Fe$_3$O$_4$**] (**20**)*

L8 (0.31 g) and $CoCl_2$ (0.03 g). Yield: 0.22 g (71 %). FT-IR (cm^{-1}): $\nu_{(C=N)}$: 1614; $\nu_{(Si-O)}$: 1118, $\nu_{(Fe-O)}$: 1036. Ms = 66.90 emu g^{-1}.

*5.2.2.4.6. Synthesis of [Fe(**L8**)$_2$Cl$_2$**@Fe$_3$O$_4$**] (**21**)*

L8 (0.31 g) and $FeCl_2$ (0.03 g). Yield: 0.27 g (88 %). FT-IR (cm^{-1}): $\nu_{(C=N)}$: 1612; $\nu_{(Si-O)}$: 1114, $\nu_{(Fe-O)}$: 1028. Ms = 67.11 emu g^{-1}.

5.2.3. General procedure for ethylene oligomerization reactions

The ethylene oligomerization reactions catalysed by the immobilized complexes were performed on stainless steel reactor (100 mL volume) fitted with a magnetic stirrer bar. A pre-weighed amount of the immobilized pre-catalyst (10 µmol) was transferred into a dry Schlenk tube under nitrogen atmosphere and *n*-heptane solvent (10 mL) was added using a syringe. The amount of the complex used was calculated based on the metal contents determined using ICP-OES, that is, **16** (0.00040 g), **17** (0.0016 g), **18** (0.00120 g), **19** (0.00086 g), **20** (0.00060 g) and **21** (0.00090 g). Appropriate amount of a co-catalyst ethylaluminum dichloride ($EtAlCl_2$, 2 mmol) was then injected into the Schlenk tube containing the pre-catalyst. The solution mixture in the Schlenk tube was then transferred through the cannula into the reactor and heated to 30 °C while stirring on a hot plate. Prior to the reaction commencement, the reactor was flashed several times with ethylene gas and ethylene pressure was set at 10 bar and the reaction was timed for 1 h. After the reaction period, the reactor was cooled to approximately -10 °C using liquid nitrogen and excess ethylene gas vented off. The reaction was then quenched by the addition of 10 % hydrochloric acid (2 mL) and a portion was sampled in a GC-vial for GC-FID and GC-MS analyses to determine the identity and distribution of the products. The mass of the product formed was determined using the calibration curve of the R-factors for the

standards versus number of carbons of the standards (Equations 1 and 2).[21] Hexene (0.849), octene (0.744), decene (0.496), dodecene (0.389) and tetra-decene (0.327) standards were used to obtain calibration curve and tetradecene was used as an internal standard during analysis. The R-factor for butene was extrapolated as 0.981 from the calibration curve. The catalytic activity (g oligomer/mol. metal. h) was determined using the percentage metal content in the immobilized complexes as determined from ICP-OES analyses.

5.2.4. Catalytic recycling experiments

The recycling experiments were performed in a similar manner described for ethylene oligomerization reactions. In recycling the spent catalyst, an external magnet was used to attract and hold the catalyst intact while removing the products for analyses. The recovered pre-catalyst was washed with ethanol (3 x 10 mL) and weighed prior to the subsequent experiment. The subsequent recycling experiment was accomplished by adding 30 mL of fresh *n*-heptane and the appropriate amount of $EtAlCl_2$ co-catalyst (2 mL, Al:M ratio of 200).

5.3. Results and discussion

5.3.1 Syntheses and characterization of Fe_3O_4 magnetically supported metal complexes

The syntheses of the N^O donor Schiff base pre-ligands, iron magnetic nanoparticles, immobilized ligands and their respective Ni(II), Co(II) and Fe(II) complexes is summarized by **Scheme 5.1**. The Schiff base organosilane pre-ligands **L7H** and **L8H** were first synthesized through the reaction of equimolar amounts of either 2'hydroxyacetophenone or salicylaldehyde and (3-aminopropyl)triethoxysilane (APTES) respectively in ethanol (30 mL) and refluxing for 24 h. [22-23] Light yellow oils of the compounds were obtained in very high yields of 85 % and

96 % respectively after removing the solvent and characterized using NMR and IR spectroscopies and mass spectrometry. The Fe_3O_4 magnetic nanoparticles were prepared *via* a co-precipitation method and were obtained as black powder in good yields.[18] The pre-ligands **L7H** and **L8H** were immobilized on the Fe_3O_4 MNPs surfaces to achieve the immobilized ligands **L7** and **L8** respectively (**Scheme 5.1**). Reactions of the anchored ligands **L7** or **L8** with the appropriate metal halides in acetonitrile afforded the corresponding immobilized complexes **16**, **17**, **18**, **19**, **20** and **21** in good to high yields with respect to the amount of the ligand used (71 % - 94 %) as shown in **Scheme 5.1**. Complexes of **L7** were isolated as black solids while those of **L8** were obtained as light brown powders.

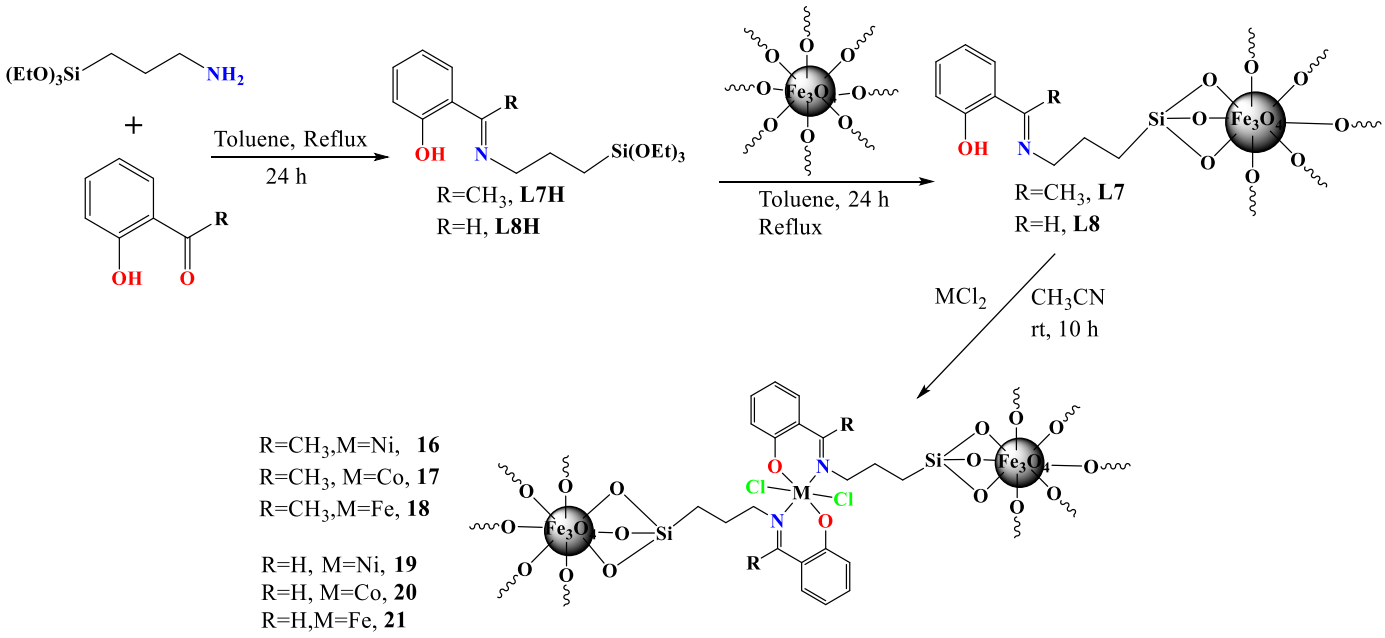

Scheme 5.1. Synthetic protocol of N^O donor Ni(II), Co(II) and Fe(II) complexes immobilized on Fe_3O_4 magnetic nanoparticles for ethylene oligomerization reactions.

Structural elucidation of the Schiff base ligands **L7H** and **L8H** using both ^1H and $^{13}C\{^1H\}$ NMR spectroscopies confirmed the successful formation of the respective pre-ligands. For example, **Figure 5.1** shows the chemical shift of the imine methyl around 2.4 ppm which

appeared as a singlet peak in the ^{1}H NMR of **L7H**. The formation of Schiff base ligands was confirmed using ^{13}C{^{1}H} NMR spectroscopy. For example, the ^{13}C{^{1}H} NMR spectrum of the **L7H** (**Figure 5.2**) and **L8H**, showed peaks at 165.30 ppm and 160.90 ppm corresponding to the imine carbons resulting from the condensation reaction of 2'hydroxyacetophenone (C=O = ~199.8 ppm) and salicylaldehyde (C=O = ~191.0 ppm) with (3-aminopropy)triethoxysilane (APTES) respectively. The ^{13}C{^{1}H} NMR spectrum of ligand **L7H** in **Figure 5.2** further showed all the types of carbons present in the molecule at their respective chemical shifts.

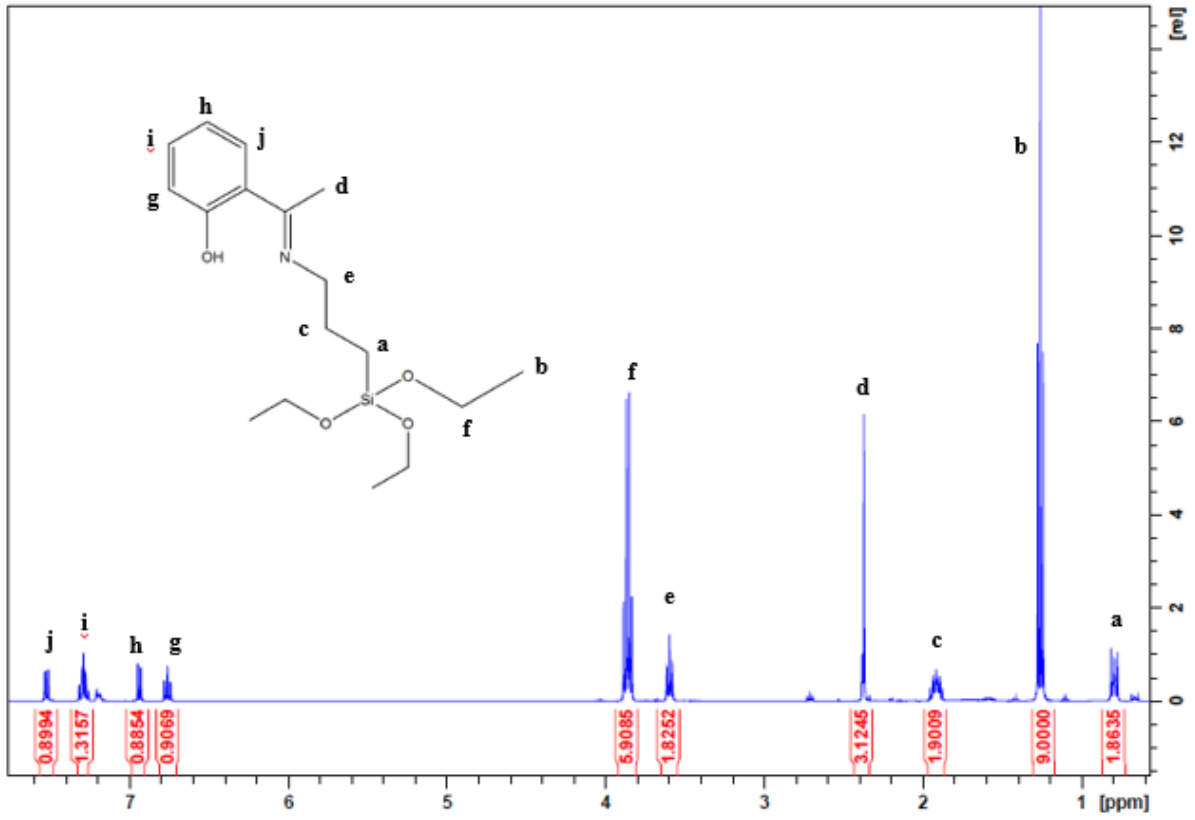

Figure 5.1: ^{1}H NMR of **L7H** showing the chemical shift of the imine methyl around 2.4 ppm which appeared as a singlet.

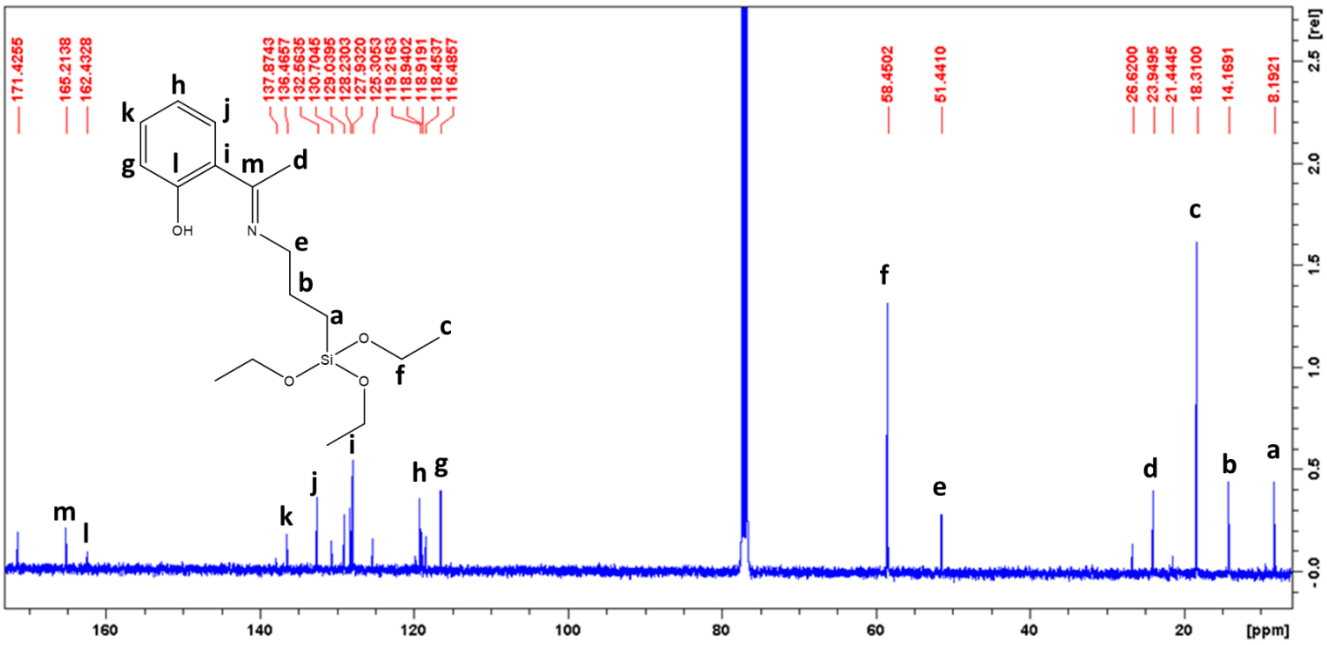

Figure 5.2: The $^{13}C\{^{1}H\}$ NMR of **L7H** showing the chemical shift of the respective carbons in the molecule.

The mass spectrometry was also helpful in determining the exact molecular masses of the silanol ligands. For example, in **Figure 5.3** is the mass spectrum obtained for ligand **L7** showing molecular ion peak at 362.0655 amu corresponding to $[M+Na]^+$ fragment of the ligand. Similarly, the mass spectrum of **L8H** showed the molecular ion peak at 348.1611 amu corresponding to $[M+Na]^+$ fragment of the ligand.

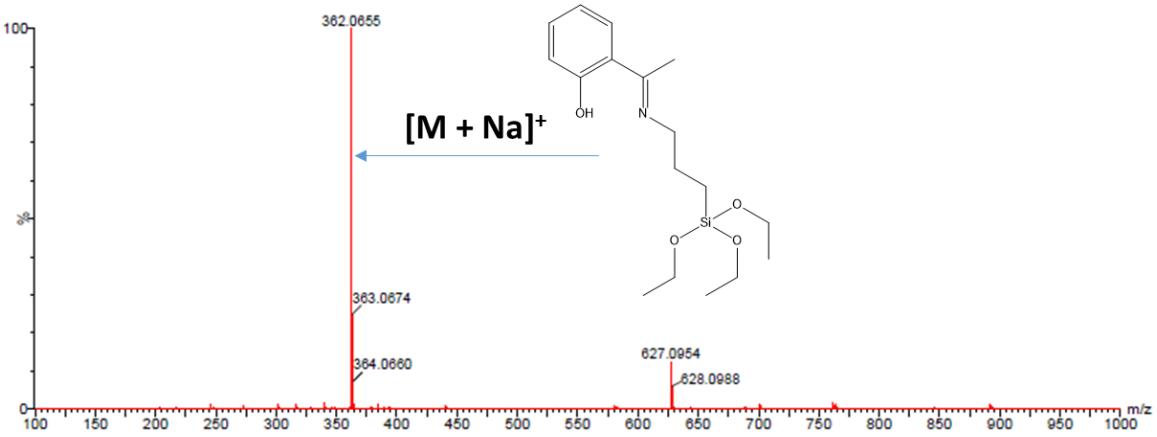

Figure 5.3: The mass spectrum of **L7H** showing molecular ion peak at 362.0655 amu corresponding to $[M+Na]^+$ fragment.

Due to the heterogeneous nature of the supported complexes, they were characterized using FT-IR spectroscopy, TGA, TEM, SEM, XRD, EDX, ICP-OES and VSM. **Figure 5.4** shows the IR spectra of the pure Fe_3O_4 MNPs, Schiff base organosilane pre-ligand **L7H**, immobilized compounds **L7** and **16**. The successful modification of Fe_3O_4 MNPs by **L7H** and **L8H** was manifested by the disappearance of the Si-O-C sharp singlet peaks around 1100 cm^{-1} in the IR spectra of **L7H** and **L8H** and the appearance of doublet peaks between 1112 cm^{-1} and 1025 cm^{-1} in IR spectra of **L7** and **L8** corresponding to the $\nu_{(Si-O)}$ and $\nu_{(Fe-O)}$ stretching frequencies respectively as depicted in **Figure 5.4**.

The formation of the respective immobilized complexes was derived from blue shifts of the $\nu_{(C=N)}$ group (**Figures 5.4**). For example, the $\nu_{(C=N)}$ vibration shifted from 1604 cm^{-1} in the IR spectrum of **L7** to 1612 cm^{-1} in the respective immobilized complex **16** (**Figure 5.4**), indicative of coordination of the imine nitrogen to the Ni metal atom.[24] The disappearance of the OH peak from the IR spectrum of the immobilized complex pointed to the deprotonation of the phenolic hydroxyl group upon complexation.[25] The broad peaks around 3 000 – 3 500 cm^{-1} could be

ascribed to the free OH groups from the nanoparticles and also possibly the presence of H_2O molecules in the compounds.

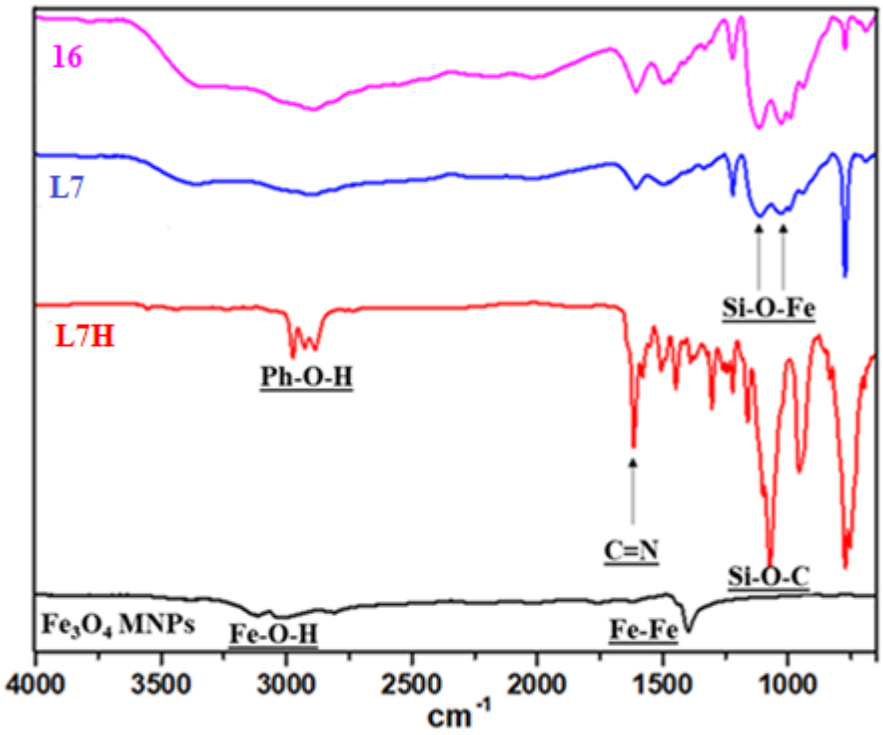

Figure 5.4: IR spectra of pure Fe_3O_4 MNPs, silanol ligand **L7H**, immobilized ligand **L7** and its respective Ni(II) complex **16** showing shifts in the Si-O-Fe bond signals.

The thermal stability of the immobilized ligands and complexes was studied using thermogravimetric analyses as illustrated in **Figure 5.5**. The TGA curves in **Figure 5.5** revealed improved stability of the immobilized ligands **L7** and **L8** in comparison to the free ligands **L7H** and **L8H**. In addition, the immobilized complexes **16**, **17**, **18**, **19**, **20** and **21** also showed enhanced thermal stability when compared to the free ligands. The weight loss around the 300 ˚C in TGA curves of the complexes was attributed to the loss of adsorbed water molecules,[26] while the weight loss of 5% around 500 ˚C was assigned to the decomposition of the organic and inorganic silica materials from the functionalized Fe_3O_4 magnetic nanoparticles.[27]

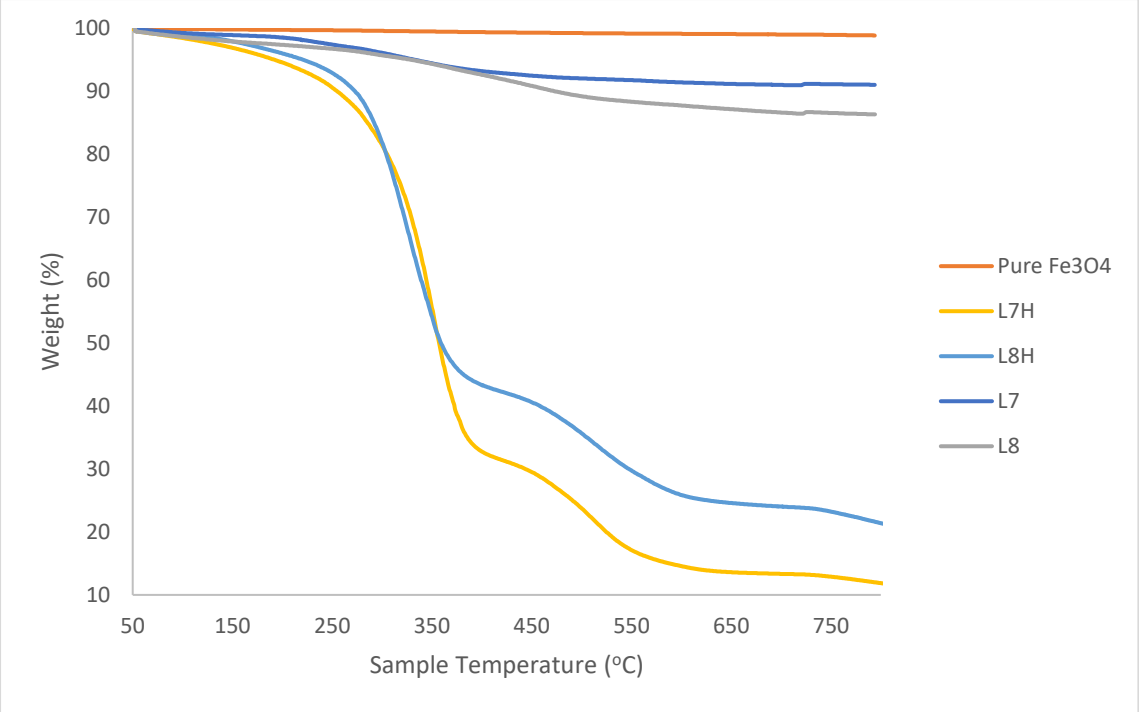

Figure 5.5: The TGA curves showing the thermal stability of the pure Fe_3O_4 MNPs, silanol ligands **L7H** and **L8H** and their immobilized counterparts **L7** and **L8** respectively.

The morphology and particle size estimate of the immobilized compounds was studied using TEM (**Figure 5.6**). The TEM images revealed the nanometre sized (2 nm < d < 50 nm) agglomerated particles of the Fe_3O_4 magnetic nanoparticles immobilized compounds.[28] The dark spots confirmed the presence of the iron oxide nanoparticles coated with the ash coloured Schiff base complex shell. In addition, using TEM, we were able to determine the estimated particle sizes of the immobilized ligands and their respective complexes (**Table 5.1**). For example, compounds **L7** and **16** gave particle sizes of 10.41 ± 0.1266 nm and 10.94 ± 0.1068 nm respectively.

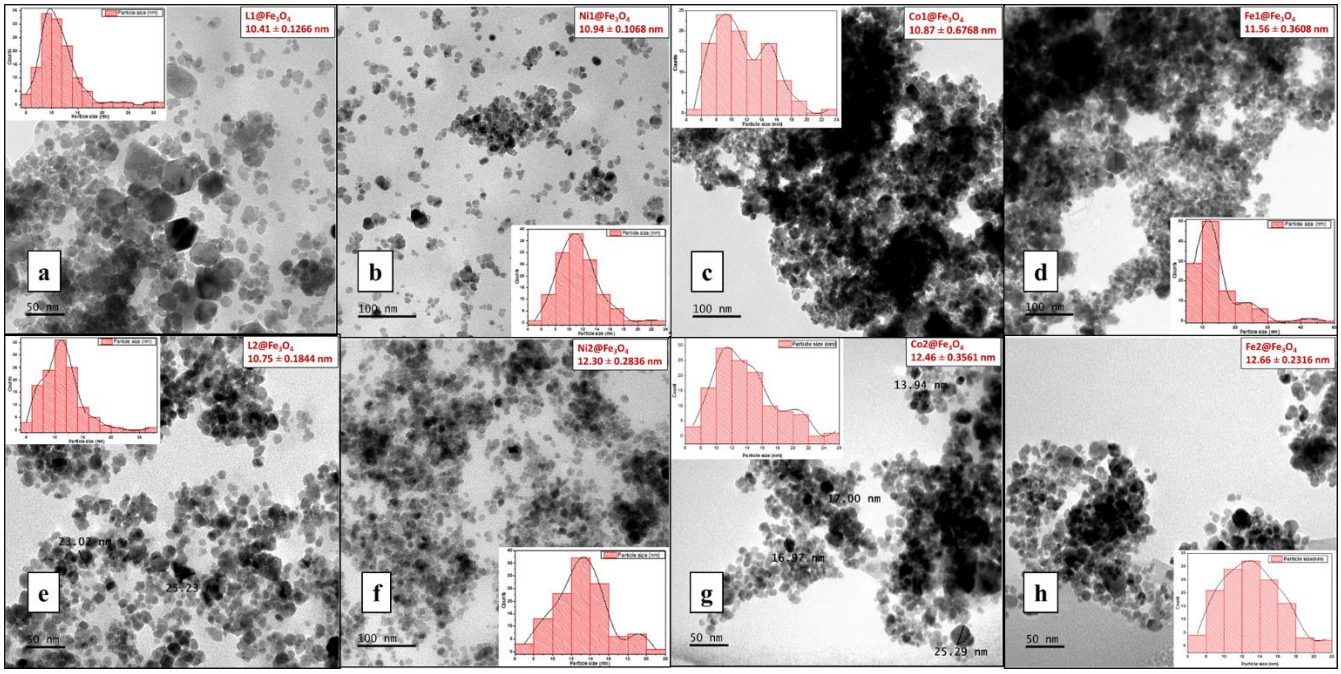

Figure 5.6: TEM images showing the shapes and sizes of the immobilized ligands **L7** (a), **L8** (e) and their complexes **16** (b), **17** (c), **18** (d), **19** (f), **20** (g) and **21** (h).

The morphology of the Fe_3O_4 immobilized complexes was further probed using scanning electron microscopy. The immobilized complexes exhibited spherical granules with some aggregations due to the magnetometric interactions within the complexes (**Figure 5.7**).[29] The comparisons of the SEM images of the immobilized ligands and their complexes revealed that the morphology of the ligands was not altered upon complexation (**Figure 5.7**).

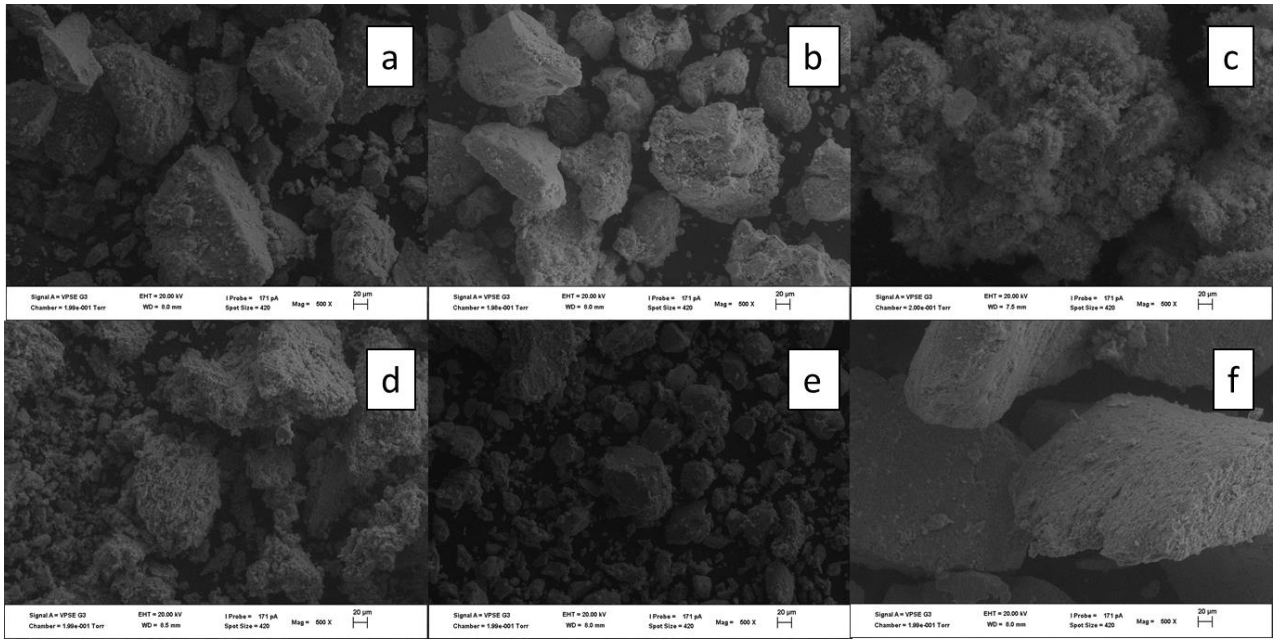

Figure 5.7: SEM micrographs of pure **Fe_3O_4** MNPs (a) immobilized ligands **L7** (b) and **L8** (c) and the complexes of **L7**, which are, **16** (d), **17** (e) and **18** (f).

Powder X-ray diffraction (PXRD) was employed to determine the crystallinity of the supported complexes (**Figure 5.8**). The XRD patterns of the complexes were comparable with signature peaks at 2θ of 35.40, 41.8˚, 50.7˚, 63.5˚, 67.7˚ and 74.6˚ corresponding to (220), (311), (400), (422), (511) and (440) Bragg reflections respectively. These indices are characteristic of cubic spinel structure of the Fe_3O_4 MNPs immobilized complexes.[30] The peak at 2θ of 21.6˚ was common in all the XRD spectra and was attributed to Si-O functional group.[26] The comparisons of the XRD spectra of the complexes and that of the Fe_3O_4 MNPs reveal the stability of the crystalline phasic state of the Fe_3O_4 MNPs upon ligand coating to form the complexes.[18]

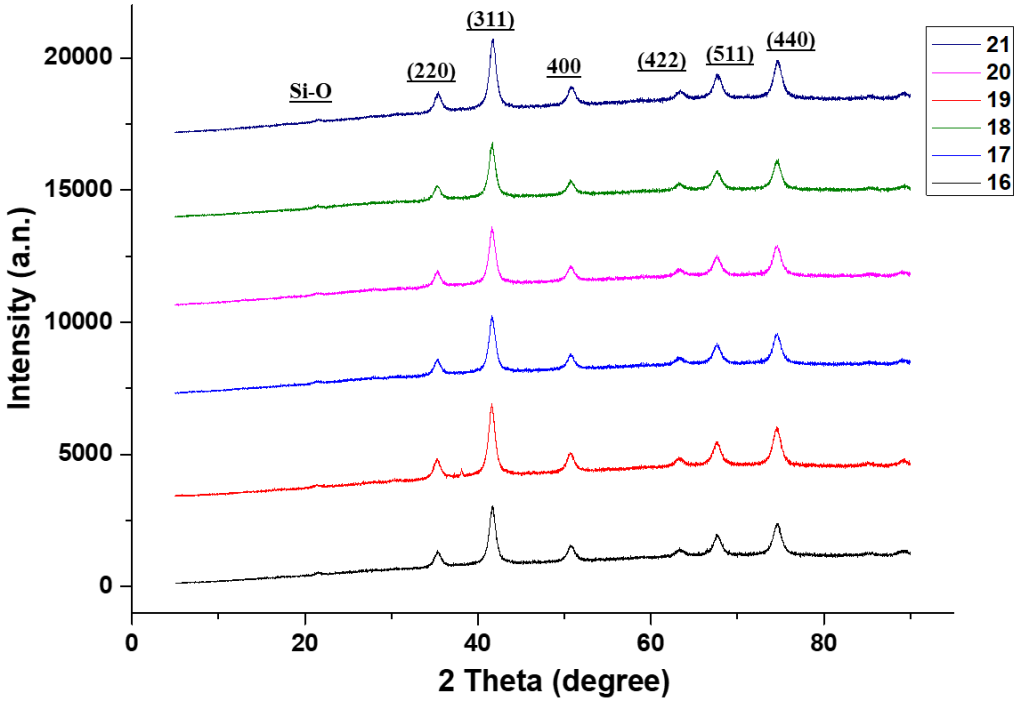

Figure 5.8: XRD pattern and Bragg's reflections observed for the immobilized complexes **16**–**21** showing indices corresponding to the cubic spinel structure of the complexes.

Determination of the magnetic properties of the compounds is an important parameter in the magnetically aided catalyst recycling. The immobilized complexes were thus analysed using vibrating sample magnetometer (VSM) which is illustrated in **Figure 5.9**. The immobilized complexes displayed no obvious remanence and resistance for an external magnetic field (coercivity), confirming their superparamagnetic phenomenon.[31] Nevertheless, the saturation magnetization (Ms) of the immobilized complexes in **Table 5.1**, **16** (62.06 emu/g), **17** (54.46 emu/g), **18** (52.11 emu/g), **19** (67.96 emu/g), **20** (66.90 emu/g), and **21** (67.00 emu/g) showed enhanced superparamagnetic nature of the complexes in comparison to pure Fe_3O_4 MNPs (50.8 emu/g).[31] In general, Ni complexes, showed the highest Ms values, while interestingly, the Fe complexes displayed the lowest values. The lower Ms values reported for the Fe complexes,

could be attributed to the magnetic quenching from the two Fe atoms as in **18**, consistent with literature reports.[32-35] In general, complexes derived from ligand **L8** gave higher Ms values, as in **18** (52.11 emu/g) and the corresponding **21** (67.00 emu/g). We also observed dependence of VSM on the metal concentrations. For example, **16** and **19** with metal contents of 0.542 % and 0.668 % recorded Ms values of 62.06 emu/g and 67.96 emu/g.

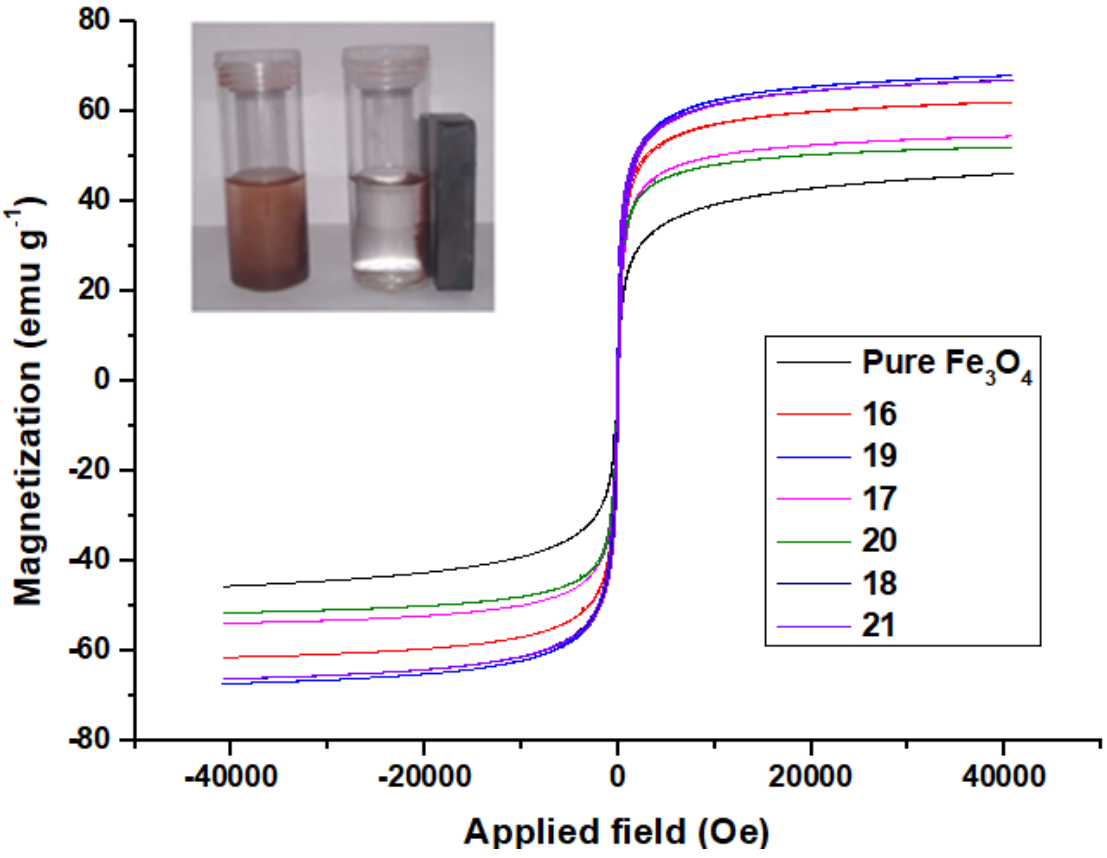

Figure 5.9: The magnetization curves of the pure Fe_3O_4 MNPs and immobilized complexes **16**-**21** measured at room temperature (300 K).

Energy dispersive X-ray (EDX) was initially used in quantitatively determining the metal contents in the immobilized complexes as illustrated in **Figure 5.10** and the summary of the results is given in **Table S5.1**. EDX data revealed metal contents in the range of 0.360 - 4.43

%. A more precise ICP-OES method was used to validate the results obtained from the EDX analyses (**Table 5.1**). Notably, there were significant differences between the EDX and ICP-OES metal contents. For example, immobilized complex **16** recorded metal contents of 1.49 % and 0.542 % using EDX and ICP-OES respectively. Thus we used the data derived from the more sensitive ICP-OES analyses in the catalysis applications.

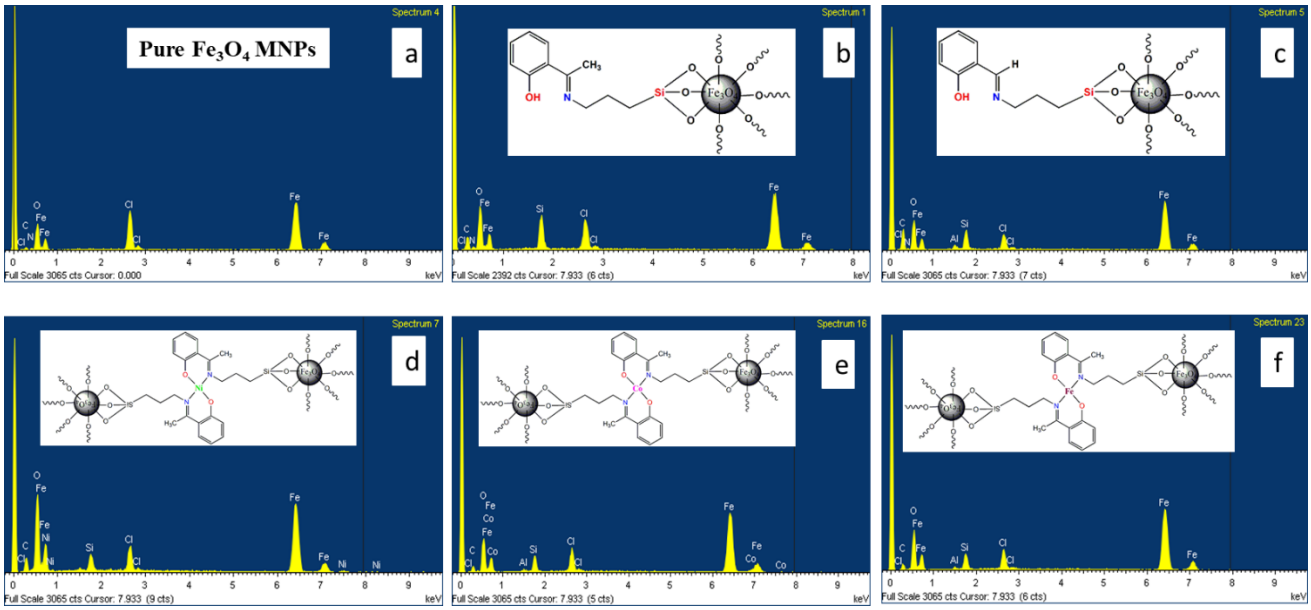

Figure 5.10: Elemental analysis (EDX) spectra of pure **Fe_3O_4** MNPs-a, **L7** -b, **L8** -c and the **16** -d, **17** -e and **18** -f complexes of the immobilized complex **L7**.

Table 5.1: The particle sizes, VSM results and metal loadings of the Co(II), Ni(II) and Fe(II) of Fe_3O_4 magnetically immobilized ligands and complexes determined using EDX and ICP-OES.

Entry	Compound	Particle sizes (nm)	VSM (emu g^{-1})	EDX %	ICP-OES %
1	**L7**	10.41 ± 0.1266	-	-	-
2	**L8**	10.75 ± 0.1844	-	-	-
3	**16**	10.94 ± 0.1068	62.06	1.49	0.542
4	**17**	10.86 ± 0.6768	54.46	1.86	0.379
5[a]	**18**	11.56 ± 0.3608	52.11	4.43	0.456
6	**19**	12.30 ± 0.2836	67.96	1.10	0.688
7	**20**	12.46 ± 0.3561	66.90	0.360	0.447
8[a]	**21**	12.66 ± 0.2315	67.00	3.30	0.656
9[b]	**19**	12.30 ± 0.2836	67.96	0.880	0.632

[a]Calculated according to the chloride halide (0.997:1.20). [b]Post-catalytic experiments catalyst composition.

5.3.2 Ethylene oligomerization reactions catalyzed by Fe_3O_4 MNPs immobilized Ni(II), Co(II) and Fe(II) complexes.

5.3.2.1 Preliminary studies of ethylene oligomerization reactions

Preliminary evaluation of the ability of Fe_3O_4 immobilized metal complexes to catalyze ethylene oligomerization reactions was performed using $EtAlCl_2$ as the co-catalyst (Al/M ratio of 200) in *n*-heptane, *n*-hexane, toluene and chlorobenzene solvents, at 10 bar and temperature of 30 °C for 1 h, (**Table 5.2**). Analyses of the ethylene oligomerization products using GC-FID (**Figures 5.11** and **5.13**) and GC-MS (**Figure 5.12**) established the formation of ethylene oligomers and alkylated products depending on the solvent used as shown in **Scheme 5.2**. On

the other hand, activation of the complexes with MMAO did not result in any active catalyst systems.[36] With respect to the role of solvent, lower catalytic activities were generally observed in *n*-heptane and *n*-hexane solvents, in comparison to toluene and chlorobenzene solvents. For example, catalyst **19** afforded catalytic activities of 20 500 $g_{oligomers}$ mol^{-1} (M) h^{-1}, 15 400 $g_{oligomers}$ mol^{-1} (M) h^{-1}, 12 500 $g_{oligomers}$ mol^{-1} (M) h^{-1} and 10 500 $g_{oligomers}$ mol^{-1} (M) h^{-1} in chlorobenzene, toluene, *n*-hexane and *n*-heptane solvents respectively (**Table 5.2, entries 4** and **7-9**). This is common and has been attributed to the poor solubility of ethylene monomer in *n*-heptane and *n*-hexane solvents.[37]

The nature of the solvent also had a significant influence on the product distribution in ethylene oligomerization reactions. For example, the use of *n*-heptane and *n*-hexane solvents resulted in the formation of mainly C_4 (8% and 28% respectively) and C_6 (87% and 72% respectively) oligomers, **Table 5.2**, **entries 4** and **7**. It remains unclear to us the reasons behind the increased selectivity towards C_4 oligomers in *n*-hexane solvent. On the other hand, the use chlorobenzene and toluene solvents led to partial and complete alkylation of the pre-formed oligomers. While alkylation of toluene solvent by the pre-formed oligomers is now well established,[38] to date, there is only one report of tandem alkylation of chlorobenzene solvent by ethylene oligomers using (phenoxyimidazolyl-salicyaldimine) Fe(II) catalysts.[39] We thus used *n*-heptane and *n*-hexane solvents in further experiments due to the selectivity towards the targeted ethylene oligomers.

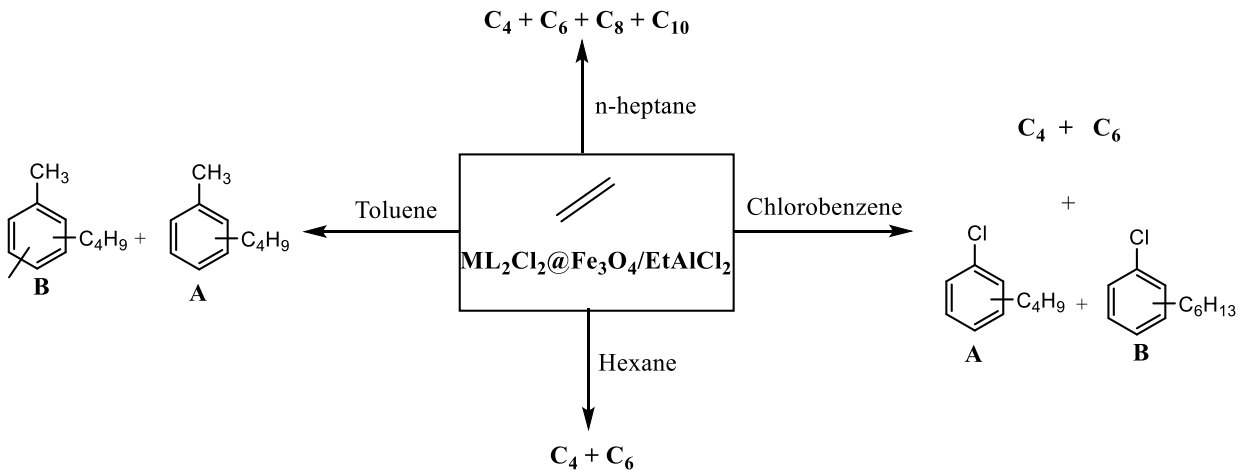

Scheme 5.2: Ethylene oligomerization reaction products using Fe_3O_4 MNPs anchored Fe(II), Ni(II) and Co(II) catalysts in different solvents.

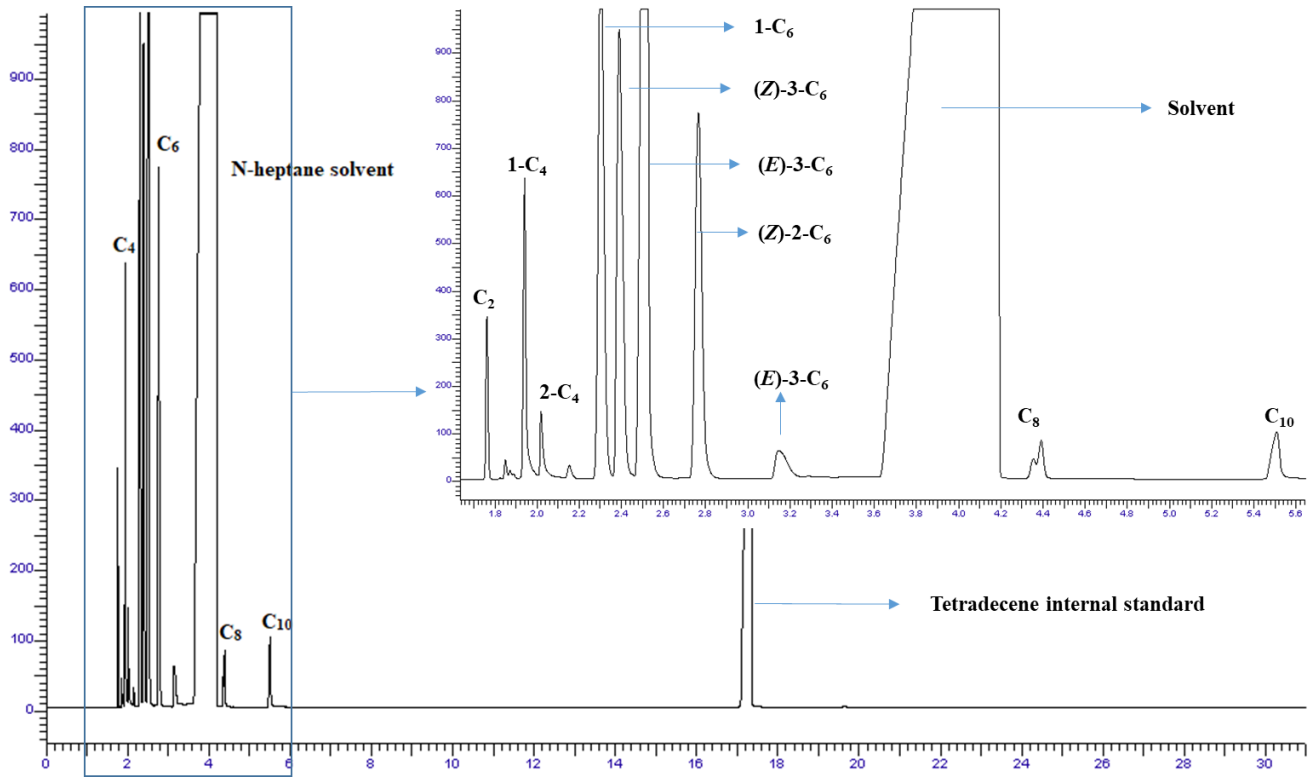

Figure 5.11: An example of a GC plot obtained when complex **19** is used as a catalyst in an inert *n*-heptane solvent illustrating a good selectivity towards oligomers C_4 and C_6 short chain products (**Table 5.2**, **entry 4**).

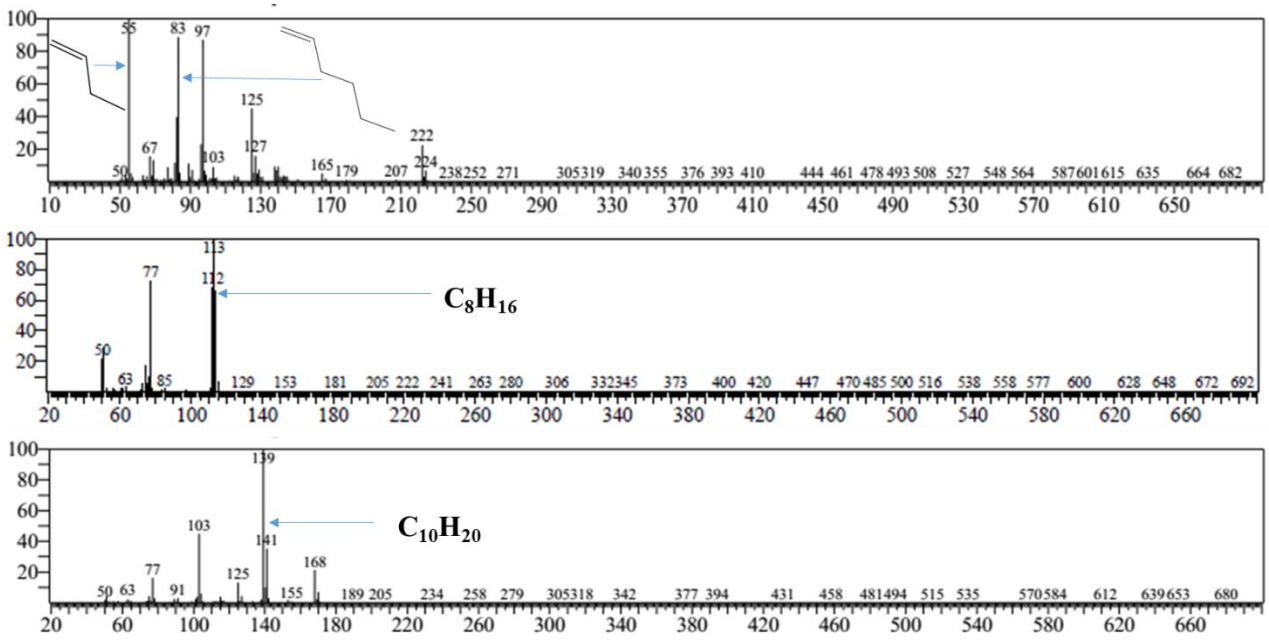

Figure 5.12: The gas chromatogram mass spectra showing C_4 and C_6 major products and fractions of C_8 and C_{10} when Fe_3O_4 immobilized complex **19** is activated with $EtAlCl_2$ co-catalyst and used to catalyze ethylene oligomerization reactions (**Table 5.2**, **Entry 4**).

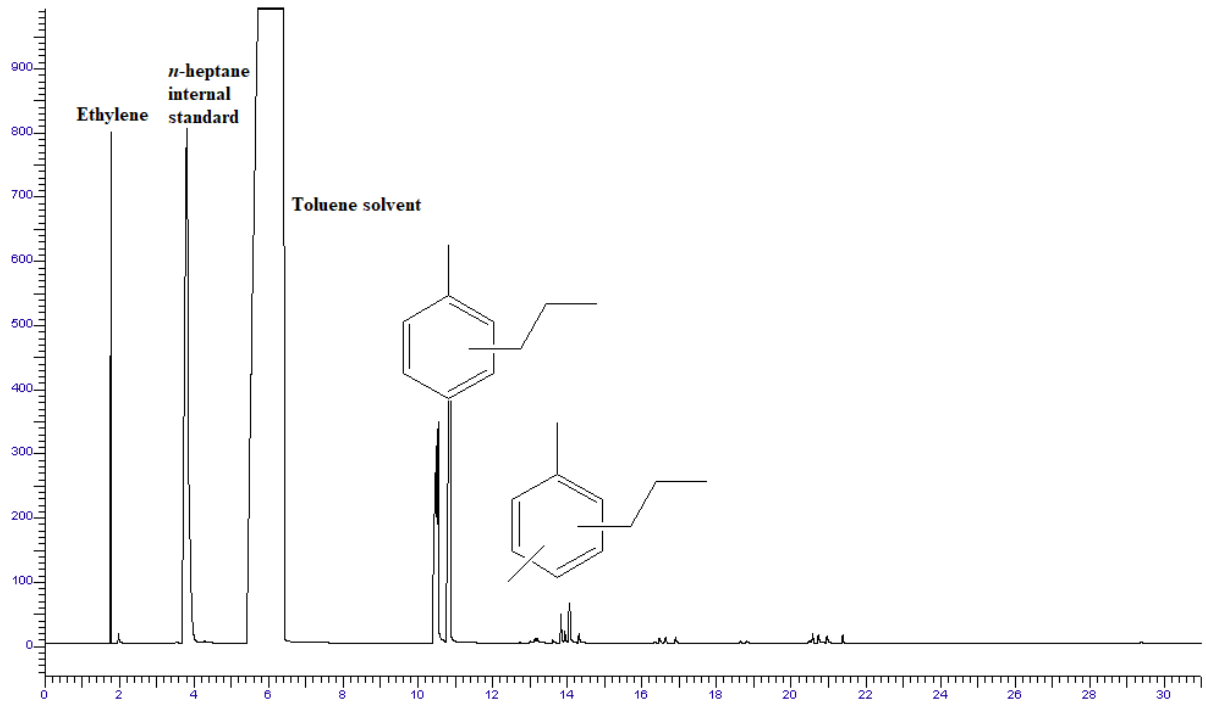

Figure 5.13: The typical GC-FID plot showing a complete alkylation of C_4 oligomers into alkylated toluene products when **19**/$EtAlCl_2$ system is used catalyze the oligomerization of ethylene reaction (**Table 5.2**, **entry 8**).

Detailed analyses of the C_4 and C_6 oligomer fractions revealed some interesting isomerization trends. While there was minimum isomerization of the C_4 oligomers (>96% of α-C_4) for all the catalysts, there was significant isomerization of the C_6 oligomers to give over 80% of internal hexenes (**Figure 5.11**). While higher composition of internal hexenes is expected due to more possible scenarios, this alone cannot account for the lack of C_4 isomerization. In order to understand the product distribution observed for the Fe_3O_4 immobilized catalysts, we have proposed **Scheme 5.3**, showing a possible mechanism for the formation of the shorter chain C_4 and C_6 oligomers. The agnostic interaction in the alkyl intermediate **C1** is favoured leading to *β*-H elimination (over chain propagation) to give the olefinic complex **D**.

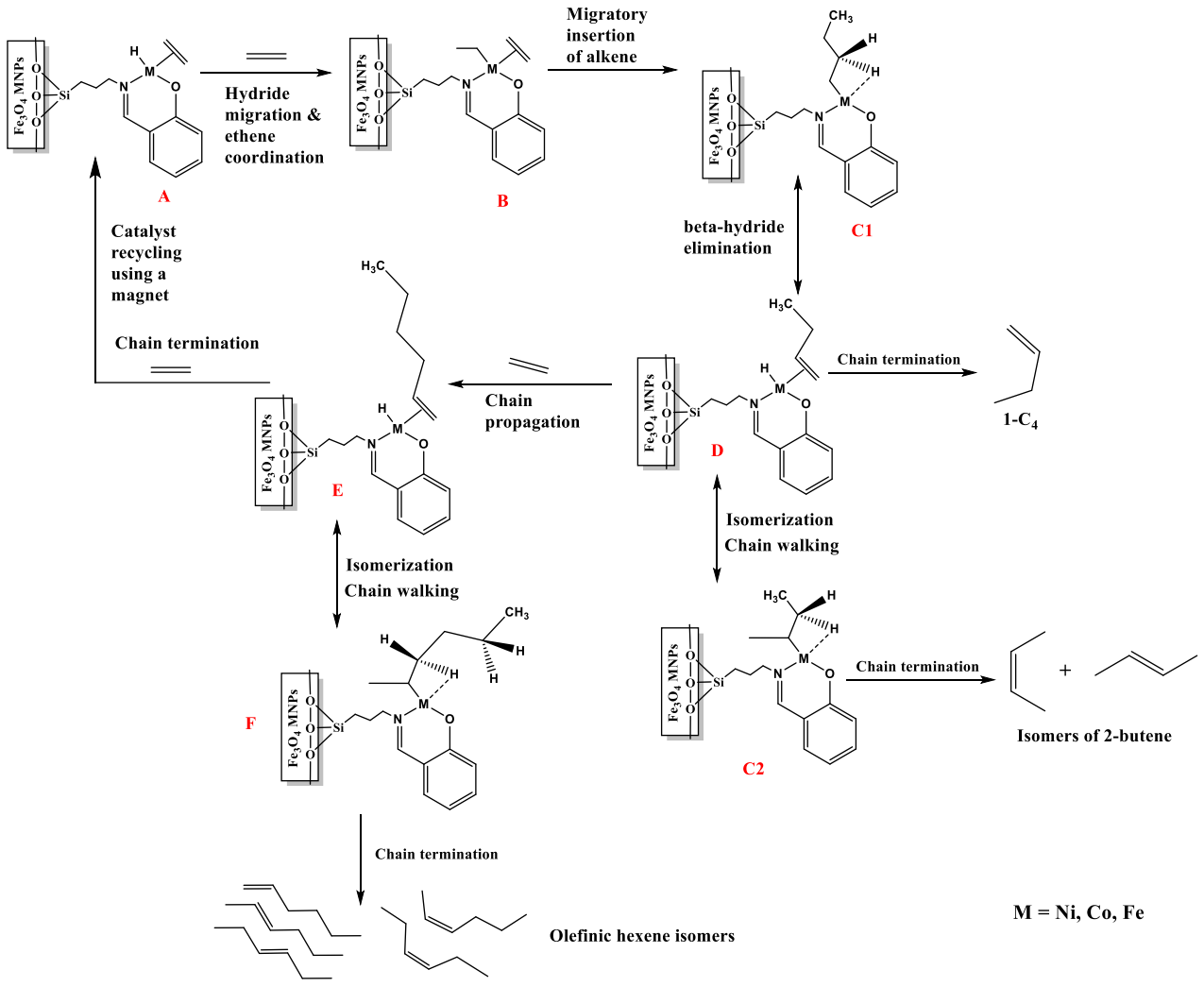

Scheme 5.3: Illustration of the formation and isomerization of 1-C_4 and 1-C_6 oligomers to give

internal oligomers during ethylene oligomerization reaction using the N^O chelated Fe_3O_4 magnetic nanoparticles immobilized Fe(II), Ni(II) and Co(II) complexes.

Table 5.2: Ethylene oligomerization reactions catalyzed by Fe_3O_4 MNPs immobilized N^O donor Ni(II), Co(II) and Fe(II) complexes.[a]

Entry	Solvent	Catalyst	Yield (g)[b]	Activity[c] $g_{oligomers}$ mol^{-1}(M) h^{-1}	Product Distribution (%)[d]		
					C_4 (α-C_4)	C_6 (α-C_6)	$C_{8\ \&10}$
1	n-heptane	**16**	0.0915	9 150	5 (77)	92 (23)	3
2	n-heptane	**17**	0.0810	8 100	4 (92)	94 (23)	2
3	n-heptane	**18**	0.0720	7 200	6 (85)	89 (21)	5
4	n-heptane	**19**	0.105	10 500	8 (74)	87 (23)	5
5	n-heptane	**20**	0.0856	8 560	9 (88)	89 (22)	2
6	n-heptane	**21**	0.0813	8 130	8 (92)	88 (21)	4
7	n-hexane	**19**	0.125	12 500	28 **(**80)	72 **(**27)	-
8[e]	Toluene	**19**	0.154	15 400	-	-	-
9[f]	Chlorobenzene	**19**	0.205	20 500	41 (97)	49 (11)	-
10[g]	Chlorobenzene	**[Ni(L8)$_2$]**	19	1.9 x 10^6	31 (87)	69 (75)	-

[a]Reaction conditions: [**Metal**] = 10 µmol (based on the metal contents determined from ICP-OES), Co-catalyst, $EtAlCl_2$ (2 mL); solvent, 30 mL; Temperature, 30 ˚C; time, 1 h; Pressure, 10 bar; Al/M ratio=200. [b]Determined using tetradecene as an internal standard. [c]Activity; g oligomer/mol [M] hour. [d]Olefinic products were detected by GC-FID and GC-MS. [e]100% alkylated products. [f]10 % balance was Friedel-Crafts alkylated products. [g]Previous report.[20]

This is plausible from the limited steric crowding around the active metal sites.[40] The observation of the internal hexenes originates from the chain-walking/chain migration of the

coordinated olefin (**E**).[41] As depicted in **Scheme 5.3**, the π-bonded olefinic complex **D** undergoes metal hydride re-insertion into the growing chain with an opposite region-chemistry to form the intermediate complex **C2**. Further *β*-H elimination, results in the production of internal olefins. The higher composition of internal hexenes, in comparison to butenes could be explained rapid combination of C_2 monomer with the C_4 oligomers to give C_6 oligomers (**D** to **E**), at the expense of chain walking/migration, hence minimal C_4 isomerization.[42] This is supported by higher composition of the hexenes (72% - 90%) and the trace amounts of C_8 and C_{10} oligomers (>5%) observed. Thus the limited chain propagation once C_6 is formed, result in chain migration of the metal-coordinated C_6 to give internal hexenes as depicted in **Scheme 5.3** by species **F**. This trend has also been observed in literature using different metal catalysts.[40, 43-44]

5.3.2.2. Effect of catalyst structure in the oligomerization reactions of ethylene

Having established the viability of the magnetically immobilized complexes to promote ethylene oligomerization reactions, we then examined the influence of complex properties on their catalytic activities and selectivity. First, we observed that the identity of the metal atom controlled the catalytic activities. In general, the Ni(II) complexes were the most active compared to their respective Fe(II) and Co(II) catalysts. For instance, complexes **18**, **17** and **16** displayed catalytic activities of 7200 $g_{oligomers}$ mol^{-1}(M) h^{-1}, 8100 $g_{oligomers}$ mol^{-1}(M) h^{-1} and 9150 $g_{oligomers}$ mol^{-1}(M) h^{-1} respectively (**Table 5.2, entries 1-3**). These results are in good accord with a review article by Suo *et. al*,[45] which highlights the potential of Ni(II) complexes to form more active catalyst systems. In terms of product distribution, Co catalysts appeared to favour trimerization reactions. For example, while **17** afforded 94% of C_6, the respective

catalysts **18**, and **16** gave selectivities of 89% and 92% towards C_6 oligomers respectively (**Table 5.2**, **entries 1-3**). Similar trends were observed for the other catalysts.

In terms of ligand motif effect, complexes **21**, **20** and **19** of **L8** displayed higher catalytic activities than their analogous complexes **18**, **17** and **16** derived from ligand **L8**. For example, complexes **16** and **19** showed catalytic activities of 9150 $g_{oligomers}$ mol^{-1}(M) h^{-1} and 10 500 $g_{oligomers}$ mol^{-1}(M) h^{-1} respectively (**Table 5.2**, **entries 3** and **6**). This could be ascribed to electronic properties of the catalysts where the electron donating methyl substituent in **L7** results in lower electropositive metal centres.[20, 25] The steric parameters of the immobilized ligands also affected the selectivity of the catalysts. Expectedly, the sterically bulky methyl substituted complexes supported on ligand **L7** favoured the formation of C_6 oligomers as opposed to the respective complexes anchored on the unsubstituted ligand **L8**.[46] As an illustration, catalysts **16** and **19** displayed selectivity of 94 % and 87 % towards C_6 oligomers respectively (**Table 5.2**, **entries 1** and **4**). In general, all the catalysts demonstrated comparable isomerization behaviour.

In comparisons to the previously reported homogeneous systems,[20] the current Fe_3O_4 magnetic nanoparticle immobilized catalysts afforded lower catalytic activities. For instance, the homogeneous complex [Ni(**L8**)$_2$] gave catalytic activity of 1.9 x 10^6 $g_{oligomers}$ mol^{-1} (M) h^{-1}, compared to the TOF of 2.0 x 10^4 $g_{oligomers}$ mol^{-1} (M) h^{-1} displayed by the current immobilized complex **19** (**Table 5.2**, **entry 10** *vs* **4**). The lower catalytic activities of the immobilized catalysts could be attributed to the limited number of active sites (lower metal contents) in addition to their insolubility in the reaction medium.[47] Most significantly, the MNP immobilized complex **19**, showed remarkable selectivity towards C_6 oligomers (87 %) in comparison to the homogeneous counterpart of 69 % (**Table 5.2**, **entry 4** *vs* **10**).

5.3.2.3 Effect of reaction conditions on the catalytic activity and selectivity of the complexes.

To investigate the dependence of the catalytic performance of the immobilized complexes on reaction parameters, we varied reaction conditions such as co-catalyst to metal ratio, reaction time, temperature and pressure using the most active catalyst **19** (**Table 5.3**). The role of metal concentration was also investigated using catalyst **19**, **20** and **21** (**Figure 5.5**). The Al/Ni ratio was varied from 50 to 250 using catalyst **19** at fixed concentration of the pre-catalyst. We reported an increase in catalytic activities from 4 640 $g_{oligomers}$ mol^{-1}(M) h^{-1} to 10 500 $g_{oligomers}$ mol^{-1}(M) h^{-1} when the Al/Ni ratio was increased from 50 to 200 respectively (**Table 5.3**, entries 1 and 3). Beyond this ratio (Al/Ni = 250), a decline in the catalytic activity was observed. Lower catalytic activities at higher Al/M ratios have been associated with higher contents of aluminium ash/impurities.[48-49] The product distribution was also affected by the variation of the amount of the co-catalyst, where higher Al/M ratios shifted the oligomers towards the C_4 and C_6 fractions (**Table 5.3**, entries 1-4). Expectedly, an increase in catalytic activity of complex **19** was observed with increasing ethylene pressure (**Table 5.3**, entries 5-8).[50] In addition, an increase towards the C_4 oligomer fractions with concomitant decrease in the C_6 proportion was observed.[51]

In order to establish the stability of the immobilized catalysts, the reaction time was varied from 0.5 h to 4 h (**Table 5.4**). Increasing the reaction period from 0.5 h to 2 h was marked by a drastic increase in catalytic activities of catalyst **19** from 5 920 $g_{oligomers}$ mol^{-1}(M) h^{-1} to 10 875 $g_{oligomers}$ mol^{-1}(M) h^{-1} respectively (**Table 5.4**, entries 1-3 respectively). Beyond this period, a drop in catalytic activity was observed (6 500 $g_{oligomers}$ mol^{-1}(M) h^{-1} at 4 h), indicative of catalyst degradation with time.[52]

Table 5.3: The influence of co-catalyst concentration and ethylene pressure on the performance of catalyst **19** in ethylene oligomerization reactions.[a]

Entry	Al/M	Pressure bar	Yield (g)[b]	Activity[c] $g_{oligomers}$ mol^{-1}(M) h^{-1}	Product Distribution (%)[d]		
					C_4 (α-C_4)	C_6 (α-C_6)	C_8 & C_{10}
1	50	10	0.0464	4 640	6 (99)	80 (19)	14
2	100	10	0.0551	5 510	9 (89)	81 (19)	10
3	200	10	0.105	10 500	8 (74)	87 (23)	5
4	250	10	0.0950	9 500	14 (72)	85 (15)	1
5	200	5	0.0928	9 280	6 (70)	86 (28)	8
6	200	10	0.105	10 500	8 (74)	87 (23)	5
7	200	15	0.137	13 700	16 (86)	81 (13)	3
8	200	20	0.251	25 100	23 (99)	75 (15)	1

[a]Reaction conditions: [**Ni**] = 10 µmol (amount of active species in mol, was calculated based on the metal contents determined by ICP-OES and weighed accordingly), Co-catalyst, $EtAlCl_2$; solvent, *n*-heptane, 30 mL; Temperature, 30 ˚C; time, 1 h; [b]Determined using tetradecene as an internal standard. [c]Activity; g oligomers/mol [M] hour. [d]Olefinic products were detected by GC-FID and GC-MS.

The thermal stability of the immobilized complexes was studied by varying the reaction temperatures from 30 ˚C to 120 ˚C using complexes **19**, **20** and **21** (**Table 5.4**, entries 2 and 5-9). From the data, an increase in reaction temperature from 30 ˚C to 120 ˚C resulted in appreciable increase in catalytic activities of catalyst **19** from 10 500 $g_{oligomers}$ mol^{-1}(M) h^{-1} to 48 000 $g_{oligomers}$ mol^{-1}(M) h^{-1} (**Table 5.4**, entries 2 and 5-7). The results demonstrate good thermal stability of these immobilized catalysts. With respect to product distribution, there was no discernible dependence of oligomer selectivity of reaction temperature using catalyst **19** (**Table 5.4,** entries 2, 5-7). For example, while only 8% of C_4 oligomers were realized at 30 ˚C,

36% and 9% of C_4 fractions were obtained at 60 °C and 120 °C respectively. This erratic pattern may be associated with the drastic changes in the catalysts' properties, such as acidity, with temperature.[53-55]

Table 5.4: The effect of reaction time and temperature on the catalytic activity and selectivity of the immobilized complexes **19**, **20** and **21**.

Entry	Catalyst	Time (h)	T (°C)	Yield (g)[b]	Activity[c] $g_{oligomers}$ mol^{-1}(M) h^{-1}	Product Distribution (%)[d]		
						C_4 (α-C_4)	C_6 (α-C_6)	C_8 & C_{10}
1	**19**	0.5	30	0.0296	5 920	17 (98)	80 (9)	3
2	**19**	1	30	0.105	10 500	8 (74)	87 (23)	5
3	**19**	2	30	0.217	10 875	7 (82)	88 (17)	5
4	**19**	4	30	0.260	6500	12 (28)	65 (17)	13
5	**19**	1	60	0.167	16 700	36 (99)	56 (19)	7
6	**19**	1	90	0.285	28 500	29 (97)	63 (11)	8
7	**19**	1	120	0.480	48 000	9 (53)	85 (19)	6
8	**20**	1	120	0.254	25 400	7 (72)	89 (26)	5
9	**21**	1	120	0.380	38 000	4 (69)	87 (18)	9

[a]Reaction conditions: [**Metal**] = 10 µmol (amount of active species in mol, was calculated based on the metal contents determined by ICP-OES and weighed accordingly), Co-catalyst, $EtAlCl_2$ (2 mL); solvent, *n*-heptane, 30 mL; Pressure, 10 bar; Al/M ratio = 200. [b]Determined using tetradecene as an internal standard. [c]Activity; g oligomer/mol [M] hour. [d]Olefinic products were detected by GC-FID and GC-MS.

To ventilate if the metal content/catalyst loading may influence the catalytic activities and selectivity of the materials, we varied the metal concentration from 10 µmol to 40 µmol (based on ICP-OES) using complexes **19**, **20** and **21** (**Figure 5.5**). Interestingly, catalytic activities decreased with increasing metal loadings/concentrations. For instance, catalytic activities of 10

500 $g_{oligomers}$ mol^{-1}(M) h^{-1} and 3 702 $g_{oligomers}$ mol^{-1}(M) h^{-1} were obtained at metal loadings of 10 µmol and 40 µmol respectively for catalyst **16**. A similar trend was observed for the **20** and **21** catalysts (**Figure 5.14**). A plausible explanation for this observation could be that effective dispersion of active sites at lower loading is possible, while catalyst agglomeration at higher loadings may hinder ethylene monomer adsorption/coordination to the active sites.[56]

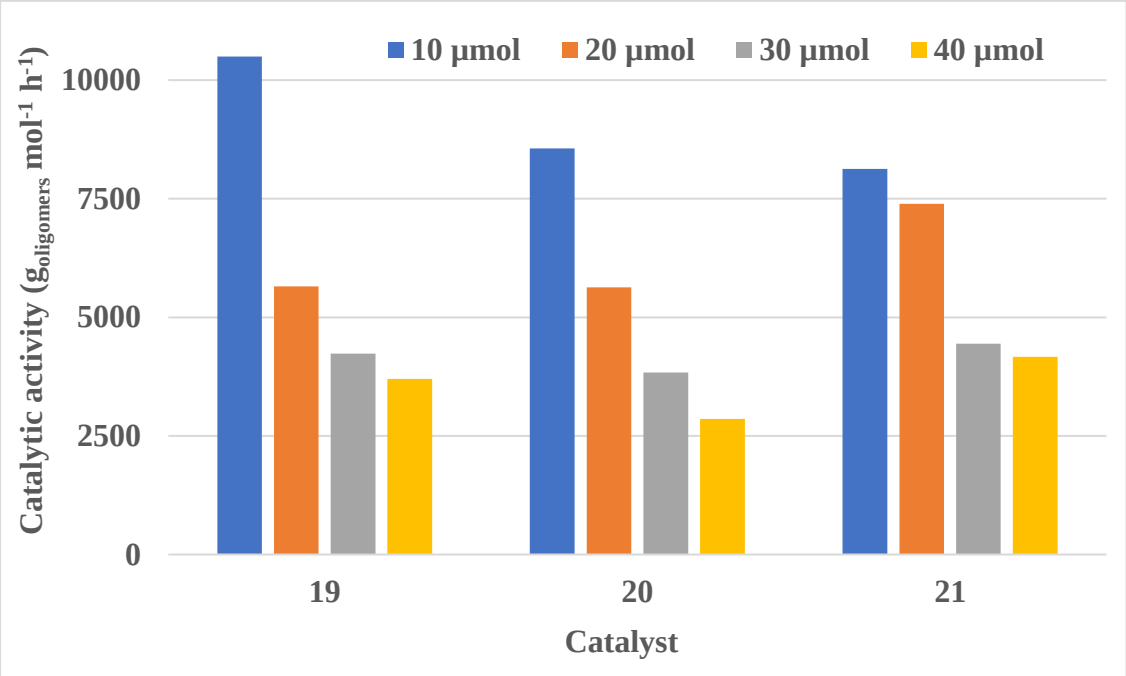

Figure 5.14: The influence of varying metal concentration on the catalytic activity of **19**, **20** and **21** immobilized catalysts under general conditions.

The optimum conditions determined (Al/M ratio = 200; P = 20 bar, t = 2 h and T = 120 ˚C) were then applied to all the catalysts for complete comparative analyses (**Table 5.5**). Under these conditions, complex **19** was still the most active giving catalytic activities of 97 900 $g_{oligomers}$ mol^{-1}(M) h^{-1}, while complex **18** was the least active (67 300 $g_{oligomers}$ mol^{-1}(M) h^{-1}). The catalytic trends, both with respect to activity and selectivity were the same to those observed in the preliminary studies.

Table 5.5: Comparative catalytic performance of the immobilized catalysts under optimized conditions.[a]

Entry	Catalyst	Yield (g)[b]	Activity[c] $g_{oligomers}$ $mol^{-1}(M)$ h^{-1}	Product Distribution (%)[d]		
				C_4 (α-C_4)	C_6 (α-C_6)	C_8 & C_{10}
1	**16**	0.850	85 000	23 (87)	75 (33)	2
2	**17**	0.755	75 500	21 (97)	78 (29)	1
3	**18**	0.673	67 300	16 (89)	81 (28)	3
4	**19**	0.979	97 900	28 (97)	70 (32)	2
5	**20**	0.798	79 800	23 (95)	86 (24)	1
6	**21**	0.758	75 800	21 (96)	77 (26)	2

[a]Reaction conditions: [**Metal**] = 10 µmol (amount of active species in mol, was calculated based on the metal contents determined by ICP-OES and weighed accordingly), Co-catalyst, $EtAlCl_2$ (2 mL); solvent, *n*-heptane, 30 mL; Temperature, 120 ˚C; time, 2 h; Pressure, 20 bar; Al/M ratio = 200. [b]Determined using tetradecene as an internal standard. [c]Activity; g oligomer/mol [M] hour. [d]Olefinic products were detected by GC-FID and GC-MS.

5.3.2.4. Recycling experiments of the immobilized catalysts in ethylene oligomerization reactions.

The main aim of this work was to design magnetically separable ethylene oligomerization catalysts. We thus performed recycling experiments of the immobilized catalyst *via* magnetic separation (**Table 5.6** and **Figure 5.15**). The recycling experiments revealed that the complexes could be re-used in three runs, without significant loss of catalytic activity and selectivity (**Table 5.6** and **Figure 5.15**). In contrast to the work of Kumar *et al.*,[57] where the immobilized complexes were only activated in the initial run, we introduced a fresh $EtAlCl_2$ co-catalyst in each subsequent cycle. In our case, similar to the previous reports by Rossetto *et. al*,[40] no catalytic activities were observed in recycling experiments without the addition of fresh co-

catalyst. This is not surprising as it is known that excess amounts of the Al co-catalysts are generally required to activate the metal pre-catalysts. The observed drastic drop in the catalytic activities in the third run (over 80 % loss of activity) in Kumar *et al.*[57] work argument this hypothesis.

All the catalysts showed good stability and recyclability, since up to 95% of the original catalysts were recovered (**Table 5.6**). Generally, complexes with higher Ms values showed higher catalyst recovery efficiency (**Table 5.6**). For example, catalyst **16** (Ms of 62.06 emu/g) displayed a loss of 5% and 14% of its original catalytic activity and metal content respectively in the final run (**Table 5.6**, **entry 1**). In contrast, catalyst **19** (Ms of 67.96 emu/g) recorded lower losses in the original catalytic activity and metal content of 2% and 8% respectively (**Table 5.6**, **entry 2**). This is not a well-established trend since even Fe_3O_4@TiO_2 (2.01 emu/g) can be efficiently recycled using a small magnet.[37]

Table 5.6: The recyclability experiments of the immobilized N^O donor Ni(II), Co(II) and Fe(II) complexes.[a]

Entry	Pre-catalyst	VSM (emu/g)	Activity ($g_{oligomers}$ mol^{-1}(M) h^{-1})[b]					
			Initial	1st Recycle	2nd Recycle	Δ (%) Mass[c]	Δ (%) Metal[d]	% activity retained[e]
1	**16**	62.06	9 205	9 425	8 797	91	14	95
2	**17**	54.46	8 076	8 137	7 753	90	16	96
3	**18**	52.11	7 246	7 088	7 063	94	11	97
4	**19**	67.96	10 452	10 312	10 223	96	8	98
5	**20**	66.90	8 510	8 445	8 422	94	9	99
6	**21**	67.00	8 169	8 129	8 071	97	10	98

[a]Reaction conditions: [**Metal**] = 10 µmol (amount of active species in mol, was calculated based on the metal contents determined by ICP-OES and weighed accordingly), Co-catalyst, $EtAlCl_2$; solvent, chlorobenzene (30 mL); Temperature, 30 ˚C; time, 1 h; Pressure, 10 bar; Al/M ratio = 200. [b]Activity, g oligomers produced per mol metal per hour. [c]Mass % change between final and initial run. [d]Metal content % change between final and initial run [e]Catalytic activities retained between initial and final experiments.

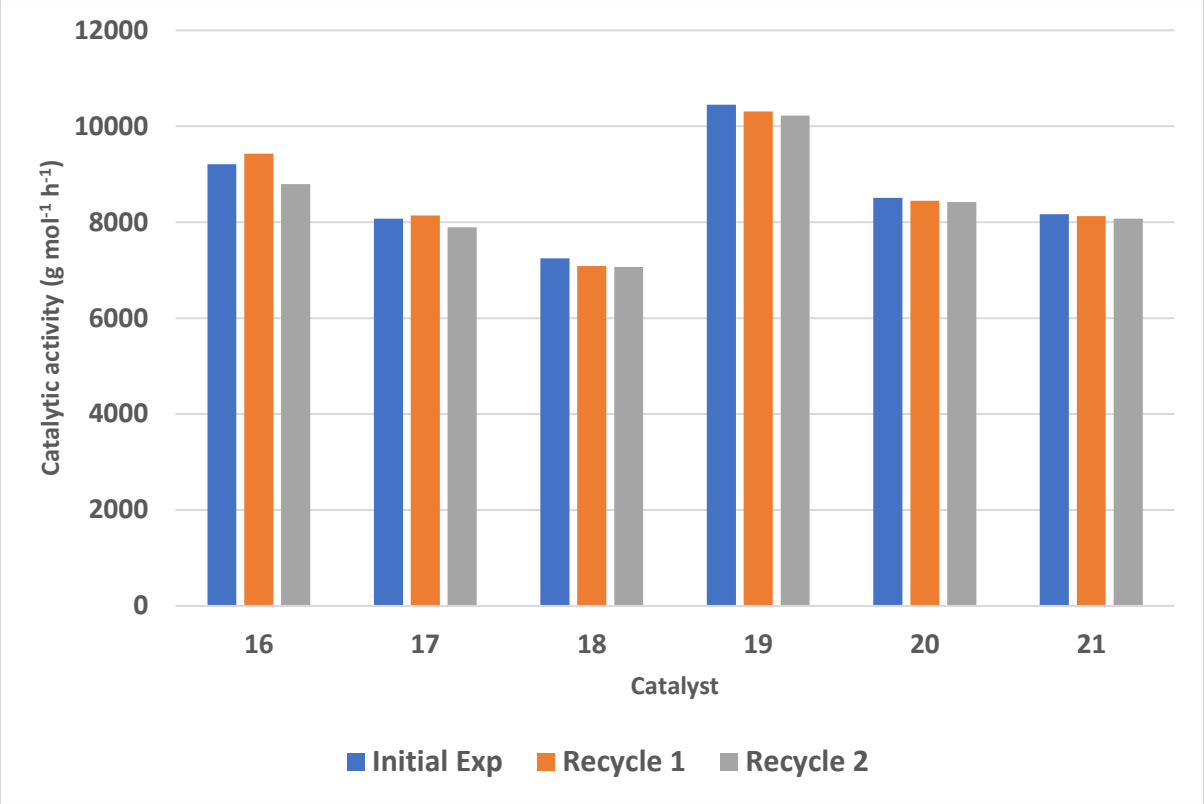

Figure 5.15: Catalytic activities of the Fe_3O_4 immobilized late transition metal complexes in the recycling experiments for ethylene oligomerization reactions (**Table 5.6**).

Most importantly, the selectivity of the immobilized catalysts was not compromised in the recycling experiments as depicted in **Figure 5.16**. For example, selectivities towards C_6 oligomer fractions of 87% and 86% were recorded in the initial and fifth experiments respectively (**Figure 5.16**). Similar trends were observed for the other catalysts. From this data, it is clear that the selectivity of the catalysts in the recycling experiments was retained, pointing to the absence of any significant changes in the nature of the active species (relative stabilities) during recycling experiments.

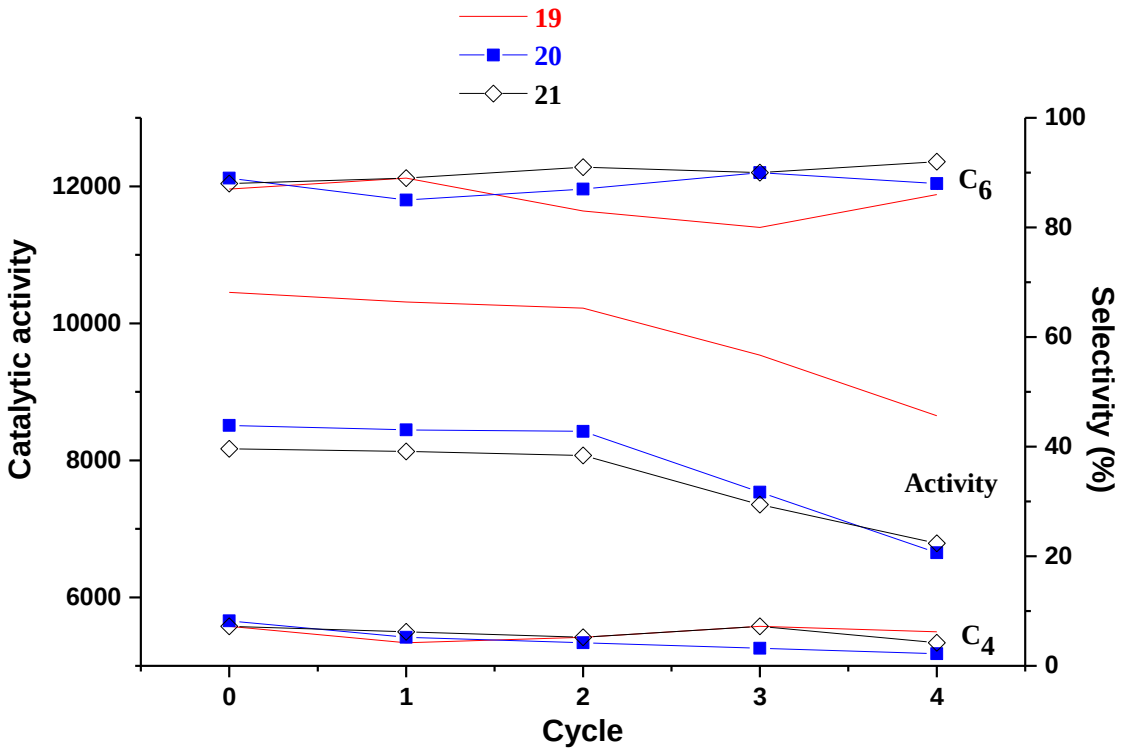

Figure 5.16: Comparative catalytic activity ($g_{oligomers}$ mol^{-1}(**M**) h^{-1}) and selectivity of catalysts **19**, **20** and **21** in the recycling experiments under standard conditions.

Even though the immobilized catalysts retained significant catalytic activities in the recycling experiments, the slight declines reported pointed to structural changes or degradation of the active species. We therefore attempted to understand the possible contributing factors to the loss of catalytic activities. In order to verify any possible structural changes, we carried out TEM and SEM analyses of the spent catalysts and compared with those of the fresh **19** catalysts. Notably, there were no remarkable changes on the morphology of used catalyst **19**, when compared to the images of the fresh catalysts (**Figure 5.17**). However, the SEM images of the fresh catalyst (**C**) and the spent catalyst (**D**) shown in **Figure 5.17**, revealed the presence of minor cracks in the spent catalyst. Thus, this data points to some structural changes, which

may be implicated for the observed reduction in catalytic activities in the recycling experiments.[18]

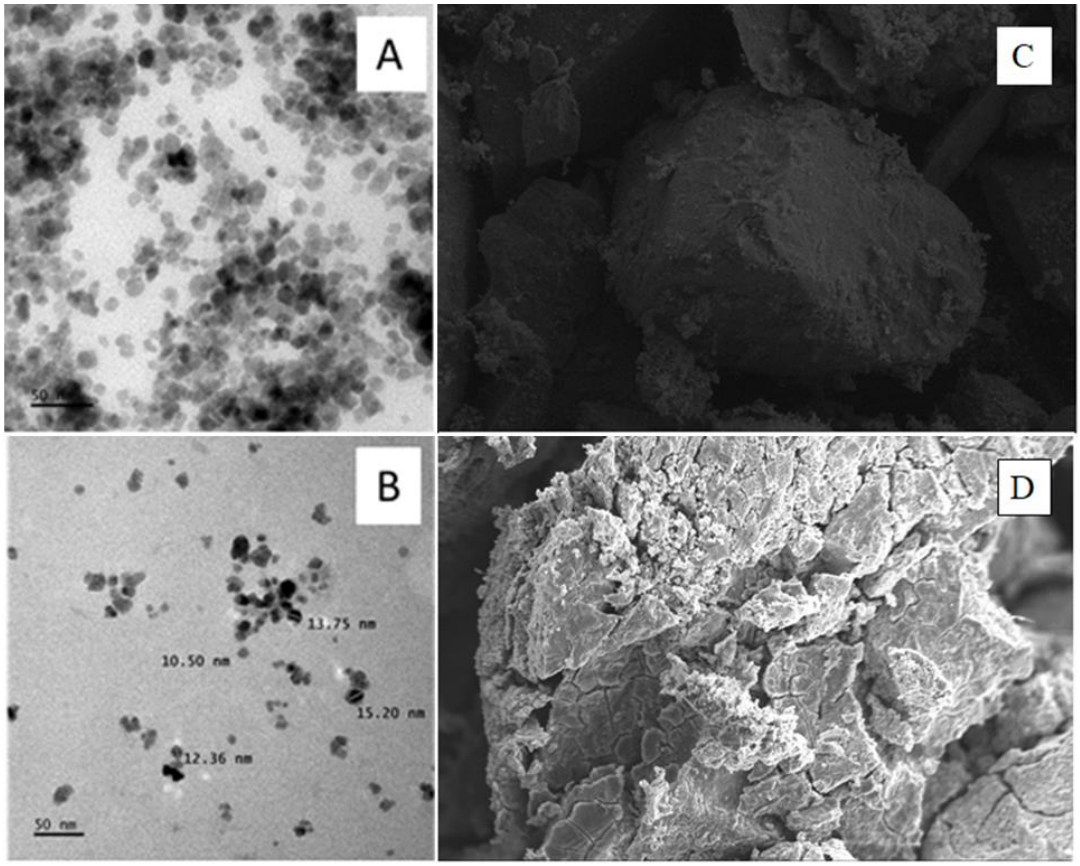

Figure 5.17: The TEM micrograms of the fresh (**A**) and spent (**B**) catalyst **19** showing slightly deformed morphology of the used catalyst. The SEM images of the fresh (**C**, Magnification = 20 µm) and gold coated spent (**D**, Magnification = 10 µm) catalyst **19**.

In another investigation, we analyzed the spent catalyst for metal content using EDX and ICP-OES (**Table 5.1**, entry 9 and **Table 5.7**). In the EDX analyses, a loss of 20% of the metal was recorded for catalyst **19@Fe_3O_4**, (**Table 5.1**, entry 9), hinting to possible leaching of the active species. This is consistent with the ICP-OES data, where metal content losses of 10 % -16 % were observed (**Table 5.7**). Hot filtration was then employed to determine if leaching could account for the reduced catalytic activities in the recycling experiments. This was performed

by adding 2.0 mL of the $EtAlCl_2$ equivalent to Al/M ratio of 200 to the filtrate and subjecting the system to ethylene pressure under the normal oligomerization conditions. Quantitatively, no catalytic activities were observed, pointing to minimal/absence of leaching of the active species. From these investigations, degradation of the active species may thus account for the observed minor reductions in catalytic activities in the recycling experiments.

Table 5.7: The % mass recovered after each run and metal contents recorded prior and post catalysts recycling experiments.

Entry	Complex	VSM (emu/g)	Mass recovered (%)		Metal contents (%)		
			1st % Catalyst recovery[a]	2nd % Catalyst recovery[b]	Fresh catalyst	Spent catalyst	% loss
1	**16**	62.06	93	98	0.542	0.468	14
2	**17**	54.46	96	94	0.379	0.319	16
3	**18**	52.11	95	99	0.456	0.406	11
4	**19**	67.96	99	97	0.688	0.632	8
5	**20**	66.90	98	96	0.447	0.407	9
6	**21**	67.00	99	98	0.656	0.593	10

[a]Calculated based on the amount of catalyst used in the initial run. [b]Calculated based on the amount of catalyst recovered and used in the second reaction.

5.4. Conclusions

This work captures the syntheses of Fe(II), Co(II) and Ni(II) complexes immobilized on Fe_3O_4 magnetic nanoparticles and their applications as recyclable catalysts in ethylene oligomerization reactions. The immobilized compounds were characterized using FT-IR, TGA, TEM, SEM, XRD, EDX, ICP-OES and VSM techniques. Activation of the Fe_3O_4 immobilized complexes using $EtAlCl_2$ in *n*-heptane and *n*-hexane solvents, predominantly produced C_6 oligomers. The use of aromatic solvents led to the formation of alkylated products. High catalytic activities to the tune of 97 600 $g_{oligomer}$ mol^{-1} (M) h^{-1} could be realized under optimized conditions. Both the nature of the anchoring ligand and metal atom affected the catalytic performance of the immobilized complexes. The immobilized catalysts were active in five consecutive runs, without significant loss in both catalytic activity and selectivity. The recovery efficiencies of the catalysts were dependent on their respective magnetic strengths. This work therefore represents a rare example of magnetically supported metal catalysts in ethylene oligomerization reactions, and thus opens a new paradigm shift in this field.

5.5. References

1. Busatta, C. A., Mignoni, M. L., de Souza, R. F., Bernardo-Gusmao, K., *Appl. Sci.* **2018**, *8*, 717-183.

2. Wang, S., Sun, W. -H., Redshaw, C., *J. Organomet. Chem.* **2014**, *751*, 714-717.

3. Adams, G. M., Weller, A. S., *Coord. Chem. Rev.* **2018**, *355*, 150-172.

4. Nyamato G. S., A., M. G., Ojwach, S. O., Akerman, M. P., *Appl. Organometal. Chem.* **2016**, *30*, 89-94.

5. Ojwach, S. O., Tshivhase, M. G., Guzei, I. A., Mapolie, S. F., Darkwa, J., *Can. J. Chem.*, **2005**, *83*, 843-853.

6. Severn, J. R., Chadwick, J. C., Duchateau, R., Friederichs, N., *Chem. Rev.* **2005**, *105*, 4073-4147.

7. Borges, P., Ramos Pinto, R., Lemos, M. A. N. D. A., Lemos, F., Vedrine, J. C., Derouane, E. G., Ribeiro, F. R., *Appl. Catal. A.* **2007**, *324*, 20-29.

8. Derouane, E. G., Lefebvre, C., Nagy, J. B., *J. Mol. Catal.* **1986**, *38*, 387-391.

9. Burwell, R. L., *Chem. Rev.* **1952**, *57*, 1034.

10. Dos Santos, J. H. Z., Krug, C., da Rosa, M. B., Stedile, F. C., Dupont, J., Camargo Forte, M., *J. Mol. Catal A: Chem* **1999**, *139*, 199-207.

11. Huang, Y., Zhang, R., Liang, T., Hu, X., Solan, G, A., Sun, W.-H., *Organometallics* **2019**, *38*, 1143-1150.

12. Henry, R., Komurcu, M., Ganjkhanlou, Y., Brogaard, R. Y., Lu, L., Jens, K.-J., Berlier, G., Olsbye, U., *Catal. Today* **2018**, *299*, 154-163.

13. Chughtai, A. H., Ahmad, N., Younus, H. A., Laypkov, A., Verpoort, F., *Chem. Soc. Rev.* **2015**, *DOI:10.1039/c4cs00395k*.

14. Kim, M. J., Ahn, S., Yi, J., Hupp, J. T., Notestein, J. M., Farha, O. K., Lee, S. J., *Catal. Sci. Technol.* **2017**, *7*, 4351-4354.

15. Shin, D. Y., Yoon, J. H., Baik, H., Lee, S. J., *Appl. Catal. A: Gen.* **2020**, *590*, 117363.

16. Azarifar, D., Mahmoudi-GomYek, S., Ghaemi, M., *App. Organometal. Chem.* **2018**, *DOI: 10.1002/aoc.4541*, 1-13.

17. Soleimani, E., Namivandi, M. N., Sepahvand, H., *Appl. Organometal. Chem.* **2016**, *31*, 1-8.

18. Keypour, H., Saremi, S. G., Noroozi, M., Veisi, H., *Appl. Organometal. Chem.* **2017**, *31*, 1-7.

19. Rezaei, S., Ghorbani-Choghamarani, A., Badri, R., *Appl. Organometal. Chem.* **2016**, *30*, 985-990.

20. Ngcobo, M., Ojwach, S. O., *J. Organomet. Chem.* **2017**, *846*, 33-39.

21. Rome, K., Mclntyre, A., *Chromatography Today.* **2012**, *52*, 52-55.

22. Chisem, I. C., Rafelt, J., Sheih, M. T., Chisem, J., Clark, J. H., Jachuck, R., Macquarrie, D., Ramshav, C., Scott, K., *Chem. Commun.* **1949**.

23. Jayamani, A., Nyamato, G. S., Ojwach, S. O., *J. Organomet. Chem.* **2019**, *903*, 120987.

24. Motswainyana. M, W., Onani, M. O., Ojwach, S. O., Omondi, B., *Inorganica. Chimica. Acta.* **2012**, *391*, 93-97.

25. Ngcobo, M., Nyamato, G. S., Ojwach, S. O., *Mol. Catal.* **2019**, *478*, 110590.

26. Tong, R., Wang, Y., Yang, G., Ma, A., Sun , K., Yang, H., Wang, J., *S. Afr. J. Chem.* **2015**, *68*, 99-104.

27. Campelj, S., Makovec, D., Drofenik, M., *J. Magn. Magn. Mater.* **2009**, *321*, 1346-1350.

28. Thanasekaran, P., Luo, T.-T., Wu, J.-Y, Lu, K.-L., *Dalton Trans.* **2012**, *41*, 5437-5453.

29. Jang, S., Hira, S. A., Annas, D., Song, S., Yusuf, M., Park, J. C., Park, S., Park, K. H., *Processes* **2019**, *7*, 422-453.

30. Yu, L., Zheng, L., Yang, J., *Mater. Chem. Phys.* **2000**, *66*, 6-9.

31. Lu, T., Zhang, S., Qi, D., Zhang, D., Vance, G. F., Zao, H., *Appl. Surf. Sci.* **2017**, *396*, 1604-1612.

32. Deng, H., Li, X., Peng, Q., Wang, X., Chen, J., Li, Y., *Angew. Chem. Int. Ed.* **2005**, *44*, 2782-2785.

33. Kolhatkar, A. G., Jamison, A. C., Litvinov, D., Willson, R. C., Lee, T. R., *Int. J. Mol. Sci.* **2013**, *14*, 15977-16009.

34. Lee, J.-H., Huh, Y.-M., Jun, Y.-W., Seo, J.-W., Jang, J.-T., Song, H.-T., Kim, S., Cho, E. J., Yoon, H.-G., Suh, J.-S., Cheon, J., *J. Nat. Med* **2006**, *13*, 95-99.

35. Sun, P., Hui, C., Khan, R. A., Di, J., Zhang, Q., Zhao, Y-H., *Sci. Rep.* **2015**, *5*, 12638-12650.

36. Favero, C., Closs, M. B., Galland, G. B., Stieler, R., Rossetto, E., Bernardo-Gusmao, K., *J. Catal.* **2019**, *377*, 63-71.

37. Hannaert, H., Haccuria, M., Mathieu, M. P., *Ind. Chim. Belge* **1967**, *67*, 156.

38. Ojwach, S. O., Darkwa, J., *J. Catal. Sci. Technol.* **2019**, *9*, 2078-2096.

39. Yankey, M., Obuah, C., Guzei, I, A., Osei-Twum, E., Hearne, G., Darkwa, J., *Dalton Trans.* **2014**, *43*, 13913-13923.

40. Rossetto, E., Nicola, B. P., de Souza, R. F., Bernardo-Gusmao, K., Pergher, S. B. C., *J. Catal.* **2015**, *323*, 45-54.

41. Pierro, I., Zanchin, G., Parisini, E., Marti-Rujas, J., Canetti, M., Ricci, G., Bertini, F., Leone, G., *Macromelecules* **2018**, *51*, 801-814.

42. Smarun, A. V., Shahreel, W., Pramono, S., Koo, S. Y., Tan, L. Y., Ganguly, R., Vidovic, D., *J. Organomet. Chem.* **2017**, *834*, 1-9.

43. Andrei, R. D., Popa, M. I., Fajula, F., Hulea, V., *J. Catal.* **2015**, *323*, 76-84.

44. Rossetto, E., Caovilla, M.,Thiele, D., de Souza, R. F., Bernardo-Gusmao, K., *Appl. Catal. A.* **2013**, *454*, 152-159.

45. Suo, H., Solan, G. A., Ma, Y., Sun, W.-H., *Coord. Chem. Rev.* **2018**, *372*, 101-116.

46. Johnson, L. K., Killian, C. M., Brookhart, M., *J. Am. Chem. Soc.* **1995**, *117*, 6414.

47. Rossetto, E., Nicola, B. P., de Souza, R. F., Bernardo-Gusmao, K., Pergher, S. B. C., *Appl. Catal. A: Gen.* **2015**, *502*, 221-229.

48. Moussa, S., Arribas, M. A., Concepcion, P., Martinez, A., *Catal. Today* **2016**, *277*, 78-88.

49. Shin, M., Jeong, H., Park, M.-J., Suh, Y.-W., *Appl. Catal. A: Gen.* **2020**, *591*, 117376.

50. Canivet, J., Aguado, S., Schuurman, Y., Farrusseng, D., *J. Am. Chem. Soc.* **2013**, *135*, 4195-4198.

51. Nyamato, G. S., Ojwach, S. O., Akerman, M. P., *Organometallics* **2015**, *34*, 5647-5657.

52. Huang, C., Zakharov, V. A., Semikolenove, N. V., Matsko, M. A., Mahmood, Q., Talsi, E. P., Sun, W.-H., *J. Catal.* **2019**, *372*, 103-108.

53. Li, Y.-G., Pan, L., Zheng, Z.-J., Li, Y.-S., *J. Mol. Catal A: Chem* **2008**, *287*, 57.

54. Liu, S., Zhang, Y., Huo, Q., He, S., Han, Y., *J. Spectrosc.* **2014**, *2015*, 1-7.

55. Xiao, L., Jonson, K. E., Treble, R. G., *J. Mol. Catal A: Chem.* **2014**, *214*, 121-127.

56. Mlinar, A. N., Shylesh, S., Ho, C. O., Bell, A. T., *ACS. Catal.* **2014**, *4*, 337-343.

57. Kumar, K., Godeto, T., Darkwa, J., *J. Organomet. Chem* **2016**, *818*, 137-144.

CHAPTER SIX

Probing the effect solid supports using SBA-15 and MCM-41 immobilized Fe(II), Ni(II) and Co(II) complexes for ethylene oligomerization reactions

6.1. Introduction

Production of oligomers from ethylene gas is one of the most considerable subject both in academic and industrial sectors owing to its vital contribution in providing building blocks for petrochemical industries.[1] Products of ethylene oligomerization are also used in the synthesis of lubricants, surfactants, alcohols, amines and acids. Homogeneous and heterogeneous catalysts both can efficiently catalyse ethylene oligomerization reactions.[2] Over the past decades, significant role of the homogeneous catalysts in the oligomerization of ethylene reactions have been highlighted with nickel being the most studied late transition metal.[3-5] Nevertheless, characterized by well-defined active sites, these catalysts suffer a major drawback, which is the difficulty in separating catalysts, products and solvent from the reaction mixture.[6] As a result, the designing and developing a separable single-sited catalyst for these catalytic transformations would be breakthrough. In addition, this will also bridge the gap between homogenous and heterogeneous catalysis in the oligomerization of ethylene by combining advantages of both catalysis processes.

Among various methods available for immobilizing homogeneous catalysts, covalent binding on the inorganic or organic support seem to be the most attractive alternative to retaliate on this major drawback.[7] These support materials include metal organic frameworks (MOFs),[8-9] porous organic polymers (POPs),[10] zeolites,[11] and silica.[12] Another alternative which has not been fully explored, is the use of biphasic ionic liquids for metal-catalyzed ethylene

oligomerization reactions.[13] Nevertheless, using silica as an inorganic support to immobilise the homogeneous catalyst is accompanied by various advantages including enhanced thermal and chemical stability, large surface area and large number of sites to bind the organic molecules due to the flexible silanol functional groups.[14]

In an attempt to combat difficulties in catalyst separation using silica support, Kumar *et al.*,[15] recently reported both homogeneous and MCM-41 mesoporous heterogenized nickel(II) and palladium(II) pre-catalysts for ethylene oligomerization reactions. After activation with $EtAlCl_2$, these complexes form catalytically active catalysts capable of dimerizing acetylene to mainly butenes and Friedel-Crafts alkylation of the solvent toluene resulting to the formation of regioisomers of *mono*-, *di*- and *tri*-butyltoluenes being reported. Most importantly, they able to recover (through filtration process), recycle and reuse the immobilized catalysts for up three runs with some loss of catalytic activity due to the catalyst deactivation by the oxygen invasion. It also worth mentioning that the pre-catalyst was activated once with $EtAlCl_2$ and remained active throughout the three experiments.

In another instance, using the β-diimine nickel(II) complexes, Rossetto *et al.*[16] showed that their SBA-15 immobilized complexes can be recovered by the removal of the products using a cannula and catalyst reused for three successive runs with a marginal loss of catalytic activity observed after the third recycling experiment. In another study, using the iron(II) based catalysts chelated by tridentate di(imino)pyridine ligands both in homogeneous and heterogeneous processes, Schmidt *et al.*,[17] showed that immobilization can also be achieved by fixing the homogeneous catalyst on the heterogenized co-catalyst. In this work they heterogenized MAO. The complexes in this interesting work showed high catalytic activity

after activation with either MAO or with a heterogeneous co-catalyst composed of partially hydrolysed triethylaluminum and silica gel. It is noteworthy mentioning that supported catalysts often display reduced catalytic activities in comparison with their homogeneous analogues.[18] Nevertheless, we cannot turn a blind eye on the recent report by Tuskaev *et al*.,[19] where it was observable that immobilized complexes sometimes display higher catalytic activity and unsurprisingly better product selectivity, especially towards 1-butene formation. This is better understood based on the coordination environment of the metal centre. Similarly, Baluheyan *et al*.[20] has previously reported enhanced catalytic activity of the immobilized complexes than their homogeneous counterparts.

Over the past decade, our research focus has been largely centred on the design and development of late transition metal based homogeneous catalysts for ethylene oligomerization reaction.[21-24] Compelled by the previously reported catalytic performances of the immobilized complexes and in the pursuit of designing separable versions of our homogeneous catalysts, herein we report the synthesis, structural characterization and application of the immobilized Ni(II), Co(II) and Fe(II) complexes in ethylene oligomerization reactions. The effect of immobilizing the complexes is described in detail together with their leaching experiments and post-catalytic characterization.

6.2. Experimental section

6.2.1. Chemicals and characterization instrumentation

All synthetic manipulations were performed using standard Schlenk-line techniques under a nitrogen atmosphere. The solvents were obtained from Merck and dried or distilled using appropriate methods. The chemicals; salicylaldehyde (98 %), 2'-hydroxyacetophenone (98 %),

(3-aminopropyl)triethoxysilane (APTES ≥98 %), cobalt(II) chloride (97 %), iron(II) chloride (98 %), nickel(II) chloride (98 %), Santa Barbara Amorphous-15 (SBA-15, 99 %), Mobil Composition of Matter number 41 (MCM-41, 98 %) and ethylaluminum dichloride solution (1.0 M in hexanes) were obtained from Sigma Aldrich and used as received. ^{1}H NMR and ^{13}C NMR (100 MHz) spectra were recorded on a 400 MHz Bruker Ultra shield NMR spectrometer in $CDCl_3$ and DMSO-d_6 solvents. The infrared spectra were recorded on a Perkin Elmer, Spectrometer 100. LC Premier micro-mass Spectrometer model LCMS-2020, was used for mass spectral analyses. Thermogravimetric data was collected on a Perking-Elmer TGA 4000 instrument equipped with Pyris software at 50-800˚C at a heating rate of 20 ˚C/min. Approximately 10-50 mg of each sample was used for each run. Varian CP-3800 gas chromatograph equipped with a flame ionization detector (FID) and a CP-Sil 5 CB (30 m x 0.2 mm x 0.25 µm) capillary column capillary column was used for GC analyses (GC conditions: starting temperature 40 ˚C for 5 min, the heating rate of 10 ˚C/min up to 250 ˚C) while GC-MS analyses were performed on a Shimadzu GCMS-QP2010SE.

6.2.2. Synthesis of the SBA-15 and MCM-41 immobilized Ni(II), Fe(II) and Co(II) complexes.

6.2.2.1. Synthesis of SBA-15 and MCM-41 immobilized ligands.

*6.2.2.1.1. Synthesis of **L8H**@SBA-15 (**L9**)*

The solid support SBA-15 (1.01 g) was transferred into 100 mL round-bottomed flask and to it 0.12 g of ligand **L8H** was added followed by the addition of dry toluene (20 mL). The slurry was sonicated for 15 minutes at room temperature and was then refluxed for 14 h under nitrogen atmosphere. When the reaction period was over, the solid was filtered and washed repeatedly with toluene (3 x 20 mL) followed by copious amounts of dichloromethane. The light yellow

solid obtained was dried under vacuum at ambient temperature for ~10 h. Mass of yellow product obtained: 0.953 g. FT-IR (cm^{-1}): $\nu_{(O-H)}$: 2305; $\nu_{(C=N)}$:1641; $\nu_{(Si-O)}$: 1035, 801.

*6.2.2.1.2. Synthesis of **L8H**@MCM-41 (**L10**)*

The immobilized ligand was synthesized in a similar manner described for **L9**. The solid support MCM-41 (1.01 g) was transferred into 100 mL round-bottomed flask and to it 0.10 g of ligand **L8** was added followed by the addition of dry toluene (20 mL). The slurry was sonicated for 15 minutes at room temperature and refluxed for 14 h under nitrogen atmosphere. The filtered solid was washed repeatedly with toluene (3 x 20 mL) followed by copious amounts of dichloromethane. The light yellow solid obtained was dried under vacuum at ambient temperature for ~10 h. Yield: 1.048 g. FT-IR (cm^{-1}): $\nu_{(O-H)}$: 2107; $\nu_{(C=N)}$: 1630; $\nu_{(Si-O)}$: 1058, 965.

6.2.2.2. Synthesis of silica immobilized complexes.

*6.2.2.2.1. **[**Ni(**L9**)$_2$Cl$_2$@SBA-15] (**22**)*

The complex **22** was synthesized by dissolving the ethanol solution of **L9** (0.11 g, 10 mL) in a 10 mL ethanol solution of $NiCl_2$ (0.065 g, 0.50 mmol) resulting in a light-yellow solution. The resultant-coloured solution was allowed to reflux for 24 h at 60 ˚C under nitrogen atmosphere. After the reaction completion the reaction was cooled to room temperature, filtered and the product dried in the oven at 100 ˚C for 1 h. Light yellow powder filtered. Yield: 0.066 g. FT-IR (cm^{-1}): $\nu_{(O-H)}$: 2240, 2099; $\nu_{(C-O)}$: 1740; $\nu_{(C=N)}$: 1635; $\nu_{(Si-O)}$: 1055, 798.

The subsequent complexes were **23**-**25** were synthesized in a similar manner described for complex **22**.

*6.2.2.2.2 [Co(**L9**)$_2$Cl$_2$@SBA-15] (**23**)*

L9 (0.10 g) and $CoCl_2$ (0.051 g, 0.50 mmol). Light blue powder recovered. Yield: 0.058 g. FT-IR (cm^{-1}): $\nu_{(O-H)}$: 2103, 2114; $\nu_{(C=N)}$: 1623; $\nu_{(Si-O)}$: 1058, 800.

*6.2.2.2.3. [Fe(**L9**)$_2$Cl$_2$@SBA-15] (**24**)*

L9 (0.12 g) and $FeCl_2$ (0.065 g, 0.50 mmol). Brown powder. Yield: 0.081 g. FT-IR (cm^{-1}): $\nu_{(O-H)}$: 2324, 2119; $\nu_{(C-O)}$: 1740; $\nu_{(C=N)}$: 1616; $\nu_{(Si-O)}$: 1049, 800.

*6.2.2.2.4. [Ni(**L10**)$_2$Cl$_2$@MCM-41] (**25**)*

Synthesis of **25** was achieved through a dissolution of **L10** (0.11 g) in 10 mL dry ethanol and a subsequent addition of 10 mL solution of $NiCl_2$ (0.065 g, 0.50 mmol) resulting in a light-yellow solution. The resultant-coloured solution was allowed to reflux for 24 h at 60 ˚C under nitrogen atmosphere. After the reaction completion the reaction was cooled to room temperature, filtered and the product dried in the oven at 100 ˚C for 1 h. Cream white powder was obtained. Yield: 0.060 g. FT-IR (cm^{-1}): $\nu_{(O-H)}$: 3422, 2295, 2226, 2120; $\nu_{(C=N)}$:1630; $\nu_{(Si-O)}$:1051, 962.

6.2.3. Ethylene oligomerization reaction catalytic experiments

The ethylene oligomerization experiments catalysed by the silica immobilized complexes were carried out in a stainless-steel reactor fitted with a 100 mL glass chamber and a magnetic stirrer bar. A pre-weighed amount of the immobilized pre-catalyst (10 µmol) was transferred into a dry Schlenk tube under nitrogen atmosphere and chlorobenzene (10 mL) was added using a syringe. The amount of the complex used was calculated based on the metal contents determined using ICP-OES. Appropriate amount of a co-catalyst ethylaluminum dichloride ($EtAlCl_2$, 2 mmol) was then injected into the Schlenk tube containing the pre-catalyst. The solution mixture in the Schlenk tube was then transferred through the cannula into the reactor

and heated to 30 °C while stirring on a hot plate. Prior to the reaction commencement, the reactor was flashed several times with ethylene gas and ethylene pressure was set at 10 bar and the reaction was timed for 1 h. After the reaction period, the reactor was cooled to approximately -10 °C using liquid nitrogen and excess ethylene gas vented off. The reaction was then quenched by the addition of 10 % hydrochloric acid (2 mL). A portion was sampled in a GC-vial for GC-FID and GC-MS analyses to determine the identity and distribution of the products. The mass of the product formed was determined using the calibration curve of the R-factors for the standards versus number of carbons of the standards (Equations 1 and 2).[25] Hexene (0.849), octene (0.744), decene (0.496), dodecene (0.389) and tetra-decene (0.327) standards were used to obtain calibration curve and tetradecene was used as an internal standard. The R-factor for butene was extrapolated as 0.981 from the calibration curve. The catalytic activity ($g_{oligomer}$ mol^{-1} (M) h^{-1}) was determined using the percentage metal content in the immobilized complexes as determined from ICP-OES analyses.

6.2.4. Recycling experiments

The recycling experiments were performed in a similar manner described for standard ethylene oligomerization reaction procedure. In recycling the spent catalyst, centrifugation and filtration techniques were used to recover the spent catalyst and the products were removed for analyses. The recovered pre-catalyst was washed several times with the solvent used for the reactions and with ethanol. The dried spent catalyst was weighed prior to the subsequent experiment. Recycling experiments were accomplished by adding 30 mL of fresh *n*-heptane and the appropriate amount of a fresh $EtAlCl_2$ co-catalyst (2 mL).

6.3. Results and discussion

6.3.1. The synthesis of SBA-15 and MCM-41 silica immobilized ligands and Ni(II), Co(II) and Fe(II) complexes.

The synthesis of N^O phenol((triethoxysilyl)propylimino) pre-ligand **L8H** have been previously reported in **Chapter 5**. Therefore, the silanol ligand **L8H**, was immobilized on SBA-15 and MCM-41 silica supports to produce ligands **L9** and **L10** respectively (**Scheme 6.1**). The reactions of **L9** and **L10** with either $NiCl_2$ or $FeCl_2$ or $CoCl_2$ salts in dry ethanol produced the desired Ni(II), Co(II) and Fe(II) silica immobilized complexes **22-25**. Overall, a sequential approach was adopted in the synthesis of silica immobilized complexes as depicted in **Scheme 6.1**. The formation of the compounds was confirmed using NMR and IR spectroscopies, mass spectrometry, thermogravimetric analysis (TGA), transmission electron microscopy (TEM), scanning electron microscopy (SEM), energy dispersive x-ray microscopy (EDX) and inductively coupled plasma atomic emission spectroscopy (ICP-AES).

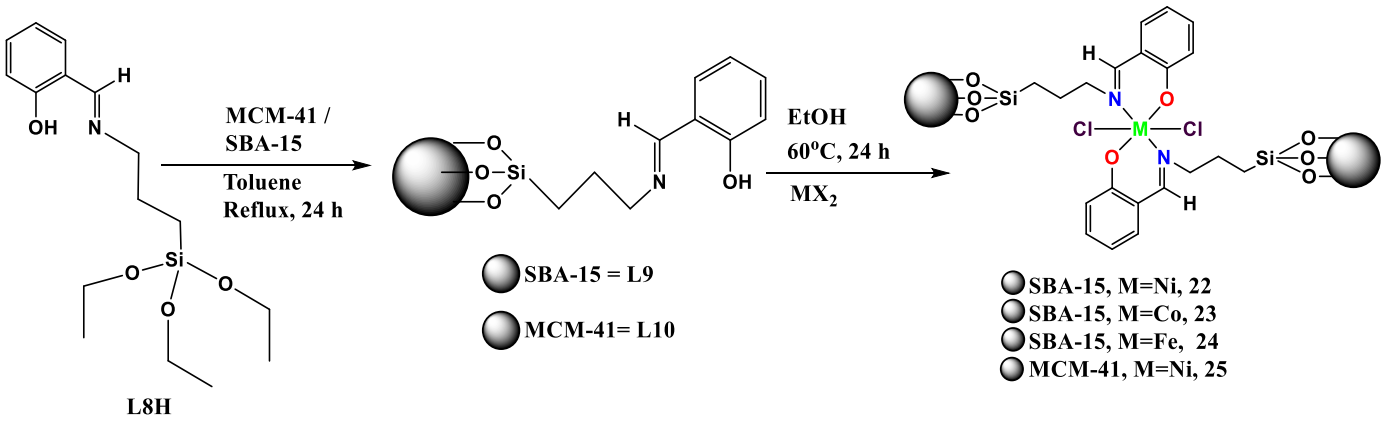

Scheme 6.1: The synthetic procedure of the SBA-15 and MCM-41 immobilized Ni(II), Fe(II) and Co(II) complexes of imino(phenol) N^O donor ligands.

Infrared spectroscopy was very helpful in confirming the formation of the anchored ligands and their respective complexes. **Figure 6.1** illustrates the functional groups changes that

occurred during the synthesis of the respective immobilized complexes **22** and **25**. Firstly, the $\nu_{C=N}$ peak which appeared around 1610 cm^{-1} for the free silanol ligand shifted to a higher frequency (~ 1630 cm^{-1}) in the IR spectra of the immobilized ligands and complexes with very low intensity. This showed that the ligand was successfully anchored on SBA-15 and MCM-41 silica supports which appeared to cloud other functional groups of the ligand.[26] Furthermore, a successful conversion of the Si-OCH_2CH_3 functional group to Si-O-Si was manifested by the disappearance of the doublet peak around 1106 cm^{-1} and 1013 cm^{-1} in the fingerprint region of the immobilized ligands and complexes. This peak appeared as a singlet peak around 1052-1068 cm^{-1} as illustrated in **Figure 6.1** revealing that the silanol was successfully grafted onto SBA-15 and MCM-41 silica supports.

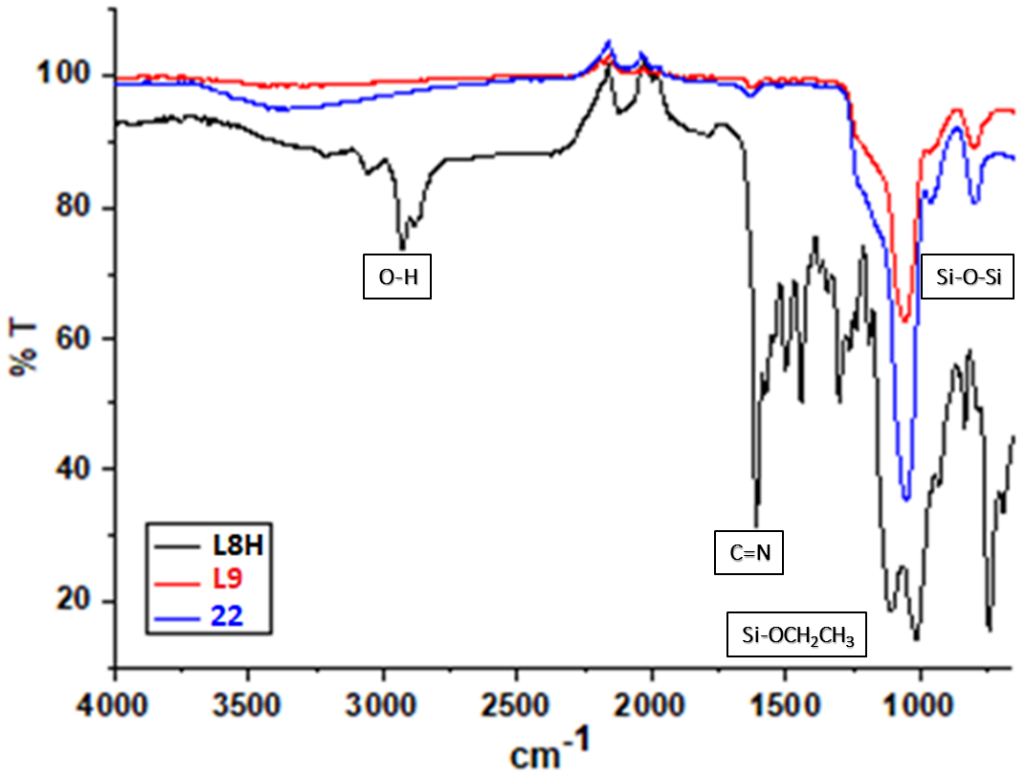

Figure 6.1: IR spectra of the silanol ligand **L8H**, immobilized ligand **L9** and its corresponding immobilized Ni(II) complex **22**, showing the disappearance of the doublet peak around 1100 cm^{-1} of Si-OCH_2CH_3 group in IR spectrum of **L8H** manifesting the success of immobilization.

The thermal stability of the synthesized compounds was investigated with the aid of the thermogravimetric analyses (TGA). The success of covalently binding the ligand on SBA-15 and MCM-41 was clearly manifested by the resistance of the material to the temperature increment implying that the thermal stability of the compounds was improved upon immobilization as shown in **Figure 6.2**. The weight loss occurred at temperature below 130 °C was attributed to the loss of adsorbed water molecules whilst the decomposition of the organic material occurred at a temperature between 220-480 °C. Approximately 75 - 85 % of the immobilized ligands and complexes remained after each TGA run revealing that the ligands and complexes were successfully immobilized on the SBA-15 matrix. The TGA results obtained, are very comparable to those reported by Rossetto *et al*.[27]

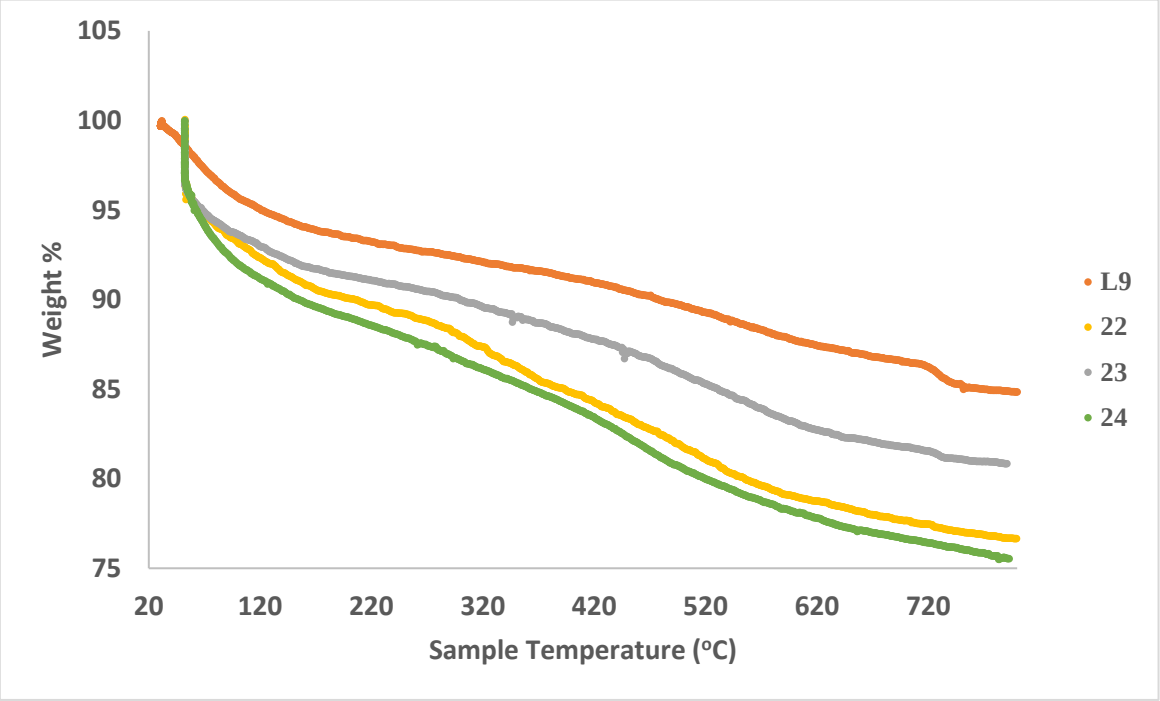

Figure 6.2: The TGA curves of the MCM-41 immobilized ligand **L9** and its Ni(II), Co(II) and Fe(II) complexes **22-24** respectively.

Transmission electron microscopy was used to determine the morphology of immobilized ligands and complexes. **Figure 6.3** and **Figure 6.4** are showing the TEM images of the

immobilized ligands and complexes respectively. The TEM images depict the distribution of the ligands (ash-dark spots) and metal (very dark spots) in the matrix. Furthermore, low magnitude of agglomeration was revealed by the images implying an even distribution of the ligands and metals in the silica support. In addition, the TEM images of the complexes illustrated spherical shapes and size variations of the complexes.

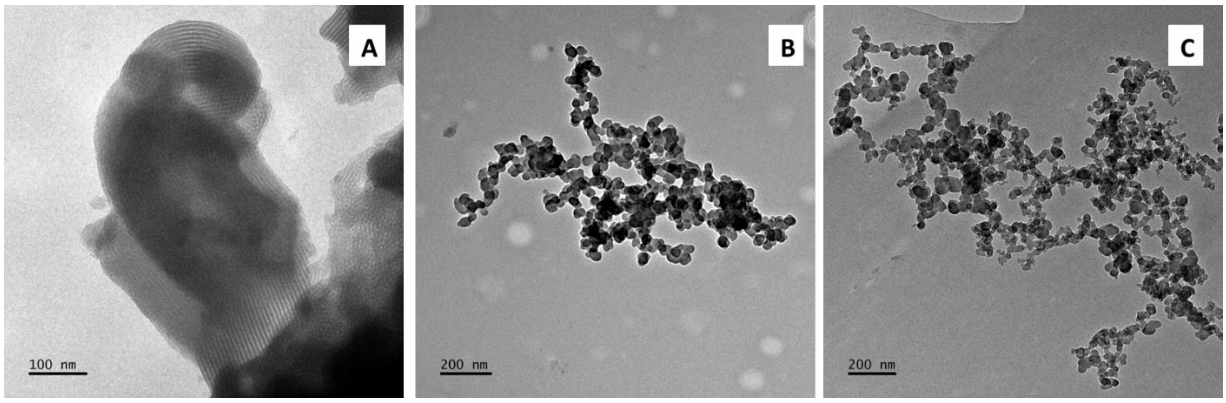

Figure 6.3: The TEM images of functionalized thick-walled hexagonal shaped SBA-15-A, immobilized ligand **L9**-B and **L10**-C respectively.

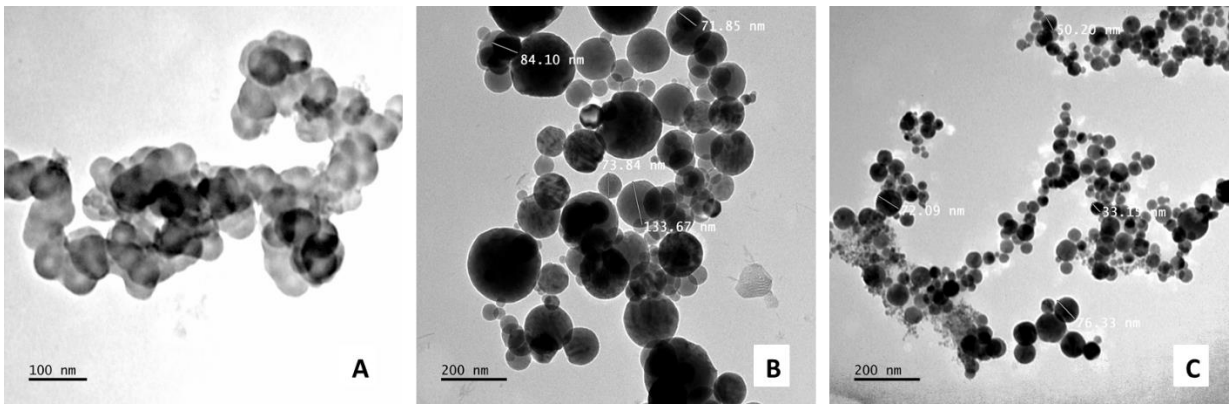

Figure 6.4: The TEM images of immobilized complexes **22-24** of ligand **L9** showing spherical shapes of the SBA-15 immobilized complexes.

Scanning electron microscopy (SEM) was also utilized in the determination of the morphology of the synthesized compounds. The SEM images of SBA-15 immobilized ligand **L9** and its

respective complexes shown in **Figure 6.5**, revealed no extensive changes on morphology of the ligand upon the formation of the respective immobilized Ni(II), Co(II) and Fe(II) complexes. Accordingly, the results obtained were in good agreement with TEM data which showed that all the compounds exhibit spherical particle shapes.

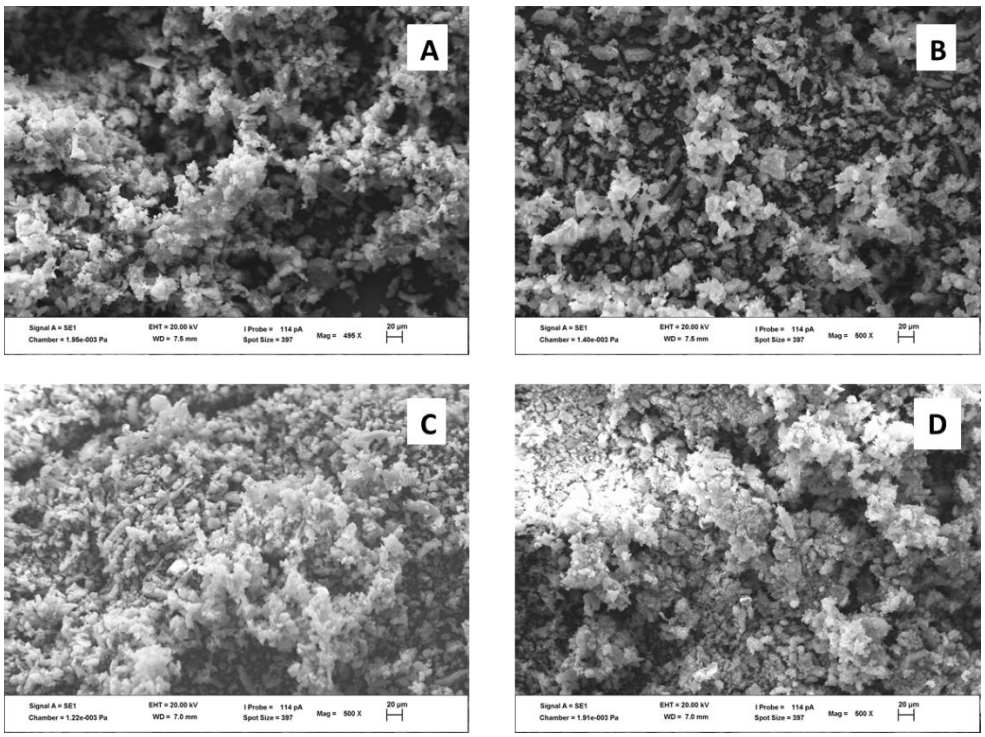

Figure 6.5: SEM Micrographs of the ligand **L9**-A and its complexes **22**-B, **23**-C and **24**-D respectively.

X-ray diffractometer was also utilised in the determination of the crystallinity possessed by the complexes. The diffractogram of the immobilized complexes (**Figure 6.6**) showed reflections (Miller indices: d_{100}, d_{110}, d_{200}) which are typically a characteristic of a hexagonal lattice of SBA-15.[27] Lower intensities observed for 110 and 200 reflections are due to the anchoring of the organic surfaces and the addition of the metal centre to the matrix which may distort the regularly ordered SBA-15. Nevertheless, the presence of d_{100}, d_{110} and d_{200} reflection indices

was an indication that the matrix was not severely distorted upon the formation of the respective complexes.

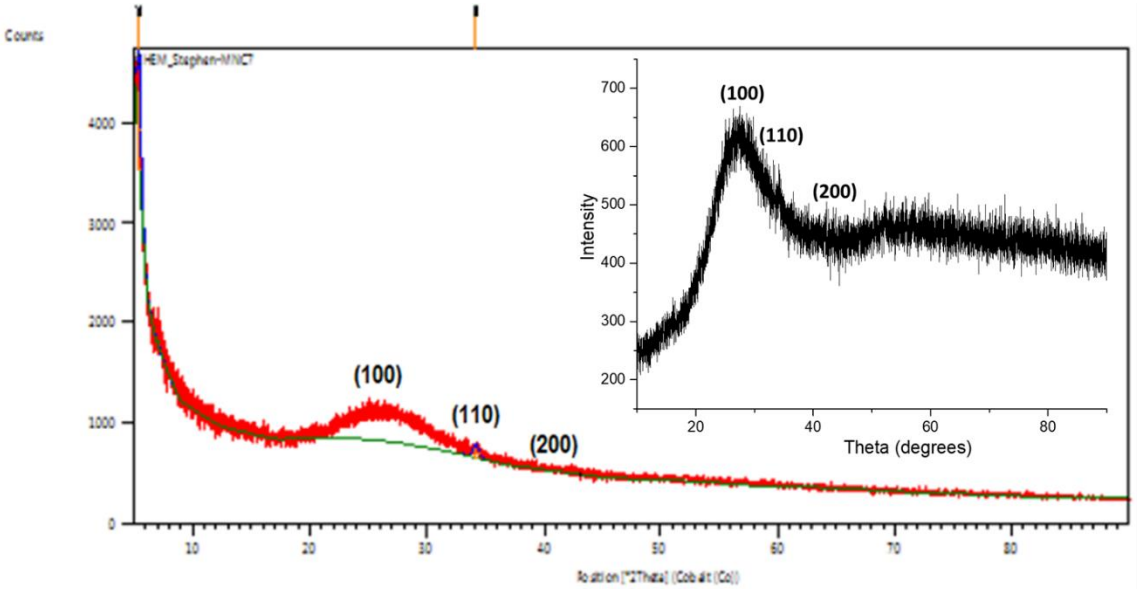

Figure 6.6: The typical XRD pattern observed for the immobilized Ni(II) complex, **22**.

Energy dispersive X-ray microscopy (EDX) was used to investigate the composition of the catalysts. The EDX spectra of the complexes in **Figure 6.7** revealed the presence of Si, C, O and Cl and the respective metal. The presence of carbon, oxygen and nitrogen confirmed that the silica support is covered with the functional groups of the ligands. The weight percentage content of the metal in the immobilized complexes was determined to be in the range of 0.577-7.35 % and the results are summarized in **Table 6.1.** Kumar *et al.*[15] reported a Ni metal composition by weight of 0.82 and 0.93 % for their N^N donor immobilized complexes and these are comparable with our reported Ni content for the complexes. Nevertheless, these results suggest some variations on the ability of the ligands to chelate the Ni, Co and Fe metal centres.

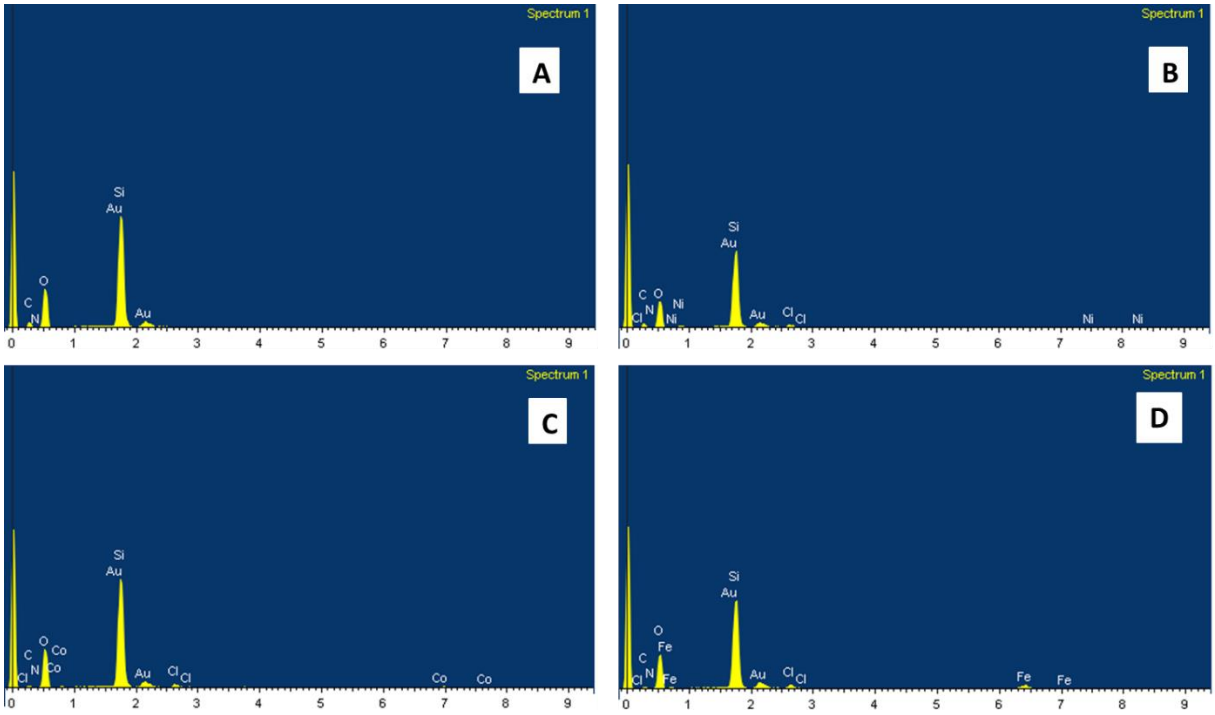

Figure 6.7: EDX spectra of the immobilized ligand **L9**-A, and its corresponding complexes **22**-B, **23**-C and **24**-D respectively.

Using ICP-OES, we further investigated the concentration of the metals in the immobilized complexes. The metal contents obtained from ICP-OES are also summarized in **Table 6.1**. Notably, there was a good agreement between the EDX and ICP-OES results. For example, 0.577 % and 0.568 % of Ni(II) metal contents was quantified for **22** using EDX and ICP-OES respectively (**Table 2**, **entry 1**). Nevertheless, slight variations observed in the metal weight percentage of the complexes was attributed to the random distribution of the metal in the solid matrix for EDX measurements whilst for ICP-OES the measurements were acquired on the sample solution which mimic a homogeneous mixture better than the solid matrix.

Table 6.1: The metal contents of Ni(II), Co(II) and Fe(II) of the SBA-15 and MCM-41 silica immobilized complexes as determined using EDX and ICP-OES.

Entry	Compound	Metal (wt%)[a] (EDX)	Metal (wt%)[b] (ICP-OES)
1	**22**	0.577	0.568
2	**23**	0.987	0.953
3	**24**	7.35	6.92
4	**25**	1.55	0.960

[a]Weight % obtained from EDX.
[b]Metal contents determined using 10 mL of standard solutions (2.5 ppm, 5 ppm, 10 ppm, 25 ppm, 50 ppm) and samples.

6.3.2. Ethylene oligomerization reactions, recyclability and reusability of the immobilized complexes.

6.3.2.1. Catalytic performance of the complexes in ethylene oligomerization reactions

The immobilized complexes **22-25** were screened as potential catalysts for ethylene oligomerization reactions in various solvents. The complexes were activated using ethylaluminum dichloride, $EtAlCl_2$, co-catalyst (1 mol/L in hexanes and 25% w/w in toluene). The pre-elementary catalytic reactions were performed in toluene, *n*-heptane, hexane and chlorobenzene solvents. Analyses of the ethylene oligomerization products using GC-FID (**Figure 6.8**) and GC-MS (**Figure 6.9**) confirmed the formation of ethylene oligomers and alkylated products depending on the solvent used as shown in **Scheme 6.2**. As we have previously discussed in Chapter 5, lower catalytic activities are generally obtained in *n*-heptane and *n*-hexane solvents, in comparison to toluene and chlorobenzene solvents. For example, catalyst **22** afforded catalytic activities of 92 800 $g_{oligomers}$ mol^{-1} (M) h^{-1}, 75 000 $g_{oligomers}$ mol^{-1} (M) h^{-1}, 58 700 $g_{oligomers}$ mol^{-1} (M) h^{-1} and 35 400 $g_{oligomers}$ mol^{-1} (M) h^{-1} in chlorobenzene,

toluene, *n*-hexane and *n*-heptane solvents respectively (**Table 6.2, entries 1** and **5-7**). This is common and has been attributed to the poor solubility of ethylene monomer in *n*-heptane and *n*-hexane solvents.[28]

Profoundly, the nature of the solvent also had a significant influence on the product distribution in ethylene oligomerization reactions. Notably, inert solvents, *n*-heptane and *n*-hexane solvents resulted in the formation of mainly C_4 (26% and 35% respectively) and C_6 (71% and 65% respectively) oligomers, **Table 6.2**, **entries 1** and **6**.[29] In contrast, the use of chlorobenzene and toluene solvents led to the partial alkylation of the aromatic solvents by the pre-formed oligomers. While alkylation of toluene solvent by the pre-formed oligomers is now well established,[23, 30] tandem alkylation of chlorobenzene solvent by ethylene oligomers is a rare scenario with few reports present in literatue.[31-32] This phenomenon is attributed to the high Lewis acidity of the activated species, SBA-15 support and $EtAlCl_2$ co-catalyst.[33] We thus used *n*-heptane solvent in further experiments due to the selectivity towards the targeted ethylene oligomers.

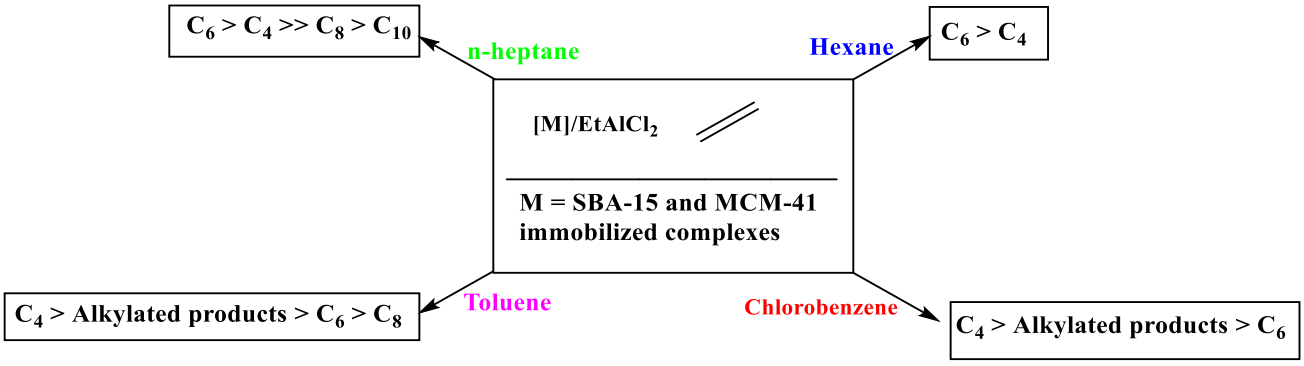

Scheme 6.2: Ethylene oligomerization reactions facilitated by SBA-15 and MCM-41 immobilized late transition metal complexes in different solvent mediums.

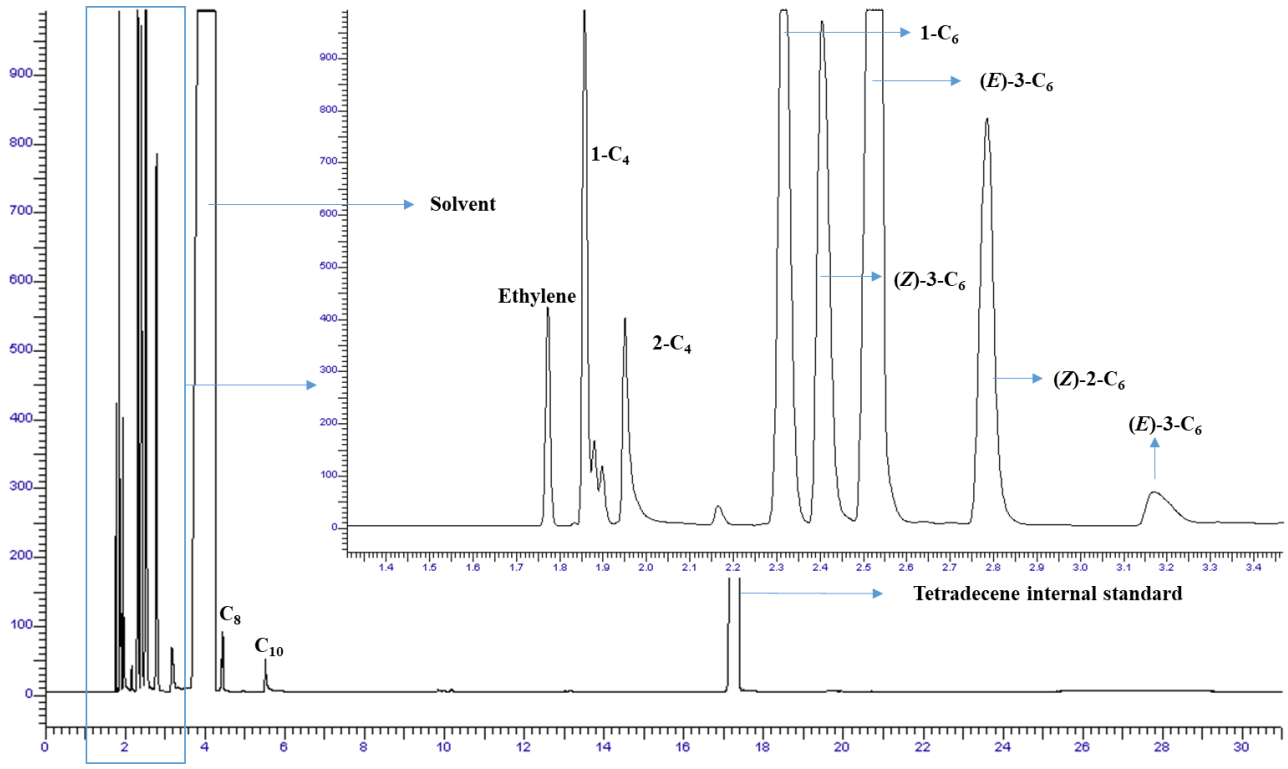

Figure 6.8: The GC-FID traces of the products formed when **22**/$EtAlCl_2$ system is used to catalyse ethylene oligomerization reaction in n-heptane solvent (**Table 6.2**, entry 1).

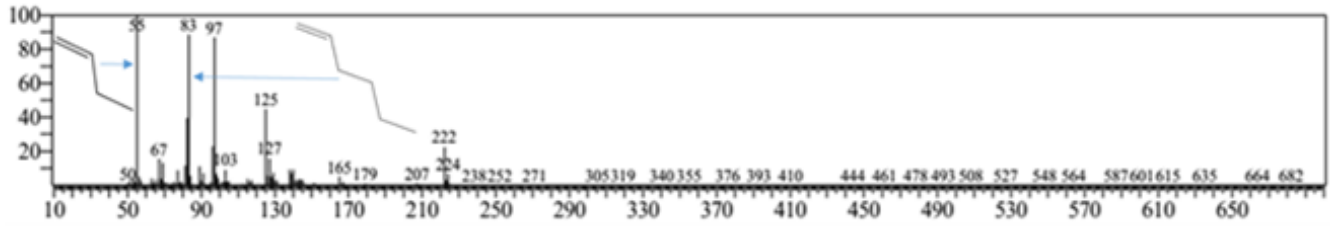

Figure 6.9: The GC-MS plot of the complexes depicting the molar masses of C_4, C_6 oligomers.

Table 6.2: Ethylene oligomerization reactions catalyzed by SBA-15 and MCM-41 immobilized N^O donor Ni(II), Co(II) and Fe(II) complexes.[a]

Entry	Catalyst	Metal[b] (%)	Yield (g)[c]	Activity[d] $g_{oligomers}$/ mol (M) h	Product Selectivity (%)[e]		
					C_4 (α-C_4)	C_6 (α-C_6)	C_8 - C_{10}
1	**22**	0.568	0.354	35400	26 (91)	71 (18)	3
2	**23**	0.953	0.322	32200	12 (56)	84 (23)	4
3	**24**	6.92	0.277	29000	5 (69)	92 (23)	3
4	**25**	0.960	0.308	30800	17 (51)	80 (33)	3
5[f]	**22**	0.568	0.75	75000	60 (97)	2 (20)	1
6[g]	**22**	0.568	0.587	58700	35 (79)	65 (38)	-
7[h]	**22**	0.568	0.928	92800	52 (98)	23 (19)	-
8[i]	**19**	0.688	0.105	10 500	8 (74)	87 (23)	5

[a]Reaction conditions: [Metal] = 10 µmol, (Calculated based on the ICP-OES data and weighed accordingly). Co-catalyst, $EtAlCl_2$; solvent, *n*-heptane (30 mL); Temperature, 30 ˚C; time, 1 h; Pressure, 10 bar; Al/M ratio = 200. [b]Metal % in the original catalyst sample. [c]Determined using tetradecene internal standard. [d]Activity, g oligomer produced per mol metal per hour. Amount of catalyst calculated using ICP-OES results. [e]Olefinic products were detected by GC-FID and GC-MS. [f]In toluene solvent, the balance of 37 % is for alkylated products. [g]In *n*-hexane medium. [h]Using chlorobenzene solvent and 25 % is alkylated products. [i]Reported in Chapter 5.

6.3.2.2. Effect of catalyst structure and morphology on the catalytic performance of the complexes in ethylene oligomerization reactions.

6.3.2.2.1. The effect of metal identity on the catalytic performance of the immobilized complexes

The identity of the central metal atom controlled the catalytic activities of the complexes. Unsurprisingly, the Ni(II) complexes showed higher catalytic activity compared to the respective Fe(II) and Co(II) catalysts. For instance, complexes **22**-**24**, displayed catalytic

activities of 35 400 $g_{oligomer}$ mol^{-1} (M) h^{-1}, 32 200 $g_{oligomer}$ mol^{-1} (M) h^{-1} and 29 000 $g_{oligomer}$ mol^{-1} (M) h^{-1} respectively (**Table 6.2**, **entries 1-3**). These results are in good agreement with the report by Bryliakov *et al*.[2] highlighting nickel metal centre to give rise to highly active catalysts the iron and cobalt metals for ethylene oligomerization reactions. The identity of the metal centre did have a significant effect on the product distribution of the complexes. Notably, the Ni(II) complexes produced higher amounts of C_4 oligomers (26 %) in comparisons to both Fe(II) and Co(II) complexes. This is in accordance with the "nickel effect" discovered by Ziegler-Natta, which is the ability of the Ni metal centre to promote the formation of short chain oligomers at a higher rate than other late transition metal centres.[34]

6.3.2.2.2. Effect of the solid support

The main objective of this research work was to examine the effect of solid support on the catalytic performance of the immobilized complexes which encompasses both catalytic activity and selectivity of the complexes. As a result, both the SBA-15 and MCM-41 immobilized complexes were screened under similar catalytic conditions and the results are summarized in **Table 6.2** and in **Figure 6.10**. The current results revealed that immobilization with SBA-15 solid support afforded more catalytically active immobilized complexes as compared to MCM-41 and Fe_3O_4 MNPs. For example, **22** displayed a catalytic activity of 35 400 $g_{oligomers}$ mol^{-1} (Ni) h^{-1} whilst its analogous MCM-41 and Fe_3O_4 MNPs immobilized complex **25** and **19** respectively showed lower catalytic activity of 30 800 $g_{oligomers}$ mol^{-1} (Ni) h^{-1} and 10 500 $g_{oligomers}$ mol^{-1} (Ni) h^{-1} respectively at a metal concentration of 10 µmol (**Table 6.2**, **entries 1** *vs* **4** and **8** respectively). The reported results are in good agreement with the data documented by Guo and co-workers,[35] whereby the SBA-15 supported catalysts showed higher catalytic activity than the MCM-41 immobilized counterparts at similar temperature. This was assigned to the larger pore size of SBA-15 and opposed to MCM-41. Despite their pore size differences,

SBA-15 and MCM-41 immobilized complexes did not show marginal influence on the selectivity of the complexes towards the formation of short and long chain oligomers.

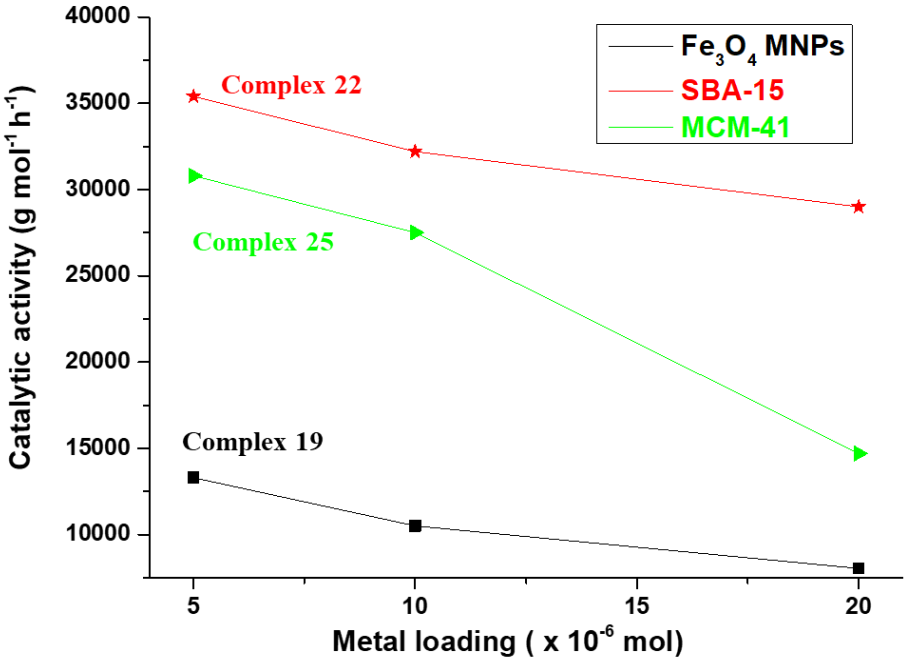

Figure 6.10: The effect of solid support properties on the catalytic activity of the SBA-15, MCM-41 and Fe_3O_4 MNPs immobilized complexes, **22**, **25** and **19** respectively.

6.3.2.3. The influence of pre-catalyst concentration on ethylene oligomerization reactions

To investigate the effect of metal loadings on the catalytic activity and selectivity of the catalysts, **22** was used and metal concentration was varied from 5 µmol to 20 µmol as illustrated in **Figure 6.11**. Generally, the productivity of the complex **22** decreased with increasing metal loadings. For example, catalytic activities of 37 500 $g_{oligomers}$ mol^{-1} (Ni) h^{-1}, 35 400 $g_{oligomers}$ mol^{-1} (Ni) h^{-1}, 26 500 $g_{oligomers}$ mol^{-1} (Ni) h^{-1} and 18 000 $g_{oligomers}$ mol^{-1} (Ni) h^{-1} were recorded for the complex metal concentrations of 5 µmol, 10 µmol, 15 µmol and 20 µmol. A plausible

explanation to the decline of catalytic activity with metal loadings firstly could be that highly dispersed active sites are readily accessible since they are well-aggregated.[36] The selectivity of the complexes was also influenced by the metal concentration, notably, while the selectivity of C_4 oligomers declined with increasing metal concentration, the selectivity of C_6 oligomers remined high. This is attributed to the agglomeration of the metal active sites at higher metal concentration as recently observed by Shin *et al*.[37]

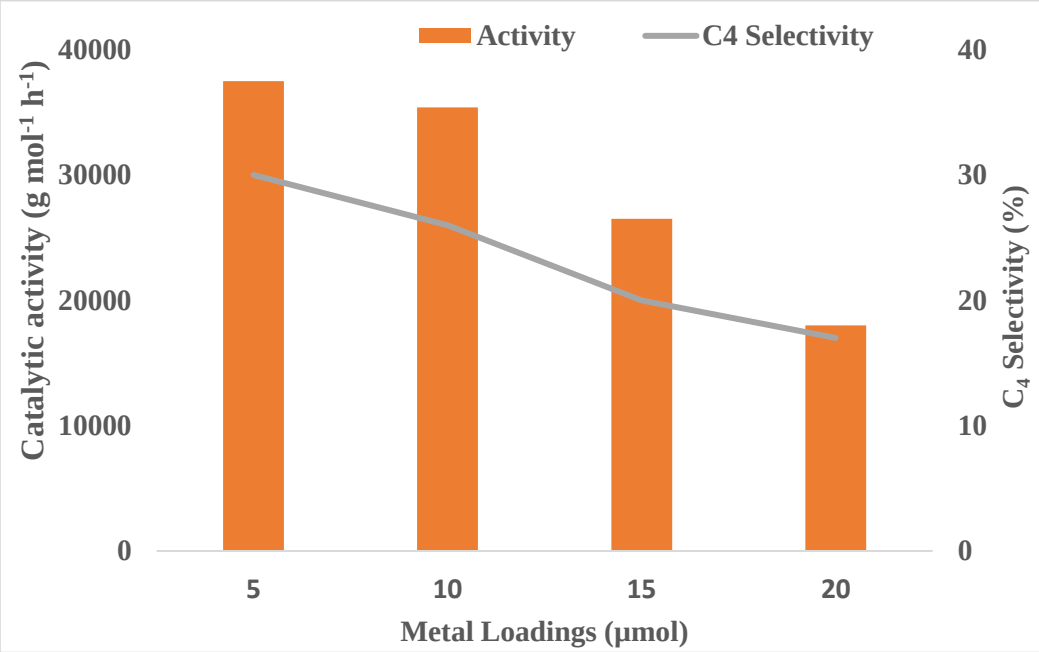

Figure 6.11: The influence of varying metal loadings of catalyst **22** on the catalytic activity and selectivity of C_4 oligomers in ethylene oligomerization reactions.

6.3.2.4. Catalyst recycling experiments in ethylene oligomerization reactions

The recyclability and reusability of the immobilized has become the subject of interest for industrial applications. As such, the recovery and reusability of the SBA-15 and MCM-41 immobilized complexes was investigated in ethylene transformation reactions and the results are given in **Figure 6.12**. After the first run, the catalysts were recovered through centrifugation and decanting of the products. The catalysts were then rinsed with hexane and chlorobenzene to thoroughly remove remaining products. This was then followed by the addition of the fresh solvent and 2 mL $EtAlCl_2$ co-catalyst (200 equivalence). Ethylene pressure was then set at 10 bar after purging and the reaction ran for 1 h at 30 ˚C. The recycling data obtained for the immobilized complexes confirmed the reusability of the immobilized complexes in ethylene oligomerization reactions yet with reductions in the catalytic activities of the complexes as illustrated in **Figure 6.12**. The catalytic selectivity of the complexes remained unchanged during recycling.

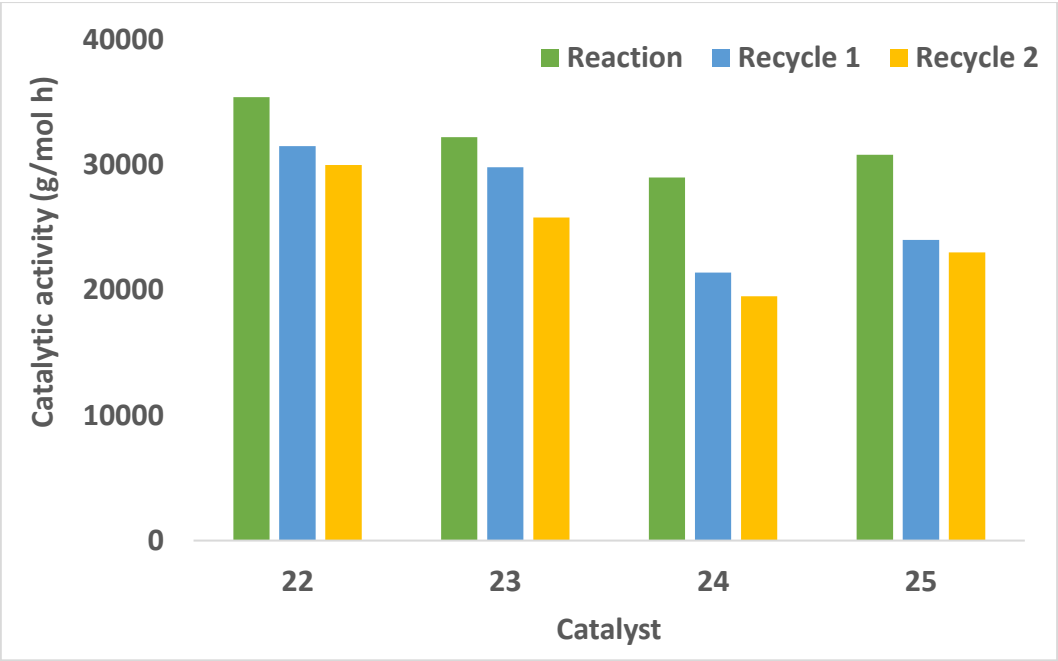

Figure 6.12: Recycling data for the immobilized complexes in ethylene oligomerization reactions.

6.3.2.5. Leaching and post catalytic characterization studies

We took a step further and performed hot filtration experiments where we tested the filtrate for any catalytic activity. This was done by collecting the filtrate after the completion of the second recycling experiment and subjecting it to the standard catalytic reaction conditions. No significant catalytic activity could be quantified from the filtrate signifying the minimal existence or absence of leaching of the active species. Nevertheless, on the light that the mass of the recovered catalysts decreases after each recycling run, EDX and ICP-OES were utilized to determine if the metal centre remains intact after each run. For example, for complex **22** we initially recorded metal contents of 1.53 % and 1.91 % using EDX and ICP-OES respectively. Analysis of the metal contents for the spent catalyst using both EDX (0.95 %) and ICP-OES (1.24) revealed that a there is a loss of almost 40 % the active species which could account for the decline in the catalytic activity of the complexes after each recycling experiment. In simple terms, the metal content loss of 35 % (from 1.91 % to 1.24 %) of complex **22** through leaching

resulted in the decline of the catalytic activity of catalyst **22** of 85 % (from 35 400 $g_{oligomers}$ mol^{-1}(Ni) h^{-1} to 30 000 $g_{oligomers}$ mol^{-1}(Ni) h^{-1}). The same trend was observed for the other immobilized complexes.

The spent catalysts were further analysed using TEM for any possible changes in the morphology after the reactions. **Figure 6.13**-B shows a slightly deformed morphology of the immobilized catalyst **25** in comparison to the TEM image of the fresh complex shown in **Figure 6.13**-A. This also explains the observed decline in the catalytic activity of the complexes and the minor variations in the catalysts' selectivity.

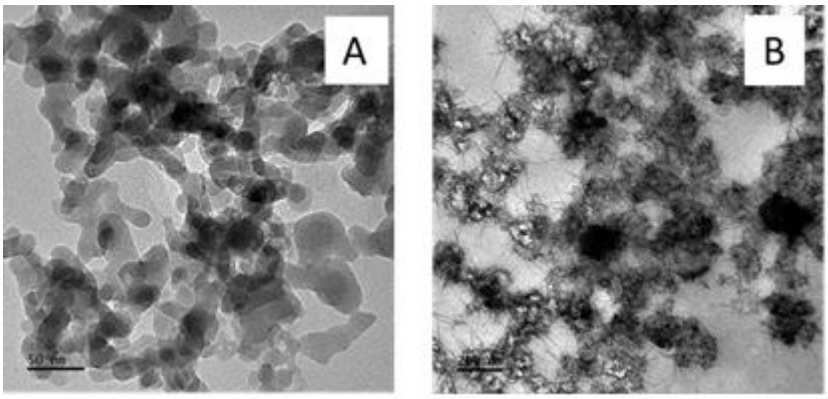

Figure 6.13: The TEM micrograms of the fresh (A) and spent (B) catalyst and diffraction pattern of the immobilized catalyst **22** showing slightly deformed morphology.

6.4. Conclusions

In this chapter, the oligomerization of ethylene using SBA-15 and MCM-41 immobilized Ni(II), Co(II) and Fe(II) complexes chelated by N^O donor ligands combination with ethylaluminum dichloride co-catalyst is reported. The influence of the structure of the immobilized catalysts, metal concentration and most importantly the immobilization support on the catalysts catalytic activity and selectivity was studied. Ordered MCM-41 supported complexes showed lower catalytic activity than their SBA-15 counterparts. Decreasing the metal loading improved the catalytic activity per metal centre. The immobilized complexes could be recycled and re-used for two runs with noticeable loss of catalytic activity arising from active sites leaching and catalysts abrasion.

6.5. References

1. Zhang, H., Li, X., Zhang, Y., Lin, S., Li, G., Chen, L., Fang, Y., Xin, H., Li, X., *Energy Environ. Focus.* **2014**, *3*, 246-256.

2. Bryliakov, K. P., Antonov, A. A. , *J. Organomet. Chem.* **2018**, *867*, 55-61.

3. Ajellal, N., Kuhn, M. C. A., Boff, A. D. G., Hoener, M., Thomas, C. M., Carpentier, J.-F., Casagrande Jr., O. L., *Organometallics* **2006**, *25*, 1213-1219.

4. Boudier, A., Breuil, P. R., Magna, L., Olivier-Bourbigou, H., Braunstein, P., *J. Organomet. Chem.* **2012**, *718*, 31-37.

5. Yang, Q. Z., Kermagoret, A., Agostinho, M., Siri, O., Braunstein, P., *Organometallics* **2006**, *25*, 5518.

6. Rezaei, S., Ghorbani-Choghamarani, A., Badri, R., *Appl. Organometal. Chem.* **2016**, *30*, 985-990.

7. Zhao, X. S., Bao, X. Y., Guo, W., Lee, F. Y., *Mater. Today* **2006**, *9*, 32-39.

8. Metzger, E. D., Brozek, C. K., Comito, R. J., Dinca, M., *ACS. Cent. Sci.* **2016**, *2*, 148-153.

9. Canivet, J., Aguado, S., Schuurman, Y., Farrusseng, D., *J. Am. Chem. Soc.* **2013**, *135*, 4195-4198.

10. Kim, M. J., Ahn, S., Yi, J., Hupp, J. T., Notestein, J. M., Farha, O. K., Lee, S. J., *Catal. Sci. Technol.* **2017**, *7*, 4351-4354.

11. Desphande, S., Scrinivas, D., Ratnasamy, P., *J. Catal.* **1999**, *188*, 261-263.

12. Shin, M., Jeong, H., Park, M.-J., Suh, Y.-W., *Appl. Catal. A: Gen.* **2020**, *591*, 117376.

13. Lecocq, V., Bourbigou, H. O., *Oil Gas Sci. Technol.* **2007**, *62*, 761-773.

14. Karbach, F. F., *Silica-supported catalysts for ethylene oligomerization* **2004**, 15-21.

15. Kumar, K., Godeto, T., Darkwa, J., *J. Organomet. Chem* **2016**, *818*, 137-144.

16. Rossetto, E., Nicola, B. P., de Souza, R. F., Bernardo-Gusmao, K., Pergher, S. B. C., *Appl. Catal. A: Gen.* **2015**, *502*, 221-229.

17. Schmidt, R., Hammon, U., Gottfried, S., Welch, M. B., Alt, H. G., *J. Appl. Polym. Sci.* **2003**, *88*, 476-482.

18. Huang, C., Zakharov, V. A., Semikolenove, N. V., Matsko, M. A., Mahmood, Q., Talsi, E. P., Sun, W.-H., *J. Catal.* **2019**, *372*, 103-108.

19. Tuskaev, V. A., Zubkevich, S. V., Saracheno, D., Gagieva, S. Ch., Dorovatovskii, P. V., Kononova, E. G., Khrustalev, V. N., Zarubin, D. N., Bulychev, B. M., Kissin, Y. V., *J. Mol. Catal.* **2019**, *464*, 29-38.

20. Bahuleyan, B. K., Park, D.-W., Ha, C.-S., Kim, I., *Catal. Sury, Asia.* **2006**, *10*, 65.

21. Ngcobo, M.; Ojwach, S., *Inorg. Chim. Acta.* **2017**, *467*, 1-5.

22. Nyamato, G. S., Ojwach, S. O., Akerman, M. P., *Organometallics* **2015**, *34*, 5647-5657.

23. Nyamato, G. S., Ojwach, S. O., Akerman, M. P., *J. Mol. Catal. A: Chem.* **2014**, *394*, 274-282.

24. Ojwach, S. O., Guzei, I. A., Benade, L. L., Mapolie, S. F., Darkwa, J., *Organometallics* **2009**, *28*, 2127-2133.

25. Rome, K., Mclntyre, A., *Chromatography Today.* **2012**, *52*, 52-55.

26. Wei, S., Ma, Z., Wang, P., Dong, Z., Ma, J., *J. Mol. Catal A: Chem* **2013**, *370*, 175-181.

27. Rossetto, E., Nicola, B. P., de Souza, R. F., Bernardo-Gusmao, K., Pergher, S. B. C., *J. Catal.* **2015**, *323*, 45-54.

28. Hannaert, H., Haccuria, M., Mathieu, M. P., *Ind. Chim. Belge* **1967**, *67*, 156.

29. Rossetto, E., Caovilla, M.,Thiele, D., de Souza, R. F., Bernardo-Gusmao, K., *Appl. Catal. A.* **2013**, *454*, 152-159.

30. Hulea, V., Fajula, F., *J. Catal* **2004**, *225*, 213-222.

31. Obuah, C., Omondi, B., Nozaki, K., Darkwa, J., *J. Mol. Catal. A: Chem.* **2014**, *382*, 31-40.

32. Ojwach, S. O., Darkwa, J., *J. Catal. Sci. Technol.* **2019**, *9*, 2078-2096.

33. Bouchmella, K., Mutin, P. H., Stoyanova, M., Poleunis, C., Eloy, P., Rodemerck, U., Gaigneaux, E. M., Debecker, D. P., *J. Catal.* **2013**, *301*, 233-241.

34. Bianchini, C., Giambastiani, G., Luconi, L., Meli, A., *Coord. Chem. Rev.* **2010**, *254* 431-455.

35. Guo, C.-Y., Xu, H., Zhang, M., Zhang, X., Yan, F., Yuan, G., *Catal. Commun.* **2009**, *10*, 1467-1471.

36. Mlinar, A. N., Shylesh, S., Ho, C. O., Bell, A. T., *ACS. Catal.* **2014**, *4*, 337-343.

37. Shin, D. Y., Yoon, J. H., Baik, H., Lee, S. J., *Appl. Catal. A: Gen.* **2020**, *590*, 117363

CHAPTER SEVEN

General conclusive remarks, summary and future prospects

7.1. General conclusions

In summary, this thesis covers the finding of the study of both homogeneous and immobilized nitrogen-oxygen late transition metal complexes as catalysts for the oligomerization of ethylene reactions. The N^O (ethylimino-methyl)phenol ligands (**L1**-**L3**) reacted with $CoCl_2$ and $FeCl_2$ salts produced the Fe(II) and Co(II) metal complexes **1**-**6**. Molecular structure of **2** confirmed the formation of mononuclear complexes of **1**-**4**, containing two tridentate bound anionic ligands **L1** or **L2**. On the other hand, the solid-state structure of **5** established the formation of dinuclear complexes of **5**-**6** bearing a bidentate zwitterionic ligand **L3**. Activation of the Fe(II) and Co(II) complexes with $EtAlCl_2$ or MAO co-catalysts, gave active catalysts in oligomerization of ethylene to give C_4 and C_6 oligomers. Generally, the Co(II) complexes exhibited higher catalytic activities than their Fe(II) analogues. While activation with MAO produced mainly C_4 oligomers (96 %), $EtAlCl_2$ gave predominantly C_6 oligomers. Density functional theory data provided insights on the catalytic activity trends and effect of complex/ligand structure on the ethylene oligomerization reactions.

In **Chapter 4**, the N^O donor 2,4-dibromo-6-((pyridin-2-ylimino) and N^N^O donor (quinolin-8-ylimino)methyl)phenol ligands (**L4**-**L6**) employed produced both bidentate and tridentate Fe(II), Co(II) and Ni(II) complexes (**7**-**15**). The solid state of complex **13a** and **15** confirmed the isoleptic *bis*-chelated nature and the distorted octahedral arrangement of the mononuclear complexes. The complexes formed active species after activation with $EtAlCl_2$ co-catalyst and selectively converted ethylene monomer into C_4 and C_6 oligomers. The

catalytic activities and product distribution of the catalyst relied significantly on the complex structure. The reactions conditions such as Al/M molar ratio, time, pressure and temperature were also optimized. Density Functional Theory calculations, both the NBO charge and HOMO-LUMO energy gaps influenced the catalytic activities of the complexes.

Chapter 5 deals with the synthesis and application of Fe_3O_4 magnetic nanoparticles immobilized N^O phenol((triethoxysilyl)propylimino) (**L7**-**L8**) Fe(II), Ni(II) and Co(II) metal complexes (**16**-**21**) as separable single site catalysts in the oligomerization of ethylene reactions. Activation of the complexes with $EtAlCl_2$ co-catalyst in *n*-heptane, *n*-hexane, toluene and chlorobenzene solvents afforded active catalysts in ethylene oligomerization reactions to give C_4-C_{10} oligomers and alkylated products depending on the solvent medium. Both the identity of the ligand motif and metal atom influenced the catalytic performance of the complexes in the ethylene oligomerization reactions. The complexes were recycled *via* magnetic separation in five successive runs without significant loss of catalytic activity and selectivity. Minimal leaching may be responsible for minor losses in catalytic activities in the recycling experiments.

Chapter 6 focuses on the attempt to examine the influence of solid supports on the catalytic performance of the immobilized late transition metal complexes. The new family of N^O phenol((triethoxysilyl)propylimino) ligands immobilized on SBA-15 and MCM-41 solid supports (**L9**-**L10**) utilized produced Fe(II), Ni(II) and Co(II) complexes (**22**-**25**). Combination of the complexes with $EtAlCl_2$ co-catalyst formed active species for the oligomerization of ethylene reactions. All the complexes exhibited appreciable catalytic activities producing significant amounts of C_4 and C_6 oligomers as well as traces of C_8 and C_{10} oligomers. The SBA-15 immobilized complex was more active in comparisons to the MCM-41 immobilized

complex. The complexes were separable using centrifugation and decantation and were reusable for up to three cycles without drastic drop of catalytic activity.

7.2. Summary

This current work has established and communicated the effect of ligand architecture, identity of central metal atom, and catalytic conditions on the catalytic performance of the late transition metal catalysts. In addition, the influence of immobilization using Fe_3O_4 magnetic nanoparticles and silica solid supports was also investigated and realized.

a) Nickel(II) based late transition metal complexes exhibited higher catalytic activities than their corresponding iron(II) and cobalt(II) counterparts. The bidentate late transition metal complexes, both mononuclear and dinuclear complexes were more active than tridentate late transition metal complexes in ethylene oligomerization reactions.

b) The ligands electronic properties influenced the electrostatic charge distribution of the late transition metal centres, and consequently had significant influence on the respective catalytic activities of both homogenous and immobilized complexes. The increase in the effective net positive charge of the metal centres due to ligand architecture variations increased the catalytic activities of the respective catalysts.

c) The N^O (ethylimino-methyl)phenol ligands resulted in more catalytically active late transition metal based complexes for the dimerization and trimerization of ethylene reactions than the N^N and N^N^O 2,4-dibromo-6-((pyridin-2-ylimino) / (quinolin-8-ylimino)methyl)phenol ligands upon activation using $EtAlCl_2$.

d) Immobilization of the late transition metal catalysts on Fe_3O_4 magnetic nanoparticles, SBA-15 and MCM-41 solid support produced highly active and separable catalysts for the oligomerization of ethylene. The silica (SBA-15) immobilized complexes exhibited higher catalytic activity than the Fe_3O_4 immobilized catalysts. The selectivity of the immobilized complexes was comparable but great influenced by the reaction conditions. The immobilized catalysts were separable and reusable for five consecutive cycles with the Fe_3O_4 magnetic nanoparticles complexes showing high catalysts recovery and minimal or absence of leaching.

e) Comparisons between the homogeneous and immobilized systems containing N^O (ethylimino-methyl)phenol ligands revealed that homogeneous systems are catalytically more active than the heterogenized systems in the oligomerization of ethylene reactions. Both the homogeneous and heterogenized systems formed higher amounts of C_6 oligomers compared to C_4 oligomers implying that they are suitable candidates for ethylene trimerization.

f) The reaction conditions such as co-catalyst, aluminium to metal ratio, time, pressure, temperature and metal concentration greatly influenced the catalytic activity and selectivity of the complexes in ethylene oligomerization reactions. Notably, the immobilized complexes displayed greater thermal stability than the homogeneous systems.

7.3. Future prospects

The value of this contribution towards the design, development and synthesis of catalytically active, selective and separable catalysts for ethylene oligomerization is realized in **Chapters 3-6**. The findings of this research work comprise of both catalytically active and selective homogeneous and heterogeneous catalysts used in ethylene oligomerization. In addition to continuing pursuit of achieving active, selective and separable late transition metal complexes, direct modification of catalysts particle sizes in order affects the catalysts' catalytic performance will also add a value.

The use of biphasic technology is another alternative which can be applied to recycle and reuse costly catalysts in compliance with the principles of Green Chemistry. The Shell Higher Olefin Process (SHOP) was the first industrial manufacturing company to benefit from biphasic technology using P^O chelated Ni(II) complex which operated in butanediol, a phase in which the oligomeric products produced are sparingly soluble. Ionic liquids (ILs) are salts comprising of steric bulky organic cations and inorganic or organic anions. **Figure 7.1** provides general formulas of the most used ILs.

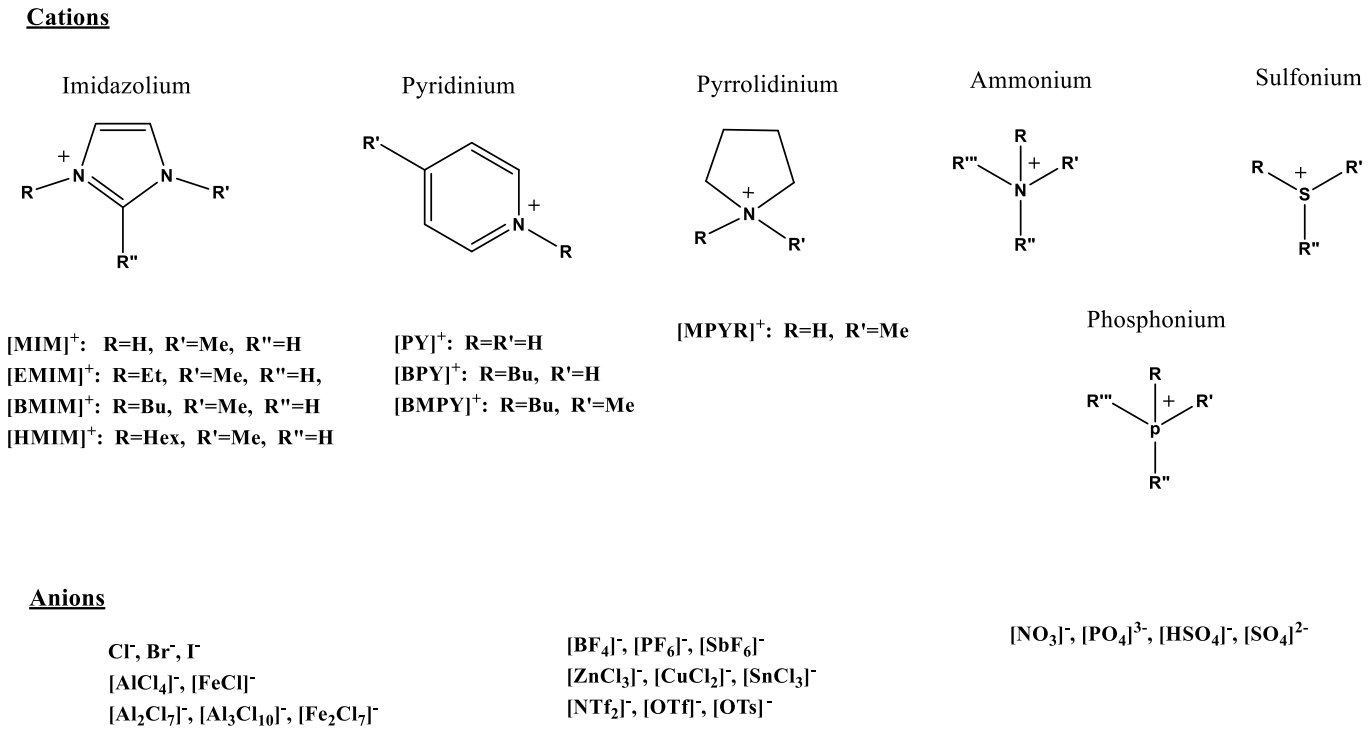

Figure 7.1: General formulae of the some common ILs.

ILs are characterized by their low melting points (< 100 ºC) and their ability to stabilize the transition metal complexes in low oxidation states, makes them suitable solvents for transition metal catalyzed ethylene oligomerization reactions. Furthermore, in ethylene oligomerization reactions, these solvents can serve a very important purpose (biphasic systems) since they do not dissolve apolar compounds which are products of ethylene oligomerization. Therefore, when the polarity of the products is reasonably low, biphasic reactions take place and the complete separation of the catalysts can be attained through decantation. Another advantage of using ionic liquids for ethylene oligomerization reactions such chloroaluminate in biphasic systems, is in the prevention of organometallic complexes hydrolysis arising from the use of protonated solvents. The paramount advantage of using ILs is in the possibility of catalyst recycling, this is a very crucial approach for industrial applications which is in compliance with

the Green Chemistry principles. Therefore, ILs will be used to stabilize and support the previously reported Ni(II) complexes shown in **Figure 7.2**.

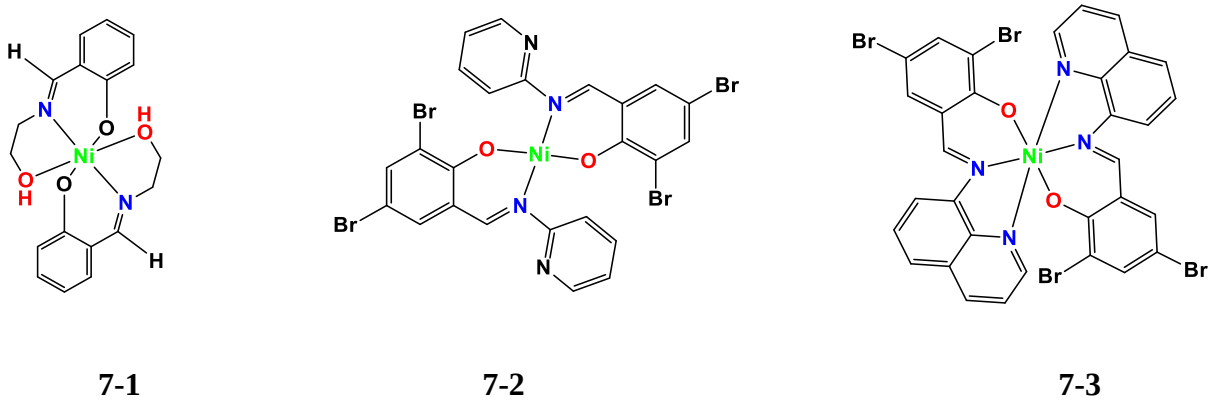

7-1 **7-2** **7-3**

Figure 7.2: Late transition metal complexes reported for ethylene oligomerizations to be used in ILs biphasic systems.